

**Universität Stuttgart**

Germany

**Institut für Mechanik (Bauwesen)**

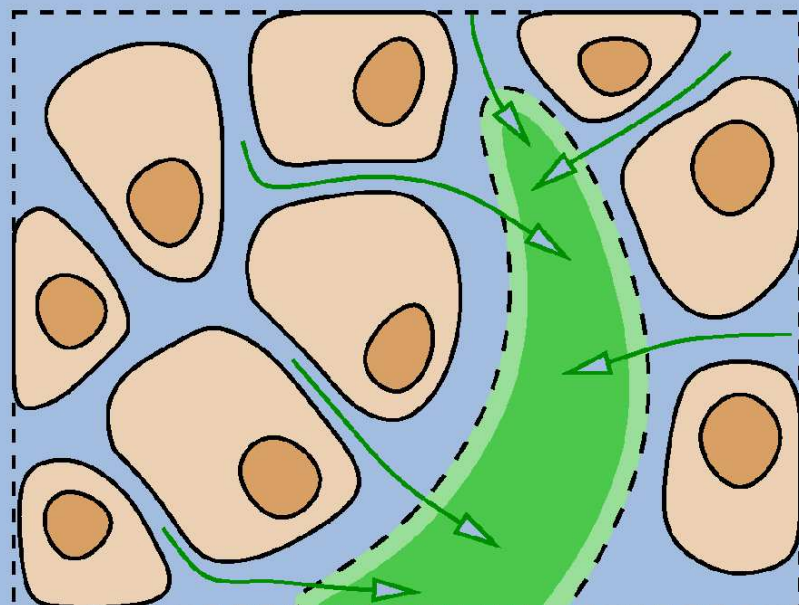
Lehrstuhl für Kontinuumsmechanik

Prof. Dr.-Ing. Dr. h. c. W. Ehlers

## **Continuum Mechanics of Multicomponent Materials**

**Modelling, Numerics and Applications  
for Biological Materials in the Framework  
of the Theory of Porous Media**

Arndt Wagner



Report No.: II-39 (2021)



# Continuum Mechanics of Multicomponent Materials

—

## Modelling, Numerics and Applications for Biological Materials in the Framework of the Theory of Porous Media

Vom Stuttgarter Zentrum für Simulationswissenschaften  
und der Fakultät Bau- und Umweltingenieurwissenschaften  
der Universität Stuttgart genehmigte Habilitationsschrift

vorgelegt von

Dr.-Ing. Arndt Wagner

aus

Waiblingen

Hauptberichter: Prof. Dr.-Ing. Dr. h. c. Wolfgang Ehlers

Mitberichter: Prof. Dr.-Ing. Rainer Helmig

Mitberichter: apl. Prof. Dr.-Ing. Joachim Bluhm

Mitberichter: Prof. Dr. Laura De Lorenzis

Tag der mündlichen Prüfung: 17. Juni 2021

Institut für Mechanik (Bauwesen) der Universität Stuttgart

Lehrstuhl für Kontinuumsmechanik

Prof. Dr.-Ing. H. Steeb

2021

Report No. II-39  
Institut für Mechanik (Bauwesen)  
Lehrstuhl für Kontinuumsmechanik  
Universität Stuttgart, Germany, 2021

**Editor:**

Prof. Dr.-Ing. Dr. h. c. W. Ehlers

© Arndt Wagner  
Institut für Mechanik (Bauwesen)  
Lehrstuhl für Kontinuumsmechanik  
Universität Stuttgart  
Pfaffenwaldring 7  
70569 Stuttgart, Germany

All rights reserved. No part of this publication may be reproduced, stored in a retrieval system, or transmitted, in any form or by any means, electronic, mechanical, photocopying, recording, scanning or otherwise, without the permission in writing of the author.

ISBN 978-3-937399-39-3  
(D 93 – Habilitation, Universität Stuttgart)

## Acknowledgements

This habilitation thesis was created during my profession as an Academic Senior Councilor at the Institute of Applied Mechanics (Civil Engineering), Chair of Continuum Mechanics, at the University of Stuttgart. The mandatory habilitation colloquium took place at the special time of the coronavirus with its associated circumstances. Therefore, I particularly want to take this opportunity to gratefully acknowledge numerous people who contributed in many ways to the realisation of this work.

First of all, I would like to express my deepest appreciation to Professor Wolfgang Ehlers for giving me the privilege to prepare this thesis under his conscionable supervision and reliable scientific and personal support. Undoubtedly, this work would not have been possible without him. I am also very grateful to Professor Rainer Helmig (University of Stuttgart), Professor Joachim Bluhm (University Duisburg-Essen) and Professor Laura De Lorenzis (ETH Zurich) for taking the co-chairs in my habilitation procedure. Furthermore, I want to thank the head of our institute, Professor Holger Steeb, for granting me the scientific freedom to make this work possible and for most valuable discussions which helped me to quickly enter into various related topics.

I have truly enjoyed the outstanding atmosphere among colleagues at the institute, providing an excellent basis for a pleasant and efficient working environment. Furthermore, I really appreciate the countless enjoyable contacts with great people at our university, essentially facilitated by the environments of the Stuttgart Center for Simulation Science, the faculty of civil and environmental engineering and the SFB 1313. Beyond that, I owe special thanks to the colleagues with whom I have worked closely together on individual topics of this habilitation thesis. In particular, these were Professor Oliver Röhrle, Dr.-Ing. Christian Bleiler and Zubin Trivedi, regarding bone-cement injections into vertebra, Dr.-Ing. Jan Lukas Eurich, regarding heat and mass transport in plants and Dr.-Ing. Davina Fink and Patrick Schröder, regarding brain-tumour treatment. Also the effort of my former master students is hereby acknowledged. In this regard, special thanks to Tobias Kattmann and Louise Sauter with whom I worked on the modelling of lymphatic drainage and David Krach for pore-scale simulations using smoothed particle hydrodynamics.

Moreover, the financial support by the Deutsche Forschungsgemeinschaft (DFG, German Research Foundation) is gratefully acknowledged. In particular, findings from funded projects of the Cluster of Excellence in Simulation Technology (ExC 310/2 and ExC 2075 – 390740016), the SFB 1313 (327154368) and the SFB/Transregio 141 have been incorporated here.

Finally, I want to thank my wonderful family and especially my parents for always believing and trusting in me. Last but not least, I want to express my deepest gratitude to my beloved wife Sabine who essentially contributed to the successful completion of this work. She kept my back free by taking over the majority of the mental and physical load requested by our three wonderful children and never got tired of pushing me forward.



# Contents

<b>Deutschsprachige Zusammenfassung</b>	<b>V</b>
Motivation . . . . .	V
Stand der Forschung . . . . .	VII
Themenkomplex und Problemstellung . . . . .	VIII
Gliederung der Arbeit . . . . .	IX
Dokumentation eigener Publikationen . . . . .	XI
<b>I Modelling and Numerics of Multiconstituent Materials</b>	<b>1</b>
<b>1 Introduction</b>	<b>3</b>
1.1 Motivation . . . . .	3
1.2 Scope and range of topics . . . . .	5
1.3 Documentation of own publications . . . . .	7
<b>2 Continuum-mechanical foundations</b>	<b>11</b>
2.1 Historical review of mechanics . . . . .	11
2.2 Historical review of the Theory of Porous Media . . . . .	15
2.3 Fundamentals of the Theory of Porous Media . . . . .	18
2.4 Kinematics of superimposed constituents . . . . .	21
2.5 Stress state of multiconstituent materials . . . . .	26
2.6 Balance equations . . . . .	27
<b>3 Numerical treatment</b>	<b>35</b>
3.1 The finite-element method (FEM) . . . . .	35
3.1.1 Boundary conditions . . . . .	35
3.1.2 Ansatz and test functions . . . . .	36
3.1.3 Weak formulations of governing equations . . . . .	36
3.1.4 Monolithic solution of the coupled problem . . . . .	37
3.2 Application of model-reduction techniques . . . . .	39
3.2.1 Proper orthogonal decomposition . . . . .	41
3.2.2 Discrete empirical interpolation method . . . . .	43

<b>4</b>	<b>Multiscale modelling aspects</b>	<b>47</b>
4.1	Consideration of pore-scale models . . . . .	47
4.1.1	Computational fluid dynamics (CFD) . . . . .	47
4.1.2	Smoothed particle hydrodynamics (SPH) . . . . .	56
4.2	Experimental-data-based approaches . . . . .	74
4.2.1	Inclusion of $\mu$ CT data . . . . .	74
4.2.2	Inclusion of DTI data . . . . .	78
<b>II</b>	<b>Selected Applications for Biological Materials</b>	<b>81</b>
<b>5</b>	<b>Introductory notes to Part II</b>	<b>83</b>
5.1	A brief introduction to continuum biomechanics . . . . .	83
5.2	Classification of the selected continuum-biomechanical applications . . . . .	84
<b>6</b>	<b>Lymphatic drainage</b>	<b>87</b>
6.1	Motivation and introduction . . . . .	87
6.2	Anatomy of the lymphatic system . . . . .	88
6.3	Modelling approach and constitutive settings . . . . .	90
6.4	Numerical examples . . . . .	95
6.4.1	General study of the mass-exchange process . . . . .	95
6.4.2	Application to a human leg . . . . .	98
<b>7</b>	<b>Heat and mass transport in plants</b>	<b>103</b>
7.1	Motivation and introduction . . . . .	103
7.2	Freezing plant tissues . . . . .	104
7.2.1	Stems and wood . . . . .	105
7.2.2	Leaves . . . . .	106
7.3	Modelling approach and constitutive settings . . . . .	107
7.3.1	Basic model setup . . . . .	107
7.3.2	Ice formation via interfacial mass interactions . . . . .	108
7.3.3	Cell dehydration . . . . .	109
7.4	Selected numerical examples . . . . .	109
7.4.1	Basic water transport in a stem . . . . .	110
7.4.2	Water supply in a leaf . . . . .	110
7.4.3	Ice nucleation in a winter horsetail . . . . .	111

---

<b>8</b>	<b>Bone-cement injections into vertebra</b>	<b>113</b>
8.1	Motivation and introduction . . . . .	113
8.2	Modelling approach and constitutive settings . . . . .	115
8.3	Material parameters . . . . .	117
8.4	Numerical treatment . . . . .	118
8.4.1	Weak formulation of the governing equations . . . . .	118
8.4.2	Geometrical modelling and numerical implementation . . . . .	119
8.4.3	Boundary conditions . . . . .	119
8.5	Results . . . . .	120
8.5.1	Image homogenisation by diffusion . . . . .	120
8.5.2	Permeability field . . . . .	121
8.5.3	Finite-element simulation . . . . .	121
8.5.4	Validation . . . . .	124
8.5.5	Sensitivity analysis . . . . .	125
8.6	Discussion . . . . .	125
<b>9</b>	<b>Tumour treatment within brain tissue</b>	<b>129</b>
9.1	Motivation and introduction . . . . .	129
9.2	Anatomy of the human brain . . . . .	129
9.3	Modelling approach for brain tissues . . . . .	130
9.4	Numerical case studies for therapeutic infusions . . . . .	132
9.4.1	Influence and optimisation of the catheter placement . . . . .	134
9.4.2	Application of multiple infusion catheters . . . . .	134
9.5	Multiscale aspects for constitutive equations . . . . .	135
9.5.1	Motivation . . . . .	135
9.5.2	Microscopic model settings . . . . .	136
9.5.3	Geometrical evaluation . . . . .	136
9.5.4	Macroscopic constitutive relation . . . . .	138
9.5.5	Results and discussion . . . . .	139
9.6	Application of model-reduction techniques . . . . .	141
9.6.1	Introduction . . . . .	141
9.6.2	Underlying brain-tissue models . . . . .	142
9.6.3	Further adaptations . . . . .	146
9.6.4	Numerical example for the POD application . . . . .	147
9.6.5	Numerical example for the POD-DEIM application . . . . .	152
9.6.6	Discussion . . . . .	157

9.7	Simulation of brain tumours . . . . .	158
9.7.1	Model adaptation . . . . .	158
9.7.2	Numerical example of apoptosis due to therapeutic treatment . . .	161
<b>10</b>	<b>Concluding remarks</b>	<b>165</b>
	<b>Bibliography</b>	<b>169</b>

# Deutschsprachige Zusammenfassung

## Motivation

Seit jeher befassen sich Menschen in ihrem alltäglichen Leben mit mechanischen Sachverhalten. In diesem Zusammenhang trägt die zielgerichtete und problembezogene Mechanik bis heute durch ein analytisch-mathematisches und numerisches Vorgehen wesentlich dazu bei sowohl unsere Umwelt als auch technische Entwicklungen maßgeblich zu gestalten.

Die Mechanik ist ein Teilgebiet der Physik und repräsentiert dabei eine der ältesten und fundamentalsten Disziplinen der Wissenschaft. Der Ursprung des Begriffs Mechanik lässt sich im altgriechischen Wort *mechané* finden, welches für Maschine, Kunstgriff oder Wirkungsweise steht. Dies spiegelt sich im heutigen Verständnis der Mechanik sehr schön wieder. Im wesentlichen lässt sich im weitläufigen Gebiet der Mechanik alles einordnen, was mit Bewegungen von Körpern und den dabei wirkenden Kräften zu tun hat.

In ihren Ursprüngen war die Mechanik stark empirisch geprägt, frei nach dem Motto „Probieren geht über Studieren“. Die wachsenden technischen Herausforderungen motivierten dann zur Modellbildung, welche auch die Möglichkeit einer Vorhersage von physikalischen Prozessen bietet. Dabei entwickelte sich im Laufe der Zeit eine mathematische Beschreibung der Prozesse durch Gleichungen.

Die Modellierung und die damit verbundene numerische Behandlung mechanikbasierter Fragestellungen erfordert heute immer häufiger eine zusätzliche Einbeziehung verschiedener wissenschaftlicher Disziplinen. Dies zeigt sich deutlich an den immer komplexeren Problemen in der Materialmodellierung (Materialtheorie) der Festkörper sowie an der Notwendigkeit, Festkörper- oder Fluidprobleme nicht nur isoliert zu betrachten, sondern sie immer dann, wenn sie gekoppelt auftreten, sie auch gekoppelt zu behandeln.

Ein poröses Medium (Material) ist, nach allgemeinem Verständnis, ein Festkörper, der Poren (Hohlräume) enthält. Es ist daher nicht überraschend, dass poröse Medien (Materialien) in der Natur und in der gebauten Umgebung allgegenwärtig sind. Bei vielen dieser Materialien kann die poröse Struktur mit bloßem Auge erkannt werden. Bei manchen ist aber eine genauere Betrachtung oder sogar die Verwendung eines (hochauflösenden) Mikroskops erforderlich, um ihre poröse Struktur überhaupt zu identifizieren.

Ein Festkörper mit geschlossenen (nicht zusammenhängenden) Poren (Hohlräumen) stellt einen Sonderfall für poröse Materialien dar, da eine Bewegung des Poreninhalts aufgrund der nicht miteinander verbundenen Poren verhindert wird. Im Gegensatz dazu haben die in dieser Monographie betrachteten porösen Materialien mindestens einen verbundenen Porenraum, oder sogar mehrere Porenräume, die voneinander getrennt sind, aber jeweils für sich durchlässig sind. Eine solche durchgängige Architektur ermöglicht es grundsätzlich, dass der Poreninhalt innerhalb des porösen Gebiets mobil ist. Dabei wird das gesamte Materialverhalten durch die individuellen Eigenschaften der einzelnen Komponenten sowie durch ihre (lokalen) gegenseitigen Wechselwirkungen (wie beispielsweise Massen- oder Impulsaustausch) bestimmt.

Der Porenraum eines porösen Körpers ist typischerweise mit einem Porenfluid (oder auch mehreren Porenfluiden) gefüllt, die sich jeweils in einem flüssigen oder gasförmigen Aggregatzustand befinden können. Darüber hinaus kann jedes Porenfluid selbst eine reale Mischung (Lösung) sein, die aus mehreren Komponenten (Lösungsmittel und darin gelöste Stoffe) bestehen kann.

Aufgrund der vorherrschenden Porengrößen können poröse Materialien zudem in mikro-, meso- oder makroporöse Materialien klassifiziert werden. Der Durchströmungswiderstand eines porösen Materials, welcher üblicherweise als Permeabilität bezeichnet wird, korreliert dabei offensichtlich mit der Porengröße. Grundsätzlich bewirken kleinere Poren einen größeren Widerstand gegen Durchströmung und ergeben somit eine geringere Permeabilität. Es gibt jedoch keine allgemein gültige Relation zwischen Porösität und Permeabilität, da diese noch von anderen Eigenschaften, wie beispielsweise Porenmorphologie oder Eigenschaften der internen Oberflächen (Rauigkeit, Grenzflächenspannung), abhängt.

Beispiele für mikroporöse Materialien sind verschiedene geologische Materialien (Sandstein oder Boden) oder biologische (pflanzliche oder tierische) Gewebe. Ein Beispiel für makroporöse (und hochporöse) Materialien sind Knochen. Bei diesen besitzt die feste Trabekelstruktur typischerweise nur 15 % Volumenanteil und macht diese (harten) biologischen Gewebe ultraleicht.

Das stark gekoppelte Materialverhalten eines flüssigkeitsgesättigten porösen Festkörpers kann am bekannten Konsolidationsproblem der Geotechnik verdeutlicht werden. Dazu nimmt man an, dass ein wassergesättigter Boden spontan belastet wird. Sobald die Last aufgebracht ist, wirkt sie sowohl auf das Bodenskelett als auch auf das Porenwasser. Da die Bodenkörner und das Porenwasser (für moderate Spannungen) materiell inkompressibel sind und das Porenwasser unmittelbar nach dem Aufbringen der äußeren Last noch keine Zeit hatte aus dem Porenraum zu entweichen, kann sich das poröse Festkörperskelett nicht verformen. Ohne Verformung besitzt das Bodenskelett keine effektiven Spannungen und die gesamte Last muss somit vom Porenwasser aufgenommen werden, das heißt vom auftretenden Porenüberdruck. Dies resultiert infolge des sich einstellenden Druckgradienten zu einem wegfließen (ausquetschen) des Porenwassers aus dem belasteten Bereich unter der Last. Die daraus entstehende Verkleinerung des lokalen Porenraums ermöglicht dann erst eine Verformung des Festkörperskeletts und somit resultierende effektive Spannungen. Am Ende des Konsolidierungsvorgangs stellt sich ein Gleichgewicht zwischen der äußeren Last und den effektiven Spannungen des Festkörperskeletts ein, das heißt der Boden trägt die äußere Last, der Flüssigkeitsausfluss stoppt und der Porenüberdruck verschwindet wieder.

Ausgehend von diesem einfachen Beispiel ist es leicht zu erkennen, dass mit zunehmender Anzahl der beteiligten Komponenten das gekoppelte Materialverhalten zunehmend komplexer wird. Es ist daher offensichtlich, dass ein allgemeiner Rahmen (Strategie) zur strukturierten und übersichtlichen Modellierung beliebiger poröser Materialien von immensen Nutzen ist. Solch eine stringente Vorgehensweise ermöglicht dabei die Theorie der porösen Medien (TPM) par excellence.

Auf dem wissenschaftlichen Gebiet der porösen Medien gibt es bis heute unzählige offene Fragen und damit dringenden Forschungsbedarf. Obwohl neue Erkenntnisse aus Experimenten gewonnen werden können, tragen heutzutage auch Modellierung und Simulation

maßgeblich zum Erkenntnisgewinn beim Verhalten poröser Materialien bei und initiieren dabei technische oder biotechnologische Anwendungen und Innovationen.

## Stand der Forschung

Über den zuvor beschriebenen Konsolidationsvorgang hinaus finden sich unzählige weitere Beispiele für gekoppelte Prozesse in porösen Materialien sowohl in der gewachsenen als auch in der gebauten Umwelt. Durch meine wissenschaftliche Arbeit am Institut für Mechanik (Bauwesen) an der Universität Stuttgart unter der Leitung von Wolfgang Ehlers lernte ich die Mächtigkeit und Schönheit der Theorie der porösen Medien (TPM) kennen, einer auf ersten Prinzipien basierenden Methodik zur rigorosen kontinuumsmechanischen Beschreibung gekoppelter Prozesse in porösen Medien. Im Rahmen von makroskopischen Ansätzen gibt es neben der TPM noch alternative Ansätze. Berühmte Beispiele sind die Biot-Theorie (Poroelastizität), die hybride Mischungstheorie oder allgemeine (oft nicht näher spezifizierte) Mischungsbasierte Ansätze. Sicherlich haben alle diese Theorien ihre jeweiligen Rechtfertigungen sowie auch ihre individuellen Stärken und Schwächen, auf die hier jedoch nicht näher eingegangen werden soll.

Die Wurzeln der TPM reichen zurück bis zum Ende des 18. Jahrhunderts, als Reinhard Woltman (1757–1837) das Konzept der Volumenanteile als Verhältnis der volumetrischen Anteile des Bodens und des Porenwassers zum Volumen eines Gesamtdeiches beschrieb. Im 19. Jahrhundert war es dann Henry (Philibert Gaspard) Darcy (1803–1858), der mehrere wichtige Beiträge zur Hydraulik leistete, darunter auch sein berühmtes nach ihm benannte Gesetz (1856) für den Fluss in porösen Medien. Diese konstitutive Gleichung kann auch unter Verwendung von Modellannahmen innerhalb der TPM in moderner Notation gefunden werden.

Die Untersuchungen von Woltman und Darcy basierten damals hauptsächlich auf experimentellen Beobachtungen und Schlussfolgerungen aus anderen wissenschaftlichen Gesetzen. Dies änderte sich erstmals, als Josef Stefan (1835–1893) Diffusionsprozesse im Sinne der Kontinuumsmechanik untersuchte. Stefan beschrieb die Diffusion von Gasen durch poröse Wände und durch starre Membranen auf der Grundlage der Porosität des Festkörpers. Dabei führte er erstmalig das Konzept der Volumenanteile in eine Kontinuumstheorie ein. Zudem wurden von Gustav Jaumann (1863–1924) durch die Verwendung der Tensorrechnung wichtige Grundlagen zur Entwicklung der Kontinuumsmechanik gelegt.

Im Rahmen von ingenieur- und geotechnischen Problemen tauchen immer wieder die Namen zweier berühmter Personen auf, Karl von Terzaghi (1883–1963) und Maurice (Anthony) Biot (1905–1985). Da Terzaghi kein Mathematiker war, fand er keine kontinuumsmechanisch basierten Ansätze. Als Ingenieur versuchte Terzaghi aber immer Theorie und Praxis zu verbinden. Daher führte Terzaghis Arbeit zu einigen Widersprüchen, insbesondere mit Paul Fillunger (1883–1937). Im Gegensatz zu Terzaghi betrachtete Fillunger das Problem als ein binäres Medium aus zwei miteinander wechselwirkenden Kontinua, Boden und Wasser. Unter diesem Gesichtspunkt kann Fillunger als Pionier der modernen TPM angesehen werden. Im Gegensatz zu den vielzitierten Werken von Biot, die Terzaghis

Grundideen folgten, ging Fillungers Werk fast verloren. Erst Reint de Boer (1935–2010) als Begründer der TPM fand die Artikel von Fillunger wieder und setzte die Beiträge zur TPM in dieser wissenschaftlichen Ideologie fort.

Der letzte Stand der Forschung begann mit der Aufarbeitung der Kontinuumsmechanik zu Beginn der 1950er Jahre, als Clifford (Ambrose) Truesdell (der III, 1919–2000) die sogenannte rationale Mechanik als moderne Sicht auf Kontinuumsmechanik und Thermodynamik einschließlich Mischungstheorien manifestierte. Ray Bowen (geboren 1936) war es dann schließlich, der 1967 die ersten konstitutiven Gleichungen für Mischungen formulierte. Diese wegweisenden Beiträge von Bowen erkannte Wolfgang Ehlers (geboren 1951) in den 1980er Jahren. Ehlers identifizierte das große Potenzial von Bowens Beiträgen für eine Übertragung auf die Beschreibung mehrphasiger poröser Materialien und überzeugte de Boer, in dieses sich stark weiterentwickelnde Forschungsfeld einzusteigen. Zur gleichen Zeit arbeitete auch Joachim Bluhm am Lehrstuhl von de Boer und beteiligte sich an der Entwicklung der kontinuumsmechanischen Basis der TPM. Die aktuelle Generation von TPM Forschern wurde unter diesen wissenschaftlichen Lehrern ausgebildet.

## Themenkomplex und Problemstellung

Wie bereits erwähnt bestehen poröse Materialien typischerweise aus mehreren (untereinander wechselwirkenden oder voneinander abhängigen) Komponenten (im Sinne von Materie oder Substanz), die das integrale Gesamttaggregat bilden. Dabei kann jede Komponente in unterschiedlichen Phasen (Aggregatzuständen) also fest, flüssig oder gasförmig vorliegen. Der Begriff Konstituierende wird im Kontext eines Modells verwendet. Beispielsweise kann eine Konstituierende abhängig vom gewählten Modellansatz mehrere Komponenten enthalten und ein Konstituierende kann auch unterschiedliche Phasenzustände annehmen. Für den einfachsten Fall eines TPM Modells, welches ausschließlich aus einem Festkörperskelett und einer einzelnen Porenflüssigkeit besteht, ist die Verwendung der Begriffe „zweiphasen“, „zweikomponenten“ und „zweikonstituierenden“ deckungsgleich.

Für die Behandlung von mehrphasigen Materialien in einem kontinuumsmechanischen Rahmen ist es erforderlich, dass die zugrundeliegende Mikrostruktur für die Beschreibung auf der Makroskala initial homogenisiert wird. Dazu werden die einzelnen Konstituierenden durch ein volumetrisches Mittelungsverfahren im (Gedanken)modell in eine makroskopische Betrachtung des Gesamttaggregats überführt. Auf diese Weise geht die TPM von Anfang an von einem idealisierten Gesamttaggregat (Mischung aus nicht mischbaren Konstituierenden) aus, bei dem angenommen wird, dass sich die zugrunde liegenden Konstituierenden des mehrphasigen Materials über ein bestimmtes repräsentatives Elementarvolumen (REV) in einer idealen Verteilung befinden. Dies impliziert, dass alle Konstituierende gleichzeitig das gesamte Volumen des betrachteten Gebiets einnehmen, was eine kontinuierliche Beschreibung und damit auch das Aufstellen von Gradienten ermöglicht. Infolgedessen werden jedoch die geometrischen und physikalischen Parameter des Gesamttaggregats (wie Verformung oder Spannungsgrößen) im gesamten Bereich definiert und müssen daher als statistische Mittelwerte tatsächlich auftretender Variablen ver-

standen werden. Diese Grundvoraussetzung für die Anwendung einer Kontinuumstheorie für das Gesamtaggregat beschränkt die lokale Aussage, ermöglicht jedoch die Behandlung realistischer Ingenieursprobleme mit großen Längenabmessungen.

In den letzten Jahren lag mein wissenschaftlicher Schwerpunkt auf der Entwicklung und Umsetzung von Modellierungs- und Simulationstechniken der TPM. Diese Methoden wurden dabei auf vielfältige Anwendungsmöglichkeiten poröser Materialien, wie beispielsweise technische, geotechnische oder biomedizinische Fragestellungen, angepasst. Darüber hinaus gilt mein derzeitiges Interesse dem sich aktuell sehr stark entwickelnden Feld der Kontinuumsbiomechanik. Dieses Interesse wurde bereits während der Anfertigung meiner Dissertation über die Modellierung von Gehirngewebe geweckt.

Die Forschung in der Kontinuumsbiomechanik besitzt neben dem benötigten Erkenntnisgewinn (Prozessverständnis), durch geeignete Modelle biologischer Materialien, zudem ein sehr großes Potenzial für medizinische und klinische Anwendungen und Innovationen. So wird bis heute die klinische Standardbehandlung fast immer ohne Berechnungen (Vorhersagen), mit zugrunde liegenden Modellen und Simulationen, durchgeführt. Deshalb liegt in der Anwendungsweitergabe zur Medizin eine der Hauptaufgaben für die nähere Zukunft. Wenn die entwickelten leistungsstarken Simulationswerkzeuge in der Medizin Anwendung finden kann die Entscheidungsgrundlage für behandelnde Ärzte verbessert werden. Dies beinhaltet dabei beispielsweise eine Verbesserung der patientenspezifischen Behandlung oder die Minimierung von unerwünschten Nebenwirkungen. Die rechnergestützte Kontinuumsbiomechanik ist jedoch ein herausforderndes und interdisziplinäres Gebiet welches sich in der Schnittstelle der Disziplinen Biologie, Chemie und Physik befindet. Demzufolge muss die klassische Kontinuumsmechanik um zusätzliche Bestandteile erweitert werden und darüber hinaus der mehrphasigen Zusammensetzung biologischer Materialien Rechnung tragen.

Diese Monographie soll den aktuellen Stand der Forschung sowie aktuelle Entwicklungen auf dem wachsenden Gebiet der Kontinuumsbiomechanik mehrphasiger Materialien aufzeigen. Die Inhalte dieser Arbeit wurden während meiner Postdoktorandenzeit am Institut für Mechanik (Bauwesen) erstellt, wo ich die großartige Gelegenheit hatte, mit vielen Menschen in mehreren thematisch zugehörigen Projekten zusammenzuarbeiten. Die daraus resultierenden Erkenntnisse und Beiträge haben diese Habilitationsschrift maßgeblich geprägt.

## Gliederung der Arbeit

Nach einer allgemeinen Motivation und Einführung in **Kapitel 1** besteht die Arbeit im Wesentlichen aus zwei Teilen, einem theoretischen/methodischen **Teil 1** und einem anwendungsbezogenen **Teil 2**.

In Teil 1 werden die Modellierung und die numerischen Grundlagen für die Beschreibung von mehrphasigen Materialien zusammengestellt. Dies umfasst die kontinuumsmechanischen Grundlagen, die numerische Umsetzung sowie einige Aspekte der Mehrskalenmodellierung poröser Medien.

Im Einzelnen bietet **Kapitel 2** einen historischen Überblick über die Mechanik im All-

gemeinen sowie die Entstehungsgeschichte der TPM. Darüber hinaus wird die kontinuumsmechanische Modellierung von Mehrphasenmaterialien vorgestellt. Das folgende **Kapitel 3** befasst sich mit der Numerik von Mehrphasenmaterialien. Darin werden zunächst etablierte Ansätze wie die Finite-Elemente-Methode (FEM) sowie neuere Entwicklungen wie die Anwendung von Modellreduktionstechniken diskutiert. In **Kapitel 4** werden einige Aspekte der Mehrskalenmodellierung vorgestellt. Dies beinhaltet die Berücksichtigung zugrunde liegender Porenskalenmodelle sowie datenbasierte (experimentelle) Ansätze.

In Teil 2 werden ausgewählte Anwendungen für biologische Materialien vorgestellt, die zunächst in **Kapitel 5** einführend beschrieben und klassifiziert werden. Die einzelnen Anwendungsbeispiele umfassen dann die Lymphdrainage, Eisbildungsprozesse in Pflanzen, Knochenzementinjektionen in Wirbelkörper und ausgewählte Aspekte der Modellierung von Gehirngewebe inklusive der Beschreibung des Verhaltens von Hirntumoren während ihrer Wachstumsphase und unter einer medikamentösen Behandlung.

Die erste Anwendung in **Kapitel 6, Lymphdrainage**, betrifft die (manuelle oder instrumentelle) Behandlung (Mobilisierung) von Lymphödemen, die durch eingelagerte interstitielle Flüssigkeit in menschlichen Geweben, beispielsweise im Bein, verursacht werden. Neben eigenen Originalarbeiten wurden hierbei auch weitere Beiträge verwendet, die durch meine Betreuung der studentischen Arbeiten von Tobias Kattmann (Forschungsmodul) und Louise Sauter (Bachelorarbeit) entstanden.

In der zweiten Anwendung in **Kapitel 7, Wärme- und Massentransport in Pflanzen**, werden Modellierungsstrategien für frostbeständige Pflanzen unter Gefrierbedingungen vorgestellt. Die Ergebnisse entstammen einer Zusammenarbeit im Rahmen des von der Deutschen Forschungsgemeinschaft (DFG) finanzierten Projekts „*Transport of heat and mass in natural porous materials with graded structure: from functional properties of plant tissues towards customised construction materials (A01)*“ als Teil des transregionalen Sonderforschungsbereichs (SFB/Transregio) 141 „*Biological Design and Integrative Structures – Analysis, Simulation and Implementation in Architecture*“. Die Projektleitung hatten die Antragsteller Wolfgang Ehlers und Anita Roth-Nebelsick und verantwortlich für die Projektbearbeitung war Lukas Eurich.

Die dritte Anwendung in **Kapitel 8, Knochenzementinjektionen in Wirbelkörper**, wurde bereits 2012 durch die Betreuung der Diplomarbeit von Christian Bleiler ins Auge gefasst. Basierend auf diesen Vorarbeiten wurde das Projekt „*Modelling of material injection processes into porous structures applied to vertebroplasty (C03)*“ erfolgreich als Teil des Sonderforschungsbereichs (SFB) 1313 „*Interface-Driven Multi-Field Processes in Porous Media – Flow, Transport and Deformation*“ eingerichtet. Gefördert wird dieses Projekt demzufolge von der DFG. Für dieses Projekt sind Oliver Röhrle und ich die Projektleiter und die Projektbearbeitung erfolgt durch Zubin Trivedi.

Die vierte Anwendung in **Kapitel 9, Hirntumorbehandlung**, geht auf meine Doktorarbeit zurück. Ausgehend von den damals erarbeiteten Grundlagen werden hier weitere Entwicklungen vorgestellt. Insbesondere werden drei Themen diskutiert: *(i)* Mehrskalenaspekte, *(ii)* die Anwendung von Modellreduktionstechniken und *(iii)* die Simulation von Tumorstwachstumsprozessen. Das letztgenannte Thema wurde ebenfalls von der DFG gefördert und stellte das Projekt „*Tumour growth and atrophy of lung cancer metastases in the brain (PN 4-7)*“ im Rahmen des Exzellenzclusters EXC 310 „*Simulationstechnik*

(*SimTech*)“ dar. Für dieses Projekt waren die Projektkoordinatoren Wolfgang Ehlers und ich und der Projektbearbeiter war Patrick Schröder. Darüber hinaus wurde kürzlich ein Nachfolgeprojekt „*Data-integrated simulation of tumour growth and regression in brain tissue (PN 2-2B)*“ von der DFG im Rahmen des Exzellenzclusters EXC 2075 „*Data-Integrated Simulation Science (SimTech)*“ gefördert, das von mir in Zusammenarbeit mit Tim Ricken geleitet wird. Für die Projektbearbeitung ist Marlon Suditsch zuständig.

Schließlich wird die Arbeit in **Kapitel 10** mit einigen abschließenden Bemerkungen und zukünftigen Perspektiven abgeschlossen.

## Dokumentation eigener Publikationen

Bei dieser Habilitationsschrift handelt es sich um eine semikumulative Arbeit. Diese enthält somit sowohl (noch) unveröffentlichte wie auch bereits veröffentlichte (eigene) Inhalte. Um dabei dem Charakter einer Habilitationsschrift gerecht zu werden, wurde bei der Erstellung dieser Monographie ein besonderes Augenmerk auf ein einheitliches Gesamterscheinungsbild sowie einen thematisch klar zusammenhängenden Aufbau gelegt. Um dies zu erreichen wurden die aus Publikationen entnommenen Inhalte dabei entsprechend sinngemäß in die Monographie eingebettet, so dass einzelne Textteile entweder identisch übernommen, umformuliert, entfallen oder hinzugekommen sind. Eine eindeutige Unterscheidung aller direkter und indirekter Zitierungen war demzufolge kaum umzusetzen. Darüberhinaus ist eine direkte Kennzeichnung aller bereits wörtlich veröffentlichten Textpassagen mit Anführungszeichen meiner Ansicht nach auch nicht zielführend, da dies zu einer sehr unübersichtlichen Darstellung mit schlechter Lesbarkeit führen würde.

Deshalb sind alle zugrunde liegenden Veröffentlichungen in dieser Arbeit jeweils zu Beginn ihrer Verwendung in einer einführenden bibliografischen Anmerkung dokumentiert (in der Regel in den Kapiteleinführungen). Um dabei aber trotzdem den enthaltenen wörtlichen Textbausteinen Rechnung zu tragen sind die aufbereiteten Veröffentlichungsabschnitte jeweils komplett mit  $\gg (\cdot) \ll_{\text{(Seite des Zitatbeginns)}}$  gekennzeichnet. Im Umkehrschluss sind alle nicht gekennzeichneten Texte Originalbeiträge dieser Habilitationsschrift. Zur Übersicht ist im Folgenden eine (ausgewählte) Liste von (eigenen) wissenschaftlichen Arbeiten aufgeführt, die nach meiner Promotion entstanden und in diese Arbeit eingeflossen sind.

### Veröffentlichungen und Buchbeiträge (peer-reviewed):

1. Bleiler, C.; **Wagner, A.**; Stadelmann, V. A.; Windolf, M.; Köstler, H.; Boger, A.; Gueorguiev-Rüegg, B.; Ehlers, W. & Röhrle, O.: Multiphasic modelling of bone-cement injection into vertebral cancellous bone. *International Journal for Numerical Methods in Biomedical Engineering* **31**, 37–57 (2015). <https://doi.org/10.1002/cnm.2696>
2. Eurich, L.; Schott, R.; **Wagner, A.**; Roth-Nebelsick, A. & Ehlers, W.: Fundamentals of heat and mass transport in frost-resistant plant tissues. In J. Knippers, K. Nickel & T. Speck (Eds.) *Biomimetic Research for Architecture and Building*

- Construction* (pp. 97–108). Springer, Cham (2016). [https://doi.org/10.1007/978-3-319-46374-2\\_6](https://doi.org/10.1007/978-3-319-46374-2_6)
3. Fink, D.; **Wagner, A.** & Ehlers, W.: Application-driven model reduction for the simulation of therapeutic infusion processes in multi-component brain tissue. *Journal of Computational Science* **24**, 101–115 (2018). <https://doi.org/10.1016/j.jocs.2017.10.002>
  4. Ehlers, W. & **Wagner, A.**: Multiscale Aspects in the Multiphasic Modelling of Human Brain Tissue. In P. Wriggers & T. Lenarz (Eds.) *Biomedical Technology* (Vol. 84, pp. 3–13). Springer, Cham (2018). [https://doi.org/10.1007/978-3-319-59548-1\\_1](https://doi.org/10.1007/978-3-319-59548-1_1)
  5. Ehlers, W. & **Wagner, A.**: Modelling and simulation methods applied to coupled problems in porous-media mechanics. *Archive of Applied Mechanics* **89**, 609–628 (2019). <https://doi.org/10.1007/s00419-019-01520-5>
  6. Ehlers, W. & **Wagner, A.**: Coupled problems in biological systems. In H. Altenbach & A. Öchsner (Eds.) *Encyclopedia of Continuum Mechanics* (pp. 453–465). Springer, Berlin, Heidelberg (2020). [https://doi.org/10.1007/978-3-662-55771-6\\_32](https://doi.org/10.1007/978-3-662-55771-6_32)
  7. **Wagner, A.**; Eggenweiler, E.; Weinhardt, F.; Trivedi, Z.; Krach, D.; Lohrmann, C.; Jain, K.; Karadimitriou, N.; Bringedal, C.; Volland, P.; Holm, C.; Class, H.; Steeb, H. & Rybak, I.: Permeability estimation of regular porous structures: a comparison of methods. *Transport in Porous Media* **138**, 1–23 (2021). <https://doi.org/10.1007/s11242-021-01586-2>
  8. Eurich, L.; Schott, R.; Shahmoradi, S.; **Wagner, A.**; Borja, R. I.; Roth-Nebelsick, A. & Ehlers, W.: A thermodynamically consistent quasi double-porosity thermo-hydro-mechanical model for cell dehydration of plant tissues at subzero temperatures. *Archive of Applied Mechanics* (2021). <https://doi.org/10.1007/s00419-021-01947-9>

### Konferenzbeiträge (Proceedings):

1. Schröder, P.; **Wagner, A.** & Ehlers, W.: Towards the continuum-mechanical modelling of metastatic tumour growth in the brain. *Proceedings in Applied Mathematics and Mechanics* **15**, 107–108 (2015).
2. **Wagner, A.** & Ehlers, W.: Theoretical and numerical aspects in the multiphasic modelling of human brain tissue. *Proceedings in Applied Mathematics and Mechanics* **15**, 117–118 (2015).
3. Schröder, P.; **Wagner, A.** & Ehlers, W.: Multi-component modelling and simulation of metastases proliferation within brain tissue. *Proceedings in Applied Mathematics and Mechanics* **16**, 101–102 (2016).

4. Eurich, L.; Schott, R.; **Wagner, A.**; Roth-Nebelsick, A. & Ehlers, W.: From functional properties of frost-resistant plant tissues towards customised construction materials – A continuum-mechanical approach. *Proceedings in Applied Mathematics and Mechanics* **16**, 81–82 (2016).
5. Ehlers, W. & **Wagner, A.**: Simulation technology applied to coupled problems in continuum mechanics. In A. Zingoni (Ed.) *Insights and Innovations in Structural Engineering, Mechanics and Computation* (pp. 378–381). Taylor & Francis Group, London (2016).
6. Schröder, P.; **Wagner, A.**, Stöhr, D.; Rehm, M. & Ehlers, W.: Data-driven simulation of metastatic processes within brain tissue. *Proceedings in Applied Mathematics and Mechanics* **17**, 221–222 (2017).
7. **Wagner, A.**; Fink, D.; Schröder, P. & Ehlers, W.: Towards a virtual mechanical human brain. *Proceedings in Applied Mathematics and Mechanics* **17**, 225–226 (2017).
8. Eurich, L.; **Wagner, A.** & Ehlers, W.: A new material description for plant tissues under frost exposure. In M. Papadrakakis, E. Onate & B. Schrefler (Eds.) *Proceedings of the VII International Conference on Coupled Problems in Science and Engineering* (pp. 275–286). Barcelona (2017).
9. Eurich, L.; **Wagner, A.** & Ehlers, W.: Modelling functional properties of frost-resistant plant tissues for transfer to construction materials. In M. von Scheven, M.-A. Keip & N. Karajan (Eds.) *Proceedings of the 7th GACM Colloquium on Computational Mechanics* (pp. 238–241). Stuttgart (2017).
10. Schröder, P.; **Wagner, A.**; Stöhr, D.; Rehm, M. & Ehlers, W.: Variation of different growth descriptions in a metastatic proliferation model. In M. von Scheven, M.-A. Keip & N. Karajan (Eds.) *Proceedings of the 7th GACM Colloquium on Computational Mechanics* (pp. 259–262). Stuttgart (2017).
11. Eurich, L.; **Wagner, A.** & Ehlers, W.: Numerical realisation of freezing processes in frost-resistant plant tissues. *Proceedings in Applied Mathematics and Mechanics* **17**, 185–186 (2017).
12. Eurich, L.; **Wagner, A.** & Ehlers, W.: Coupled mass interactions in plant tissues under frost conditions. *Proceedings in Applied Mathematics and Mechanics* **18**, e201800143 (2018).
13. Schröder, P.; **Wagner, A.**; Stöhr, D.; Rehm, M.; Jensch, A.; Radde, N. & Ehlers, W.: Modelling of lung-metastases apoptosis within brain tissue. *Proceedings in Applied Mathematics and Mechanics* **18**, e201800323 (2018).
14. **Wagner, A.**; Fink, D. & Ehlers, W.: Efficient numerical simulations of drug delivery in multi-component brain tissue. *Proceedings in Applied Mathematics and Mechanics* **18**, e201800127 (2018).

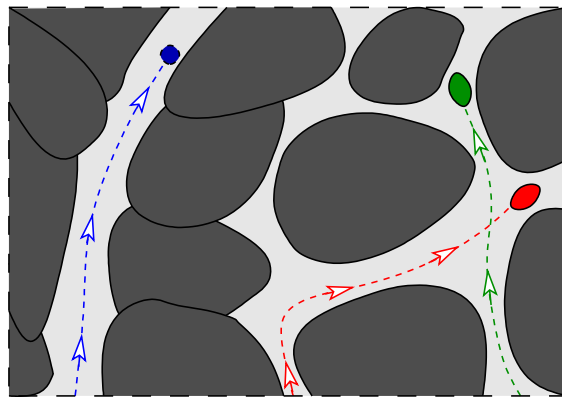
15. Schröder, P.; **Wagner, A.**; Stöhr, D.; Rehm, M. & Ehlers, W.: Continuum-mechanical modelling of apoptosis. *Proceedings in Applied Mathematics and Mechanics* **19**, e201900310 (2019).
16. Eurich, L.; Shahmoradi, S.; **Wagner, A.**; Borja, R. I. & Ehlers, W.: Simulating plant-cell dehydration using a double-porosity formulation based on the Theory of Porous Media. *Proceedings in Applied Mathematics and Mechanics* **19**, e201900243 (2019).
17. Trivedi, Z.; Bleiler, C.; **Wagner, A.** & Röhrle, O.: A parametric permeability study for a simplified vertebra based on regular microstructures. *Proceedings in Applied Mathematics and Mechanics* **19**, e201900383 (2019).

#### Sonstige Veröffentlichungen:

1. Ehlers, W. & **Wagner, A.**: Die Bedeutung der Mechanik für die Gesellschaft: gestern heute und morgen. *Österreichische Ingenieur- und Architekten-Zeitschrift (OIAZ)* **161**, 167–171 (2016).
2. Schott, R.; Eurich, L.; **Wagner, A.**; Roth-Nebelsick, A. & Ehlers, W.: Gefrieren – aber richtig. In J. Knippers, U. Schmid & T. Speck (Eds.) *Baubionik - Biologie beflügelt Architektur, Stuttgarter Beiträge zur Naturkunde* (pp. 62–71). Naturkundemuseum Stuttgart (2017).

# Part I

## Modelling and Numerics of Multiconstituent Materials based on the Theory of Porous Media





# Chapter 1: Introduction

## 1.1 Motivation

According to the common understanding, a porous medium is a solid material containing pores (voids). Therefore, it is not surprising that porous media are ubiquitous in nature and build environment. In some of these materials, the porous structure can be seen with the naked eye, others require a closer look or even the use of high-resolution imaging to identify their porous structure. In general, solid materials with closed pores (voids), as sketched in Figure 1.1 (a), represent a special case of porous materials, since a movement of the pore content is not allowed due to the non-connected pores. In contrast, the porous materials considered in this monograph have at least one connected pore space, cf. Figure 1.1 (b), or multiple pore spaces which are separated from each other but individually connected, cf. Figure 1.1 (c). Such a pervasive architecture basically allows a pore content to be mobile within the porous domain.

Obviously, the overall material behaviour of these porous media is governed by the individual behaviour (properties) of the components as well as by their (local) mutual interactions, such as mass or momentum exchanges. Typically, the pore space is filled by one or multiple pore fluid(s), which can be in a liquid or gaseous state of aggregation. Moreover, a pore-fluid component can be itself a real mixture (solution), which can be composed of several components (solvent and solutes). Depending on the pore size, porous materials can be further divided into micro-, meso- or macro-porous materials. Obviously, the pore size is somehow related to the resistance of the porous material to flow, commonly denoted as permeability. Basically, smaller pores indicate a lower permeability. However, there is no generally valid relation. Examples for micro-porous materials can be found by various geological materials (sandstone or soil) or biological (plant and animal) tissues. An example for macro-porous (and highly porous) materials are bones. In particular, the trabecular structure typically own only 15% solidity, this means that the bulk volume barely contains the base material and make these biological (hard) tissues ultralight.

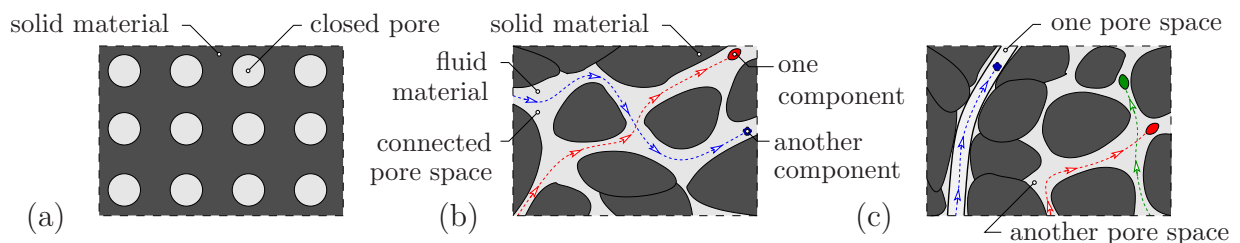


**Figure 1.1:** (a) non-connected pore space (b) single connected pore space with multiple pore content (c) two separated pore spaces with individual connectivity.

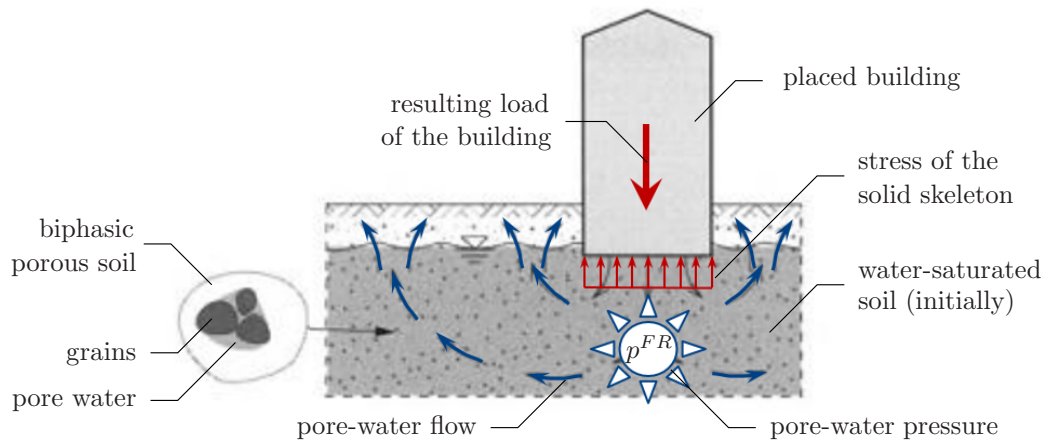


**Figure 1.2:** Sketch of the basic consolidation problem for a ground-water-saturated soil during loading, adapted from Ehlers [80].

The strongly-coupled behaviour of a fluid-saturated porous skeleton can be nicely discussed at the well-known consolidation problem of geotechnical engineering, extracted from Ehlers & Wagner [96]. As an example, a ground-water-saturated soil is loaded by a building that is assumed to be wished in place, cf. Figure 1.2. Once the load is applied, it acts upon both soil skeleton and pore water. However, since the soil grains and the pore water are basically materially incompressible and the pore water has no time to escape from the pore space right after having applied the external load, the solid skeleton cannot deform. Without deformation, the soil skeleton does not perform effective stresses, cf. Ehlers [84], and the complete load has to be carried by the pore water, i. e. by the appearing pore pressure. This, in turn, leads to an excess pressure gradient and the pore water flows out from the loaded region beneath the footing of the building. This shrinks the local pore space, while the solid deforms and produces effective stresses. After a while, the solid stresses become large enough such that equilibrium between the external load and the effective stresses is reached. This marks the end of the consolidation procedure, where the soil is carrying the external load alone, the fluid efflux stops and the excess pore pressure vanishes again, cf. Figure 1.3.

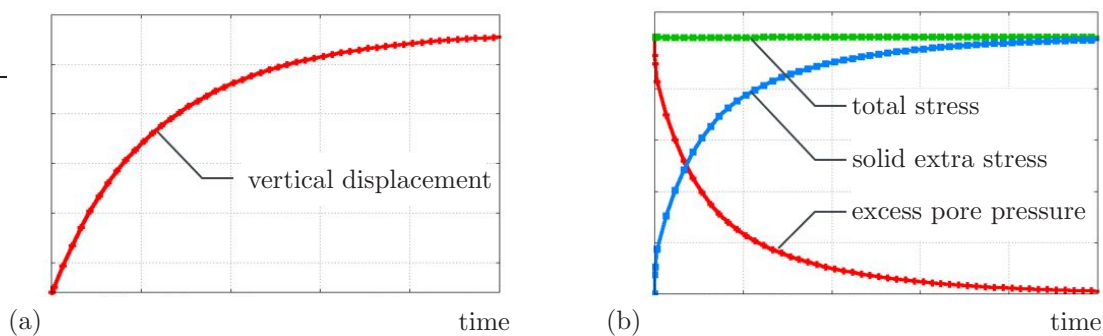


**Figure 1.3:** Qualitative temporal development of the vertical settlement under the footing of the building in (a) and (b) related vertical stress partitioning.

It is easily recognised that with an increasing number of participating components the coupled material behaviour becomes more and more complex. Therefore, a general framework to describe porous materials is of immense benefit.

Up to now, there are countless open questions and, thus, challenges in this scientific field. Although knowledge can be obtained from experiments, reliable simulations based on sound models of the porous material behaviour help to foster the understanding and drive engineering or bioengineering applications/innovations.

## 1.2 Scope and range of topics

Beyond the previously described fundamental consolidation procedure, countless comparable examples for coupled processes within multiphasic materials can be found in the grown and build environment. Due to my scientific work at the Institute of Applied Mechanics (IAM) in Stuttgart under the leadership of Wolfgang Ehlers, I got to know the power and beauty of the Theory of Porous Media (TPM), a first-principle-based framework for the rigorous continuum-mechanical description of coupled processes in porous materials. However, there exist alternative macroscopic (REV-scale) approaches besides the TPM. Famous examples are the Biot theory (or theory of poroelasticity), cf., e.g., Biot [25], the hybrid mixture theory, cf., e.g., Bennethum & Cushman [23], or general (often not further specified) mixture-based approaches, cf., e.g., Coussy *et al.* [67], Hassanizadeh & Gray [138] or Helmig [145]. Surely, all of these approaches have their justification and their individual strengths and weaknesses.

During the last years, my scientific focus was on modelling and simulation techniques of the TPM applied to various kinds of porous materials, e.g., geotechnical, engineering and biological tissues. Furthermore, my particular interest is currently related to continuum-biomechanical problems, which already arised during the conduction of my dissertation thesis about brain-tissue modelling.

Research in continuum biomechanics provides a high potential for clinical/medical innovations. Until today, standard treatment is almost always performed without underlying models and simulations. Bringing powerful simulation tools into the clinic will help to improve the patient-specific clinical success and minimise unwanted side effects. However, computational biomechanics is a challenging and interdisciplinary field, covering significant ingredients from the disciplines biology, chemistry and physics.

This monograph aims to show the current state-of-the art and recent developments in the growing field of continuum biomechanics of multiphasic materials. The work was carried out during my post-doctoral period at the IAM, where I had the great opportunity to work and collaborate with many people in several related projects. These contributions have significantly shaped this monograph.

After this introducing **Chapter 1**, the thesis is basically structured in two parts, the theoretical **Part 1** and the application-related **Part 2**.

In Part 1, the modelling and numerical fundamentals for the description of multiconstituent materials are composed. This includes the continuum-mechanical foundations, the numerical treatment and multiscale modelling aspects.

The comprehensive fundamental **Chapter 2** provides a historical overview of mechanics in general as well as the formation of the TPM. Furthermore, the continuum-mechanical modelling of multiconstituent materials is introduced based on the review articles of Ehlers & Wagner [96, 97]. The subsequent **Chapter 3** concerns the numerics of multiconstituent materials. Therein, established approaches, such as the finite-element method (FEM), as well as recent developments, such as the application of model-reduction techniques, are discussed. Therefore, content from Fink *et al.* [109] was incorporated. In **Chapter 4**, multiscale modelling aspects are composed. This includes the consideration of underlying pore-scale models based on Wagner *et al.* [278] as well as (experimental) data-inclusion approaches based on Bleiler *et al.* [27].

In Part 2, selected applications for biological materials are presented which are classified in **Chapter 5**. The first application in **Chapter 6, lymphatic drainage**, concerns the (manual or instrumental) treatment (mobilisation) of lymph oedema caused by trapped interstitial fluid in human tissues, for example in the leg. Besides own original work, further contributions were obtained during the supervision of student works, conducted by Tobias Kattmann (research module) and Louise Sauter (bachelor thesis).

In the second application in **Chapter 7, heat and mass transport in plants**, modelling strategies for frost-resistant plants under freezing conditions are presented, cf. Eurich *et al.* [102]. The results were obtained during the collaboration within the project “*Transport of heat and mass in natural porous materials with graded structure: from functional properties of plant tissues towards customised construction materials (A01)*”, funded by the German Research Foundation (DFG) as part of the Transregional Collaborative Research Centre (SFB/Transregio) 141 “*Biological Design and Integrative Structures*”. For this project, the Principal Investigators were Wolfgang Ehlers and Anita Roth-Nebelsick. The research responsible for the project was Lukas Eurich.

The third application in **Chapter 8, bone-cement injections into vertebra**, was initiated by a supervision of the diploma thesis of Christian Bleiler [26] resulting in the article of Bleiler *et al.* [27]. Based on this preliminary work, the project “*Modelling of material injection processes to describe bone-cement injections during vertebroplasty (C03)*” was successfully established as a part of the Collaborative Research Centre (SFB) 1313 “*Interface-Driven Multi-Field Processes in Porous Media – Flow, Transport and Deformation*” funded by the German Research Foundation (DFG). For this project, the Principal Investigators are Oliver Röhrle and myself. The research responsible for the project is Zubin Trivedi.

The fourth application in **Chapter 9, brain-tumour treatment**, trace back to my doctoral thesis. Proceeding from these fundamentals, further contributions are presented here. In particular, three issues are discussed: (i) multiscale aspects published in Ehlers & Wagner [95], (ii) the application of model-reduction techniques published in Fink *et al.* [109] and (iii) the simulation of tumour-growth processes. The latter topic was studied in the project “*Tumour growth and atrophy of lung cancer metastases in the brain (PN4-7)*” funded by the German Research Foundation (DFG) as part of the Cluster of Excellence EXC 310 “*Simulation Technology (SimTech)*”. For this project, the Project Coordinators were Wolfgang Ehlers and myself. The research responsible for the project was Patrick Schröder. Furthermore, a succeeding project “*Data-integrated simulation of*

*tumour growth and regression in brain tissue (PN 2-2B)*” was funded by the German Research Foundation (DFG) as part of the Cluster of Excellence EXC 2075 “*Data-integrated Simulation Science (SimTech)*”, which is led by myself in collaboration with Tim Ricken. The research responsible for the project is Marlon Suditsch.

Finally, the thesis is closed in **Chapter 10** with some concluding remarks and future perspectives.

### 1.3 Documentation of own publications

This habilitation thesis is of semicummulative nature. Therefore, it contains both, (yet) unpublished and already published (own) content. In order to guarantee the character of a habilitation thesis as a monograph, special attention was paid to a uniform overall appearance and a thematically clear structure. In order to achieve this, the content taken from the publications was correspondingly embedded in the monograph such that individual parts of the text were either taken over identically, reformulated, deleted or added. It was therefore difficult to make a clear distinction between all direct and indirect citations. In this regard, a direct marking (with quotation marks) of all word-for-word passages that have already been published is, in my opinion, also not reasonable, since this would lead to an inconvenient appearance and results in a poor readability.

Therefore, all of the underlying publications in this work are documented in a bibliographic note at the beginning of their use (typically in the introduction of a chapter or a section). However, in order to account for the word-for-word text modules, the customised publication parts are entirely indicated using  $\gg (\cdot) \ll_{(\text{page of citation beginning})}$ . If this is not the case, all unmarked texts are original contributions (with usual citation technique for external literature) to this habilitation thesis. This includes parts which are prefaced by an introductory note, accounting for provided inspiration. For an overview, a (selected) list of (own) scientific papers (emerged after my doctorate) which are incorporated into this habilitation thesis is given below.

#### Full papers and book chapters (peer-reviewed):

1. Bleiler, C.; **Wagner, A.**; Stadelmann, V. A.; Windolf, M.; Köstler, H.; Boger, A.; Gueorguiev-Rüegg, B.; Ehlers, W. & Röhrle, O.: Multiphasic modelling of bone-cement injection into vertebral cancellous bone. *International Journal for Numerical Methods in Biomedical Engineering* **31**, 37–57 (2015). <https://doi.org/10.1002/cnm.2696>
2. Eurich, L.; Schott, R.; **Wagner, A.**; Roth-Nebelsick, A. & Ehlers, W.: Fundamentals of heat and mass transport in frost-resistant plant tissues. In J. Knippers, K. Nickel & T. Speck (Eds.) *Biomimetic Research for Architecture and Building Construction* (pp. 97–108). Springer, Cham (2016). [https://doi.org/10.1007/978-3-319-46374-2\\_6](https://doi.org/10.1007/978-3-319-46374-2_6)
3. Fink, D.; **Wagner, A.** & Ehlers, W.: Application-driven model reduction for the simulation of therapeutic infusion processes in multi-component brain tissue. *Jour-*

- Journal of Computational Science* **24**, 101–115 (2018). <https://doi.org/10.1016/j.jocs.2017.10.002>
4. Ehlers, W. & **Wagner, A.**: Multiscale Aspects in the Multiphasic Modelling of Human Brain Tissue. In P. Wriggers & T. Lenarz (Eds.) *Biomedical Technology* (Vol. 84, pp. 3–13). Springer, Cham (2018). [https://doi.org/10.1007/978-3-319-59548-1\\_1](https://doi.org/10.1007/978-3-319-59548-1_1)
  5. Ehlers, W. & **Wagner, A.**: Modelling and simulation methods applied to coupled problems in porous-media mechanics. *Archive of Applied Mechanics* **89**, 609–628 (2019). <https://doi.org/10.1007/s00419-019-01520-5>
  6. Ehlers, W. & **Wagner, A.**: Coupled problems in biological systems. In H. Altenbach & A. Öchsner (Eds.) *Encyclopedia of Continuum Mechanics* (pp. 453–465). Springer, Berlin, Heidelberg (2020). [https://doi.org/10.1007/978-3-662-55771-6\\_32](https://doi.org/10.1007/978-3-662-55771-6_32)
  7. **Wagner, A.**; Eggenweiler, E.; Weinhardt, F.; Trivedi, Z.; Krach, D.; Lohrmann, C.; Jain, K.; Karadimitriou, N.; Bringedal, C.; Voland, P.; Holm, C.; Class, H.; Steeb, H. & Rybak, I.: Permeability estimation of regular porous structures: a comparison of methods. *Transport in Porous Media* **138**, 1–23 (2021). <https://doi.org/10.1007/s11242-021-01586-2>
  8. Eurich, L.; Schott, R.; Shahmoradi, S.; **Wagner, A.**; Borja, R. I.; Roth-Nebelsick, A. & Ehlers, W.: A thermodynamically consistent quasi double-porosity thermo-hydro-mechanical model for cell dehydration of plant tissues at subzero temperatures. *Archive of Applied Mechanics* (2021). <https://doi.org/10.1007/s00419-021-01947-9>

#### Conference contributions (Proceedings):

1. Schröder, P.; **Wagner, A.** & Ehlers, W.: Towards the continuum-mechanical modelling of metastatic tumour growth in the brain. *Proceedings in Applied Mathematics and Mechanics* **15**, 107–108 (2015).
2. **Wagner, A.** & Ehlers, W.: Theoretical and numerical aspects in the multiphasic modelling of human brain tissue. *Proceedings in Applied Mathematics and Mechanics* **15**, 117–118 (2015).
3. Schröder, P.; **Wagner, A.** & Ehlers, W.: Multi-component modelling and simulation of metastases proliferation within brain tissue. *Proceedings in Applied Mathematics and Mechanics* **16**, 101–102 (2016).
4. Eurich, L.; Schott, R.; **Wagner, A.**; Roth-Nebelsick, A. & Ehlers, W.: From functional properties of frost-resistant plant tissues towards customised construction materials – A continuum-mechanical approach. *Proceedings in Applied Mathematics and Mechanics* **16**, 81–82 (2016).

5. Ehlers, W. & **Wagner, A.**: Simulation technology applied to coupled problems in continuum mechanics. In A. Zingoni (Ed.) *Insights and Innovations in Structural Engineering, Mechanics and Computation* (pp. 378–381). Taylor & Francis Group, London (2016).
6. Schröder, P.; **Wagner, A.**, Stöhr, D.; Rehm, M. & Ehlers, W.: Data-driven simulation of metastatic processes within brain tissue. *Proceedings in Applied Mathematics and Mechanics* **17**, 221–222 (2017).
7. **Wagner, A.**; Fink, D.; Schröder, P. & Ehlers, W.: Towards a virtual mechanical human brain. *Proceedings in Applied Mathematics and Mechanics* **17**, 225–226 (2017).
8. Eurich, L.; **Wagner, A.** & Ehlers, W.: A new material description for plant tissues under frost exposure. In M. Papadrakakis, E. Onate & B. Schrefler (Eds.) *Proceedings of the VII International Conference on Coupled Problems in Science and Engineering* (pp. 275–286). Barcelona (2017).
9. Eurich, L.; **Wagner, A.** & Ehlers, W.: Modelling functional properties of frost-resistant plant tissues for transfer to construction materials. In M. von Scheven, M.-A. Keip & N. Karajan (Eds.) *Proceedings of the 7th GACM Colloquium on Computational Mechanics* (pp. 238–241). Stuttgart (2017).
10. Schröder, P.; **Wagner, A.**; Stöhr, D.; Rehm, M. & Ehlers, W.: Variation of different growth descriptions in a metastatic proliferation model. In M. von Scheven, M.-A. Keip & N. Karajan (Eds.) *Proceedings of the 7th GACM Colloquium on Computational Mechanics* (pp. 259–262). Stuttgart (2017).
11. Eurich, L.; **Wagner, A.** & Ehlers, W.: Numerical realisation of freezing processes in frost-resistant plant tissues. *Proceedings in Applied Mathematics and Mechanics* **17**, 185–186 (2017).
12. Eurich, L.; **Wagner, A.** & Ehlers, W.: Coupled mass interactions in plant tissues under frost conditions. *Proceedings in Applied Mathematics and Mechanics* **18**, e201800143 (2018).
13. Schröder, P.; **Wagner, A.**; Stöhr, D.; Rehm, M.; Jensch, A.; Radde, N. & Ehlers, W.: Modelling of lung-metastases apoptosis within brain tissue. *Proceedings in Applied Mathematics and Mechanics* **18**, e201800323 (2018).
14. **Wagner, A.**; Fink, D. & Ehlers, W.: Efficient numerical simulations of drug delivery in multi-component brain tissue. *Proceedings in Applied Mathematics and Mechanics* **18**, e201800127 (2018).
15. Schröder, P.; **Wagner, A.**; Stöhr, D.; Rehm, M. & Ehlers, W.: Continuum-mechanical modelling of apoptosis. *Proceedings in Applied Mathematics and Mechanics* **19**, e201900310 (2019).

16. Eurich, L.; Shahmoradi, S.; **Wagner, A.**; Borja, R. I. & Ehlers, W.: Simulating plant-cell dehydration using a double-porosity formulation based on the Theory of Porous Media. *Proceedings in Applied Mathematics and Mechanics* **19**, e201900243 (2019).
17. Trivedi, Z.; Bleiler, C.; **Wagner, A.** & Röhrle, O.: A parametric permeability study for a simplified vertebra based on regular microstructures. *Proceedings in Applied Mathematics and Mechanics* **19**, e201900383 (2019).

#### Other publications:

1. Ehlers, W. & **Wagner, A.**: Die Bedeutung der Mechanik für die Gesellschaft: gestern heute und morgen. *Österreichische Ingenieur- und Architekten-Zeitschrift (OIAZ)* **161**, 167–171 (2016).
2. Schott, R.; Eurich, L.; **Wagner, A.**; Roth-Nebelsick, A. & Ehlers, W.: Gefrieren – aber richtig. In J. Knippers, U. Schmid & T. Speck (Eds.) *Baubionik - Biologie beflügelt Architektur, Stuttgarter Beiträge zur Naturkunde* (pp. 62–71). Naturkundemuseum Stuttgart (2017).

# Chapter 2:

## Continuum-mechanical foundations

### 2.1 Historical review of mechanics

BIBLIOGRAPHIC NOTE: The content of this section is based on the following original article: Ehlers, W. & Wagner, A.: Die Bedeutung der Mechanik für die Gesellschaft: gestern heute und morgen. (The importance of mechanics for the society: yesterday, today and tomorrow.) *Österreichische Ingenieur- und Architekten-Zeitschrift*, **161** (2016), 167–171 [94]. This manuscript is originally published in German and has been translated into English for use here.

» People have always been concerned in their everyday life with mechanical facts; Initially certainly, without to know this explicitly, later targeted and problem-related from empirical beginnings towards analytical-mathematical and numerical procedures. Within the framework of this approach, mechanics has significantly contributed to shape the environment and the technology in the way we know it today.

Mechanics is a branch of physics and represents one of the oldest and most fundamental disciplines in science (Gross *et al.* [130]). The origin of the term mechanics can be found in the Greek word *mechané* (*μηχανή*), which stands for “machine”, “art grip” or “mode of action”. In this sense the beginnings of mechanics go back to the theatre of antiquity in the fifth century before our calculations. Here the acts in tragedies and comedies required, in part, complicated apparatuses, such as, for example, cranes with which a “flight” or the sudden appearance of persons or gods could be realised. These cranes were called *mechané*, a notion which can be understood as the original form of the term mechanics. Originally, the term *mechané* referred to devices with which something could be moved to create surprising effects, cf. Schneider [238]. This is reflected very nicely in today’s understanding of mechanics. In the broad field of mechanics, everything can be classified as related to the movement of bodies and forces acting on them.

In 1687, Newton<sup>1</sup> laid the foundations for classical mechanics in his work “*Philosophiae Naturalis Principia Mathematica*” (Principia), cf. Szabó [262], in which Newton, among other things, declared the law of gravitation and the three world-known principles (axioms) of movement. In doing so, he profoundly benefited from Galileo’s<sup>2</sup> revolutionary and socio-economic view of the world, exploring nature through the combination of experiments, measurements and mathematical analyses. Newton’s formulations were taken

---

<sup>1</sup>Sir Isaac Newton (1643–1727) was an English mathematician, astronomer, and physicist (described in his own day as a “natural philosopher”) who is widely recognised as one of the most influential scientists of all time and laid the foundations of classical mechanics. In particular, Newton formulated the laws of motion and universal gravitation that dominated scientists’ view of the physical universe [WIKIPEDIA].

<sup>2</sup>Galileo Galilei (1564–1642) was an Italian polymath (astronomer, physicist, engineer, philosopher and mathematician). He played a major role in the scientific revolution of the 17<sup>th</sup> century [WIKIPEDIA].

up and further developed by famous contemporaries. In particular, Huygens<sup>3</sup>, Hooke<sup>4</sup>, Leibniz<sup>5</sup> and Bernoulli<sup>6</sup>, who worked intensively on problems of mechanics and gained important insights in this area. However, these findings had yet to be translated into a mathematical calculus, which in the course of the 18<sup>th</sup> and 19<sup>th</sup> century was decisively influenced by Euler<sup>7</sup>, d’Alembert<sup>8</sup>, Lagrange<sup>9</sup>, Laplace<sup>10</sup> and Hamilton<sup>11</sup>. Finally, these theories led to Newtonian mechanics (rational mechanics), which is nowadays also called classical mechanics. It is unquestionable that mechanics play a fundamental role for all engineering services carried out in the past and in the present as well as for future engineering work. Civilian and military applications have brought the “builder” and the “military technician” relatively early on, with the categorisation of the builder as a civil engineer who planned and supervised civilian commissioning work only in the late 18<sup>th</sup> century (Gipsen [123]), while the field of activity of the military engineer later extended to the entire mechanical engineering sector. From today’s point of view, this has played a major role in shaping the professional fields of construction engineers and mechanical engineers. In the following, the influence of mechanics on these occupational images will be examined and elucidated in its historical development for many other areas in which mechanics have played an important role.

---

<sup>3</sup>Christiaan Huygens (1629–1695) was a prominent Dutch mathematician and scientist. He is known particularly as an astronomer, physicist, probabilist and horologist [WIKIPEDIA].

<sup>4</sup>Robert Hooke (1635–1703) was an English natural philosopher, architect and polymath. His adult life comprised three distinct periods: as a scientific inquirer lacking money; achieving great wealth and standing through his reputation for hard work and scrupulous honesty following the great fire of 1666, but eventually becoming ill and party to jealous intellectual disputes. These issues may have contributed to his relative historical obscurity [WIKIPEDIA].

<sup>5</sup>Gottfried Wilhelm (von) Leibniz (1646–1716) was a German polymath and philosopher who occupies a prominent place in the history of mathematics and the history of philosophy, having developed differential and integral calculus independently of Newton. Leibniz’s notation has been widely used ever since it was published [WIKIPEDIA].

<sup>6</sup>Jakob I. Bernoulli (1655–1705) was one of many prominent mathematicians in the famous Bernoulli family. He was an early proponent of Leibnizian calculus and did important contributions in the field of probability [WIKIPEDIA].

<sup>7</sup>Leonhard Euler (1707–1783) was a Swiss mathematician, physicist, astronomer, logician and engineer who made important and influential discoveries in many branches of mathematics like infinitesimal calculus. He also introduced much of the modern mathematical terminology and notation. He is also known for his work in mechanics, fluid dynamics, optics, astronomy, and music theory. He was one of the most eminent mathematicians of the 18<sup>th</sup> century and one of the greatest in history [WIKIPEDIA].

<sup>8</sup>Jean-Baptiste le Rond d’Alembert (1717–1783) was a French mathematician, mechanician, physicist, philosopher and music theorist [WIKIPEDIA].

<sup>9</sup>Joseph-Louis Lagrange (1736–1813) was an Italian mathematician and astronomer. He made significant contributions to the fields of analysis, number theory and mechanics [WIKIPEDIA].

<sup>10</sup>Pierre-Simon Laplace (1749–1827) was an influential French scholar whose work was important to the development of mathematics, statistics, physics and astronomy. He summarised and extended the work of his predecessors by translating the geometric study of classical mechanics to one based on calculus, opening up a broader range of problems. In statistics, the Bayesian interpretation of probability was developed mainly by Laplace [WIKIPEDIA].

<sup>11</sup>William Rowan Hamilton (1805–1865) was an Irish physicist, astronomer, and mathematician, who made important contributions to classical mechanics, optics, and algebra. His studies of mechanical and optical systems led him to discover new mathematical concepts and techniques. His best known contribution to mathematical physics is the reformulation of Newtonian mechanics, now called Hamiltonian mechanics [WIKIPEDIA].

**The beam theory in the 17<sup>th</sup> century and the Lamé-Navier equations:** The beginnings of the beam theory go back to Galileo. In his famous work “Discorsi e Dimostrazioni Matematiche Intorno a Due Nuove Scienze” (Discorsi) of 1638, Galileo already raised elementary questions of strength theory, in particular the question of cracking or breaking of load-bearing structures. He also dealt with questions of “similarity mechanics” (scalability and large-scale effects), cf. Szabó [262]. A relationship with which elastic material behaviour could be described for the first time was formulated by Hooke after the Galileo death in 1678 by the famous Hooke’s law named after him. Therefore, Hooke used the anagram “ceiinossttuv”, which stands for “ut tensio sic vis” (as the strain, so the force). Thus, he described the linearly proportional relationship between the spring force and the associated spring deflection. This connection was supported by experiments on different springs. The ideas on the way to a consistent beam theory were followed by many other important mechanicians of the 17<sup>th</sup> and 18<sup>th</sup> century, with regard to a general elasticity theory. To name only a few prominent personalities of this period, Mariotte<sup>12</sup>, Leibniz, J. I Bernoulli, Euler, Coulomb<sup>13</sup>, Lamé<sup>14</sup>, Navier<sup>15</sup> and Cauchy<sup>16</sup>. Today, the theory of elasticity in the form of the Lamé-Navier equations together with the Bernoullian beam theory form one of the essential foundations for the calculation of structures. Both developments are of fundamental importance to the civil engineer.

**The industrial revolution in the 18<sup>th</sup> and 19<sup>th</sup> centuries:** In contrast to the questions posed by the civil engineer, the occupational profile of the mechanical engineer is closely linked to the construction of machines. This connection can also be seen in the almost identical English terms “engineer” and “engine”. The development of mechanical engineering was essentially shaped by the industrial revolution and the age of the steam in Great Britain in the 18<sup>th</sup> and 19<sup>th</sup> century. During this time, Newton’s mechanics became more and more propagated and increasingly popular. The emerging mechanisation helped to reduce the labour costs and thereby increase the profits. This led to a profound and lasting transformation of the economic and social conditions, whereby the classes of society (originally divided into entrepreneurs and proletarians) were circulated. As a result of this upheaval, the transition from an agricultural society to an industrial society emerged. In this society a common technical language developed with drawings, models and mathematical formulas, which was of fundamental importance for all engineering-related, technical questions and is still essential until today. In general, mechanics serve as a basis for any calculation of structures and machines and, thus, for the disciplines of the civil and the mechanical engineer.

---

<sup>12</sup>Edme Mariotte (1620–1684) was a French physicist and priest (Abbé) [WIKIPEDIA].

<sup>13</sup>Charles Augustin de Coulomb (1736–1806) was a French physicist. He was best known for developing Coulomb’s law, the definition of the electrostatic force of attraction and repulsion, but also did important work on friction [WIKIPEDIA].

<sup>14</sup>Gabriel Léon Jean Baptiste Lamé (1795–1870) was a French mathematician who contributed to the theory of partial differential equations by the use of curvilinear coordinates and the mathematical theory of elasticity [WIKIPEDIA].

<sup>15</sup>Claude Louis Marie Henri Navier (1785–1836) was a French engineer and physicist who specialised in mechanics [WIKIPEDIA].

<sup>16</sup>Baron Augustin-Louis Cauchy (1789–1857) was a French mathematician reputed as a pioneer of analysis. He was one of the first to state and prove theorems of calculus rigorously, rejecting the heuristic principle of the generality of algebra of earlier authors [WIKIPEDIA].

**Fields of activity of the civil engineer:** The first areas of activity of the Civil Engineer included art and cultural buildings. At the same time, very early masterpieces of engineering skill were achieved. An outstanding and very long span of a supporting structure was realised at the dome in the interior of the Pantheon in Rome (125 according to our chronology). In the Middle Ages, with its society of free, less-favoured, unfree and privileged minority from clergy and nobility, the erection of protective structures was of particular importance to the privileged, in order to make it possible for them to live an advantageous life. In today's society, the picture has changed. Modern public utilities and transport structures are of great importance for the modern society. Such structures, however, can often only be created with the use of high engineering skills. Once again, this highlights the immense influence of mechanics (in its capacity as a basic science) on manifold social developments. Think of bridges, as an example, which connect the separate, thereby exerting, among other things, infrastructural influences on society. The influence of engineering art through history also extends to questions of energy supply, ranging from historic buildings to water supply in the Roman Empire through imposing dam constructions to wind power plants, just to name a few examples.

**Fields of activity of the mechanical engineer:** It is obvious that the design and development of machines can fundamentally contribute to the benefit of man but also to the contrary. In this respect, every engineer must be aware of his or her great ethical responsibilities. Examples that can have a very positive impact on the society are found in mechanical engineering contributions to increase productivity, improve mobility, secure supply and increase the quality of life, while it is worth mentioning that the construction and development of military equipment can have devastating effects on the society.

**The combination of mathematics and mechanics:** In its origins, mechanics was strongly empirical, free according to the motto “the proof of the pudding is in the eating”. The growing technical challenges motivated the formation of theory, which also offered the possibility of predicting physical processes. In the course of time, a mathematical description of the processes developed through equations. More than 100 years ago, Lorenz [189] wrote in his contribution (written and published in German) “Die neuere Entwicklung der Mechanik und ihre Bedeutung für den Schiffbau” (“The new evolution of mechanics and its importance in shipbuilding”):

*“Unter den mannigfachen Problemen [...] gewinnen solche aus dem Gebiete der Mechanik eine immer steigende Bedeutung. Infolgedessen kommt der praktisch tätige Ingenieur heute öfter als früher in die Lage, auf dieses als Grundlage alles technischen Wirkens ebenso anerkannte, wie wegen seiner vorwiegend mathematischen Ausgestaltung gern mit einer gewissen Scheu betrachtete Gebiet zurückzugreifen, seine Kenntnisse wieder aufzufrischen und gelegentlich sogar zu erweitern. Dabei stellt sich nicht selten heraus, daß die ins Auge gefaßten Probleme von der bisher überlieferten Mechanik überhaupt noch nicht in Angriff genommen wurden, so daß nichts weiter übrig bleibt, als entweder unter Verzicht auf eine exakte Lösung sich durch Probieren zu helfen oder aber selbst an die Aufgaben heranzutreten.”*

*(“Among the manifold problems [...], those from the field of mechanics are becoming increasingly important. As a result, the practical engineer has more*

*than ever been able to revert to this area as the basis of all technical work, as well as to his preoccupation with a certain awe, due to his predominantly mathematical design. It is not uncommon to see that the problems envisaged have not yet been tackled by the mechanics hitherto handed down, so that there is nothing left but to help either by trying or not to make an exact solution of these tasks.”)*

Lorenz (1906)

This detailed description already pose the necessary link between mathematics and mechanics in order to make further developments possible. Today, it is well-known that from the viewpoint of a mechanical engineer mathematics serves as a supplementary science and provides the language to formulate mechanical issues.

**Modern mechanics in simulation technology:** The modelling and the numerical treatment of mechanical-based questions increasingly require the inclusion of different scientific areas. This is clearly demonstrated by more and more complex problems in the material modelling of the solids as well as the need not only to analyse and numerically calculate solids or fluid problems but also to treat them in a coupled manner, whenever they are coupled. This motivates a continuum-mechanical treatment of multicomponent materials. For the purpose of this monograph, the TPM provides the fundamental methodology to describe such coupled processes. In addition, further quantities may play a role in both material theory and the description of coupled problems, such as electromagnetic or electrochemical fields. The calculation of complex mechanical problems, especially in the case of large numerical problems, provide a large amount of data that must be graphically processed (visualised) in order to be able to understand and interpret the results. <(p. 11)

## 2.2 Historical review of the Theory of Porous Media

Regarding the historical development of the TPM, an excellent overview is given in the pioneering works of de Boer [31], de Boer & Ehlers [35], Ehlers [82] and more recently in de Boer [33] and Ehlers [83]. The last-mentioned article of Ehlers [83] describes the development of the TPM from its origins to contemporary applications, thus presenting porous media in the light of history. Out of this article, some important milestones of the TPM are arranged in the following.

**The early days:** The roots of the TPM date back to the end of the 18<sup>th</sup> century, when Woltman<sup>17</sup> discovered the concept of volume fractions as the ratio of the volumetric portions of the soil and the pore water compared to the volume of the overall dike, cf. Woltman [293]. Therefore, he was also able to conclude to the partial densities of mud as a mixture of soil and water. Besides Woltman, Delesse<sup>18</sup> had comparable ideas. In the

<sup>17</sup>Reinhard Woltman (1757–1837) was a German hydraulic engineer [WIKIPEDIA]. He was the director of hydraulic engineering (Direktor der Strom- und Uferwerke und Leiter des gesamten Wasserbaus) of the city of Hamburg.

<sup>18</sup>Achille Ernest Oscar Joseph Delesse (1817–1881) was a French geologist and mineralogist [WIKIPEDIA]. In his early career as a mining engineer he had the problem to distinguish between the portions of the minerals in a mine.

19<sup>th</sup> century, Darcy<sup>19</sup> published his famous law in 1856, cf. Darcy [69]. In Darcy's law, the filter velocity is related to the hydraulic pressure head weighted by the fluid conductivity. This constitutive equation can also be found by modern approaches within the TPM. Apart from fluid flow in porous media, diffusion problems were studied. The first one who empirically investigated these problems was Fick<sup>20</sup>. Fick's laws were published in 1855, cf. Fick [108]. Fick's first law states that the concentration flow of a species in a mixture of two components is proportional to its concentration gradient. Inserting this finding into the mass conservation equation yields Fick's famous second law.

The investigations by Woltman, Delesse, Darcy and Fick have been based on experimental observations and conclusions from other scientific laws. This was initially changed by Stefan<sup>21</sup> who studied first diffusion behaviour in the sense of continuum mechanics. Stefan described diffusion of gases across porous walls and through rigid membranes on the basis of the porosity of the porous solid, cf. Stefan [253]. Therefore, he firstly included the concept of volume fraction into a continuum theory. Afterwards, Jaumann<sup>22</sup> contributes to the development of continuum mechanics using tensor calculus. Therefore, Jaumann's work can still be considered as modern, and he can definitely be called the pioneer of continuum mechanics and mixture theories as the bearing pillar of the modern TPM. Moreover, Clausius<sup>23</sup> achieved important contributions for merging continuum mechanics and thermodynamics.

**The period of geomechanics:** In the framework of engineering-dominated geotechnical problems, the names of two famous persons constantly recur, Terzaghi<sup>24</sup> and Biot<sup>25</sup>. Since Terzaghi was not a mathematician he did not find continuum-mechanically based approaches. As an engineer, Terzaghi always tried to combine theory and practice. Therefore, Terzaghi's work led to some oppositions, especially with Fillunger<sup>26</sup>. In contrast, Fillunger considered the problem as a binary medium of two interacting continua, soil and water. From this point of view, Fillunger can be regarded as the pioneer of the mod-

<sup>19</sup>Henry Philibert Gaspard Darcy (1803–1858) was a French engineer who made several important contributions to hydraulics including Darcy's law for flow in porous media [WIKIPEDIA]. He was working as a hydraulic engineer at the city of Dijon (1834–1840), where he became the chief engineer for the Cote d'Or in 1840 and retired in 1850.

<sup>20</sup>Adolf Eugen Fick (1829–1901) started to study mathematics but changed to medicine, later on.

<sup>21</sup>Josef Stefan (Slovene: Jožef Štefan) (1835–1893) was a Carinthian Slovene physicist, mathematician, and poet of the Austrian Empire [WIKIPEDIA].

<sup>22</sup>Gustav Jaumann (1863–1924) was an Austrian physicist [WIKIPEDIA].

<sup>23</sup>Rudolf Julius Emanuel Clausius (1822–1888) was a German physicist and mathematician and is considered one of the central founders of the science of thermodynamics [WIKIPEDIA].

<sup>24</sup>Karl von Terzaghi (Karl Anton Terzaghi Edler von Pontenuovo) (1883–1963) was an Austrian mechanical engineer and geotechnical engineer, known as the “father of soil mechanics and geotechnical engineering” [WIKIPEDIA].

<sup>25</sup>Maurice Anthony Biot (1905–1985) was a Belgian-American applied physicist. As a follower of Terzaghi, he was accredited as the founder of the so-called theory of poroelasticity (or Biot's theory) [WIKIPEDIA].

<sup>26</sup>Paul Fillunger (1883–1937) was an Austrian geotechnical engineer [WIKIPEDIA]. Fillunger was the major scientific opponent of Terzaghi. The tragedy of Fillunger's work was that his buoyancy equation included a little mistake recognised by Terzaghi. Fillunger tried to justify his result and a severe personal and scientific conflict emerged that ended with Fillunger's suicide in 1937 (after a scientific commission of the TU of Vienna came to the conclusion that Fillunger was wrong, cf. de Boer [34]).

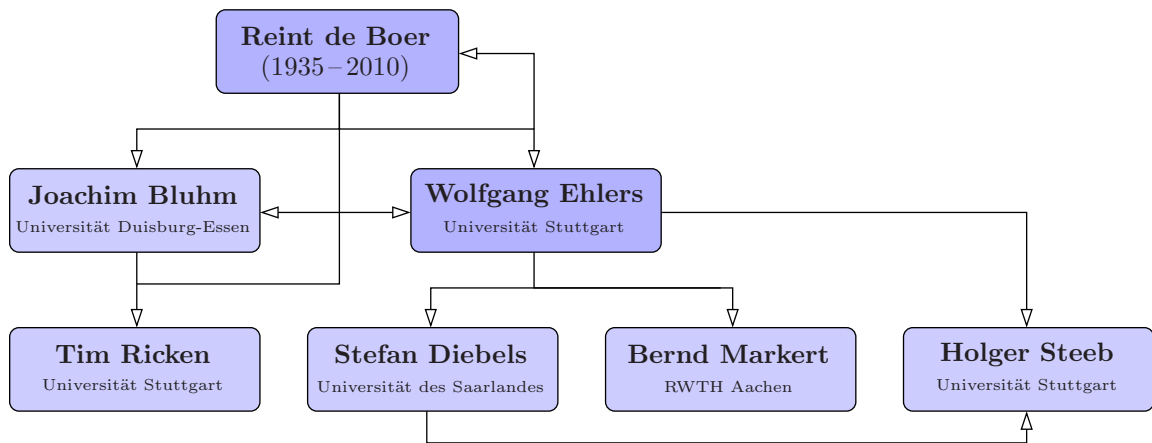


**Figure 2.1:** Selected modern-era scientists (with their current affiliation) working in the field of the TPM following the historical line of Fillunger with their respective scientific imprinting (indicated with arrows).

ern TPM, cf. de Boer [32]. In contrast to the highly cited works of Biot (e.g. Biot [25]) who followed Terzaghi’s basic ideas Fillunger’s work got nearly lost. It was the merit of de Boer<sup>27</sup> who recovered the articles of Fillunger and continued the contributions to the TPM in this scientific ideology.

**The onset of the modern era:** The modern era started with the recovery of continuum mechanics at the beginning of the 1950<sup>th</sup>, when the US-American scientist Truesdell<sup>28</sup> manifested the so-called rational mechanics as a modern view on continuum mechanics and thermodynamics including mixture theories. In 1967, Bowen<sup>29</sup> started, also with respect to his first own attempts to formulate constitutive equations for mixtures, to head into that direction. These fundamental contributions of Bowen were recognised by Ehlers<sup>30</sup> in the 1980<sup>th</sup> who was searching for a habilitation topic in that time. He identified the great potential of Bowen’s contributions for a transfer to the description of multiphasic porous materials and convinced de Boer to step into this evolving research field. During this period, the continuum-mechanical basis of the TPM was initiated. At the same time Bluhm<sup>31</sup> was working at the chair of de Boer and participated to these efforts. The current generation of TPM researchers were educated under these scientific mentors. Over time, the above mentioned historical developments constituted and settled

<sup>27</sup>Reint de Boer (1935–2010) was a German engineering scientist for mechanics. He is considered to be the founder of the Theory of Porous Media.

<sup>28</sup>Clifford Ambrose Truesdell III (1919–2000) was an American mathematician, natural philosopher, and historian of science [WIKIPEDIA].

<sup>29</sup>Ray (Raymond) M. (Morris) Bowen (born in 1936) is an American academic in the broad field of nonlinear continuum mechanics. His speciality was the non-equilibrium thermodynamics associated with the Theory of Mixtures [WIKIPEDIA], cf. Bowen [40, 41, 42, 43].

<sup>30</sup>Wolfgang Ehlers (born in 1951) is a German engineering scientist for mechanics, mainly working in the field of continuum mechanics of multicomponent materials. He played the key role in founding, developing and establishing the TPM and made the theory applicable to a broad range of engineering and biomechanical problems.

<sup>31</sup>Joachim Bluhm is a German academic in the field of continuum mechanics of multicomponent materials.

the TPM as we know it today. In Figure 9.24, selected scientists of the 20<sup>th</sup> and 21<sup>th</sup> century are shown who substantially shaped the TPM and its current understanding. A comprehensive state-of-the-art of the TPM is provided, e.g., by works of de Boer [34] and Ehlers [80, 81]. To describe the approach in one sentence, the TPM proceeds from the treatment of multicomponent materials in the sense of immiscible mixtures using the Theory of Mixtures in combination with the concept of volume fractions accounting for the local composition of the overall aggregate.

BIBLIOGRAPHIC NOTE: The following sections 2.3–2.6 use content from the two original articles: Ehlers, W. & Wagner, A.: Modelling and simulation methods applied to coupled problems in porous-media mechanics. *Archive of Applied Mechanics* **89** (2019), 609–628 [96] and Ehlers, W. & Wagner, A.: Coupled problems in biological systems. In H. Altenbach and A. Öchsner (eds.) *Encyclopedia of Continuum Mechanics*. Springer, Berlin, Heidelberg 2020, pp. 453–465 [97].

## 2.3 Fundamentals of the Theory of Porous Media

» The description of materials with an inherent multiphasic and multicomponent composition contemplates basically two fundamentally different approaches, cf. Ehlers [82]. On the one hand, individual parts can be separated from the overall aggregate in terms of using the Eulerian cut principle and addressed separately via the classical continuum-mechanical framework of singlephasic materials. Whereas, on the other hand, an idealised macroscopical substitute of the overall aggregate can be investigated, proceeding from a continuum theory of the heterogeneous composite with internal interactions. The drawback of the first-mentioned approach is found in the circumstance that all geometric and physical transition conditions at the contact surfaces of the separated individual parts have to be known. This may be possible for ordinary or regular structures, but certainly not for the arbitrary and complex multiphasic and multicomponent materials.

Porous materials are typically composed of multiple (interacting or interdependent) components (in the sense of matter or substance) that constitute the integrated whole (overall) aggregate. Thereby, each component can exist in different phase states (states of aggregation) like solid, liquid or gaseous. The notion constituent is used in the context of a model. For example, a constituent can include several components depending on the chosen model ansatz and a constituent can also take up different phase states. For the simplest case of a TPM model consisting solely of a solid skeleton and one single pore fluid, the usage of the notions two-phasic, two-component and two-constituent is equivalent.

For the treatment of multiphasic material in a continuum-mechanical framework, it is required that the porous body with separated parts on the microscale is initially homogenised on the macroscale (or REV scale). Therefore, a real or virtual volumetric averaging procedure is performed yielding to a macroscopical substitute of the overall aggregate. By doing so, the TPM proceeds from the outset on an idealised overall aggregate where the underlying particular constituents of the multiphasic material are assumed to be in an ideal disorder over a certain representative elementary volume (REV). This

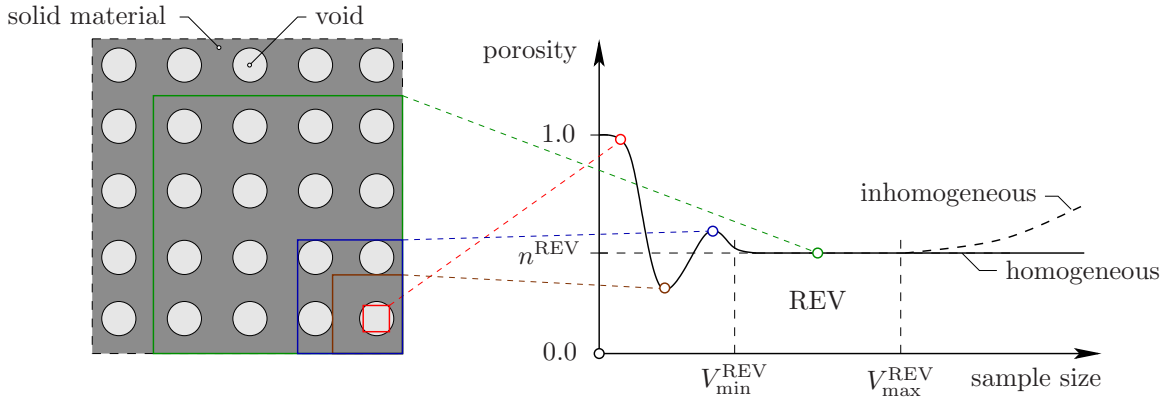


**Figure 2.2:** Evolution of the porosity with increasing size of the chosen REV.

implies that all constituents simultaneously occupy the entire volume of the considered domain allowing for a continuous description and, thus, also to set gradients up. As a consequence, however, the geometric and physical parameters of the overall aggregate (such as deformation or stress quantities) are defined in the entire domain and, thus, have to be understood as statistical averages of actually occurring variables. This basic requirement for the application of a continuum theory for the overall aggregate somehow restricts the local statement of quantities but allows the treatment of realistic problems on the engineering scale. In this regard, the question of the size of the REV is of specific importance. On the one hand, the REV needs to be large enough such that an averaged quantity represents the porous material statistically, i. e., the REV needs to include all microstructural components of the porous aggregate. On the other hand the REV needs to be small enough since it represents a local point for the continuum-mechanical treatment and needs to be able to provide a local statement. In conclusion, the properties of a porous medium may oscillate if the REV is too small, cf. Figure 2.2. With increasing REV size, the oscillations disappear. Moreover, a constant value is found for a property of a homogeneous porous material while the value for a heterogeneous porous material may still change.

As was mentioned before, the applied volumetrical averaging procedure yields an overall TPM model

$$\varphi = \bigcup_{\alpha} \varphi^{\alpha} = \varphi^S \cup \varphi^F \quad (2.1)$$

on the macroscale. Therein, the placeholder  $\alpha$  indicates the considered constituents. In general, a solid constituent  $\varphi^S$  is combined with an overall fluid constituent

$$\varphi^F = \bigcup_{\beta} \varphi^{\beta} = \varphi^L \cup \varphi^G. \quad (2.2)$$

In this regard, the solid skeleton itself can be perfused by a single pore-fluid constituent or by multiple pore-fluid constituents. In general,  $\varphi^L$  denotes a materially incompressible pore liquid, whereas,  $\varphi^G$  denotes a materially compressible pore gas. Moreover, each pore-fluid constituent  $\varphi^{\beta}$  can be treated as a real mixture (chemical solution) of multiple constituents (components of the solution), via

$$\varphi^{\beta} = \bigcup_{\gamma} \varphi^{\gamma} = \varphi^{LS} \cup \varphi^{DS}. \quad (2.3)$$

Therein,  $\varphi^\gamma$  typically contains a liquid solvent  $\varphi^{LS}$  and optionally a single dissolved solute  $\varphi^{DS}$  or multiple dissolved solutes, respectively. These can be also mobile ions (i. e. cations and anions) in the field of electrodynamics. In conclusion, the consideration of real mixtures (including species) represents an extension of the classical TPM approaches (treating solely immiscible constituents) by embedding again elements of the Theory of Mixtures, yielding to an extended Theory of Porous Media (eTPM). In current notations, the naming of a specific TPM model is often related to its included constituents, e. g. binary, ternary or quaternary model.

**Basic quantities:** In order to account for the local composition of the overall aggregate, scalar structure parameters are introduced by means of the concept of volume fractions, viz.:

$$n^\alpha := \frac{dv^\alpha}{dv}. \quad (2.4)$$

Therein, the volume fractions  $n^\alpha$  of  $\varphi^\alpha$  are defined as the local ratios of the partial volume elements  $dv^\alpha$  with respect to the volume element  $dv$  of the overall aggregate. In this regard, the saturation condition

$$\sum_\alpha n^\alpha = n^S + \sum_\beta n^\beta = 1, \quad (2.5)$$

with  $\varphi^\beta$  indicating a certain number of immiscible pore fluids, needs to be satisfied to guarantee that there is no vacant space within the overall porous-media domain. In case of more than one immiscible pore fluid in the pore space, saturation functions  $s^\beta$  of the pore fluids  $\varphi^\beta$  defined with respect to the porosity  $n^F = \sum_\beta n^\beta$  can be introduced via

$$s^\beta := \frac{n^\beta}{n^F} \quad \text{with} \quad \sum_\beta s^\beta = 1. \quad (2.6)$$

In accordance to (2.5), the saturations, as the volume fractions before, sum up to one. In terms of the applied volumetric averaging, two different densities can be introduced. These are

$$\rho^{\alpha R} := \frac{dm^\alpha}{dv^\alpha} \quad \text{and} \quad \rho^\alpha := \frac{dm^\alpha}{dv}, \quad \text{where} \quad \rho^\alpha = n^\alpha \rho^{\alpha R}. \quad (2.7)$$

Therein, the realistic (effective or material) density  $\rho^{\alpha R}$  is defined as a microscopic (local) quantity by the local mass element  $dm^\alpha$  with respect to the local volume element  $dv^\alpha$  of  $\varphi^\alpha$ , while the partial or bulk density  $\rho^\alpha$ , as a macroscopic (averaged) quantity, relates the local mass element  $dm^\alpha$  to  $dv$  of the overall aggregate. These two densities are related to each other by their volume fractions, while the summation of partial densities yields the density  $\rho := \sum_\alpha \rho^\alpha$  of the overall aggregate or the mixture density, respectively.

As mentioned before, the incorporation of miscible components in the classical framework of the TPM requires an extension via elements of the classical Theory of Mixture (TM), cf. [41]. Real mixtures, i. e. the physical combination of at least two substances in the form of a solution, basically consist of a liquid solvent and dissolved solutes, where the solvent provides the dominant volumetric part. In contrast, the volumetric contribution of the dissolved solutes is typically very small, while the dissolved components are part of the whole fluid volume. Therefore, the indication of solutes in a solution using volume fractions is basically not feasible. Instead, the amount of dissolved molecules is considered

by means of concentrations. However, as the total number of molecules in systems is typically very high, molar quantities are related to the amount of particles in one mole by the Avogadro<sup>32</sup> number ( $\approx 6.022 \cdot 10^{23} \text{ mol}^{-1}$ ) and are denoted by the subscript  $(\cdot)_m$ . The molar concentration  $c_m^\gamma$  and the molar mass  $M_m^\gamma$  of a component  $\varphi^\gamma$  in a fluid-mixture constituent  $\varphi^\beta$  are defined as

$$c_m^\gamma := \frac{dn_m^\gamma}{dv^\beta} \quad \text{and} \quad M_m^\gamma := \frac{dm^\gamma}{dn_m^\gamma}. \quad (2.8)$$

Therein, the local number of moles  $dn_m^\gamma$  is related to the local fluid volume  $dv^\beta$  to obtain the molar concentration  $c_m^\gamma$ . Moreover, the component-specific constant molar mass  $M_m^\gamma$  relates the local mass element  $dm^\gamma$  of a component to its local number of moles  $dn_m^\gamma$ . In addition, mole fractions  $x_m^\gamma$  can be introduced via

$$x_m^\gamma = \frac{dn_m^\gamma}{\sum_\gamma dn_m^\gamma} = \frac{c_m^\gamma}{\sum_\gamma c_m^\gamma}, \quad \text{where} \quad \sum_\gamma x_m^\gamma = 1. \quad (2.9)$$

Proceeding from the basic chemical relations introduced above, the partial density  $\rho^\gamma$  with respect to the overall volume element  $dv$  and the partial pore density  $\rho_\beta^\gamma$  of the solutes related to  $dv^\beta$  are defined as

$$\rho^\gamma =: n^\beta \rho_\beta^\gamma, \quad \text{where} \quad \rho_\beta^\gamma = c_m^\gamma M_m^\gamma. \quad (2.10)$$

For a solution of a fluid with dissolved solutes, its effective density  $\rho^{\beta R} = \sum_\gamma \rho_\beta^\gamma$  is given by the sum of the components' partial pore densities. Regarding a considered solution of an overall fluid containing dissolved components, its effective density  $\rho^{\beta R} = \rho_\beta^{LS} + \rho_\beta^{DS}$  is given by the summation of the component's partial pore densities. In the case that the concentration of the solute within the overall solution represents only a very small part, the volume fraction of the solute can be neglected in comparison to the volume fraction of the overall solution. This means that changes in the solute's concentration do not change the volume fraction of the overall solution.

## 2.4 Kinematics of superimposed constituents

In this section, the well-established finite kinematics for superimposed continua are collected. For a comprehensive introduction, the interested reader is referred to, e.g., Altenbach [3], Haupt [140] or Holzapfel [151] for singlephasic materials and Ehlers [78, 80, 82] for multiphasic materials. In terms of the eTPM, kinematical relations considering miscible constituents are discussed in, e.g., Acartürk [1], Ehlers [81], Wagner [277] or Thom & Ricken [268].

**Basic kinematic relations:** Due to the underlying volumetrical averaging of multiphasic materials within the TPM, a spatial position  $\mathbf{x}$  in the current configuration of the body

---

<sup>32</sup>Lorenzo Romano Amedeo Carlo Avogadro (1776–1856) was an Italian scientist, most noted for his contribution to molecular theory [WIKIPEDIA].

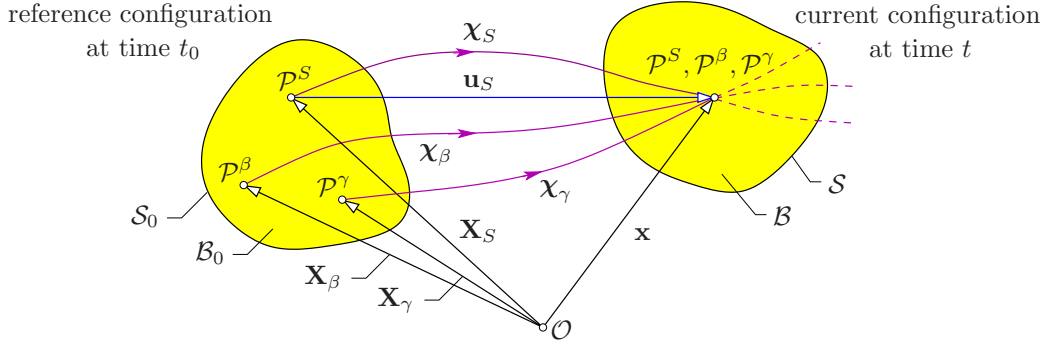


**Figure 2.3:** Kinematics of superimposed continua, adapted from Wagner [277].

$\mathcal{B}$  is coincidentally occupied by material points  $\mathcal{P}^\alpha$  of all constituents, cf. Figure 2.3. To provide a required independent motion

$$\mathbf{x} = \chi_\alpha(\mathbf{X}_\alpha, t) \quad (2.11)$$

of the different constituents, each constituent  $\varphi^\alpha$  (as well as  $\varphi^\beta$  and  $\varphi^\gamma$ ) follows its own (Lagrangian) placement function  $\chi_\alpha(\mathbf{X}_\alpha, t)$ . Therein, the material points are identified with their initial position  $\mathbf{X}_\alpha$ . In addition, the (Eulerian) inverse motion function  $\chi_\alpha^{-1}$  assigns each material an unique reference position

$$\mathbf{X}_\alpha = \chi_\alpha^{-1}(\mathbf{x}, t) \quad \text{if} \quad \det \frac{\partial \chi_\alpha}{\partial \mathbf{X}_\alpha} \neq 0. \quad (2.12)$$

Based on the general introduction of the motion function as a field function, cf. (2.11), the partial temporal derivatives yield the velocity and acceleration fields, respectively, for each constituent via

$$\dot{\mathbf{x}}_\alpha = \frac{\partial \chi_\alpha(\mathbf{X}_\alpha, t)}{\partial t} = \dot{\mathbf{x}}_\alpha(\mathbf{X}_\alpha, t) \quad \text{and} \quad \ddot{\mathbf{x}}_\alpha = \frac{\partial^2 \chi_\alpha(\mathbf{X}_\alpha, t)}{\partial t^2} = \ddot{\mathbf{x}}_\alpha(\mathbf{X}_\alpha, t). \quad (2.13)$$

Based on (2.12), the Eulerian representatives of (2.13) read

$$\dot{\mathbf{x}}_\alpha = \dot{\mathbf{x}}_\alpha(\chi_\alpha^{-1}(\mathbf{x}, t), t) = \dot{\mathbf{x}}_\alpha(\mathbf{x}, t) \quad \text{and} \quad \ddot{\mathbf{x}}_\alpha = \ddot{\mathbf{x}}_\alpha(\chi_\alpha^{-1}(\mathbf{x}, t), t) = \ddot{\mathbf{x}}_\alpha(\mathbf{x}, t). \quad (2.14)$$

Note in passing that for field functions in an Eulerian setting<sup>33</sup> material time derivatives comes into play, cf., e. g., Ehlers [80].

The macroscopic (barycentric) velocity of the overall aggregate is motivated by conserving the local momentum of the overall aggregate with the sum of the local momenta of the constituents, yielding

$$\dot{\mathbf{x}} = \frac{1}{\rho} \sum_\alpha \rho^\alpha \dot{\mathbf{x}}_\alpha. \quad (2.15)$$

This allows for the introduction of a further macroscopic velocity, i. e. the diffusion velocity  $\mathbf{d}_\alpha$ , relating the velocity of a constituent with respect to the barycentric velocity via

$$\mathbf{d}_\alpha := \dot{\mathbf{x}}_\alpha - \dot{\mathbf{x}}, \quad \text{where} \quad \sum_\alpha \rho^\alpha \mathbf{d}_\alpha = \mathbf{0}. \quad (2.16)$$

<sup>33</sup>i. e. formulated with respect to the current position  $\mathbf{x}(t)$ , which is itself implicitly time dependent.

In analogy to (2.15), the velocity of an overall fluid mixture  $\varphi^\beta$ , composed by its miscible components (species)  $\varphi^\gamma$ , is derived by using the relation (2.10), viz.:

$$\dot{\mathbf{x}}_\beta = \frac{1}{\rho^\beta} \sum_\gamma \rho^\gamma \dot{\mathbf{x}}_\gamma = \frac{1}{\rho^{\beta R}} \sum_\gamma \rho_\beta^\gamma \dot{\mathbf{x}}_\gamma. \quad (2.17)$$

Note in passing that the pore density  $\rho_\beta^\gamma$  is used as the weighting factor in (2.17). In terms of the eTPM, the pore-diffusion velocity  $\mathbf{d}_{\gamma\beta}$  relates the velocity of a mixture component to the velocity of the overall fluid mixture, viz.:

$$\mathbf{d}_{\gamma\beta} := \dot{\mathbf{x}}_\gamma - \dot{\mathbf{x}}_\beta, \quad \text{where} \quad \sum_\gamma \rho_\beta^\gamma \mathbf{d}_{\gamma\beta} = \mathbf{0}. \quad (2.18)$$

Furthermore, the seepage velocities

$$\mathbf{w}_\beta := \dot{\mathbf{x}}_\beta - \dot{\mathbf{x}}_S \quad (2.19)$$

are defined as the liquid's velocities in relation to the velocity of the solid skeleton. For the description of dissolved components (species) in an overall fluid mixture, the seepage velocities

$$\mathbf{w}_\gamma := \dot{\mathbf{x}}_\gamma - \dot{\mathbf{x}}_S = \mathbf{d}_{\gamma\beta} + \dot{\mathbf{x}}_\beta - \dot{\mathbf{x}}_S = \mathbf{d}_{\gamma\beta} + \mathbf{w}_\beta \quad (2.20)$$

can be formulated with (2.18)<sub>1</sub> as a summation of the pore-diffusion velocity  $\mathbf{d}_{\gamma\beta}$  and the seepage velocity  $\mathbf{w}_\beta$  of the overall fluid.

**Deformation and strain measures:** The basic deformation quantity in continuum mechanics is provided by the material deformation gradient

$$\begin{aligned} \mathbf{F}_\alpha &= \frac{\partial \mathbf{X}_\alpha(\mathbf{X}_\alpha, t)}{\partial \mathbf{X}_\alpha} = \frac{\partial \mathbf{x}}{\partial \mathbf{X}_\alpha} = \text{Grad}_\alpha \mathbf{x} = \frac{\partial \mathbf{x}}{\partial \theta_\alpha^i} \otimes \frac{\partial \theta_\alpha^i}{\partial \mathbf{X}_\alpha} = \mathbf{a}_{\alpha i} \otimes \mathbf{h}_\alpha^i, \\ \mathbf{F}_\alpha^{-1} &= \frac{\partial \mathbf{X}_\alpha^{-1}(\mathbf{x}, t)}{\partial \mathbf{x}} = \frac{\partial \mathbf{X}_\alpha}{\partial \mathbf{x}} = \text{grad } \mathbf{X}_\alpha = \frac{\partial \mathbf{X}_\alpha}{\partial \theta_\alpha^i} \otimes \frac{\partial \theta_\alpha^i}{\partial \mathbf{x}} = \mathbf{h}_{\alpha i} \otimes \mathbf{a}_\alpha^i. \end{aligned} \quad (2.21)$$

Therein, the operator  $\text{Grad}_\alpha(\cdot)$  denotes the material gradient of  $\varphi^\alpha$  with respect to its reference position. Moreover, it is often convenient to express deformation and strain measures in terms of the natural basis representation, cf., e.g., Ehlers [77], Holzapfel [151], Karajan [164] or Markert [194]. It follows directly from (2.21) that the material deformation gradient, in its capacity as a two-field tensor, maps a local line element<sup>34</sup> of  $\varphi^\alpha$  or the natural basis in a push-forward transformation from the reference configuration to the current configuration, viz.:

$$\begin{aligned} d\mathbf{x} &= \mathbf{F}_\alpha d\mathbf{X}_\alpha & \longleftrightarrow & d\mathbf{X}_\alpha = \mathbf{F}_\alpha^{-1} d\mathbf{x}, \\ \mathbf{a}_{\alpha i} &= \mathbf{F}_\alpha \mathbf{h}_{\alpha i} & \longleftrightarrow & \mathbf{h}_{\alpha i} = \mathbf{F}_\alpha^{-1} \mathbf{a}_{\alpha i}, \\ \mathbf{a}_\alpha^i &= \mathbf{F}_\alpha^{T-1} \mathbf{h}_\alpha^i & \longleftrightarrow & \mathbf{h}_\alpha^i = \mathbf{F}_\alpha^T \mathbf{a}_\alpha^i. \end{aligned} \quad (2.22)$$

<sup>34</sup>The transport theorems of partial referential area and volume elements are obtained via  $d\mathbf{a} = (\text{cof } \mathbf{F}_\alpha) d\mathbf{A}_\alpha$  and  $dv = (\det \mathbf{F}_\alpha) dV_\alpha$ . Therein,  $d\mathbf{A}_\alpha$  and  $dV_\alpha$  denote area and volume elements in the referential configuration, whereas  $d\mathbf{a}$  and  $dv$  represent the corresponding elements in the current configuration.

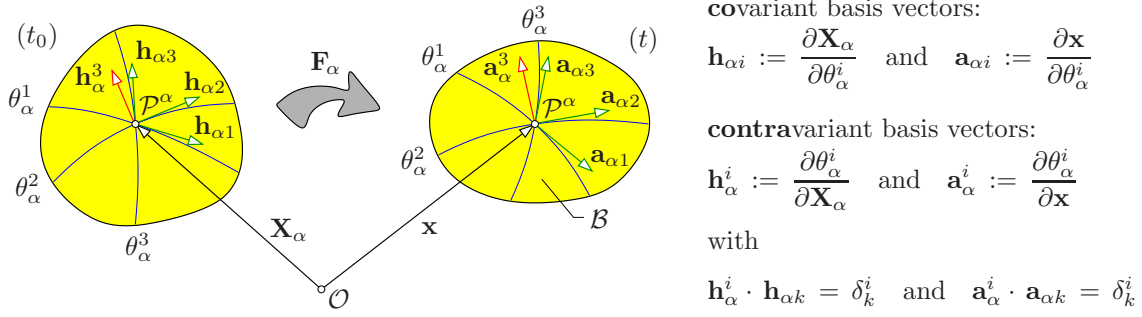


**Figure 2.4:** Natural basis representation, adapted from Wagner [277].

The so-called pull-back transformation in (2.22) of an current line element to the reference configuration is only feasible for existing inverse deformation gradients  $\mathbf{F}_\alpha^{-1}$  as stated in (2.12)<sub>2</sub>. Investigating the initial condition of the deformation gradient, it is concluded for the continuous and non-zero Jacobian that  $J_\alpha = \det \mathbf{F}_\alpha > 0$  needs to be fulfilled. In natural basis representation, the covariant natural basis vectors are introduced with respect to contravariant convective curvilinear coordinate lines  $\theta_\alpha^i$ , cf. Figure 2.4. These coordinate or material lines are attached to the solid's body and continuously follow the deformation of  $\varphi^S$ . The mixed Kronecker<sup>35</sup> delta  $\delta_k^i$  yields either one, for the case of an equal indication ( $i = k$ ), or zero for different indices ( $i \neq k$ ). Thus, a contravariant basis vector  $(\cdot)^i$  is, for  $i \neq k$ , always perpendicular to the covariant basis vectors  $(\cdot)_k$ . In terms of constitutive formulations of the material behaviour, it is meaningful to extract a local rigid body movement from  $\mathbf{F}_\alpha$  via

$$\mathbf{F}_\alpha = \mathbf{R}_\alpha \mathbf{U}_\alpha = \mathbf{V}_\alpha \mathbf{R}_\alpha, \quad \text{where} \quad \mathbf{V}_\alpha = \mathbf{R}_\alpha \mathbf{U}_\alpha \mathbf{R}_\alpha^T. \quad (2.23)$$

Therein,  $\mathbf{R}_\alpha$  denotes a proper orthogonal rotation with the properties  $\mathbf{R}_\alpha^{-1} = \mathbf{R}_\alpha^T$  and  $\det \mathbf{R}_\alpha = 1$ . The right stretch tensor  $\mathbf{U}_\alpha$  and the left stretch tensor  $\mathbf{V}_\alpha$  are symmetric and positive definite measures.

As a next step, the introduction of deformation measures of  $\varphi^\alpha$  is derived from the square of line elements in the current and referential configuration and using the relations (2.21)<sub>1</sub>, (2.22)<sub>1</sub> and (2.23), yielding

$$\begin{aligned} \mathbf{C}_\alpha &= \mathbf{F}_\alpha^T \mathbf{F}_\alpha = \mathbf{U}_\alpha \mathbf{U}_\alpha = a_{\alpha ik} (\mathbf{h}_\alpha^i \otimes \mathbf{h}_\alpha^k), \\ \mathbf{B}_\alpha &= \mathbf{F}_\alpha \mathbf{F}_\alpha^T = \mathbf{V}_\alpha \mathbf{V}_\alpha = h_\alpha^{ik} (\mathbf{a}_{\alpha i} \otimes \mathbf{a}_{\alpha k}). \end{aligned} \quad (2.24)$$

Therein,  $\mathbf{C}_\alpha$  and  $\mathbf{B}_\alpha$  are the right and the left Cauchy-Green<sup>36</sup> deformation tensors, respectively. In (2.24),  $(\cdot)_{\alpha ik}$  and  $(\cdot)_\alpha^{ik}$  denote co- and contravariant metric coefficients, obtained by the scalar product of the basis vectors. Finally, strain tensors can be formulated proceeding from the difference of the squares of line elements. In the natural basis representation, it is recognised that four different strain measures can be distinguished

<sup>35</sup>Leopold Kronecker (1823–1891) was a German mathematician who worked on number theory, algebra and logic [WIKIPEDIA].

<sup>36</sup>George Green (1793–1841) was a British mathematical physicist who wrote “An Essay on the Application of Mathematical Analysis to the Theories of Electricity and Magnetism” in 1828 [WIKIPEDIA].

varying in their association to (co- or contravariant) configurations, viz.:

$$\begin{aligned}
\mathbf{E}_\alpha &= \frac{1}{2}(\mathbf{C}_\alpha - \mathbf{I}) = \frac{1}{2}(a_{\alpha ik} - h_{\alpha ik})(\mathbf{h}_\alpha^i \otimes \mathbf{h}_\alpha^k), \\
\mathbf{A}_\alpha &= \frac{1}{2}(\mathbf{I} - \mathbf{B}_\alpha^{-1}) = \frac{1}{2}(a_{\alpha ik} - h_{\alpha ik})(\mathbf{a}_\alpha^i \otimes \mathbf{a}_\alpha^k), \\
\mathbf{K}_\alpha^{\text{R}} &= \frac{1}{2}(\mathbf{I} - \mathbf{C}_\alpha^{-1}) = \frac{1}{2}(h_\alpha^{ik} - a_\alpha^{ik})(\mathbf{h}_{\alpha i} \otimes \mathbf{h}_{\alpha k}), \\
\mathbf{K}_\alpha &= \frac{1}{2}(\mathbf{B}_\alpha - \mathbf{I}) = \frac{1}{2}(h_\alpha^{ik} - a_\alpha^{ik})(\mathbf{a}_{\alpha i} \otimes \mathbf{a}_{\alpha k}).
\end{aligned} \tag{2.25}$$

Therein,  $\mathbf{E}_\alpha$  is known as the Green-Lagrangian strain tensor and  $\mathbf{A}_\alpha$  as the Almansi<sup>37</sup> strain tensor. The covariant Karni<sup>38</sup>-Reiner<sup>39</sup>  $\mathbf{K}_\alpha^{\text{R}}$  (referential) and  $\mathbf{K}_\alpha$  (spatial) strains allow for a proper constitutive stress-strain relation in finite theories with respect to the same natural basis of classical stress tensors.

**Kinematics of the solid skeleton:** Obviously, the solid skeleton plays an exceptional role in the TPM approach, since the solid skeleton serves as a (Lagrangian) reference for the description of any (relative) movement of other considered constituents. This implies that each TPM model basically requires a solid-skeleton constituent, while the adding of further constituents is, in principle, on demand of the model's scope. The Lagrangian description of the solid displacement

$$\mathbf{u}_S := \mathbf{x} - \mathbf{X}_S \tag{2.26}$$

is given with respect to the reference configuration, cf. Figure 2.3. Hence, the solid's material deformation gradient  $\mathbf{F}_S$  can be formulated in terms of the solid displacement vector  $\mathbf{u}_S$  by inserting the relation (2.26) in (2.21), yielding

$$\mathbf{F}_S = \frac{\partial \mathbf{x}}{\partial \mathbf{X}_S} = \frac{\partial (\mathbf{X}_S + \mathbf{u}_S)}{\partial \mathbf{X}_S} = \mathbf{I} + \text{Grad}_S \mathbf{u}_S. \tag{2.27}$$

Note in passing that, based on (2.27), the solid's deformation and strain tensors can be alternatively expressed using the solid displacement vector  $\mathbf{u}_S$ , cf., e. g., Wagner [277]. This is convenient in terms of the numerical solution of the set of governing equations.

**Velocity gradients and deformation rates:** The spatial velocity gradient

$$\mathbf{L}_\alpha = \text{grad } \dot{\mathbf{x}}_\alpha \tag{2.28}$$

can be additionally split into a symmetric deformation velocity  $\mathbf{D}_\alpha$  and a skew-symmetric spin tensor  $\mathbf{W}_\alpha$  via

$$\mathbf{L}_\alpha = \mathbf{D}_\alpha + \mathbf{W}_\alpha, \quad \text{where} \quad \begin{cases} \mathbf{D}_\alpha = \frac{1}{2}(\mathbf{L}_\alpha + \mathbf{L}_\alpha^T) & \text{with } \mathbf{D}_\alpha = \mathbf{D}_\alpha^T, \\ \mathbf{W}_\alpha = \frac{1}{2}(\mathbf{L}_\alpha - \mathbf{L}_\alpha^T) & \text{with } \mathbf{W}_\alpha = -\mathbf{W}_\alpha^T. \end{cases} \tag{2.29}$$

<sup>37</sup>Emilio Almansi (1869–1948) was an Italian mathematician [WIKIPEDIA].

<sup>38</sup>Zvi Karni was an Israelian scientist working with Reiner at the Israel Institute of Technology.

<sup>39</sup>Markus Reiner (1886–1976) was an Israelian scientist and a major figure in rheology strain tensors [WIKIPEDIA].

As a result of the skew symmetry of the spin tensor  $\mathbf{W}_\alpha$ , it is found that

$$\mathbf{L}_\alpha \cdot \mathbf{I} = \mathbf{D}_\alpha \cdot \mathbf{I} = (\text{grad } \dot{\mathbf{x}}_\alpha) \cdot \mathbf{I} = \text{div } \dot{\mathbf{x}}_\alpha. \quad (2.30)$$

Based on the spatial velocity gradient  $\mathbf{L}_\alpha$ , the velocities of line, area and volume elements are given as

$$\begin{aligned} (d\mathbf{x})'_\alpha &= \mathbf{L}_\alpha d\mathbf{x}, \\ (d\mathbf{a})'_\alpha &= [(\mathbf{L}_\alpha \cdot \mathbf{I}) \mathbf{I} - \mathbf{L}_\alpha^T] d\mathbf{a}, \\ (dv)'_\alpha &= (\text{div } \dot{\mathbf{x}}_\alpha) dv. \end{aligned} \quad (2.31)$$

Finally, the rate of the right Cauchy-Green deformation tensor is obtained as

$$(\mathbf{C}_\alpha)'_\alpha = 2 \mathbf{F}_\alpha^T \mathbf{D}_\alpha \mathbf{F}_\alpha. \quad (2.32)$$

As mentioned at the beginning of this section, a selection of relevant kinematical relations for the presented applications in Part II is briefly collected here, since this field is well established. For a more detailed discussion of kinematics of multiconstituent materials, the interested reader is referred to, e. g., Markert [194], Wagner [277] or Ehlers [78, 80, 81, 82].

## 2.5 Stress state of multiconstituent materials

Any deformation process of a multiconstituent material and, thus, the discussion of kinematical relations basically requires some kind of loading onto the body. In contrast to singlephasic materials, each constituent  $\varphi^\alpha$  of the multiphase overall aggregate  $\mathcal{B}$  can be subjected to individual volume and surface forces, cf. Figure 2.5. In addition, the body can be exposed to temperature effects by heat influx  $\mathbf{q}^\alpha$ ,  $\mathbf{q}^\beta$  and external heat supply  $r^\alpha$ ,  $r^\beta$ . To set an example for the volume forces, this could be of relevance for the description

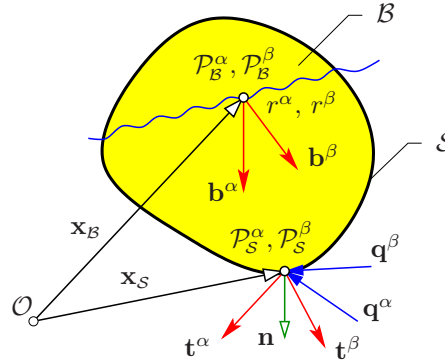


**Figure 2.5:** Individual volume and surface forces as well as heat influx and external heat supplies, acting at the current configuration on a multiconstituent body.

of a magnetic liquid moving within a non-magnetic solid skeleton. For the derivation of the balance equations in the next section, the summation of volume ( $\mathbf{k}_V^\alpha$ ) and surface ( $\mathbf{k}_O^\alpha$ ) forces yielding the total force  $\mathbf{k}^\alpha$  acting on the constituent  $\varphi^\alpha$ , is given, viz.:

$$\mathbf{k}^\alpha = \mathbf{k}_V^\alpha + \mathbf{k}_O^\alpha = \int_B \rho^\alpha \mathbf{b}^\alpha dv + \int_S \mathbf{t}^\alpha da. \quad (2.33)$$

Therein, the surface force  $\mathbf{t}^\alpha = \mathbf{t}^\alpha(\mathbf{x}, \mathbf{n}, t)$  is dependent on the surface orientation  $\mathbf{n}$ . Therefore, Cauchy's theorem

$$\mathbf{t}^\alpha(\mathbf{x}, t, \mathbf{n}) = [\mathbf{T}^\alpha(\mathbf{x}, t)] \mathbf{n} \quad (2.34)$$

is commonly applied to describe the full state of stress at a local material point using the partial Cauchy stress  $\mathbf{T}^\alpha$ , which is independent from the surface (cut) orientation. Based on the general definition of stresses, different partial stress tensors of the constituents  $\varphi^\alpha$  can be introduced via

$$\begin{aligned} d\mathbf{k}_O^\alpha &= \mathbf{t}^\alpha da = \mathbf{T}^\alpha d\mathbf{a}, \\ d\mathbf{k}_O^\alpha &= \mathbf{t}^\alpha da = \boldsymbol{\tau}^\alpha d\bar{\mathbf{a}}_\alpha, \quad \text{where } \bar{\mathbf{a}}_\alpha = (\det \mathbf{F}_\alpha)^{-1} d\mathbf{a}, \\ d\mathbf{k}_O^\alpha &= \mathbf{T}^\alpha \text{cof } \mathbf{F}_\alpha d\mathbf{A}_\alpha = \mathbf{P}^\alpha d\mathbf{A}_\alpha, \quad \text{with } \mathbf{P}^\alpha = \boldsymbol{\tau}^\alpha \mathbf{F}_\alpha^{T-1}, \\ \mathbf{F}_\alpha^{-1} d\mathbf{k}_O^\alpha &= \mathbf{S}^\alpha d\mathbf{A}_\alpha, \quad \text{with } \mathbf{S}^\alpha = \mathbf{F}_\alpha^{-1} \mathbf{P}^\alpha = \mathbf{F}_\alpha^{-1} \boldsymbol{\tau}^\alpha \mathbf{F}_\alpha^{T-1}. \end{aligned} \quad (2.35)$$

Therein, the Cauchy stress  $\mathbf{T}^\alpha$  is also called true stress as the current force increment is referred to the oriented current area element  $d\mathbf{a} = \mathbf{n} da$ . The Kirchhoff<sup>40</sup> stress  $\boldsymbol{\tau}^\alpha$ , is derived by relating the current force element  $d\mathbf{k}_O^\alpha$  to a weighted (but still current) area element. The relation of the current force element to an area element  $d\mathbf{A}_\alpha$  of the referential configuration yields the first Piola<sup>41</sup>-Kirchhoff stress  $\mathbf{P}^\alpha$ . This measure is often used in experiments since the geometry of a sample is conveniently measured before the experiment is started. During the execution of the experiment, the current forces are then still related to the geometry of the undeformed reference configuration. Finally, the symmetric second Piola-Kirchhoff stress  $\mathbf{S}^\alpha$  is introduced by mapping  $d\mathbf{k}_O^\alpha$  to the reference configuration. All stress measures introduced in (2.35) are of covariant nature in terms of a natural basis representation.

## 2.6 Balance equations

In accordance to continuum mechanics of single-phasic materials, the global master balances for the overall aggregate  $\varphi$  are introduced via

$$\begin{aligned} \frac{d}{dt} \int_{\mathcal{B}} \psi dv &= \int_{\mathcal{S}} \boldsymbol{\phi} \cdot \mathbf{n} da + \int_{\mathcal{B}} \sigma dv + \int_{\mathcal{B}} \hat{\psi} dv && : \text{scalar-valued}, \\ \frac{d}{dt} \int_{\mathcal{B}} \boldsymbol{\psi} dv &= \int_{\mathcal{S}} \boldsymbol{\Phi} \mathbf{n} da + \int_{\mathcal{B}} \boldsymbol{\sigma} dv + \int_{\mathcal{B}} \hat{\boldsymbol{\psi}} dv && : \text{vector-valued}. \end{aligned} \quad (2.36)$$

<sup>40</sup>Gustav Robert Kirchhoff (1824–1887) was a German physicist who contributed to the fundamental understanding of electrical circuits, spectroscopy, and the emission of black-body radiation by heated objects [WIKIPEDIA].

<sup>41</sup>Gabrio Piola (1794–1850) was an Italian mathematician and physicist. He studied in particular the mechanics of the continuous, linking his name to the Piola-Kirchhoff stress tensor [WIKIPEDIA].

Therein, the volume-integrated temporal changes (by means of the material time derivative  $d(\cdot)/dt$ ) of volume-specific mechanical quantities  $\psi$  (scalar-valued) or  $\boldsymbol{\psi}$  (vector-valued) are balanced by the effluxes  $\boldsymbol{\phi} \cdot \mathbf{n}$  with flux vector  $\boldsymbol{\phi}$  or by  $\boldsymbol{\Phi} \mathbf{n}$  with flux tensor  $\boldsymbol{\Phi}$  of the mechanical quantities through the surface (actions at a vicinity) with outward-oriented surface normal  $\mathbf{n}$ , the volume-integrated supplies  $\sigma$  or  $\boldsymbol{\sigma}$  of mechanical quantities (actions from a distance) and the volume-integrated productions  $\hat{\psi}$  or  $\hat{\boldsymbol{\psi}}$  of mechanical quantities (exchange with the environment). By use of standard arguments, the local formulations of the master balances read

$$\begin{aligned} \dot{\psi} + \psi \operatorname{div} \dot{\mathbf{x}} &= \operatorname{div} \boldsymbol{\phi} + \sigma + \hat{\psi} & : \text{scalar-valued,} \\ \dot{\boldsymbol{\psi}} + \boldsymbol{\psi} \operatorname{div} \dot{\mathbf{x}} &= \operatorname{div} \boldsymbol{\Phi} + \boldsymbol{\sigma} + \hat{\boldsymbol{\psi}} & : \text{vector-valued.} \end{aligned} \quad (2.37)$$

The development of a general frame for the structure of balance relations for the individual constituents  $\varphi^\alpha$  and the overall aggregate or the mixture  $\varphi$ , respectively, is based on Truesdell's famous "metaphysical principles":

- (1) All properties of the mixture must be mathematical consequences of properties of the constituents.
- (2) So as to describe the motion of a constituent, we may in imagination isolate it from the rest of the mixture, provided we allow properly for the actions of the other constituents upon it.
- (3) The motion of a mixture is governed by the same equations as is a single body.

(Truesdell [270], p. 221)

Truesdell posed some explanatory notes on his principles:

"The first principle asserts, roughly, that the whole is no more than the sum of its parts, and the third, that in its motion as a whole a body does not know whether it is a mixture or not. The second is an extension of the familiar principle of solidification, by which the parts of a body occupying different regions of space are imagined cut asunder in geometry but united in physics by suitable forces or energies. Here we distinguish in imagination different constituents occupying the same region of space."

Based on his second principle, global balance relations exist for every constituent  $\varphi^\alpha$  and can be formulated in analogy to (2.36) via

$$\begin{aligned} \frac{d_\alpha}{dt} \int_{\mathcal{B}} \psi^\alpha dv &= \int_{\mathcal{S}} \boldsymbol{\phi}^\alpha \cdot \mathbf{n} da + \int_{\mathcal{B}} \sigma^\alpha dv + \int_{\mathcal{B}} \hat{\psi}^\alpha dv & : \text{scalar-valued,} \\ \frac{d_\alpha}{dt} \int_{\mathcal{B}} \boldsymbol{\psi}^\alpha dv &= \int_{\mathcal{S}} \boldsymbol{\Phi}^\alpha \mathbf{n} da + \int_{\mathcal{B}} \boldsymbol{\sigma}^\alpha dv + \int_{\mathcal{B}} \hat{\boldsymbol{\psi}}^\alpha dv & : \text{vector-valued.} \end{aligned} \quad (2.38)$$

Therein, the terms  $(\cdot)^\alpha$  have the same physical meaning as the terms  $(\cdot)$  before. Note that  $d_\alpha(\cdot)/dt$  defines the material time derivative of  $\varphi^\alpha$  with the convective part following the

**Table 2.1:** Collection of physical quantities, efflux, supply and production terms for the overall aggregate (mixture) as well as for the individual constituents.

Ingredients for the balances of the overall aggregate (mixture) $\varphi$				
	$\psi, \boldsymbol{\Psi}$	$\phi, \boldsymbol{\Phi}$	$\sigma, \boldsymbol{\sigma}$	$\hat{\psi}, \hat{\boldsymbol{\Psi}}$
mass	$\rho$	0	0	0
momentum	$\rho \dot{\mathbf{x}}$	$\mathbf{T}$	$\rho \mathbf{b}$	$\mathbf{0}$
m. o. m.	$\mathbf{x} \times \rho \dot{\mathbf{x}}$	$\mathbf{x} \times \mathbf{T}$	$\mathbf{x} \times \rho \mathbf{b}$	$\mathbf{0}$
energy	$\rho (\varepsilon + \frac{1}{2} \dot{\mathbf{x}} \cdot \dot{\mathbf{x}})$	$\mathbf{T}^T \dot{\mathbf{x}} - \mathbf{q}$	$\rho (\mathbf{b} \cdot \dot{\mathbf{x}} + r)$	0
entropy	$\rho \eta$	$-\mathbf{q} / \theta$	$\rho r / \theta$	$\hat{\eta} \geq 0$
Ingredients for the balances of the individual constituents $\varphi^\alpha$				
	$\psi^\alpha, \boldsymbol{\Psi}^\alpha$	$\phi^\alpha, \boldsymbol{\Phi}^\alpha$	$\sigma^\alpha, \boldsymbol{\sigma}^\alpha$	$\hat{\psi}^\alpha, \hat{\boldsymbol{\Psi}}^\alpha$
mass	$\rho^\alpha$	0	0	$\hat{\rho}^\alpha$
momentum	$\rho^\alpha \dot{\mathbf{x}}_\alpha$	$\mathbf{T}^\alpha$	$\rho^\alpha \mathbf{b}^\alpha$	$\hat{\mathbf{s}}^\alpha$
m. o. m.	$\mathbf{x} \times \rho^\alpha \dot{\mathbf{x}}_\alpha$	$\mathbf{x} \times \mathbf{T}^\alpha$	$\mathbf{x} \times \rho^\alpha \mathbf{b}^\alpha$	$\hat{\mathbf{h}}^\alpha$
energy	$\rho^\alpha (\varepsilon + \frac{1}{2} \dot{\mathbf{x}}_\alpha \cdot \dot{\mathbf{x}}_\alpha)$	$\mathbf{T}^{T\alpha} \dot{\mathbf{x}}_\alpha - \mathbf{q}^\alpha$	$\rho^\alpha (\mathbf{b}^\alpha \cdot \dot{\mathbf{x}}_\alpha + r^\alpha)$	$\hat{\varepsilon}^\alpha$
entropy	$\rho^\alpha \eta^\alpha$	$-\mathbf{q}^\alpha / \theta^\alpha$	$\rho^\alpha r^\alpha / \theta^\alpha$	$\hat{\eta}^\alpha$

motion of the individual constituent. By use of the same standard arguments as before, the local forms of the constituent master balances read

$$\begin{aligned}
 (\psi^\alpha)'_\alpha + \psi^\alpha \operatorname{div} \dot{\mathbf{x}}_\alpha &= \operatorname{div} \phi^\alpha + \sigma^\alpha + \hat{\psi}^\alpha : \text{scalar-valued,} \\
 (\boldsymbol{\Psi}^\alpha)'_\alpha + \boldsymbol{\Psi}^\alpha \operatorname{div} \dot{\mathbf{x}}_\alpha &= \operatorname{div} \boldsymbol{\Phi}^\alpha + \boldsymbol{\sigma}^\alpha + \hat{\boldsymbol{\Psi}}^\alpha : \text{vector-valued.}
 \end{aligned}
 \tag{2.39}$$

Based on the general structure of the master balances, the specific balances of mass (density  $\rho$ ), momentum  $\rho \dot{\mathbf{x}}$ , moment of momentum (angular momentum)  $\mathbf{x} \times \rho \dot{\mathbf{x}}$ , energy  $\rho \varepsilon + \frac{1}{2} \rho \dot{\mathbf{x}} \cdot \dot{\mathbf{x}}$  with  $\varepsilon$  as the internal energy, and entropy  $\eta$  can be obtained by the evaluation of individually postulated axioms. Table 2.1 summarises the results for the overall aggregate and for the individual components, where  $(\cdot)$  is substituted by  $(\cdot)^\alpha$ .

In Table 2.1,  $\mathbf{T}$  and  $\mathbf{T}^\alpha$  are the Cauchy stress tensors,  $\mathbf{q}$  and  $\mathbf{q}^\alpha$  are the heat influx (convection) vectors,  $\mathbf{b}$  and  $\mathbf{b}^\alpha$  are mass-specific body force vectors,  $r$  and  $r^\alpha$  are mass-specific external heat supplies (radiations), and  $\theta$  and  $\theta^\alpha$  are absolute Kelvin<sup>42</sup>'s temperatures.

<sup>42</sup>Sir William Thomson, 1<sup>st</sup> Baron Kelvin (1824–1907) was an Irish-Scottish mathematical physicist

For the individual constituents, the total production terms  $\hat{\rho}^\alpha$ ,  $\hat{\mathbf{s}}^\alpha$ ,  $\hat{\mathbf{h}}^\alpha$ ,  $\hat{e}^\alpha$  and  $\hat{\eta}^\alpha$  can be non-zero even for the consideration of closed overall aggregates, as they describe the mutual interaction (coupling) exerted on the individual constituent  $\varphi^\alpha$  by the existence of all other constituents in the system.

For the overall aggregate, the production terms  $\hat{\psi}$  are zero in closed systems, except for the entropy production  $\hat{\eta}$ , which describes the interaction of the system with “the outer world”. This term is never negative, meaning that it is zero in fully reversible systems and positive else. Note that a comparable statement does not hold for  $\hat{\eta}^\alpha$ , since  $\hat{\eta}^\alpha$  has a twofold physical meaning. It includes the entropy interaction between the constituents and their exchange with “the outer world”. As a result, not  $\hat{\eta}^\alpha$  alone but only the sum  $\sum_\alpha \hat{\eta}^\alpha$  is either zero or positive.

Inserting the axiomatically introduced ingredients given in Table 2.1 into the local formulations of the master balance yields the specific balance relations for the overall aggregate

$$\begin{aligned}
\text{mass:} & \quad \dot{\rho} + \rho \operatorname{div} \dot{\mathbf{x}} = 0 \\
\text{momentum:} & \quad \rho \ddot{\mathbf{x}} = \operatorname{div} \mathbf{T} + \rho \mathbf{b} \\
\text{m. o. m.:} & \quad \mathbf{0} = \mathbf{I} \times \mathbf{T} \quad \rightarrow \quad \mathbf{T} = \mathbf{T}^T \\
\text{energy:} & \quad \rho \dot{\varepsilon} = \mathbf{T} \cdot \mathbf{L} - \operatorname{div} \mathbf{q} + \rho r \\
\text{entropy:} & \quad \rho \dot{\eta} \geq \operatorname{div} \left( -\frac{1}{\theta} \mathbf{q} \right) + \frac{1}{\theta} \rho r
\end{aligned} \tag{2.40}$$

as well as for the individual constituents

$$\begin{aligned}
\text{mass:} & \quad (\rho^\alpha)'_\alpha + \rho^\alpha \operatorname{div} \dot{\mathbf{x}}_\alpha = \hat{\rho}^\alpha \\
\text{momentum:} & \quad \rho^\alpha \ddot{\mathbf{x}}_\alpha = \operatorname{div} \mathbf{T}^\alpha + \rho^\alpha \mathbf{b}^\alpha + \hat{\mathbf{p}}^\alpha \\
\text{m. o. m.:} & \quad \mathbf{0} = \mathbf{I} \times \mathbf{T}^\alpha + \hat{\mathbf{m}}^\alpha \\
\text{energy:} & \quad \rho^\alpha (\varepsilon^\alpha)'_\alpha = \mathbf{T}^\alpha \cdot \mathbf{L}_\alpha - \operatorname{div} \mathbf{q}^\alpha + \rho^\alpha r^\alpha + \hat{\varepsilon}^\alpha \\
\text{entropy:} & \quad \rho^\alpha (\eta^\alpha)'_\alpha = \operatorname{div} \left( -\frac{1}{\theta^\alpha} \mathbf{q}^\alpha \right) + \frac{1}{\theta^\alpha} \rho^\alpha r^\alpha + \hat{\zeta}^\alpha
\end{aligned} \tag{2.41}$$

In this procedure, the hierarchical structure of the balances governs their order, since the result of the lower-order balances is included in the formulation of the higher-order ones. Note that the entropy equation for  $\varphi^\alpha$  is not an inequality, since  $\hat{\zeta}^\alpha$  as the direct part of  $\hat{\eta}^\alpha$  has no specific value. According to Truesdell’s first and third metaphysical principle, the balances of  $\varphi$  obtained by summation over the constituents must equal the balances of the overall aggregate  $\varphi$ . This leads to the following rules for the relations between the sum of mechanical quantities of the constituents and the mechanical quantities of the

---

and engineer. Absolute temperatures are stated in units of kelvin in his honour. While the existence of a lower limit to temperature (absolute zero) was known prior to his work, Kelvin is known for determining its correct value as approximately -273.15 degree Celsius or -459.67 degree Fahrenheit [WIKIPEDIA].

overall aggregate:

$$\begin{aligned}
\psi &= \sum_{\alpha} \psi^{\alpha} & ; \boldsymbol{\psi} &= \sum_{\alpha} \boldsymbol{\psi}^{\alpha} & : \text{mechanical quantity} \\
\phi &= \sum_{\alpha} (\phi^{\alpha} - \psi^{\alpha} \mathbf{d}_{\alpha}) & ; \boldsymbol{\Phi} &= \sum_{\alpha} (\boldsymbol{\Phi}^{\alpha} - \boldsymbol{\psi}^{\alpha} \otimes \mathbf{d}_{\alpha}) & : \text{efflux} \\
\sigma &= \sum_{\alpha} \sigma^{\alpha} & ; \boldsymbol{\sigma} &= \sum_{\alpha} \boldsymbol{\sigma}^{\alpha} & : \text{supply} \\
\hat{\psi} &= \sum_{\alpha} \hat{\psi}^{\alpha} & ; \hat{\boldsymbol{\psi}} &= \sum_{\alpha} \hat{\boldsymbol{\psi}}^{\alpha} & : \text{production}
\end{aligned} \tag{2.42}$$

Given (2.42), the following relations between quantities of the overall aggregate and their counterparts of the individual constituents can be found as

$$\begin{aligned}
\rho \mathbf{b} &= \sum_{\alpha} \rho^{\alpha} \mathbf{b}^{\alpha}, \\
\mathbf{T} &= \sum_{\alpha} (\mathbf{T}^{\alpha} - \rho^{\alpha} \mathbf{d}_{\alpha} \otimes \mathbf{d}_{\alpha}), \\
\rho \varepsilon &= \sum_{\alpha} \rho^{\alpha} (\varepsilon^{\alpha} + \frac{1}{2} \mathbf{d}_{\alpha} \cdot \mathbf{d}_{\alpha}), \\
\mathbf{q} &= \sum_{\alpha} \{ \mathbf{q}^{\alpha} - (\mathbf{T}^{\alpha})^T \mathbf{d}_{\alpha} + \rho^{\alpha} \varepsilon^{\alpha} \mathbf{d}_{\alpha} + \frac{1}{2} \rho^{\alpha} (\mathbf{d}_{\alpha} \cdot \mathbf{d}_{\alpha}) \mathbf{d}_{\alpha} \}, \\
\rho r &= \sum_{\alpha} \rho^{\alpha} (r^{\alpha} + \mathbf{b}^{\alpha} \cdot \mathbf{d}_{\alpha}), \\
\rho \eta &= \sum_{\alpha} \rho^{\alpha} \eta^{\alpha}.
\end{aligned} \tag{2.43}$$

Finally, the constraints for the coupling of production terms read

$$\begin{aligned}
\sum_{\alpha} \hat{\rho}^{\alpha} &= 0, \\
\sum_{\alpha} \hat{\mathbf{s}}^{\alpha} &= \mathbf{0} \quad \text{with} \quad \hat{\mathbf{s}}^{\alpha} = \hat{\mathbf{p}}^{\alpha} + \hat{\rho}^{\alpha} \dot{\mathbf{x}}_{\alpha}, \\
\sum_{\alpha} \hat{\mathbf{h}}^{\alpha} &= \mathbf{0} \quad \text{with} \quad \hat{\mathbf{h}}^{\alpha} = \hat{\mathbf{m}}^{\alpha} + \mathbf{x} \times \hat{\mathbf{s}}^{\alpha}, \\
\sum_{\alpha} \hat{e}^{\alpha} &= 0 \quad \text{with} \quad \hat{e}^{\alpha} = \hat{\varepsilon}^{\alpha} + \hat{\mathbf{p}}^{\alpha} \cdot \dot{\mathbf{x}}_{\alpha} + \hat{\rho}^{\alpha} (\varepsilon^{\alpha} + \frac{1}{2} \dot{\mathbf{x}}_{\alpha} \cdot \dot{\mathbf{x}}_{\alpha}), \\
\sum_{\alpha} \hat{\eta}^{\alpha} &\geq 0 \quad \text{with} \quad \hat{\eta}^{\alpha} = \hat{\zeta}^{\alpha} + \hat{\rho}^{\alpha} \eta^{\alpha}.
\end{aligned} \tag{2.44}$$

Note that the production terms split into first terms as the direct productions coming into play during the hierarchy of balance equations with the respective next higher-order balance, while the reminder of the total production generates from direct productions and further terms of the lower balances.

Based on the above set of materially independent balance relations, a broad variety of multicomponent models can be set up. Following this, it is in the nature of the closure problem of continuum mechanics to describe further necessary quantities by the introduction of constitutive equations. This necessity allows to include the specific material behaviour of the individual constituents into the overall model.

**Selected special cases:** The constituent's balance of mass (2.41)<sub>1</sub> can be adapted to its related volume balance

$$(n^\alpha)'_\alpha + n^\alpha \operatorname{div} \dot{\mathbf{x}}_\alpha = 0 \quad \text{or} \quad (n^\beta)'_S + \operatorname{div} (n^\beta \mathbf{w}_\beta) + n^\beta \operatorname{div} (\mathbf{u}_S)'_S = 0 \quad (2.45)$$

if the individual effective density  $\rho^{\alpha R}$  is assumed to be constant, commonly known as materially incompressible constituent. Furthermore, if dissolved components (species) within a solution are considered, the partial pore densities  $\rho_\beta^\gamma$  of the mixture components can be expressed in terms of the molar concentrations (2.10)<sub>2</sub>, yielding

$$(n^\beta c_m^\gamma)'_S + \operatorname{div} (n^\beta c_m^\gamma \mathbf{w}_\gamma) + n^\beta c_m^\gamma \operatorname{div} (\mathbf{u}_S)'_S = 0. \quad (2.46)$$

This form is known as the concentration balance of a dissolved component  $\varphi^\gamma$ , cf. Wagner [277]. Note in passing that this formulation implies convection- and diffusion-driven contributions to the spreading process, cf. (2.20).

Beside mechanical and thermodynamical balance relations also electrodynamical balances can be derived within the framework of the master balance principle. Fundamental contributions of including electrodynamical processes within the TPM are given, e. g., in Acartürk [1], Markert [195, 196] or Bluhm *et al.* [29]. If coupled thermo- and electrodynamical processes of multicomponent continua are described, the previously introduced balances can be further extended. In this context, these issues are only briefly introduced. In a closed system the charge density  $\rho_e$  of the overall aggregate stays always constant. In terms of an axiomatic statement, this can be formulated via

$$\frac{d}{dt} \int_{\mathcal{B}} \rho_e \, dv = 0. \quad (2.47)$$

In contrast, the temporal change of charge density for an individual constituent can differ from zero, yielding

$$\frac{d_\alpha}{dt} \int_{\mathcal{B}} \rho_e^\alpha \, dv = \int_{\mathcal{B}} \hat{\rho}_e^\alpha \, dv, \quad (2.48)$$

where  $\hat{\rho}_e^\alpha$  denotes the charge production. A comparison of (2.47) and (2.48) with the master balances results the local formulations of the charge balances of the overall aggregate and the specific constituent

$$\dot{\rho}_e + \rho_e \operatorname{div} \dot{\mathbf{x}} = 0 \quad \text{and} \quad (\rho_e^\alpha)'_\alpha + \rho_e^\alpha \operatorname{div} \dot{\mathbf{x}}_\alpha = \hat{\rho}_e^\alpha. \quad (2.49)$$

Again, the summation over the productions  $\hat{\rho}_e^\alpha$  must vanish in total.

The continuity of electric flux does not classically fit into the basic idea of balancing a quantity using the master balance principle, since  $\Psi = 0$ . However, the equations can be analogously derived for the overall aggregate as well as for the individual constituent via

$$0 = \operatorname{div} \mathbf{d}_e - \rho_e \quad \text{and} \quad 0 = \operatorname{div} \mathbf{d}_e^\alpha - \rho_e^\alpha + \hat{\kappa}_e^\alpha. \quad (2.50)$$

Therein,  $\mathbf{d}_e$  denotes the electric flux density and  $\hat{\kappa}_e^\alpha$  the total production term. Finally, the equations for the magnetic flux continuity can be given via

$$0 = \operatorname{div} \mathbf{b}_e \quad \text{and} \quad 0 = \operatorname{div} \mathbf{b}_e^\alpha + \hat{\omega}_e^\alpha. \quad (2.51)$$

Therein,  $\mathbf{b}_e$  denotes the magnetic flux density and  $\hat{\omega}_e^\alpha$  the total production term.  $\ll_{(p.18)}$



# Chapter 3:

## Numerical treatment

The purpose of this chapter is to provide a general introduction to the numerical foundations required for the selected applications presented in the second part of this monograph. Therefore, the basics of the finite-element method (FEM) are discussed in terms of its application to multiphase materials. This includes the derivation of weak formulations and the solution procedure of coupled problems. Moreover, basic model-reduction techniques are discussed in terms of data-integrated approaches to increase the numerical efficiency of the solution procedure.

### 3.1 The finite-element method (FEM)

The finite-element method represents a standard and well-established numerical method for solving boundary-value problems for partial differential equations. The basic idea can be summarised in three steps: (i) the unknowns are approximated at a certain number of spatial points, (ii) the problem is subdivided into smaller parts denoted as finite elements and (iii) the finite-element formulations are assembled into a larger system of algebraic equations representing the entire problem. Since the FEM is an extremely popular method for the solution of engineering (particularly solid-mechanical) problems, there are various comprehensive textbooks on the market, cf., e. g., Bathe [20], Braess [44], Brezzi & Fortin [45], Hughes [155], Schwarz [247], Zienkiewicz & Taylor [301]. Needless to say that there is a broad variety of alternative methods for the numerical solution of partial differential equations on the market such as continuum methods (besides the FEM), for example, finite difference methods (FD, cf., e. g., Smith [251]), finite-volume methods (FVM, cf., e. g., Moukalled *et al.* [212]), boundary-element methods (BEM, cf., e. g., Gaul *et al.* [118]), discrete (pore-scale) methods such as the lattice Boltzmann<sup>1</sup> Method (LBM, cf., e. g., Succi *et al.* [256]) or discrete (or distinct) element methods (DEM, cf., e. g., Luding [191]) or other meshfree methods, such as smoothed-particle hydrodynamics (SPH, cf., e. g., Monaghan [205] and Section 4.1.2). However, at this point, the FEM is briefly introduced.

#### 3.1.1 Boundary conditions

The formulation of an initial-boundary-value problem (IBVP) basically requires the application of boundary conditions. In general, so-called Neumann<sup>2</sup> and Dirichlet<sup>3</sup> boundary conditions can be distinguished. Therefore, the boundary  $\Gamma = \partial\Omega$  (surface of the body)

---

<sup>1</sup>Ludwig Eduard Boltzmann (1844–1906) was an Austrian physicist and philosopher [WIKIPEDIA].

<sup>2</sup>Carl Gottfried Neumann (1832–1925) was a German mathematician [WIKIPEDIA].

<sup>3</sup>Johann Peter Gustav Lejeune Dirichlet (1805–1859) was a German mathematician. He is credited with being one of the first mathematicians to give the modern formal definition of a function [WIKIPEDIA].

is split for each governing equation ( $GE$ ), i. e.  $\Gamma_D^{GE} \cap \Gamma_N^{GE} = \emptyset$ . The Dirichlet boundary  $\Gamma_D$  directly corresponds to the primary variables. In contrast, the Neumann boundary  $\Gamma_N$  contains the natural boundary conditions, depending on the chosen surface term in the weak formulation. For different primary variables ( $PV_i$ ), overlapping boundary conditions related to different governing equations are possible, i. e.  $\Gamma_D = \{\Gamma_D^{PV_1}, \Gamma_D^{PV_2}, \dots, \Gamma_D^{PV_n}\}$  and  $\Gamma_N = \{\Gamma_N^{PV_1}, \Gamma_N^{PV_2}, \dots, \Gamma_N^{PV_n}\}$ .

### 3.1.2 Ansatz and test functions

For the primary variables, ansatz functions  $\mathcal{A}^{PV}$  and corresponding test functions  $\mathcal{T}^{PV}$  are introduced, viz.:

$$\begin{aligned} \mathcal{A}^{PV}(t) &:= \{ PV \in \mathcal{H}^1(\Omega)^d : PV(\mathbf{x}) = \bar{P}V(\mathbf{x}, t) \text{ on } \Gamma_D^{PV} \}, \\ \mathcal{T}^{PV} &:= \{ \delta PV \in \mathcal{H}^1(\Omega)^d : \delta PV(\mathbf{x}) = 0 \quad \text{on } \Gamma_D^{PV} \}. \end{aligned} \quad (3.1)$$

Therein,  $\mathcal{H}^1(\Omega)$  denotes the corresponding Sobolev<sup>4</sup> space (i. e. functions with square-integrable first derivatives within the domain  $\Omega$ ) and the superscript  $d \in \{1, 2, 3\}$  indicates the dimension of the problem. In (3.1), the ansatz functions are constrained to yield the Dirichlet values at the boundary, whereas the test functions are zero at the Dirichlet boundary.

### 3.1.3 Weak formulations of governing equations

Basically, the strong formulations (or local formulations) of the governing balances are valid at each material point  $\mathcal{P}$  within a considered body  $\mathcal{B}$ . However, to solve such a system in an exact analytical way is only possible for a few very specific examples. In contrast, a numerical (approximate) solution of this system of strongly coupled differential-equations allows to consider arbitrary initial-boundary-value problems with any desired geometry. Using the FEM as the numerical solution scheme, it is essential to transform the strong formulations to so-called weak (integral) formulations which fulfil the governing equations in an integral manner. Following this, the strong formulation of each governing balance equation is weighted by the corresponding test function  $\delta PV$  of the primary variable and integrated over the spatial domain  $\Omega$ , resulting in

$$\mathcal{G}_{PV} \equiv \int_{\Omega} ([\text{governing equation}] \cdot \delta PV) dv = 0. \quad (3.2)$$

Therein, the Gaußian integral theorem can be used to transfer vector- or tensor-valued quantities within the volume integral of the weak formulation to the boundary  $\Gamma$  of the

---

<sup>4</sup>Sergei Lvovich Sobolev (1908–1989) was a Soviet mathematician working in mathematical analysis and partial differential equations [WIKIPEDIA].

overall aggregate, via

$$\begin{aligned} \int_{\Omega} \operatorname{div} \boldsymbol{\psi} \, dv &= \int_{\Gamma} \boldsymbol{\psi} \cdot \mathbf{d}\mathbf{a} = \int_{\Gamma} \boldsymbol{\psi} \cdot \mathbf{n} \, da, \\ \int_{\Omega} \operatorname{div} \boldsymbol{\Psi} \, dv &= \int_{\Gamma} \boldsymbol{\Psi} \, \mathbf{d}\mathbf{a} = \int_{\Gamma} \boldsymbol{\Psi} \mathbf{n} \, da. \end{aligned} \quad (3.3)$$

This allows for an alternative representation of weak formulations, where Neumann boundary conditions can be applied explicitly.

### 3.1.4 Monolithic solution of the coupled problem

Initially, the continuous domain  $\Omega$  is spatially discretised using non-overlapping finite subdomains  $\Omega_e$ , the so-called finite elements. Therein, each finite element  $\Omega_e$  is build of  $N_e$  nodal points, referred to as  $P^j$ , which can be mutually interconnected with shared nodes of neighbour elements. This spatial discretisation yields a finite-element mesh with (in total)  $N$  nodes, approximating the discretised spatial domain  $\Omega^h$ .

Within a monolithic solution procedure, all primary variables are approximated simultaneously using the discrete ansatz

$$PV(\mathbf{x}, t) \approx PV^h(\mathbf{x}, t) = \bar{P}V^h(\mathbf{x}, t) + \sum_{j=1}^N \phi_{PV}^j(\mathbf{x}) PV^j(t) \in \mathcal{A}^{PV^h}(t) \quad (3.4)$$

and the corresponding test functions

$$\delta PV(\mathbf{x}) \approx \delta PV^h(\mathbf{x}) = \sum_{j=1}^N \phi_{PV}^j(\mathbf{x}) \delta PV^j \in \mathcal{T}^{PV^h} \quad (3.5)$$

are defined. Therein, the over-lined primary variable denotes the respective Dirichlet boundary conditions and  $\mathcal{A}^{PV^h}$  and  $\mathcal{T}^{PV^h}$  are the discretised ansatz and test functions, respectively. In (3.4) and (3.5), the same global basis functions  $\phi_{PV}^j$  are used indicating a Bubnov<sup>5</sup>-Galerkin<sup>6</sup> (or simply Galerkin) approach. If different basis functions are chosen for the ansatz and the test functions, a Petrov<sup>7</sup>-Galerkin method is applied, which is found, e.g., in the context of numerical stabilisation techniques, cf. Ehlers *et al.* [86]. As common in the TPM, the set of equations is formulated in the current configuration with respect to the solid skeleton. In this regard, the solid displacement field is chosen as the basic (first) primary variable, where the global functions of the displacement are  $\phi_{u_{S1}}^j$ ,  $\phi_{u_{S2}}^j$  and  $\phi_{u_{S3}}^j$ , related to the three spatial dimensions.

<sup>5</sup>Ivan Grigoryevich Bubnov (1872–1919) was a Russian marine engineer and designer of submarines for the Imperial Russian Navy [WIKIPEDIA].

<sup>6</sup>Boris Grigoryevich Galerkin (1871–1945) was a Soviet mathematician and an engineer [WIKIPEDIA].

<sup>7</sup>Georgy Petrov (1912–1987) was a Soviet engineer [WIKIPEDIA].

In (3.4) and (3.5), the unknown nodal quantities  $PV^j$  are denoted as degrees of freedom (DOF) of the system. Each nodal point  $P^j$  in attached finite elements  $E^*$  is assigned to a local basis function

$$\phi_{\text{dof}}^j(\mathbf{x}_i) = \delta_i^j \quad \text{and} \quad \phi_{\text{dof}}^j(\mathbf{x}) = 0 \quad \text{if} \quad \mathbf{x} \notin \bigcup_{e \in E^*} \Omega_e. \quad (3.6)$$

Obviously, this results sparse matrices allowing for an efficient implementation. In (3.6), the basis functions  $\phi_{\text{dof}}^j$  are normalised by the Kronecker delta. Therefore, the nodal quantities correspond exactly to the value of the approximated solution (except of Dirichlet boundary nodes) at every nodal position  $\mathbf{x}_i$ . Tracing back to the weak formulation (3.2), the spatially discretised problem is posed as “find  $PV^h \in \mathcal{A}^{PV^h} \forall \delta PV^h \in \mathcal{T}^{PV^h}$  such that  $\mathcal{G}_{PV}^h = 0$ ” for a given set of Neumann boundary conditions at any time  $t \in [0, T]$ .

Within a spatial discretisation of strongly-coupled problems, the approximation of all DOF is investigated simultaneously for a monolithic<sup>8</sup> solution. The main difficulty in the arising mixed formulation is to find appropriate ansatz functions. In particular, to ensure the stability of the numerical solution, the chosen ansatz functions have to fulfil the so-called inf-sup condition (also known as Ladyshenskaya-Babuška-Brezzi (LBB) condition), cf., e. g., Brezzi & Fortin [45], Hughes [155] or Krischok & Linder [173]. Therefore, the commonly used finite elements are of Taylor-Hood type and approximate the solid displacements one spatial order higher than the other primary variables. At the example of a biphasic model, quadratic ansatz functions for the solid displacements and linear ansatz functions for the pore pressure are used. Due to the spatial discretisation of the continuous weak formulations, the so-called semi-discrete system can be formulated in an abstract manner via

$$\mathcal{F}(t, \mathbf{y}, \mathbf{y}') = [\mathcal{D} \mathbf{y}' + \mathbf{k}(\mathbf{y}) - \mathbf{f}] \stackrel{!}{=} \mathbf{0}. \quad (3.7)$$

Therein, the only appearing material time derivative with respect to the deforming solid skeleton  $(\cdot)'_S$  is expressed for convenience via  $(\cdot)'$ . Moreover, all degrees of freedom of the system, namely the  $N$  nodal unknowns of each primary variable, are gathered in the abstract vector  $\mathbf{y}$ . The global system of equations (3.7) includes the generalised damping matrix  $\mathcal{D}$ , the generalised stiffness vector<sup>9</sup>  $\mathbf{k}(\mathbf{y})$  and the generalised force vector  $\mathbf{f}$  consisting of the Neumann boundary conditions.

In a next step, the semi-discrete system (3.7) is further discretised in the time domain, cf., e. g., Ellsiepen [101], Ammann [5] or Rempfer [225] for a comprehensive discussion. In the simplest (single-step) numerical investigation, the solution only depends on the previous time-step. From the general class of Runge<sup>10</sup>-Kutta<sup>11</sup> methods, the implicit Euler time-integration method is chosen. Within this method, the temporal discretisation of

<sup>8</sup>In contrast, decoupled solution strategies, such as a customised operator-splitting scheme (cf., e. g., Markert *et al.* [198]) can be beneficial for the solution of weakly coupled problems.

<sup>9</sup>Due to the nonlinear dependencies in  $\mathbf{y}$ , the generalised stiffness matrix  $\mathbf{K}$  is obtained after a linearisation of the generalised stiffness vector  $\mathbf{k}$ . Afterwards, the matrix  $\mathbf{K}$  exhibits a similar structure like the matrix  $\mathcal{D}$ , but contains the particular blocks  $\mathbf{K}_{ij} = \partial \mathbf{k}_i / \partial \mathbf{y}_j$ .

<sup>10</sup>Carl David Tolmé Runge (1856–1927) was a German mathematician [WIKIPEDIA].

<sup>11</sup>Martin Wilhelm Kutta (1867–1944) was a German mathematician [WIKIPEDIA].

the unknowns  $\mathbf{y}$  is based on the (backward) Taylor<sup>12</sup>-series expansion, evaluated at the current time  $t_{n+1}$ , viz.:

$$\mathbf{y}_n = \mathbf{y}_{n+1} - h_n \mathbf{y}'_{n+1} \quad \longrightarrow \quad \mathbf{y}'_{n+1} = \frac{1}{h_n} (\mathbf{y}_{n+1} - \mathbf{y}_n). \quad (3.8)$$

Therein, the introduced quantity  $h_n = t_{n+1} - t_n > 0$  denotes the actual time-step, while the time  $t_n$  serves as the old (previous) time-step, respectively. This implicit and unconditionally stable time-integration strategy, cf., e. g., Ehlers *et al.* [98], is then applied to the basic set of differential-algebraic equations (3.7), yielding

$$\mathcal{F}_{n+1}(t_{n+1}, \mathbf{y}_{n+1}, \mathbf{y}'_{n+1}(\mathbf{y}_{n+1})) = [\mathcal{D}(\mathbf{y}_{n+1})\mathbf{y}'_{n+1} + \mathbf{k}(\mathbf{y}_{n+1}) - \mathbf{f}_{n+1}] \stackrel{!}{=} \mathbf{0}. \quad (3.9)$$

The resulting set of nonlinear equations (3.9) is solved using a Newton iteration scheme at each time-integration step. Therefore, the required residual tangent

$$D\mathcal{F}_{n+1}^k := \frac{d\mathcal{F}_{n+1}^k}{d\mathbf{y}_{n+1}^k} = \frac{\partial\mathcal{F}_{n+1}^k}{\partial\mathbf{y}_{n+1}^k} + \frac{1}{h_n} \frac{\partial\mathcal{F}_{n+1}^k}{\partial(\mathbf{y}')_{n+1}^k} \quad (3.10)$$

of the system can be computed either numerically or analytically. In general, the numerical implementation of the numerical tangent is rather simple in comparison to the analytical tangent. However, the use of a numerical tangent may lead to instable, or even non-converging, numerical solutions. In this regard, the theoretical derivation and numerical implementation of an analytical tangent can help to avoid numerical instabilities. Due to the knowledge of the global residual tangent  $D\mathcal{F}_{n+1}^k$ , the vector  $\Delta\mathbf{y}_{n+1}^k$  of stage increments at the current Newton iteration step  $k$  can be solved via the linear system of equations

$$D\mathcal{F}_{n+1}^k \Delta\mathbf{y}_{n+1}^k = -\mathcal{F}_{n+1}^k. \quad (3.11)$$

In particular, this can be achieved by direct or iterative solvers, cf., e. g., Ellsiepen [101]. Finally, the solution vector  $\mathbf{y}_{n+1}^{k+1}$  is updated via

$$\mathbf{y}_{n+1}^{k+1} = \mathbf{y}_{n+1}^k + \Delta\mathbf{y}_{n+1}^k, \quad \text{until} \quad \|\mathcal{F}_{n+1}^{k+1}\| < \varepsilon_{\text{tol}}, \quad (3.12)$$

where  $\varepsilon_{\text{tol}}$  is the desired tolerance of the residual norm. The applicability of the numerical procedure is demonstrated by means of selected initial-boundary-value problems (IBVP) which are discussed in the second part of this monograph.

## 3.2 Application of model-reduction techniques

BIBLIOGRAPHIC NOTE: The content of this section is based on the following original article: Fink, D., Wagner, A. & Ehlers, W.: Application-driven model reduction for the simulation of therapeutic infusion processes in multi-component brain tissue. *Journal of Computational Science* **24** (2018), 101–115 [109].

<sup>12</sup>Brook Taylor (1685–1731) was an English mathematician who is best known for Taylor's theorem and the Taylor series [WIKIPEDIA].

» Projection-based model-reduction techniques are used to transform a high-dimensional system (in terms of the system's degrees of freedom) to a low-dimensional subspace. The advantage of these approaches is to maintain the detailed theoretical basis of the modelling approach and to provide an efficient numerical computation. Besides model-reduction techniques, parallelised solution methods or decoupled solution strategies may also be considered as alternatives to increase the solution speed and, thus, reducing the computational expenses. On the one hand, parallelised solution methods can be applied to the original system (pre-computation for reduced simulations) and the reduced system. However, the combination of parallelised solution methods with model-reduction techniques is not intended here. On the other hand, decoupled solution strategies can break the problem down to smaller subproblems, which can be subsequently integrated in a staggered manner, cf. Zinatbakhsh [302]. Nevertheless, this process may generate non-dissipative subproblems and thus render the problem just conditionally stable, cf. Ehlers *et al.* [98]. The interested reader is referred to Markert *et al.* [198] for a comprehensive comparison between the performance of monolithic and decoupled solution algorithms applied to dynamic porous media problems.

Restricting to projection-based model-reduction methods, there basically exist two main approaches. The so-called Krylov<sup>13</sup>-based methods and the singular-value-decomposition-based (SVD-based) methods, cf. Antoulas [8] and Antoulas & Sorensen [9]. Krylov-based methods are approximation methods, which are based on the matching of the coefficients of series expansions for the reduced and the full system, whereas SVD-based methods have their roots in the singular-value decomposition. One typical method of the class of SVD-based methods is the method of proper orthogonal decomposition (POD), which is considered here. The development of the POD method, also known as Karhunen<sup>14</sup>-Loève<sup>15</sup> expansion, cf. Sirovich [249], traces back to fluid-dynamic applications including turbulence, cf. Berkooz *et al.* [24]. Beyond that, the POD method was successfully applied to various problems in fluid flow (Kunisch & Volkwein [176], Rowley *et al.* [234]), optimal control (Kunisch & Volkwein [174]), aerodynamics (Bui-Thanh *et al.* [51], Hall *et al.* [136]) and structural mechanics (Herkt *et al.* [146]). The error bounds for POD-Galerkin approximations of linear and nonlinear parabolic equations have been proved in Kunisch & Volkwein [175, 176]. The POD method is independent from the type of the model and can be used for nonlinear systems as well as for systems of second order. Its flexibility in application is based on analysing a given data set. Therefore, state variables, so-called snapshots, are collected in pre-computations of the original model.

Dealing with nonlinearities, the cost of the evaluation of the nonlinear terms still scales with the dimension of the full problem. Therefore, the discrete-empirical-interpolation method (DEIM) provides a method to reduce these costs significantly, cf. Chaturantabut & Sorensen [58]. Using the DEIM, the nonlinear function is further approximated via a

---

<sup>13</sup>Aleksey Nikolaevich Krylov (1863–1945) was a Russian naval engineer, applied mathematician and memoirist [WIKIPEDIA].

<sup>14</sup>Kari Karhunen (1915–1992) was a Finnish probabilist and a mathematical statistician. He is best known for the Karhunen-Loève theorem and Karhunen-Loève transform [WIKIPEDIA].

<sup>15</sup>Michel Loève (1907–1979) was a French-American probabilist and mathematical statistician. He is known in mathematical statistics and probability theory for the Karhunen-Loève theorem and Karhunen-Loève transform [WIKIPEDIA].

projection to another low-dimensional subspace. Therefore, snapshots of the nonlinear terms are additionally stored in pre-computations. To preserve the block structure of the strongly coupled system while considering the different temporal behaviour of the primary variables, the snapshots of the state variables and the nonlinear terms are partitioned for each primary variable. These derived modifications can be transferred to various other problems where physical phenomena occur on different time-scales. Applying these model-reduction techniques, the computational effort can be split into a costly offline phase which is performed only once and an inexpensive online phase which is performed in every reduced simulation. Due to the low computation time of the online phase, it appears feasible to use such reduced models for fast but reliable simulations.

### 3.2.1 Proper orthogonal decomposition

The basic idea of the proper orthogonal decomposition (POD) method is to approximate a given data set within a Hilbert<sup>16</sup> space  $\mathcal{V}$  with the dimension  $N$  with a low-dimensional subspace  $\mathcal{V}^l$ . Using the POD method, an optimal global basis is generated from a set of state samples. These samples are numerical solutions of the discretised system and, thus, represent values  $\mathbf{u}_i \in \mathbb{R}^N$  of the vectors of unknowns at different times  $t_i$  with  $i = 1, \dots, m$ . In this regard, a pre-computation, using the initial full system, yields solutions for the values  $\mathbf{u}_i$  which provide the so-called snapshots of the system. Subsequently, the snapshots  $\mathbf{u}_i$  are summarised in a snapshot matrix  $\mathbf{U} = [\mathbf{u}_1 \ \mathbf{u}_2 \ \dots \ \mathbf{u}_m] \in \mathbb{R}^{N \times m}$ . The projection  $\bar{\mathbf{u}}_i \in \mathbb{R}^N$  of a vector  $\mathbf{u}_i$  on the subspace  $\mathcal{V}^l$  is given by

$$\bar{\mathbf{u}}_i = \sum_{j=1}^l (\mathbf{u}_i \cdot \boldsymbol{\varphi}_j) \boldsymbol{\varphi}_j. \quad (3.13)$$

Therein,  $\{\boldsymbol{\varphi}_j\}_{j=1, \dots, l} \in \mathbb{R}^N$  are the orthonormal basis vectors of the  $l$ -dimensional subspace  $\mathcal{V}^l$ . Following this, the projection error

$$PE(\mathbf{U}, \mathcal{V}^l) = \frac{1}{m} \sum_{k=1}^m \left\| \mathbf{u}_k - \sum_{j=1}^l (\mathbf{u}_k \cdot \boldsymbol{\varphi}_j) \boldsymbol{\varphi}_j \right\|^2 \quad (3.14)$$

of the data set is given, where  $\|(\cdot)\|^2 = \sqrt{(\cdot) \cdot (\cdot)}$  complies with the  $L^2$  vector norm. Therefore, the basis vectors  $\boldsymbol{\varphi}_i$  are chosen such that they minimise the projection error  $PE(\mathbf{U}, \mathcal{V}^l)$ . This leads to the following eigenvalue problem

$$\sum_{k=1}^m \mathbf{u}_k (\mathbf{u}_k \cdot \boldsymbol{\varphi}_i) = \lambda_i \boldsymbol{\varphi}_i \quad (3.15)$$

with the corresponding eigenvalues  $\lambda_1, \dots, \lambda_m$ . The eigenvalue problem (3.15) can be written in terms of the snapshot matrix  $\mathbf{U}$  as

$$\begin{aligned} \mathbf{U}\mathbf{U}^T \boldsymbol{\varphi}_i &= \lambda_i \boldsymbol{\varphi}_i \quad \text{or alternatively as} \\ \mathbf{U}^T \mathbf{U} \mathbf{v}_i &=: \mathbf{C} \mathbf{v}_i = \lambda_i \mathbf{v}_i \quad \text{for } i = 1, \dots, l \end{aligned} \quad (3.16)$$

---

<sup>16</sup>David Hilbert (1862–1943) was a German mathematician and one of the most influential and universal mathematicians of the 19<sup>th</sup> and early 20<sup>th</sup> centuries [WIKIPEDIA].

with the corresponding eigenvectors  $\mathbf{v}_i \in \mathbb{R}^m$  of the Gramian<sup>17</sup> (or correlation) matrix  $\mathbf{C} = \mathbf{U}^T \mathbf{U} \in \mathbb{R}^{m \times m}$  which usually have a reduced number of entries (namely the amount of snapshots) than the basis vectors  $\boldsymbol{\varphi}_i$ . In (3.16), the basis vectors  $\boldsymbol{\varphi}_i$  and the eigenvectors  $\mathbf{v}_i$  are related to each other via  $\boldsymbol{\varphi}_i = \mathbf{U} \mathbf{v}_i$ . Basically, all eigenvalues  $\lambda_i$  are non-negative (due to the positive semi-definite Gramian matrix  $\mathbf{C}$ ) and sorted from large to small. To generate the subspace matrix  $\boldsymbol{\Phi} = [\boldsymbol{\varphi}_{1,\text{norm}} \dots \boldsymbol{\varphi}_{l,\text{norm}}] \in \mathbb{R}^{N \times l}$ , the normalised basis vectors result in  $\boldsymbol{\varphi}_{i,\text{norm}} = \mathbf{U} \mathbf{v}_i / |\mathbf{U} \mathbf{v}_i|$ . In conclusion, the projection error can alternatively be computed via

$$PE(\mathbf{U}, \mathcal{V}^l) = \sum_{i=l+1}^m \lambda_i. \quad (3.17)$$

In a reduced computation, only the basis vectors  $\boldsymbol{\varphi}_i$  with  $i = 1, \dots, l$  of the  $l$  largest considered eigenvalues  $\lambda_i$  are included into the basis, whereas the basis vectors of small eigenvalues are neglected. The approximation  $\bar{\mathbf{u}}$  of the vector  $\mathbf{u}$  of unknowns is related to the reduced vector  $\mathbf{u}_{\text{red}} \in \mathbb{R}^l$  of unknowns (corresponding to the coefficient vector) via the subspace matrix  $\boldsymbol{\Phi}$ , yielding

$$\mathbf{u} \approx \bar{\mathbf{u}} = \boldsymbol{\Phi} \mathbf{u}_{\text{red}}. \quad (3.18)$$

Following these approaches, the reduced system of (3.7) can be constructed, viz.:

$$\underbrace{\boldsymbol{\Phi}^T \mathcal{D} \boldsymbol{\Phi}}_{\hat{\mathcal{D}}} \dot{\mathbf{u}}_{\text{red}} + \underbrace{\boldsymbol{\Phi}^T \mathcal{K} \boldsymbol{\Phi}}_{\hat{\mathcal{K}}} \mathbf{u}_{\text{red}} = \underbrace{\boldsymbol{\Phi}^T \mathbf{f}}_{\hat{\mathbf{f}}}. \quad (3.19)$$

Therein, the vector  $\mathbf{u}$  of unknowns is replaced by its approximation  $\bar{\mathbf{u}} = \boldsymbol{\Phi} \mathbf{u}_{\text{red}}$  and the equation is multiplied (from the left side) by  $\boldsymbol{\Phi}^T$ . The reduced system with degree  $l \ll N$  finally results in

$$\hat{\mathcal{D}} \dot{\mathbf{u}}_{\text{red}} + \hat{\mathcal{K}} \mathbf{u}_{\text{red}} = \hat{\mathbf{f}}. \quad (3.20)$$

In conclusion, a required task is to perform a pre-computation using the initial full system (3.7). In this pre-computation, the state variables are stored in each time step. In addition, the storage of the system matrices  $\mathcal{K}$  and  $\mathcal{D}$  within the first time step is performed for a linear system with constant system matrices. Afterwards, the reduction matrix  $\boldsymbol{\Phi}$  and the reduced system matrices  $\hat{\mathcal{K}} \in \mathbb{R}^{l \times l}$  and  $\hat{\mathcal{D}} \in \mathbb{R}^{l \times l}$  are generated for the considered basis vectors  $\boldsymbol{\varphi}_{1,\text{norm}}, \dots, \boldsymbol{\varphi}_{l,\text{norm}}$  (in the following referred to as POD modes) in an offline phase. Based on this data, the simulation is then performed in an online phase for the reduced system (3.20). Following this, it is obvious that the POD method reduces the effort to solve the linearised system of equations in each iteration step. Moreover, the reduced model is initially set up in the first step and can be used through the whole computation. However, due to the subspace construction via a snapshot-based data set, it is obvious that the reduced system can only describe processes properly which are as well represented within this data set.

<sup>17</sup>Jørgen Pedersen Gram (1850–1916) was a Danish actuary and mathematician [WIKIPEDIA].

### 3.2.2 Discrete empirical interpolation method

When applying the POD method to this model, the evaluation costs of the nonlinear terms still scales with the dimension of the original problem. In contrast, the discrete empirical interpolation method (DEIM) provides a method to reduce the evaluation costs of the nonlinear terms significantly. Chaturantabut and Sorensen [58] introduced the DEIM as the discrete variant of the empirical-interpolation method (EIM), cf. Barrault *et al.* [15]. Based on this work, Wirtz *et al.* [291] introduced concepts for a posteriori error estimation for DEIM-reduced systems. Using the DEIM, the nonlinear function of the model equation is approximated by projecting it onto a low-dimensional subspace, cf. Chaturantabut & Sorensen [58, 59, 60]. Based on these works, the DEIM is applied in combination with the POD method to construct a nonlinear reduced-order model. The nonlinear differential equation is given as  $\mathcal{D}(\mathbf{u}) \dot{\mathbf{u}} + \mathbf{k}(\mathbf{u}) = \mathbf{f}(t)$  with the nonlinear terms  $\mathcal{D}(\mathbf{u}(t))$  and  $\mathbf{k}(\mathbf{u}(t))$ . Applying the POD method to this system, the reduced system with degree  $l \ll N$  results in

$$\hat{\mathcal{D}}(\Phi \mathbf{u}_{\text{red}}) \dot{\mathbf{u}}_{\text{red}} + \hat{\mathbf{k}}(\Phi \mathbf{u}_{\text{red}}) = \hat{\mathbf{f}}. \quad (3.21)$$

As before, the different physical time behaviour of the primary variables needs to be considered. Therefore, separated snapshot matrices  $\mathbf{U}^{\text{us}}$ ,  $\mathbf{U}^{p^{BR}}$ ,  $\mathbf{U}^{p^{IR}}$  and  $\mathbf{U}^{c_m^D}$  are generated to compute separated reduction matrices which are summarised in  $\Phi$ . The reduced nonlinear terms

$$\hat{\mathbf{k}}(\Phi \mathbf{u}_{\text{red}}) := \underbrace{\Phi^T}_{\in \mathbb{R}^{l \times N}} \underbrace{\mathbf{k}(\Phi \mathbf{u}_{\text{red}})}_{\in \mathbb{R}^N} \quad \text{and} \quad \hat{\mathcal{D}}(\Phi \mathbf{u}_{\text{red}}) := \underbrace{\Phi^T}_{\in \mathbb{R}^{l \times N}} \underbrace{\mathcal{D}(\Phi \mathbf{u}_{\text{red}})}_{\in \mathbb{R}^{N \times N}} \underbrace{\Phi}_{\in \mathbb{R}^{N \times l}} \quad (3.22)$$

have a computational complexity that still depends on the full number of DOF  $N$ . Therefore, solving this system might be still as costly as solving the original system. In this regard, the nonlinear functions  $\mathcal{D}(\Phi \mathbf{u}_{\text{red}}) \Phi \dot{\mathbf{u}}_{\text{red}}$  and  $\mathbf{k}(\Phi \mathbf{u}_{\text{red}})$  in (3.21) are approximated via a projection to a subspace, spanned by a basis of dimension  $k \ll N$ . Thus, the approximation  $\bar{\mathbf{y}} \in \mathbb{R}^N$  of the composed nonlinear term  $\mathbf{y}(\Phi \mathbf{u}_{\text{red}}) = \mathcal{D}(\Phi \mathbf{u}_{\text{red}}) \Phi \dot{\mathbf{u}}_{\text{red}} + \mathbf{k}(\Phi \mathbf{u}_{\text{red}}) \in \mathbb{R}^N$  is of the form

$$\mathbf{y}(\Phi \mathbf{u}_{\text{red}}) \approx \bar{\mathbf{y}}(\Phi \mathbf{u}_{\text{red}}) = \Psi \mathbf{c}. \quad (3.23)$$

Therein,  $\Psi = [\boldsymbol{\psi}_1 \dots \boldsymbol{\psi}_k] \in \mathbb{R}^{N \times k}$  represents the subspace matrix with the orthonormal basis vectors  $\{\boldsymbol{\psi}_i\}_{i=1, \dots, k} \in \mathbb{R}^N$ , and  $\mathbf{c} \in \mathbb{R}^k$  is the corresponding coefficient vector. The projection basis  $\{\boldsymbol{\psi}_1 \dots \boldsymbol{\psi}_k\}$  is constructed by applying the POD method to the nonlinear snapshots  $\mathbf{y}_i(\mathbf{u}_i) = \mathcal{D}_i(\mathbf{u}_i) \dot{\mathbf{u}}_i + \mathbf{k}_i(\mathbf{u}_i)$ , obtained by the initial full system. In contrast to the snapshots of the state variables, the snapshots of the nonlinear terms are not only stored at the converged states but also at all non-converged states within the iterative solution process providing considerably improved results. Following this, the nonlinear snapshots are the sets  $\{\mathbf{y}_i(\mathbf{u}_i)\}_{i=1, \dots, m}$  with the vectors  $\mathbf{u}_i$  of unknowns at each Newton step (with totally  $m$  Newton steps). To determine the coefficient vector  $\mathbf{c}$ ,  $k$  rows from the overdetermined system  $\mathbf{y}(\Phi \mathbf{u}_{\text{red}}) = \Psi \mathbf{c}$  (and thus important entries of the nonlinear terms) are selected. These entries (also referred to as DEIM points or magic points) correspond to the DOF on which the nonlinear terms are computed in the reduced simulation. Therefore, a matrix  $\mathbf{P} = [\mathbf{e}_{p_1} \dots \mathbf{e}_{p_k}] \in \mathbb{R}^{N \times k}$  is considered, where  $\mathbf{e}_{p_i}$  comply with

the  $p_i$ -th column of the identity matrix  $\mathbf{I} \in \mathbb{R}^{N \times N}$ . The interpolation indices  $p_i$  can be determined by an algorithm, cf. [58]. The first interpolation index  $p_1$  corresponds to the entry of the first basis vector  $\boldsymbol{\psi}_1$  with the largest magnitude. The other interpolation indices  $p_j$  with  $j = 2, \dots, k$  correspond to the entries with the largest magnitude of the vector  $\mathbf{r}_j = \boldsymbol{\psi}_j - \boldsymbol{\Psi} \mathbf{c}_j$  and can be interpreted as the ‘‘error’’ between the basis vector  $\boldsymbol{\psi}_j$  and its approximation  $\boldsymbol{\Psi} \mathbf{c}_j$  from interpolating the projection basis  $\{\boldsymbol{\psi}_1 \dots \boldsymbol{\psi}_{j-1}\}$  at the interpolation indices  $\{p_1 \dots p_{j-1}\}$ . Following this, the coefficient vector  $\mathbf{c}$  can be determined from

$$\mathbf{P}^T \mathbf{y}_{\text{sel}}(\boldsymbol{\Phi} \mathbf{u}_{\text{red}}) = (\mathbf{P}^T \boldsymbol{\Psi}) \mathbf{c}. \quad (3.24)$$

Inserting (3.24) in (3.23) leads to the final approximation

$$\bar{\mathbf{y}}(\boldsymbol{\Phi} \mathbf{u}_{\text{red}}) = \boldsymbol{\Psi} \mathbf{c} = \boldsymbol{\Psi} (\mathbf{P}^T \boldsymbol{\Psi})^{-1} \mathbf{P}^T \mathbf{y}_{\text{sel}}(\boldsymbol{\Phi} \mathbf{u}_{\text{red}}). \quad (3.25)$$

Therefore, the nonlinear term is approximated by  $\bar{\mathbf{y}}$  in such a way that only  $k \ll N$  entries of the nonlinear term  $\mathbf{y}$  must be calculated in the reduced system (represented by  $\mathbf{y}_{\text{sel}}$ ). Again, resulting from the different physical time behaviour of the primary variables, the snapshot matrix  $\mathbf{Y} = [\mathbf{y}_1 \dots \mathbf{y}_m] \in \mathbb{R}^{N \times m}$  needs to be separated into smaller snapshot matrices  $\mathbf{Y}_{\mathbf{u}_S}$ ,  $\mathbf{Y}_{p^{BR}}$ ,  $\mathbf{Y}_{p^{IR}}$  and  $\mathbf{Y}_{c_m^D}$  for each primary variable. Following this, reduction matrices  $\boldsymbol{\Psi}_{\mathbf{u}_S}$ ,  $\boldsymbol{\Psi}_{p^{BR}}$ ,  $\boldsymbol{\Psi}_{p^{IR}}$  and  $\boldsymbol{\Psi}_{c_m^D}$  are computed and summarised in the reduction matrix  $\boldsymbol{\Psi}$ . The matrix  $\mathbf{P}$  contains the information on the selected DOF and can be separated in matrices  $\mathbf{P}_{\mathbf{u}_S}$ ,  $\mathbf{P}_{p^{BR}}$ ,  $\mathbf{P}_{p^{IR}}$  and  $\mathbf{P}_{c_m^D}$  containing the information on the selected DOF corresponding to the respective primary variable. Inserting these equations in the reduced system (3.21), the following POD-DEIM reduced system can be found:

$$\underbrace{\hat{\mathcal{D}}(\boldsymbol{\Phi} \mathbf{u}_{\text{red}})}_{\bar{\mathcal{D}}(\boldsymbol{\Phi} \mathbf{u}_{\text{red}})} \dot{\mathbf{u}}_{\text{red}} + \underbrace{\hat{\mathbf{k}}(\boldsymbol{\Phi} \mathbf{u}_{\text{red}})}_{\bar{\mathbf{k}}(\boldsymbol{\Phi} \mathbf{u}_{\text{red}})} = \underbrace{\hat{\mathbf{f}}}_{\mathbf{f}^T \mathbf{f}}. \quad (3.26)$$

The corresponding matrix formulations are derived via

$$\underbrace{\begin{bmatrix} \mathbf{0} & \mathbf{0} & \mathbf{0} & \mathbf{0} \\ \zeta_{p^{BR}} \mathcal{D}_{21,\text{sel}} \boldsymbol{\Phi}_{\mathbf{u}_S} & \zeta_{p^{BR}} \mathcal{D}_{22,\text{sel}} \boldsymbol{\Phi}_{p^{BR}} & \zeta_{p^{BR}} \mathcal{D}_{23,\text{sel}} \boldsymbol{\Phi}_{p^{IR}} & \mathbf{0} \\ \zeta_{p^{IR}} \mathcal{D}_{31,\text{sel}} \boldsymbol{\Phi}_{\mathbf{u}_S} & \zeta_{p^{IR}} \mathcal{D}_{32,\text{sel}} \boldsymbol{\Phi}_{p^{BR}} & \zeta_{p^{IR}} \mathcal{D}_{33,\text{sel}} \boldsymbol{\Phi}_{p^{IR}} & \mathbf{0} \\ \zeta_{c_m^D} \mathcal{D}_{41,\text{sel}} \boldsymbol{\Phi}_{\mathbf{u}_S} & \mathbf{0} & \mathbf{0} & \zeta_{c_m^D} \mathcal{D}_{44,\text{sel}} \boldsymbol{\Phi}_{c_m^D} \end{bmatrix}}_{\hat{\mathcal{D}}(\boldsymbol{\Phi} \mathbf{u}_{\text{red}})} \underbrace{\begin{bmatrix} \dot{\mathbf{u}}_{S,\text{red}} \\ \dot{\mathbf{p}}_{\text{red}}^{BR} \\ \dot{\mathbf{p}}_{\text{red}}^{IR} \\ \dot{\mathbf{c}}_{m,\text{red}}^D \end{bmatrix}}_{\dot{\mathbf{u}}_{\text{red}}} + \underbrace{\begin{bmatrix} \zeta_{\mathbf{u}_S} \mathbf{k}_{1,\text{sel}}(\boldsymbol{\Phi} \mathbf{u}_{\text{red}}) \\ \zeta_{p^{BR}} \mathbf{k}_{2,\text{sel}}(\boldsymbol{\Phi} \mathbf{u}_{\text{red}}) \\ \zeta_{p^{IR}} \mathbf{k}_{3,\text{sel}}(\boldsymbol{\Phi} \mathbf{u}_{\text{red}}) \\ \zeta_{c_m^D} \mathbf{k}_{4,\text{sel}}(\boldsymbol{\Phi} \mathbf{u}_{\text{red}}) \end{bmatrix}}_{\hat{\mathbf{k}}(\boldsymbol{\Phi} \mathbf{u}_{\text{red}})} = \underbrace{\begin{bmatrix} \boldsymbol{\Phi}_{\mathbf{u}_S}^T \mathbf{f}_1 \\ \boldsymbol{\Phi}_{p^{BR}}^T \mathbf{f}_2 \\ \boldsymbol{\Phi}_{p^{IR}}^T \mathbf{f}_3 \\ \boldsymbol{\Phi}_{c_m^D}^T \mathbf{f}_4 \end{bmatrix}}_{\hat{\mathbf{f}}} \quad (3.27)$$

with

$$\begin{aligned}
\zeta_{\mathbf{u}_S} &= \Phi_{\mathbf{u}_S}^T \Psi_{\mathbf{u}_S} (\mathbf{P}_{\mathbf{u}_S}^T \Psi_{\mathbf{u}_S})^{-1} \mathbf{P}_{\mathbf{u}_S}^T, \\
\zeta_{p^{BR}} &= \Phi_{p^{BR}}^T \Psi_{p^{BR}} (\mathbf{P}_{p^{BR}}^T \Psi_{p^{BR}})^{-1} \mathbf{P}_{p^{BR}}^T, \\
\zeta_{p^{IR}} &= \Phi_{p^{IR}}^T \Psi_{p^{IR}} (\mathbf{P}_{p^{IR}}^T \Psi_{p^{IR}})^{-1} \mathbf{P}_{p^{IR}}^T, \\
\zeta_{c_m^D} &= \Phi_{c_m^D}^T \Psi_{c_m^D} (\mathbf{P}_{c_m^D}^T \Psi_{c_m^D})^{-1} \mathbf{P}_{c_m^D}^T.
\end{aligned} \tag{3.28}$$

Alternatively, separated snapshots and reduction matrices for the nonlinear terms  $\mathbf{k}(\mathbf{u})$  and  $\mathcal{D}(\mathbf{u})\dot{\mathbf{u}}$  can be computed to archive more precise results. There, the nonlinear matrix  $\mathcal{D}(\mathbf{u})$  can be treated independently from the vector  $\dot{\mathbf{u}}$  by transferring the matrix in a vector. For this purpose, a matrix version of the DEIM, the so-called matrix discrete empirical interpolation method (MDEIM), has been proposed for the efficient reduction of parametrised systems arising from the discretisation of partial differential equations, cf. Negri *et al.* [216]. However, the implementation would become considerably more difficult, the offline computation more expensive and the storage demand would increase. Following this, the composite nonlinear term  $\mathbf{y}(\mathbf{u})$  is used in the following and results a sufficient accuracy. «(p.40)



# Chapter 4:

## Multiscale modelling aspects

Since the previously presented modelling approach of the TPM represents a macroscopic approach, the field quantities (at spatial positions) are understood as (averaged) mean values of an underlying REV with no explicit consideration of the resolved microstructure. In this regard, the aim of this section is to present possibilities to enrich the macroscopic TPM modelling approach using appropriate lower-scale models and available microstructural data. Therefore, two approaches to gain microscopical information from pore-scale models via scale-bridging techniques are discussed at the examples of computational fluid dynamics (CFD) and smoothed particle hydrodynamics (SPH). Beyond these two examples, there exist alternative approaches, such as pore-scale methods, mathematical homogenisation techniques or experimental investigations to estimate the permeability of a porous medium. A recent comparison of methods at the example of a benchmark problem is reported in Wagner *et al.* [278]. Furthermore, the usage of imaging data to estimate permeabilities is discussed at the examples of micro computed tomography ( $\mu$ CT) and diffusion tensor imaging (DTI) data in Section 4.2. Based on these highly resolved three-dimensional imaging data, an evaluation of a second-order permeability tensor is feasible, describing possible anisotropic perfusion characteristics of the porous material. Beyond the issues discussed in this chapter, an example to derive constitutive equations based on scale-linking considerations is given afterwards in Section 9.5 at the specific example of brain-tissue modelling.

### 4.1 Consideration of pore-scale models

Both approaches, the long-established CFD as well as the rather new-fashioned SPH, consider the fully resolved pore structure of the porous material. Therefore, the characteristics of a pore-fluid flow can be reproduced under the consideration of appropriate boundary conditions at the internal surfaces of the porous structure. However, a detailed geometrical knowledge for the preparation of the pore-scale models is required but often available for domains in the length scale of some centimetres.

#### 4.1.1 Computational fluid dynamics (CFD)

INTRODUCTORY NOTE: The content of this section was derived during the production of the master thesis: *Theoretical and numerical investigations of fluid flow in porous media with regular microstructures*, conducted by Zubin Trivedi [269].

In this section, the fluid flow through a porous medium is modelled on two scales, i. e. using a Computational Fluid Dynamics (CFD) model at the pore scale and a TPM model at the REV scale. The aim is to identify the intrinsic permeability  $K^{SF}$  as a macroscopic

quantity proceeding from the microstructure by a two-pronged approach for a scale linkage. Therefore, a simple example with a regular-shaped microstructure is studied. Based on the derived approach a parametric study is conducted for the permeability with respect to two main parameters, namely the porosity and the specific surface area (SSA). Finally, the well-known Kozeny<sup>1</sup>-Carman relation is discussed in terms of validation.

**Underlying pore-scale model:** Basically, the CFD model is investigated using the commercial software ABAQUS<sup>®</sup> (Dassault Systèmes, Vélizy-Villacoublay, France, cf. <http://www.3ds.com>). In this regard, convenient pre- and post-processing features as well as the CFD model implementation and corresponding solver methods are already available in ABAQUS. Therefore, only a brief general introduction is given here for the sake of completeness.

For the incompressible Navier-Stokes equations, there are two primary variables related to the balances of mass and momentum, namely the pressure  $p$  and the velocity  $\mathbf{v}$ . It is well known that the solution of the incompressible Navier-Stokes equations poses a number of algorithmic issues due to the divergence-free velocity condition (obtained from the mass balance) and the typically complex geometries of engineering applications. Therefore, the ABAQUS/CFD incompressible solver uses a hybrid discretisation technique which is built on the integral conservation statements for an arbitrary deforming domain. For time-dependent problems, an advanced second-order projection method is provided with a node-centred finite-element discretisation for the pressure field. This hybrid approach guarantees accurate solutions and eliminates the possibility of spurious pressure modes while retaining the local conservation properties associated with traditional finite-volume methods.

**Linking between the scales:** The general procedure is shown in form of a schematic flowchart in Figure 4.1. Note in passing that a further simplification of this procedure towards a direct permeability estimation is possible for specific initial-boundary-value problems as it is described later. Obviously, the creation of a pore-level model requires to rebuild all geometric details in an elaborating pre-processing step in the ABAQUS CAE environment. From the CFD model nodal velocities are obtained as output variables. For a scale bridging it is fundamental to apply a homogenisation procedure over these nodal velocities in order to extract a corresponding seepage velocity occurring in the TPM model. The macroscopic TPM model is pre-processed using the software toolkit CUBIT (Sandia National Laboratories, Albuquerque, USA, cf. <http://cubit.sandia.gov>). The numerical solution is then implemented in PANDAS (Porous media Adaptive Nonlinear finite element solver based on Differential Algebraic Systems, cf. <http://www.get-pandas.com>). Basically, the TPM model requires several input parameters, including the permeability, while the seepage velocity is obtained as a result of the coupled process. In the current example, the pore structure is assumed to be homogeneous and isotropic. Therefore, a constant value of the seepage velocity is obtained in the whole domain of the model. For arbitrary IBVP, the TPM model is used for trial-and-error runs to find the matching seepage velocity in correspondence to the CFD model.

---

<sup>1</sup>Josef Alexander Kozeny (1889–1967) was an Austrian hydraulic engineer and physicist. Today he is mainly remembered for the Kozeny-Carman equation which describes fluid flowing through a packed bed of solids [WIKIPEDIA].

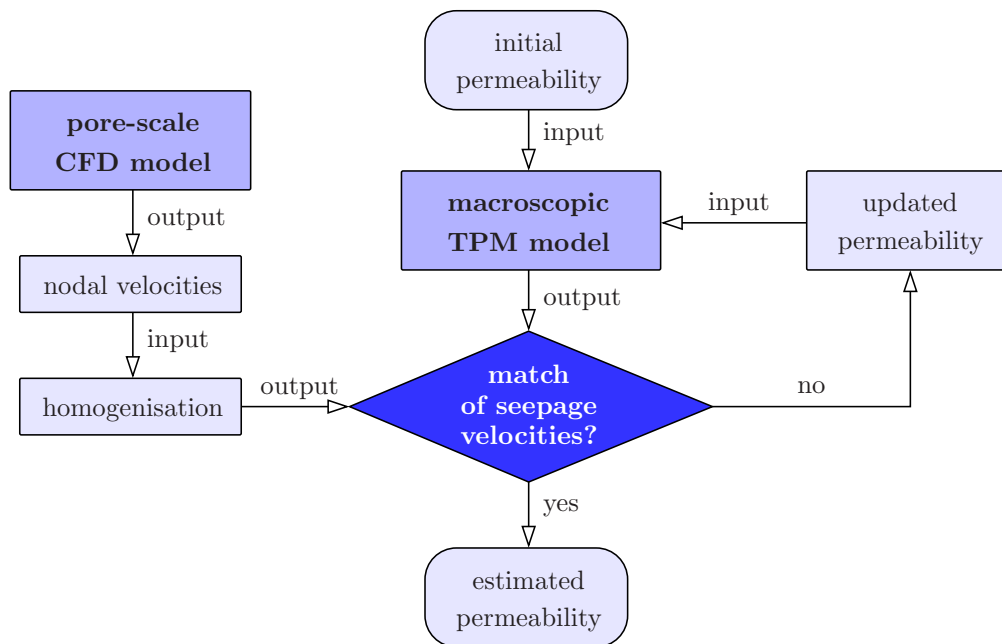


**Figure 4.1:** Schematic flowchart showing the permeability estimation via the linkage of a pore-scale CFD and a macroscopic TPM model.

**A simple example:** A regular porous sample with dimensions  $40 \times 40 \times 40$  mm (Figure 4.2) is studied, where the solid skeleton is assumed to be rigid with no-slip boundary conditions for the fluid. For the pore-scale CFD model, created in **ABAQUS**, the corresponding fluid-flow domain is obtained by cutting out the solid domain. Subsequently, this flow domain is meshed using linear tetrahedral elements, consisting of 197 287 nodes and 990 331 elements. Such a high mesh density is required to obtain convergence due to the geometry. Therefore, the numerical solution of the full-size model in Figure 4.2 (a) is time-consuming and computationally expensive. For the present case of a regular ar-

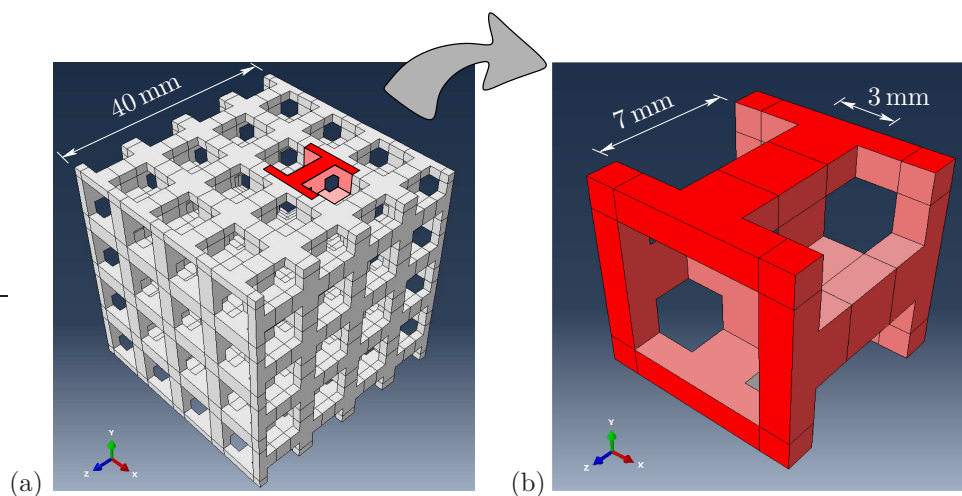


**Figure 4.2:** Solid skeleton of example problem with dimensions  $40 \times 40 \times 40$  mm in (a) and (b) shows the repeating unit (REV or unit cell) of the structure.

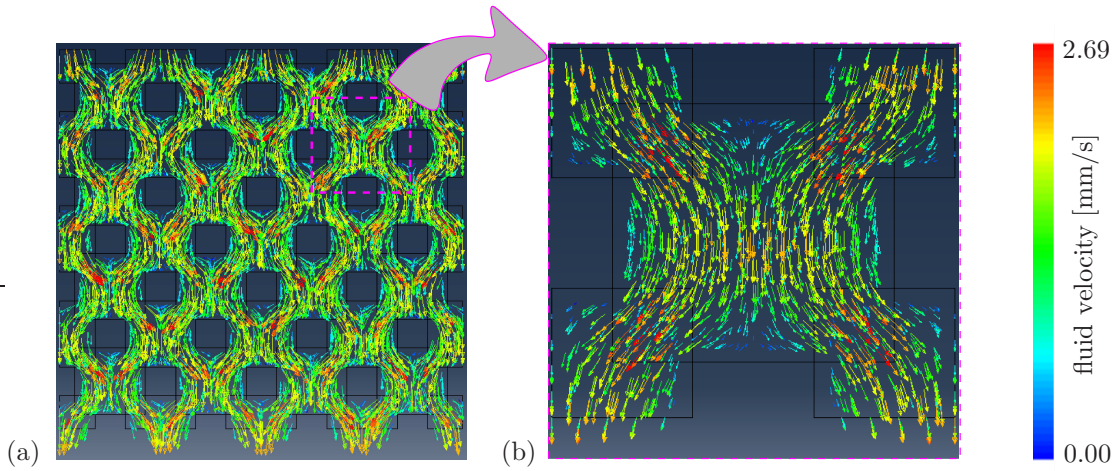


**Figure 4.3:** Results for CFD simulation on the initial model in (a) and the repeating substructure (b).

ranged (modular) microstructure, it is sufficient to consider the repeating unit (REV or unit cell) of the structure (using symmetry conditions even an eighth would be sufficient) with dimensions  $10 \times 10 \times 10$  mm, shown in Figure 4.2 (b). However, this is still a pore-scale model since the exact geometric details of the structure are still resolved and no averaging procedure has been carried out. Conserving the mesh density requires only 3138 nodes and 14311 elements and decrease the computation time significantly. An absolute pressure is applied on the top surface of the sample. In particular, the pressure applied at the top surface is 20 000 Pa, while the pressure at the bottom surface is 0 Pa. This results in a fluid flow in vertical direction due to the arising pressure gradient of  $5 \times 10^5$  Pa/m. The sides of the flow domain are assumed to allow slip but no penetration through the walls. Moreover, no slip on the internal walls of the microstructure is assumed. As material parameters, the dynamic viscosity of the fluid  $\mu^F = 200$  N s/m<sup>2</sup> and the effective density  $\rho^{FR} = 1.2 \times 10^3$  kg/m<sup>3</sup> are chosen exemplarily.

**Results:** Figure 4.3 shows the velocities obtained from the CFD simulation in the original model (a) and the repeating substructure (b). A representative averaged seepage velocity needs to be extracted from these results for a scale linking with the TPM model. From a physical point of view, the seepage velocity is the average fluid velocity within the pore space. Therefore, the straight-forward approach would obviously be to take an average of these velocities. However, the drawback of this procedure is that for irregular element sizes an averaging process would require to include all local element sizes and would become numerically expansive<sup>2</sup>. This motivates an alternative approach using the total volumetric flow rate  $Q$  through a total cross-sectional area  $A$ , perpendicular to the flow direction, via

$$Q = Av \quad \longrightarrow \quad n^F w_F = \frac{Q}{A} \quad \longrightarrow \quad w_F = \frac{Q}{n^F A}, \quad (4.1)$$

<sup>2</sup>Note in passing that a simple average using the same weighting (cross area) for all velocities would basically lead to wrong and mesh-dependent results. In particular in the present example, where the node density is higher in the vicinity of the walls than in the centre of the pores. Hence, this would overestimate (boundary) nodes with small nodal velocities leading to an underestimated averaged velocity.

where the velocity  $v$  is identified as the Darcy filter velocity  $n^F w_F$ . In particular, this procedure is handy since the flow rate  $Q$  is provided by **ABAQUS** as an output variable. Then, the Darcy filter velocity  $n^F w_F$  of the macroscopic TPM model is obtained by dividing the flow rate  $Q$  by the cross-sectional area  $A$ , where both quantities represent macroscopic values and, thus, authorises for the determination of the homogenised Darcy filter velocity  $n^F w_F$ . Upon that, the seepage velocity  $w_F$  is then also known by simply dividing the filter velocity by the porosity. For this simple example, the seepage velocity is found via

$$n^F w_F = \frac{1010.68 \text{ mm}^3/\text{s}}{40 \times 40 \text{ mm}^2} = 0.632 \text{ mm/s} \quad \longrightarrow \quad w_F \approx 1.02 \text{ mm/s},$$

where the porosity  $n^F = 0.622$  of the regular arranged geometry was used. Based on this pore-scale-based determination of the seepage velocity, the permeability can be estimated using the macroscopic TPM model. For this problem, it is possible to directly use Darcy's equation for finding the intrinsic permeability  $K^{SF}$  via

$$n^F w_F = - \frac{K^{SF}}{\mu^F} \text{grad } p \quad \longrightarrow \quad K^{SF} = \frac{n^F w_F \mu^F}{-\text{grad } p} \approx 2.53 \times 10^{-7} \text{ m}^2.$$

However, for more complex geometries this simple estimation is not feasible any more. Then an equivalent macroscopic TPM model needs to be investigated and used in the context of the previously introduced scale-linking approach, cf. Figure 4.1. In general, the geometrical creation of a macroscopic model is more convenient in comparison to a pore-scale model, since the exact geometric details of the structure are not required. For meshing purposes **CUBIT** can be used combined with an in-house developed interface for a later computation in **PANDAS**. Meaningfully, the material parameters for the fluid are the same as in the CFD simulation. Furthermore, the solid skeleton is assumed to be rigid. Therefore, a linear elastic material with sufficiently high values for the Lamé constants is suited. The solid volume fraction is obtained by the saturation condition via  $n^S = 1 - n^F$ . Since, the displacement serves as a primary variable in the TPM model, boundary conditions are required for both displacement and pressure which need to be set in accordance to the pore-scale CFD model.

**Parametric study:** The proposed scale-linking strategy given in Figure 4.1 can be used to find an isotropic scalar permeability of porous media. Based on that, the procedure is used for a parametric study of permeability with respect to two main parameters, namely the porosity and the specific surface area (SSA). In reality, however, the permeability may be further dependent on many more parameters, such as for example interface properties of internal surfaces depending on the involved materials or the degree of saturation. However, for this simple example these two are most probably the dominant quantities.

Porosity, as already explained, is the volume fraction of the fluid constituent with respect to the total bulk volume in a saturated porous medium. The specific surface area is the ratio of the surface area to the volume. For a meaningful parametric study, it is beneficial that one parameter can be varied without changing the other parameters. In order to achieve this, close-packed structures of equally-sized spheres are used. Each packing structure has a constant packing density, and therefore a constant porosity. The

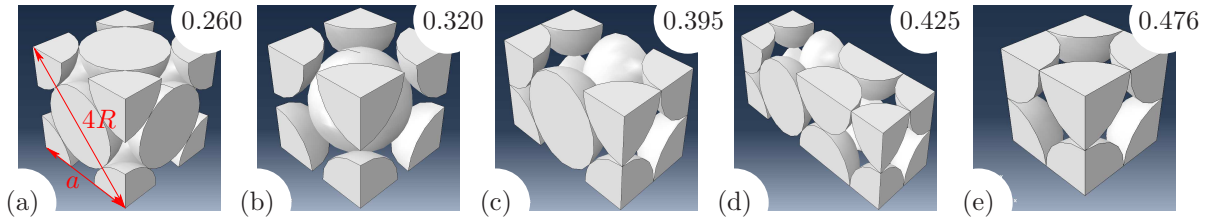


**Figure 4.4:** Lattice representative elementary volumes and their porosities.

packing density does not depend on the size of the shapes involved, whereas the specific surface area is a consequence of the shape and size of the internal features. Therefore, this can be varied by keeping the shape constant as a sphere with a changing value of radii. The idea here is to create reduced CFD models of these lattices, as explained in the previous chapter, with different sphere-packing structures and sizes, and simulate laminar fluid flow through such a structure. The resultant permeabilities are then recorded and plotted against the two parameters. The results are compared with the well-known Kozeny-Carman relation as a means of validation.

**Packing structures of spheres:** A close packing of equally sized spheres is a geometrically dense arrangement of equal spheres in an (infinite) regular lattice. The packing density depends on the arrangement of spheres in each layer and the stacking of one layer over another. Here, packings with spheres of uniform size are discussed for the parametric study. These artificial created arrangements are naturally observed in a single crystal lattice of atoms. However, the packing of sand grains in soils can also be considered as such a close-packed structure. Although, the arrangement is typically more random in natural porous media. The lattice arrangements are characterised by a so-called unit cell. These unit cells are repeating substructures of the (in general infinite) lattice and therefore used as an REV for creating the pore-scale CFD models. Each of these cells is created by placing uniform spheres with radius  $R$  at the vertices, edges, face-centres or body-centre of another imaginary shape. In this case, a cube or a cuboid. The packing density of such arrangements can not exceed 74 %, according to the Kepler<sup>3</sup> conjecture.

In Figure 4.4, five different unit cells are given with their respective porosities. For example, the face-centred cubic lattice in Figure 4.4(a) yields the maximum possible packing density. In particular, the side lengths  $a = 2\sqrt{2}R$  are determined by the diagonal of each face with length  $4R$ . This results the cube volume  $V_C = 16\sqrt{2}R^3$ . Therein, the volume is occupied by four spheres, yielding  $V_S = 16\pi R^3/3$ . Therefore, the packing density  $PD = V_S/V_C = \pi/3\sqrt{2} \approx 0.74$  determines the porosity  $n^F = 1 - PD = 0.26$ .

In general, each REV aggregation provides for a macroscopic material point a constant porosity. The radii of the spheres are varied and, thus, result different values for the specific surface area at the macroscopic points. The specific surface area of a single

<sup>3</sup>Johannes Kepler (1571–1630) was a German astronomer, mathematician, and astrologer. He is a key figure in the 17<sup>th</sup>-century scientific revolution and best known for his laws of planetary motion [WIKIPEDIA].

sphere is then calculated as

$$\text{Specific surface area (SSA)} = \frac{\text{Surface area (S)}}{\text{Volume (V)}} = \frac{4\pi R^2}{\frac{4}{3}\pi R^3} = \frac{3}{R}. \quad (4.2)$$

The specific surface area is inversely proportional to the radius of the spheres, cf. Equation (4.2). Thus, increasing the radii results in a linear decrease of specific surface area, and vice-versa. The specific surface area is used as a parameter instead of the radius itself since the specific surface area is a more general quantity applicable to any geometric shape. Note in passing that in the related literature, the specific surface area is defined in different ways, i. e. taking the surface area of the solid per unit volume of the whole space, which would include the void space. In this case, the *SSA* will be dependent on the porosity. The simpler definition is used here to avoid such dependency and make it a solely size-based parameter.

Figure 4.5 (a) shows the relation of the permeability to the specific surface area for lattice case (e) with porosity 0.476. Therefore, 15 values for the specific surface area are used ranging from  $0.06 \text{ mm}^{-1}$  to  $600 \text{ mm}^{-1}$ . This corresponds to a range of radii from  $0.005 \text{ mm}$  to  $50 \text{ mm}$  respectively. Hence, the analysis covers a range of size from as fine as micro-sized sand grains to as coarse as gravel-like particles. As expected, the permeability heavily reduces as the radius of particles increases. The evolution of permeability for two different porosities is shown in Figure 4.5 (b). In particular, the natural logarithm of permeability reduces linearly with the natural logarithm of the specific surface area. Furthermore, there is an upward shift in values for increasing porosity.

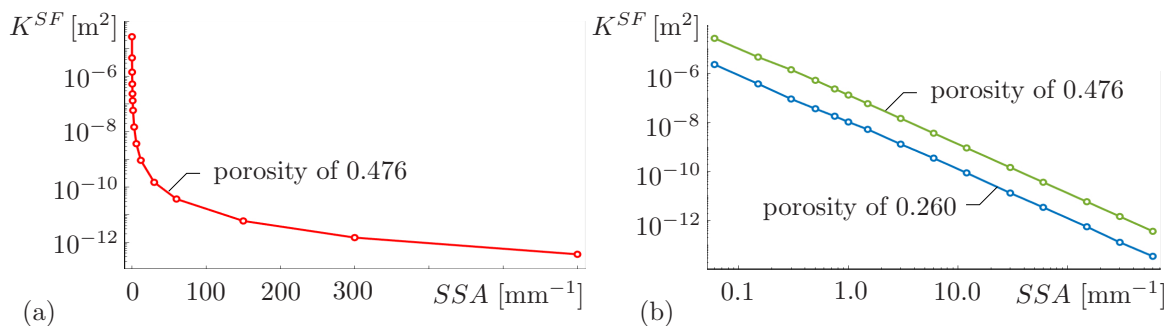


**Figure 4.5:** (a) Relation between the intrinsic permeability  $K^{SF}$  and the specific surface area  $SSA$  for the case (e) of Figure 4.4 (porosity of 0.476) and (b) the same relation for the cases (a) and (e) using a double logarithmic scale.

**The Kozeny-Carman equation:** The semi-empirical Kozeny-Carman (KC) model provides a permeability-porosity relationship for (granular) porous media and is widely used to estimate the permeability. In 1927, this formula was introduced by Kozeny [171] and further improved by Carman in 1938 and 1956, cf. Carman [56, 57].

In particular, Kozeny modelled the porous-media problem by assuming a porous-media layer (with thickness  $l$ ) as a bundle of capillary tubes with diameter  $D$  going through a solid, cf. Figure 4.6. The fluid flows through these capillary tubes which have a cumulative cross-sectional area  $A'$ , while the total cross-sectional area of the layer is  $A$ . The volumetric flow rate  $Q = Av$  assumes a fluid flows through the whole cross-section  $A$

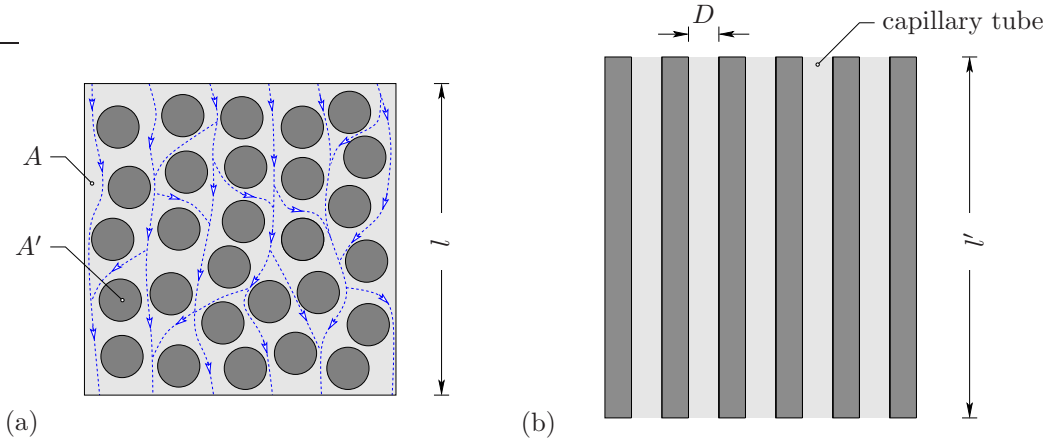


**Figure 4.6:** Sketch of the geometrical setting of Kozeny's model. Cross section with total cross-sectional area  $A$  and cumulative capillary cross-sectional area  $A'$  in (a) and capillary tubes using Poiseuille's law in (b).

with a fictitious velocity  $v$ . Obviously, this velocity  $v$  is physically identical to the macroscopic Darcy filter velocity. Accordingly, the volumetric flow rate can also be described as  $Q = A'v'$ , where  $v'$  is the mean velocity within the tubes. A comparison of these formulations results

$$v' = \frac{Av}{A'} = \frac{v}{n^F} \quad \text{with the porosity } n^F = \frac{A'l}{Al} = \frac{A'}{A}. \quad (4.3)$$

Furthermore, the pressure drop along a capillary of diameter  $D$  is given for a laminar flow by the Poiseuille<sup>4</sup>'s equation

$$\text{grad } p = -\frac{32\mu v'}{D^2}. \quad (4.4)$$

Note in passing that the gradient in (4.4) is related to the stream-line length  $l'$ , cf. Figure 4.6 (b). Carman later modified the equation by multiplying a factor of  $l'/l$ , arguing that the actual length  $l'$  of the fluid-flow path must be longer than the straight length  $l$ . Then, equation (4.4) using (4.3) modifies to

$$\text{grad } p = -\frac{32\mu v l'}{n^F D^2 l}. \quad (4.5)$$

For this idealised regular pore structure, cf. Figure 4.6, the capillary diameter  $D$  can be substituted by more convenient parameters via

$$n^F = \frac{V'}{V} = \frac{V'}{V' + V_S} \quad \longrightarrow \quad V' = \frac{n^F V_S}{(1 - n^F)}, \quad (4.6)$$

where  $V'$  is the volume of the tubes and  $V_S$  is the volume of the solid part. Dividing (4.6) by the surface area  $\hat{S}$  of capillary tubes yields

$$\frac{V'}{\hat{S}} = \frac{n^F V_S}{\hat{S}(1 - n^F)}. \quad (4.7)$$

<sup>4</sup>Jean Léonard Marie Poiseuille (1797–1869) was a French physicist and physiologist [WIKIPEDIA].

Therein, the volume  $V'$  and the surface area  $\hat{S}$  of the tubes can be found as

$$V' = \frac{\pi D^2 l'}{4} \quad \text{and} \quad \hat{S} = \pi D l'. \quad (4.8)$$

The relation  $\hat{S}/V_S$  represents the specific surface area  $S$  of the solid. Inserting the geometrical relations (4.8) in (4.7) yields

$$D = \frac{4 n^F}{S(1 - n^F)}. \quad (4.9)$$

Finally, an insertion of the above relation in (4.5) results

$$\text{grad } p = - \frac{2 \mu v l' S^2 (1 - n^F)^2}{(n^F)^3 l} \quad (4.10)$$

As mentioned before, a combination with Darcy's law

$$v = - \frac{K^{SF}}{\mu} \text{grad } p \quad (4.11)$$

yields after the insertion of (4.10) and some rearrangements the permeability estimation

$$K_{KC}^{SF} = \frac{(n^F)^3}{2 \tau^2 (1 - n^F)^2 S^2}, \quad (4.12)$$

if the ratio  $l'/l$  is identified as the so-called tortuosity  $\tau$ . Carman chose this value empirically to 2.5. The tortuosity  $\tau$  contains information about the internal geometry of the microstructure and changes for different porous aggregations.

**Comparison of permeability-estimation approaches:** The Kozeny-Carman equation (4.12) is used to judge the permeabilities obtained from the parametric study, cf. Figure 4.7 (a) for two specific cases. Obviously, the qualitative behaviour is similar. However,

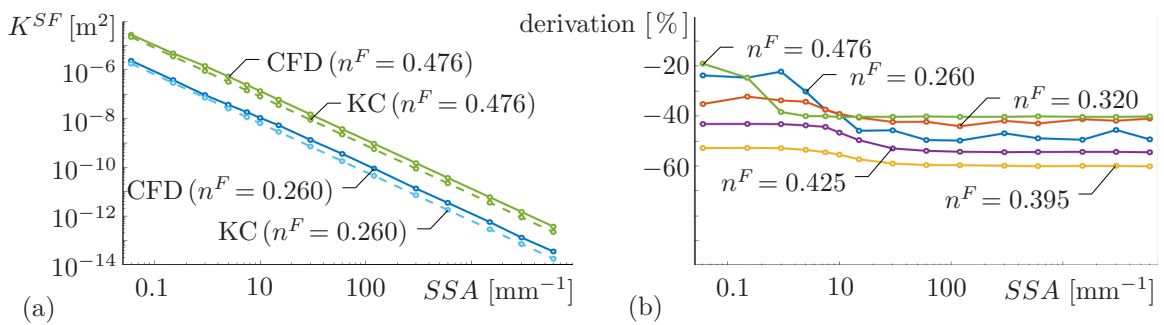


**Figure 4.7:** Intrinsic permeability computed from the numerical pore-scale CFD model and from the analytical Kozeny-Carman (KC) equation for different specific surface areas in (a) and (b) deviation of the different permeability-estimation approaches.

there is a difference in the absolute values. In this regard, the corresponding deviation graphs for all cases are shown in Figure 4.7 (b). Therein, the deviation is evaluated via

$$\text{deviation} [\%] = \frac{(K_{KC}^{SF} - K^{SF}) 100}{K^{SF}}. \quad (4.13)$$

Basically, the Kozeny-Carman equation consistently underestimates the pore-scale CFD simulations by 20 %- 60 %, with fluctuating results for small  $SSA$  values. However, for larger  $SSA$  values, the difference remains nearly constant. In general, there is no obvious relation between the deviation and the porosity. Although, the smallest deviation is obtained for the highest porosity. In contrast, the opposite is not observed for the case of the smallest porosity.

A modification of the tortuosity (contrary to the initial assumption of Carman using  $\tau = 2.5$ ) in (4.12) can be used to eliminate the observed difference. This can be achieved using an inverse evaluation of the tortuosity  $\tau$  based on (4.12). Then, the matching of these values with experimentally observed tortuosity values for porous media with spherical particles can act as an validation. Note in passing that the tortuosity is not only a function of porosity but also of the topology of the porous medium, i. e. indicated by the  $SSA$ . For different porosities with larger  $SSA$  values, the inversely evaluated tortuosities range between 1.0 and 1.6.

For a validation of these results, referential experimental observations are required. In general, the quality of experimental measurements of tortuosities increased in recent years due to modern imaging techniques. For example, there is data available for packed beds of spherical particles. Commonly, porous beds consisting of spherical or quasi-spherical particles are reported to have a tortuosity in the range 1.0 – 1.4, cf., e. g., the works of Barrande *et al.* [14], Dias *et al.* [71], Koponen *et al.* [170], Mota *et al.* [211], Yun *et al.* [297] or Neethirajan *et al.* [215]. In conclusion, this shows a good accordance between the pore-scale CFD simulations, the Kozeny-Carman estimation and the reported experiments.

### 4.1.2 Smoothed particle hydrodynamics (SPH)

INTRODUCTORY NOTE: The content of this section was derived during the production of the master thesis: *A quantitative comparison of multiscale models for single-phase flow in porous media*, conducted by David Krach [172].

The SPH approach represents a fully Lagrangean, mesh-free simulation method, developed by Lucy [190] as well as Monaghan, Gingold and their co-workers [121, 122, 203, 204]. In particular, SPH is a particle-collocation method, originally developed for astrophysical purposes but also applicable to direct numerical simulations of fluid flow on the pore scale, cf. Sivanapillai [250]. Comprehensive reviews are given by Monaghan [206], Cossins [65], Liu & Liu [188] and the textbook by Violeau [274].

**Underlying pore-scale model:** The fluid body is considered as a finite number of fluid particles, assigned with mass, velocity or other quantities, such as initial or boundary condition of the considered initial-boundary-value problem. In general, the knowledge of the exact physical state of such systems is both: (i) practically unachievable due to the large number of degrees of freedom and (ii) beyond some precision even overloaded with (useless) information. Therefore, methods of statistical mechanics are an appealing and feasible way to deal with such systems.

To describe the motion of the fluid correctly, forces have to be constructed from the stored information of single particles, cf. Monaghan [204]. In the framework of SPH,

the partial differential conservation laws of CFD are transformed into integral or discrete integral equations based on interpolation theories, cf. Libersky *et al.* [183]. Therefore, the foundation is the following identity

$$\Psi(\mathbf{x}, t) = \int_{\Omega} \Psi(\mathbf{x}', t) \delta^D(\mathbf{x} - \mathbf{x}') dv. \quad (4.14)$$

Equation (4.14) is referred as the continuous representation of the spatial convolution of a tensor field  $\Psi$  with the so-called Dirac<sup>5</sup> delta distribution  $\delta^D$ . Therein, the time dependency of  $\Psi(\mathbf{x}, t) = \Psi(\mathbf{x})$  is omitted. Moreover, the  $\delta^D$ -distribution for two position vectors  $\mathbf{x}$  and  $\mathbf{x}'$  is given by

$$\delta^D(\mathbf{x} - \mathbf{x}') = \begin{cases} \infty & \text{for } \mathbf{x} - \mathbf{x}' = 0 \text{ and} \\ 0 & \text{for } \mathbf{x} - \mathbf{x}' \neq 0. \end{cases} \quad (4.15)$$

Note in passing that the prime sign is not representing a derivation in the SPH context but indicates a position vector  $\mathbf{x}'$  to be different from  $\mathbf{x}$ . In addition, the  $\delta^D$ -distribution is constrained to satisfy the identity

$$\int_{-\infty}^{+\infty} \delta^D(\mathbf{x} - \mathbf{x}') dv = 1. \quad (4.16)$$

In a next step, the Dirac delta distribution in (4.14) is replaced with a continuously differentiable kernel function  $W(\mathbf{x}, h)$ , yielding the integral representation

$$\Psi_h(\mathbf{x}) = \int_{\Omega} \Psi(\mathbf{x}') W(\mathbf{x} - \mathbf{x}', h) dv, \quad (4.17)$$

which is fundamental for further SPH calculations. In particular, (4.17) can be interpreted as the smoothing of a particle's point quantity, e. g. mass, by the kernel in order to receive a continuous field from a considered set of particles, cf. Monaghan [204]. The quantity  $h$  is the kernels smoothing length and the limit of the  $h$ -dependent kernel has to satisfy the constraints

$$\lim_{h \rightarrow 0} W(\mathbf{x}, h) = \delta^D(\mathbf{x}) \quad \text{and} \quad \lim_{h \rightarrow 0} \Psi_h = \Psi. \quad (4.18)$$

The tensor field  $\Psi$ , representing an arbitrary physical quantity of a particle  $\mathbf{x}$ , is obtained by the summation over respective tensor fields of all other particles in the range of  $h$  around  $\mathbf{x}$ . Evaluation of the kernel provides a weight depending on the distance between the couple of particles. While  $h$  characterises the active interaction radius,  $W$  is a relative value for the intensity of the possible direct or indirect interaction of the two considered particles. For the evaluation of the later introduced motion functions, it is necessary to compute the gradient and the divergence of the tensor field  $\Psi_h$ . Using the Taylor

---

<sup>5</sup>Paul Adrien Maurice Dirac (1902–1984) was an English theoretical physicist who is regarded as one of the most significant physicists of the twentieth century. In 1933, Dirac shared the Nobel Prize in Physics with Erwin Schrödinger [WIKIPEDIA].

expansion of  $\Psi(\mathbf{x}')$ , cf. Sivanesapillai [250], yields

$$\begin{aligned}\text{grad}_h \Psi(\mathbf{x}) &= \int_{\Omega} \Psi(\mathbf{x}') \text{grad } W(\mathbf{x} - \mathbf{x}', h) \, dv \quad \text{and} \\ \text{div}_h \Psi(\mathbf{x}) &= \int_{\Omega} \Psi(\mathbf{x}') \text{grad } W(\mathbf{x} - \mathbf{x}', h) \, dv\end{aligned}\tag{4.19}$$

for a first-order tensor field  $\Psi(\mathbf{x})$ . Furthermore, Lucy [190] based the approach on Monte-Carlo theory (set of particles randomly distributed in a control volume). In this regard, a statistical kernel function to perform a kernel density estimation (KDE) is introduced. It is used to estimate the tensor field's density in the computational domain. Therefore, countless different kernels (or non-negative real valued integrable functions) can be defined in order to replace the Dirac delta distribution. Nevertheless,  $W$  has to comply several conditions to be practicable. Among others, it has to fulfil the normalisation condition, viz.:

$$\int_{-\infty}^{\infty} W(\mathbf{x}, h) \, dv = 1.\tag{4.20}$$

This ensures that the result of a KDE is a probability density function (PDF) leading to the scale preservation and satisfaction of (4.18)<sub>1</sub>. Moreover,  $W$  is required to be symmetric. To be in line with (4.20), a kernel with compact support and a compactness factor  $k$  is used, with the property

$$W(r, h) = 0 \quad \forall \quad r > kh.\tag{4.21}$$

In (4.21), the introduced compactness factor  $k$  is a positive real and constant number, depending on the particular form of  $W(r, h)$ . Inserting the non-dimensional distance  $q := r/h$ , the kernel and its gradient are obtained as

$$W(\mathbf{x} - \mathbf{x}', h) = \frac{\alpha_n}{h^n} \tilde{W}(q) \quad \text{and} \quad \text{grad } W(\mathbf{x} - \mathbf{x}', h) = \frac{\alpha_n}{h^{n+1}} \frac{\partial \tilde{W}(q)}{\partial q} \frac{\mathbf{x} - \mathbf{x}'}{r},\tag{4.22}$$

respectively. Therein,  $\alpha_n$  is the normalisation constant and  $h$  is considered to be constant in time and space. Obviously, there are still an infinite number of kernel functions satisfying the previously introduced constraints. However,  $W$  is preferably chosen in a way that evaluating the function is computationally cheap. Therefore, suited kernels are, e. g., the fifth-order quintic B-spline

$$\tilde{W}_q(q) = (3 - q)_+^5 - 6(2 - q)_+^5 + 15(1 - q)_+^5,\tag{4.23}$$

introduced by Schoenberg [239] and the so-called Wendland C4 kernel (Wendland [285]):

$$\tilde{W}_w(q) = \left(1 - \frac{q}{2}\right)_+^6 \left(3 + 9q + \frac{35q^2}{4}\right).\tag{4.24}$$

In (4.23) and (4.24), the operator  $(\cdot)_+$  computes the argumentum maximi ( $\max\{0, \cdot\}$ ). Originally used Gaussian kernels (Gingold & Monaghan [121], Monaghan [204]) are not used here due to high computational costs. In the following, the kernels (4.23) and (4.24)

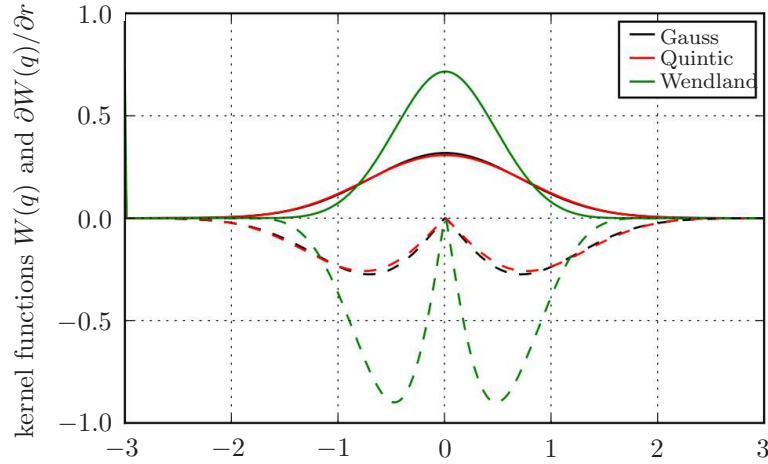


**Figure 4.8:** Wendland  $C4$ , quintic as well as Gaussian kernel with respect to the non-dimensional distance  $q$  as well as their derivations (dotted lines) with a derivations direction headed off from the origin.

are used due to the fact that these compactly supported kernels reduce the computational costs drastically. The applied kernels as well as the Gaussian and their outward orientated derivations are plotted in Figure 4.8.

To obtain a computationally exploitable form of the continuous definition, (4.17) needs to be numerically integrable. Therefore, a quadrature rule over  $N$  integration points is used for (4.17) in terms of the Riemann<sup>6</sup> sum, yielding

$$\Psi_h(\mathbf{x}) \approx \Psi_{h, \mathbf{dx}}(\mathbf{x}) = \sum_{j: \mathbf{x}_j \in \Omega_{\mathbf{x}}}^{N_n(\mathbf{x})} \Psi(\mathbf{x}_j) W(\mathbf{x} - \mathbf{x}_j, h) V_j. \quad (4.25)$$

The subscript  $(\cdot)_{h, \mathbf{dx}}$  implies that the approximation of  $\Psi_{h, \mathbf{dx}}$  relies on  $h$  and a characteristic discretionary length scale  $\mathbf{dx}$ . Furthermore, the volume element  $V_j$  is introduced as a discrete representation of  $dv$ . In order to implement the computation of this equation as computationally cheap as possible, the summation is restricted to the kernels compact support domain  $\Omega_{\mathbf{x}}$  and the set of nearest neighbours  $N_n(\mathbf{x})$  that satisfies  $\|\mathbf{x} - \mathbf{x}_j\| < kh$ . In analogy, the nodal representations of (4.19) can be found via

$$\begin{aligned} \text{grad}_{h, \mathbf{dx}} \Psi(\mathbf{x}) &= \sum_{j: \mathbf{x}_j \in \Omega_{\mathbf{x}}}^{N_n(\mathbf{x})} \Psi(\mathbf{x}_j) \text{grad} W(\mathbf{x} - \mathbf{x}_j, h) V_j \quad \text{and} \\ \text{div}_{h, \mathbf{dx}} \Psi(\mathbf{x}) &= \sum_{j: \mathbf{x}_j \in \Omega_{\mathbf{x}}}^{N_n(\mathbf{x})} \Psi(\mathbf{x}_j) \cdot \text{grad} W(\mathbf{x} - \mathbf{x}_j, h) V_j. \end{aligned} \quad (4.26)$$

<sup>6</sup>Georg Friedrich Bernhard Riemann (1826–1866) was a German mathematician who made contributions to analysis, number theory, and differential geometry. In the field of real analysis, he is mostly known for the first rigorous formulation of the integral, the Riemann integral, and his work on Fourier series [WIKIPEDIA].

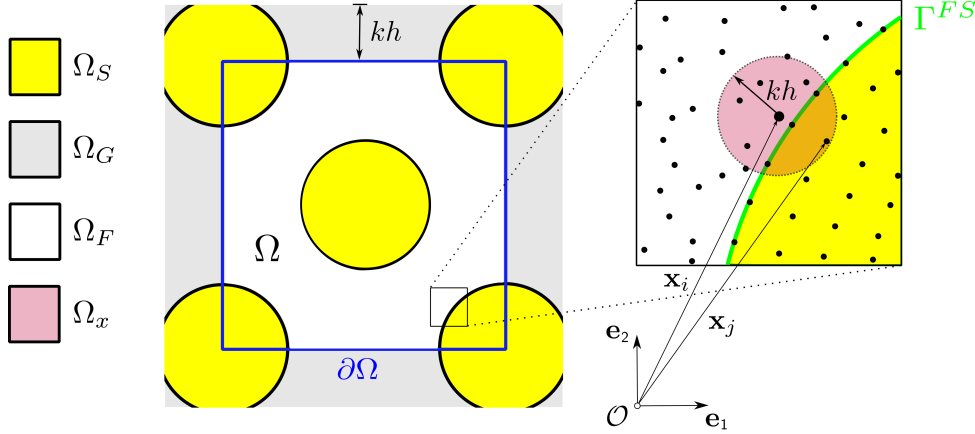


**Figure 4.9:** Subdivision of the computational domain and the adjacent ghost domain for singlephasic flow through a porous solid material, cf. Sivanesapillai [250].

For the sake of a compact notation, the relations are given in short for  $\mathbf{x} = \mathbf{x}_i$  as

$$\begin{aligned} \Psi_i &= \sum_{j:\mathbf{x}_j \in \Omega_{\mathbf{x}}} \Psi_j W_{ij} V_j, \quad \text{grad}_i \Psi = \sum_{j:\mathbf{x}_j \in \Omega_{\mathbf{x}}} \Psi_j \frac{\partial W_{ij}}{\partial r_{ij}} \frac{\mathbf{x}_i - \mathbf{x}_j}{r_{ij}} \quad \text{and} \\ \text{div}_i \Psi &= \sum_{j:\mathbf{x}_j \in \Omega_{\mathbf{x}}} \Psi_j \cdot \frac{\partial W_{ij}}{\partial r_{ij}} \frac{\mathbf{x}_i - \mathbf{x}_j}{r_{ij}}. \end{aligned} \quad (4.27)$$

Regarding cubic domains for a pore-scale study, the boundary inconsistency needs to be considered, cf. Figure 4.9. As an example, the simulation domain  $\Omega$  is periodically filled with spheres, representing the solid material  $\Omega_S \subset \Omega$ . Then, the respective non-solid part is representing the interconnected pore space of the porous material filled with fluid  $\Omega_F \subset \Omega$ . Furthermore, a computational domain  $\Omega_{\mathbf{x}} \subset \Omega$  is introduced for each particle to evaluate its properties. In case that for the compact support radius

$$kh \leq \|\mathbf{x} - \mathbf{y}\|, \quad \text{where } \mathbf{y} \text{ is the closest point on the boundary } \partial\Omega, \quad (4.28)$$

holds, the particle  $\mathbf{x}$  and its entire compactly supported domain (red-filled circle in Figure 4.9) lies within the simulation domain. In contrast, if (4.28) does not hold and the particle is located in a certain distance (smaller than  $kh$ ) from the boundary, the continuous completeness conditions are violated and leads for  $\Omega_{\mathbf{x}} \not\subseteq \Omega$  to errors. A suitable and very common corrective approach, to prevent those inconsistency errors and to met with an IBVP, is based on the introduction of so-called ghost particles, which are elements of an artificial ghost domain  $\Omega_G$ , cf. Sivanesapillai [250]. This procedure guarantees the completeness of approximations on and near the boundary via the extension of the domain by a frame of a constant thickness  $kh$ . At the beginning of each time step, a value is assigned to each ghost particle. The values are calculated such that each particle on the boundary  $\Gamma = \partial\Omega$  meets the requirements of the given BCs. In this regard, it is possible to define valid Neumann-BCs on  $\Gamma^N \subseteq \Gamma$  as well as Dirichlet-BCs on  $\Gamma^D \subseteq \Gamma$ . In the context of the given domain, BCs have to be specified for the fluid-solid boundary  $\Gamma_{FS}$  as well yielding to

a distinction of the inner and outer ghost domain  $\Omega_{Go} \cap \Omega_{Gi} = \Omega_G \subset \Omega$ . The properties of the ghost particles in both ghost domains are assigned in the same manner. Ghost particles or properties of ghost particles are subsequently indicated by the superscript  $(\cdot)^*$ . It turns out that this approach is expansive dealing with variable and constantly changing fluid surfaces. Therefore, corrective discrete reproducing approximations are beneficial to account for boundary inconsistencies. The basis to this procedure is the definition of a zeroth-order completeness kernel

$$W^{C0}(\mathbf{x}_j, h) = W(\mathbf{x}_j, h) K_0(\mathbf{x}_i), \quad (4.29)$$

with the correction coefficient  $K_0$  chosen to be specific to  $\mathbf{x}_i$ . Therein,  $K_0$  and thereby likewise  $W^{C0}$  have to be determined in order to satisfy

$$\sum_{j:\mathbf{x}_j \in \Omega_{\mathbf{x}_i}}^{N_n(\mathbf{x}_i)} W^{C0}(\mathbf{x}_j, h) V_j = \sum_{j:\mathbf{x}_j \in \Omega_{\mathbf{x}_i}}^{N_n(\mathbf{x}_i)} W(\mathbf{x}_j, h) K_0(\mathbf{x}_i) V_j \stackrel{!}{=} 1, \quad (4.30)$$

an analogue normalisation constraint according to (4.20). In this regard, the discrete nodal approximation is zeroth-order complete even if (4.28) does not hold, cf. Sivanesapillai [250]. The corrective approach for a scalar-valued field  $\Psi$  reads

$$\Psi_i^{C0} := \sum_{j:\mathbf{x}_j \in \Omega_{\mathbf{x}_i}}^{N_n(\mathbf{x}_i)} \Psi_j W_{ij}^{C0} V_j = \frac{\sum_{j:\mathbf{x}_j \in \Omega_{\mathbf{x}_i}}^{N_n(\mathbf{x}_i)} \Psi_j W_{ij} V_j}{\sum_{j:\mathbf{x}_j \in \Omega_{\mathbf{x}_i}}^{N_n(\mathbf{x}_i)} W_{ij} V_j}. \quad (4.31)$$

Furthermore, the operators

$$\begin{aligned} \text{grad}_i^{C0} \Psi &= \sum_{j:\mathbf{x}_j \in \Omega_{\mathbf{x}_i}}^{N_n(\mathbf{x}_i)} [\Psi_j - \Psi_i] \frac{\partial W_{ij}}{\partial r_{ij}} \frac{\mathbf{x}_i - \mathbf{x}_j}{r_{ij}} V_j \quad \text{and} \\ \text{grad}_i^{ASn} \Psi &= n_i \sum_{j:\mathbf{x}_j \in \Omega_{\mathbf{x}_i}}^{N_n(\mathbf{x}_i)} \left[ \frac{\Psi_i}{n_i^2} + \frac{\Psi_j}{n_j^2} \right] \frac{\partial W_{ij}}{\partial r_{ij}} \frac{\mathbf{x}_i - \mathbf{x}_j}{r_{ij}} \quad \text{with} \quad n_i = \sum_{j:\mathbf{x}_j \in \Omega_{\mathbf{x}_i}}^{N_n(\mathbf{x}_i)} W_{ij} \end{aligned} \quad (4.32)$$

are introduced, where  $\text{grad}_i^{ASn}$  is the antisymmetric gradient operator, assuming the local particle concentration  $n_i$  to be approximately constant. Analogously, the corrective approaches are applied for a tensor-valued field  $\Psi$ , yielding

$$\begin{aligned} \text{div}_i^{C0} \Psi &= \sum_{j:\mathbf{x}_j \in \Omega_{\mathbf{x}_i}}^{N_n(\mathbf{x}_i)} [\Psi_j - \Psi_i] \frac{\partial W_{ij}}{\partial r_{ij}} \frac{\mathbf{x}_i - \mathbf{x}_j}{r_{ij}} \quad \text{and} \\ \text{div}_i^{ASn} \Psi &= n_i \sum_{j:\mathbf{x}_j \in \Omega_{\mathbf{x}_i}}^{N_n(\mathbf{x}_i)} \left[ \frac{\Psi_i}{n_i^2} + \frac{\Psi_j}{n_j^2} \right] \frac{\partial W_{ij}}{\partial r_{ij}} \frac{\mathbf{x}_i - \mathbf{x}_j}{r_{ij}}. \end{aligned} \quad (4.33)$$

As a consequence, a set of discrete nodal motion equations that are globally conservative can be developed, cf., e. g., Bonet & Lok [38] or Sivanesapillai [250]. Therefore, these

conservative antisymmetric operators, (4.31)–(4.33), are used for the implementation of the discrete fluid-motion equations in the subsequent simulations.

An important task in SPH modelling is related to the specification of boundary conditions on the fluid-solid interface  $\Gamma^{FS}$  as well as on the outer boundary of the simulation domain  $\Gamma = \partial\Omega$ , cf. Figure 4.9. Adami *et al.* [2] proposed a consistent approach of a surrounding ghost-domain frame occupied by spatially and temporally fixed ghost particles which is computationally cheap and conceptually rather simple, cf. Sivanesapillai [250].

Due to the kernel approximation of the tensor field, the problem of only locally satisfied balance relations is created. This implies

$$\Psi_{h,\mathbf{x}}(\mathbf{x}_i) \neq \Psi_i W(\mathbf{x}_i - \mathbf{x}_j, h) V_j, \quad \text{since} \quad W(\mathbf{x}_i - \mathbf{x}_j, h) V_j \neq \delta^D(\mathbf{x}_i - \mathbf{x}_j), \quad (4.34)$$

for each properly defined kernel. For this reason, the method fails to reproduce boundary conditions of the form  $\Psi = \Psi_\Gamma(\mathbf{x}) \forall \mathbf{x} \in \Gamma^D$ , with  $\Gamma^D \subset \Gamma = \partial\Omega$  and  $\Gamma \cap \Gamma^{FS} = \emptyset$ . To avoid this drawback, periodic boundary conditions are typically used on  $\Gamma$ . In this regard, a system with periodic outer boundaries can be interpreted as an unbound (open) simulation domain. In case of a singlephasic flow in porous media, this is beneficial since only a single REV has to be simulated to analyse flow or porous-media properties. Besides the implementation of the ghost domain, and all its properties, further boundary effects on the outer boundary are not required. Therefore, embedding periodic boundary conditions limits the computations on several particles  $\mathbf{x} \in \Omega \cap \Omega_G$ . The particles  $\mathbf{x}_j^* \in \Omega_{Go}$  in the outer ghost domain are interpreted as reflections of the fluid particles  $\mathbf{x}_i \in \Omega_F$ . Hence  $\Psi_j^* = \Psi_i$  and  $\Psi_j^* = -\Psi_i$  hold for mass, momentum, energy, stress state and further material properties. Particles with a compact support domain, intersected by the outer ghost domain, are therefore subjected to an exchange of mass, momentum and energy with the included ghost particles. A particle crossing  $\Gamma$  in the outward direction reappears on the diametrically opposed position of the simulation domain.

Using Dirichlet boundary conditions, the desired value of the field variable is assigned to the representing amount of ghost particles on  $\Gamma^D$ . Since a biphasic system  $\Omega = \Omega_F \cap \Omega_S$  without any production is considered, no-slip and no-penetration Dirichlet boundary conditions are taken into account. Therefore, at each simulation time step the kinematical relation

$$\dot{\mathbf{x}}_F(\mathbf{x}) = \dot{\mathbf{x}}_{\Gamma^D}(\mathbf{x}) = \dot{\mathbf{x}}_{\Gamma^{FS}}(\mathbf{x}) = \mathbf{0}, \quad \forall \mathbf{x} \in \{\Gamma^D \cup \Gamma^{FS}\}, \quad (4.35)$$

holds for the boundary velocity  $\dot{\mathbf{x}}_{\Gamma^D}$  or the interface velocity  $\dot{\mathbf{x}}_{\Gamma^{FS}}$ , respectively. Restricting to no-slip and no-penetration conditions in the described simulation domain, the boundary velocity is per definition the velocity at the fluid-solid interface and, furthermore, is equal to  $\mathbf{0}$  if the boundary is considered as static and impermeable. Besides velocity, the second (primary) variable is the pressure in order to solve the momentum equation of the fluid. Therefore, a calculation of the respective properties of the ghost particles is provided for both. In particular, they are pre-calculated at the beginning of each time step such that, concerning velocities and the pressure, the interactions between both groups of particles meet the constraints of the particles on the boundary. For a no-slip Dirichlet boundary condition, the amount of ghost particles in the compact support domain has to comprise the contrary momentum to the adjacent amount of fluid particles. The velocity of a ghost

particle, often referred to as fictitious velocity, is computed by an extrapolation of fluid velocities based on (4.31) yielding

$$\dot{\mathbf{x}}_i^* = - \frac{\sum_{j:\mathbf{x}_j \in \Omega_i \cap \Omega_F} \dot{\mathbf{x}}_j W_{ij} V_j}{\sum_{j:\mathbf{x}_j \in \Omega_i \cap \Omega_F} W_{ij} V_j}, \quad \forall \mathbf{x}_i \in \Omega_G^D. \quad (4.36)$$

With the ghost domain at the vicinity of the static boundary  $\Omega_G^D$ , this term is prescribing the antisymmetric character of the fictitious velocities with respect to the fluid velocities. Note that the summation is only conducted in (4.36) over the cut set  $\Omega_i \cap \Omega_F$ . For  $W_{ij} = \delta^D$ , (4.36) yields  $\dot{\mathbf{x}}_i^* = -\dot{\mathbf{x}}_j$  and, thus, accounts for zeroth-order completeness.

To guarantee the no-penetration property of the Dirichlet boundary, a fictitious pressure  $\mathbf{p}^*$  is introduced. The fictitious pressure  $\mathbf{p}^*$  is computed such that boundary particles induce a repelling force on neighbouring fluid particles. Pressure gradients normal to the boundary add up and vanish in case of static conditions. In the case of a homogeneous and constant fluid pressure field,  $\mathbf{p}_i^* = \mathbf{p}_j$  holds. With a given volumetric (gravitational) force  $\mathbf{g}$ , the balance on the boundary is given by

$$-\text{grad } \mathbf{p} \cdot \mathbf{n} = \frac{\partial \mathbf{p}}{\partial n_\perp} = \rho^F \mathbf{g} \cdot \mathbf{n}, \quad \forall \mathbf{x} \in \Gamma^{FS}. \quad (4.37)$$

Therefore, the fictitious pressure can be obtained as

$$\mathbf{p}_i^* = \frac{\sum_{j:\mathbf{x}_j \in \Omega_i \cap \Omega_F} \mathbf{p}_j W_{ij} V_j}{\sum_{j:\mathbf{x}_j \in \Omega_i \cap \Omega_F} W_{ij} V_j} + \frac{\sum_{j:\mathbf{x}_j \in \Omega_i \cap \Omega_F} \rho_j (\mathbf{x}_i - \mathbf{x}_j) W_{ij} V_j}{\sum_{j:\mathbf{x}_j \in \Omega_i \cap \Omega_F} W_{ij} V_j} \mathbf{g}, \quad \forall \mathbf{x}_i \in \Omega_G^D. \quad (4.38)$$

For the exact derivation, the interested reader is referred to Sivanesapillai [250]. Moreover, all presented equations can be extended to non-static conditions, cf. Sivanesapillai [250] or Adami *et al.* [2].

In general, incompressible singlephasic flow with a constant fluid viscosity is described by the momentum balance (2.41)<sub>2</sub> of the fluid as

$$\rho^F \ddot{\mathbf{x}}_F = \text{div } \mathbf{T}^F + \rho^F \mathbf{g}. \quad (4.39)$$

Since the fluid constituent is treated separately in the first step, the interaction (production) terms vanishes. In (4.39), the Cauchy stress  $\mathbf{T}^F$  of the fluid has the general form

$$\mathbf{T}^F = \mathbf{T}_{\text{eq}}^F + \mathbf{T}_{\text{neq}}^F \quad \text{with} \quad \begin{cases} \mathbf{T}_{\text{eq}}^F &= -\mathbf{p} \mathbf{I} \quad \text{and} \\ \mathbf{T}_{\text{neq}}^F &= \lambda^F (\text{tr } \mathbf{D}_F) \mathbf{I} + 2 \mu^F \mathbf{D}_F. \end{cases} \quad (4.40)$$

Therein, the parameters  $\lambda^F$  and  $\mu^F$  denote the Lamé coefficients interpreted as the dilatational and dynamic viscosity, respectively. For quasi-incompressible flow of an isotropic, homogeneous and linear elastic fluid under isothermal conditions, the fluid stress  $\mathbf{T}^F$  is obtained as

$$\mathbf{T}^F = -\mathbf{p} \mathbf{I} + \mu^F (\text{grad } \dot{\mathbf{x}}_F + \text{grad }^T \dot{\mathbf{x}}_F). \quad (4.41)$$

In contrast to the TPM, where the thermodynamic pore pressure  $p^F$  is introduced via a Lagrangean multiplier, the pressure  $\mathbf{p}$  used within SPH indicates the negative rate of change of free energy per volume. If it has the form  $\mathbf{p} = \mathbf{p}(\rho^F)$ , the fluid is referred to as barotropic. The classical approach for water with the boundary condition  $\mathbf{p}(\rho_0^F) = 0$  is the so called Tait<sup>7</sup> equation (cf. Hayward [142]), given as

$$\mathbf{p}(\rho^F) = \frac{\rho_0^F c^2}{\gamma} \left[ \left( \frac{\rho^F}{\rho_0^F} \right)^\gamma - 1 \right]. \quad (4.42)$$

Herein  $c = \sqrt{K_0/\rho_0^F}$  is the speed of sound including the bulk modulus  $K_0$ . Moreover, the heat capacity ratio  $\gamma$  is given by  $\gamma = c_p/c_v \approx 7$  with the specific heat capacities at constant pressure and volume  $c_p$  and  $c_v$ , respectively. Note that  $\mathbf{p}$  is a function of the fluid density  $\rho^F$  and hence does not account for the incompressibility constraint.

In conclusion, the insertion of (4.41) into (4.39) and using the linearity of the divergence and the product rule, yields

$$\rho^F \ddot{\mathbf{x}}_F = \underbrace{\operatorname{div}(\mu^F \operatorname{grad} \dot{\mathbf{x}}_F + \mu^F \operatorname{grad}^T \dot{\mathbf{x}}_F)}_{\substack{\text{viscous interaction} \\ \text{forces } \mathbf{F}^V}} \underbrace{- \operatorname{grad} \mathbf{p}}_{\substack{\text{pressure interaction} \\ \text{forces } \mathbf{F}^P}} + \underbrace{\rho^F \mathbf{g}}_{\substack{\text{volumetric} \\ \text{forces } \mathbf{F}^G}}. \quad (4.43)$$

In terms of the SPH, (4.39) needs to be reformulated in a discrete manner. Therefore, the discrete form is obtained by a summation over a sub-domain of fluid particles  $\Omega_{\mathbf{x}}$  around the particle  $i$  via

$$m_i^F \ddot{\mathbf{x}}_{F,i} = \sum_{j:\mathbf{x}_j \in \Omega_{\mathbf{x}}}^{N_n(\mathbf{x})} \mathbf{F}_{ij}^V - \sum_{j:\mathbf{x}_j \in \Omega_{\mathbf{x}}}^{N_n(\mathbf{x})} \mathbf{F}_{ij}^p + \mathbf{F}_i^G. \quad (4.44)$$

Therein,  $m_i^F$  is the mass of a particle. Based on the antisymmetric pressure gradient (4.32)<sub>2</sub>, the inter-particle pressure force is derived as

$$\mathbf{F}_{ij}^p = \begin{cases} \left[ \frac{\mathbf{p}_i}{n_i^2} + \frac{\mathbf{p}_j}{n_j^2} \right] \frac{\partial W_{ij}}{\partial r_{ij}} \frac{\mathbf{x}_i - \mathbf{x}_j}{r_{ij}}, & \text{if } \mathbf{x}_j \in \Omega_F \vee \mathbf{x}_i \in \Omega_F, \\ \left[ \frac{\mathbf{p}_i}{n_i^2} + \frac{\mathbf{p}_j^*}{n_j^2} \right] \frac{\partial W_{ij}}{\partial r_{ij}} \frac{\mathbf{x}_i - \mathbf{x}_j}{r_{ij}}, & \text{if } \mathbf{x}_j \in \Omega_G \vee \mathbf{x}_i \in \Omega_F. \end{cases} \quad (4.45)$$

In (4.45), there is a distinction made between the fluid-fluid particle interaction and the fluid-ghost particle interaction to account for segmented compact support domains.

---

<sup>7</sup>Peter Guthrie Tait (1831–1901) was a Scottish mathematical physicist and early pioneer in thermodynamics. He is best known for the mathematical physics textbook *Treatise on Natural Philosophy*, which he co-wrote with Kelvin [WIKIPEDIA].

Finally, the viscous particle interactions are approximated via

$$\mathbf{F}_{ij}^V = \begin{cases} \left[ \frac{1}{n_i^2} + \frac{1}{n_j^2} \right] H(\mu_i, \mu_j) \frac{\dot{\mathbf{x}}_i - \dot{\mathbf{x}}_j}{r_{ij}} \frac{\partial W_{ij}}{\partial r_{ij}}, & \text{if } \mathbf{x}_j \in \Omega_F \forall \mathbf{x}_i \in \Omega_F, \\ \left[ \frac{1}{n_i^2} + \frac{1}{n_j^2} \right] H(\mu_i, \mu_j^*) \frac{\dot{\mathbf{x}}_i - \dot{\mathbf{x}}_j^*}{r_{ij}} \frac{\partial W_{ij}}{\partial r_{ij}}, & \text{if } \mathbf{x}_j \in \Omega_G^P \forall \mathbf{x}_i \in \Omega_F, \\ \left[ \frac{1}{n_i^2} + \frac{1}{n_j^2} \right] \mu_i \frac{\dot{\mathbf{x}}_i - \dot{\mathbf{x}}_j^*}{r_{ij}} \frac{\partial W_{ij}}{\partial r_{ij}}, & \text{if } \mathbf{x}_j \in \Omega_G^D \forall \mathbf{x}_i \in \Omega_F. \end{cases} \quad (4.46)$$

Therein, a so-called special harmonic mean  $H$  is included. More detailed informations and derivations concerning the relations introduced above can be found, e. g., in Sivanapillai [250], Brookshaw [47] or Hu & Adams [154].

**Linking between the scales:** The mathematical description of a biphasic system of a solid skeleton with a fluid phase within the interconnected pore space can be formulated on different mathematical scales. This needs to be considered in the interpretation of the specific results, since different physical processes can be predominant on different scales, cf. Class [64]. Furthermore, the mathematical formulations on different scales require different input variables.

The SPH formulations are derived for the microscale, also referred to as pore-scale, where all solid structures, grains and pores are fully resolved (with the required precision). The changes in fluid motion on the microscale are governed by a momentum-balance-based motion equation, cf. (4.44). The modelling approach of the TPM is of macroscopic nature, where individual pores and grains are not resolved but initially subjected via an averaging process, cf. Figure 4.10.

In this example, the porosity is equivalent to the volumetric proportion of fluid in the biphasic material. The two introduced modelling approaches require to specify the calculation of the porosity in different ways. In a continuum-mechanical sense, porosity is found as

$$n^F = \frac{V^F}{V} = \frac{V - V^S}{V} = 1 - \frac{V^S}{V} = 1 - n^S. \quad (4.47)$$

In terms of SPH simulations, the porosity is either computed after the segmentation by the ratio of fluid and total particles via

$$n^F = \frac{N_{\text{voxel}}^F}{N_{\text{voxel}}^{\text{total}}} = \frac{N_{\text{particles}}^F}{N_{\text{particles}}^{\text{total}}} \quad (4.48)$$

or analytically calculated in advance using the domain (box) dimensions and the particle radii for specific sphere packings. However, a fluid motion in an SPH simulation does not recognise porosity since the governing motion equation are formulated on the fluid domain of the resolved pore scale. Nevertheless, the porosity is an often required property to initially set up the binary material.

The estimation of the permeability is still a challenging task, from a theoretical as well as from an experimental perspective, cf. Valdes-Parada *et al.* [273]. In particular, permeability represents a measure for the hindering (or enabling) effect of the solid skeleton

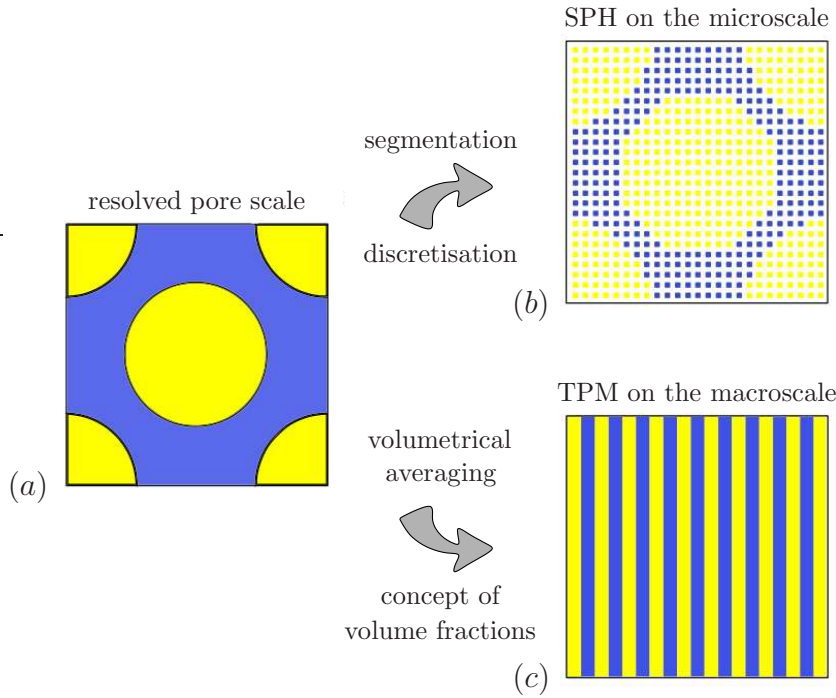


**Figure 4.10:** The regularly packed real pore-scale structure (a) of a biphasic material (yellow part  $\leftrightarrow$  solid and blue part  $\leftrightarrow$  fluid part), its splitting in SPH particles on the microscale (b) and its averaged representation for TPM simulations on the macroscale (c).

regarding a perfusion of a fluid. In accordance to Section 4.1.1, the well-known Kozeny-Carman relation (Carman [55], Xu & Yu [294]) can be used for validation purposes in terms of the considered particle-based approach, viz.:

$$K_{KC}^{SF} = \frac{D^2}{\alpha^{KC}} \frac{(n^F)^3}{(1 - n^F)^2}. \quad (4.49)$$

Therein,  $D$  is the sphere diameter and  $\alpha^{KC}$  is a material dependent factor, cf. Hwang [159]. However, the aim of this subsection is to numerically estimate the permeability by means of the introduced two-pronged approach based on SPH simulations. The procedure is described in the following paragraph.

**A simple example:** In order to show the linking between the scales, a simple approach of a binary aggregate is set up for the pore-scale SPH model and the macroscopic TPM model. The microscale simulations are investigated using HOOSPH, which is based on HOOMD [6], developed by Anderson *et al.* [7], Glaser *et al.* [124] and Nguyen *et al.* [217] for molecular dynamic purposes. The starting point for a SPH simulation is a variable amount of voxels, uniformly distributed in the 3-dim. simulation box. Typically, the simulation box contains a single REV and, therefore, the box dimensions are material specific. For the following computations, a cubic domain with an edge length  $l^{\text{edge}} = 1 \text{ mm}$  is used. Initially, the overall volume of  $V = (l^{\text{edge}})^3 = 1 \text{ mm}^3$  is divided into a chosen amount of voxels. In this regard, the ideal number of voxels results from an optimal balancing between accuracy and computational efficiency. The amount of voxels along one edge (or

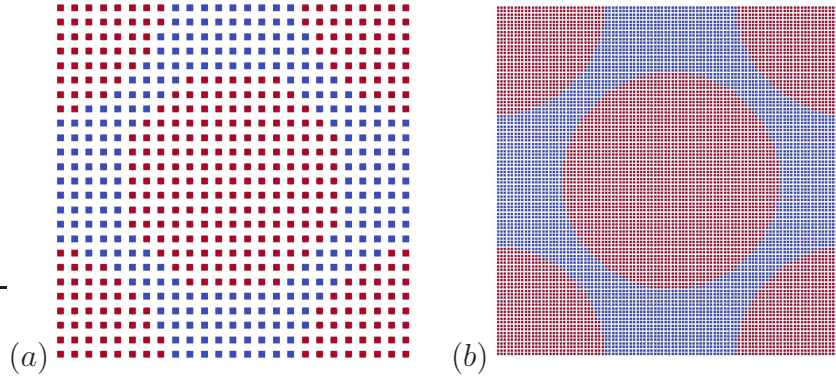


**Figure 4.11:** Slices of simulation domains for an FCC packed lattice for  $n_{NC}^F = 0.5$  with  $L = 25$  (a) and  $L = 100$  (b). Particle representing squares are independently sized due to optical reasons. Solid particles are coloured in red and fluid ones in blue.

spatial direction) is denoted as resolution  $L$ . In the center of each voxel, a particle is located, which is assigned with its specific information. In this simple example, regular and periodic sphere packings with equally sized spheres are considered. Three different packing types are used, which differ from each other by the spatial position of their grain centres. Depending on the packing type, the grain centres varies for simple cubic (SC), face-centred cubic (FCC) and body-centred cubic (BCC). For non-consolidated (NC) packings, the porosity  $n_{NC}^F$  can be computed via

$$n_{NC}^F = \begin{cases} 1 - \frac{\pi}{16} \left(\frac{D}{L}\right)^3 & \text{for SC,} \\ 1 - \frac{\pi}{4} \left(\frac{D}{L}\right)^3 & \text{for FCC and} \\ 1 - \frac{\pi}{8} \left(\frac{D}{L}\right)^3 & \text{for BCC.} \end{cases} \quad (4.50)$$

The changing factor in front of the parentheses depends on the total number of whole spheres within the unit cell. For a desired porosity, (4.50) can be used to compute  $D$  with given  $L$  and  $n^F$  via a root searching solver. An integer-valued type ID (solid  $ID^S = 1$  or fluid  $ID^F = 0$ ) is assigned to each voxel. Figure 4.11 shows a slice of a FCC packed lattice for  $n^F = 0.5$  with  $L = 25$  in (a) and  $L = 100$  in (b), respectively. These two resolutions have the overall amount of  $N_{\text{voxel}}^{(a)} = 15\,625$  or  $N_{\text{voxel}}^{(b)} = 1\,000\,000$ , which demonstrates the importance of a suited particle collocation for simulations. In this regard, the resolution in Figure 4.11 (a) is rather underestimated, since the spherical shape is not well represented. Moreover, the amount of particles in the pore channels must be high enough to be able to reproduce a parabolic velocity field. Therefore, ideal numbers are typically determined by preliminary investigation. All spheres are assumed to be rigid, cf. Hill *et al.* [148], and impermeable with no-slip and no-penetration boundary conditions on their surfaces. Since, the procedure aims to determine the permeability and to link two modelling approaches, parameters can be chosen for the fluid properties with no direct physical meaning. In fact, the fluid parameters are chosen in such a way

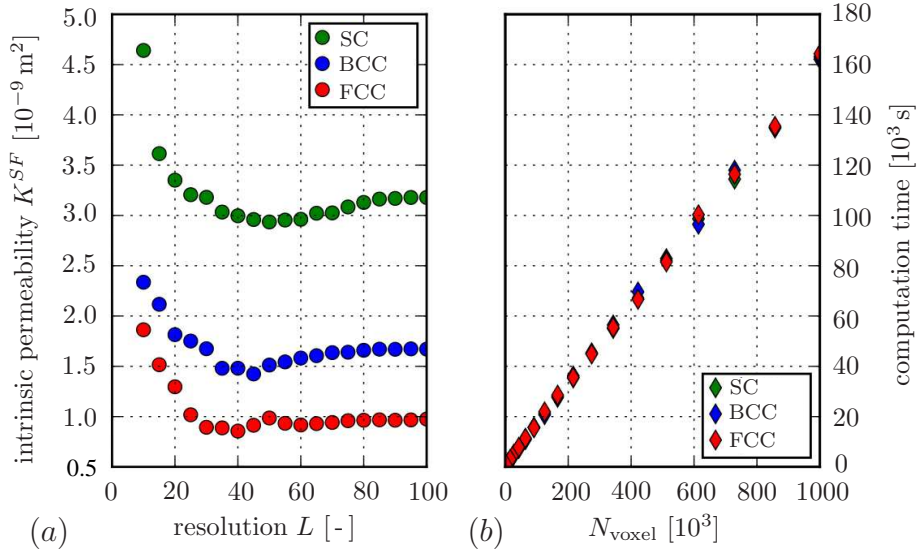


**Figure 4.12:** Dependency of the intrinsic permeability  $K^{SF}$  in (a) and computation time on the packing type as well as the particle resolution and absolute number in (b).

that a Darcy-flow regime with low Reynolds<sup>8</sup> (Re) numbers is obtained. In particular, a viscosity  $\mu^F = 1.0 \times 10^{-3} \text{ Pa s}$  and a density  $\rho^F = 1000 \text{ kg m}^{-3}$  are postulated. For initial conditions, all fluid particle velocities are set to  $\dot{\mathbf{x}}_F = \mathbf{0}$  and the body force  $\mathbf{b} = \rho^F \mathbf{g}$  is applied at the first time step. In this example, the gravitation is chosen to  $g = 0.1 \text{ m s}^{-2}$ . It is important to note that due to the periodicity of the outer boundaries no pressure gradient is present.

For a transfer toward the macroscopic Darcy permeability, it is necessary to ensure creeping flow in the domain since the second-order inertia terms of the momentum equation are neglected. At high Reynolds number flow, e.g.  $\text{Re} > 10$ , this assumption would certainly not be valid any more. Further restrictions in terms of the body force are given by the stability condition of the time-integration scheme. In HOOSPH an explicit time integration based on a predictor-corrector method is used. A time-step size

$$\Delta t \leq \frac{0.25 h^{CFL}}{c^{CFL}} \quad (4.51)$$

fulfils the criterion (Morris *et al.* [208], Sivanepillai [250]), based on the well-known Courant-Friedrichs-Lewy condition, cf. Courant *et al.* [66]. In (4.51),  $h^{CFL}$  is the characteristic length interval and  $c^{CFL}$  the characteristic velocity. Moreover, the Wendland C4 kernel and the Tait equation of state are used.

In order to bridge the scales, microscopic SPH simulations are chosen as the basis for a determination of macroscopic input parameters for the TPM-based simulations. Figure 4.12 shows initial simulation results used for validating the required minimum resolution. Moreover, it is necessary to assign at least 10 to 15 particles in the narrowest part of a pore channel to map a parabolic flow field, cf. Zhu *et al.* [300]. The simulations are performed for the previously described three different sphere packings with a fixed porosity

<sup>8</sup>The concept was introduced by George Stokes in 1851, but the Reynolds number was named by Arnold Sommerfeld in 1908 after Osborne Reynolds (1842–1912), who popularised its use in 1883 [WIKIPEDIA].

of  $n^F = 0.5$  and for resolutions of  $10 \leq L \leq 100$  with  $\Delta L = 5$ . In Figure 4.12 (a), the resolution-dependent intrinsic permeabilities are plotted. As a consequence, the minimum resolutions are set to  $L_{\min}^{FCC} = 85$ ,  $L_{\min}^{SC} = 100$  and  $L_{\min}^{BCC} = 70$ . Obviously, the specific microstructural aggregation of the individual packings causes different values for the intrinsic permeability  $K^{SF}$ . The highest value is obtained for the SC domain, indicating the most free (undisturbed) flow path through the centre of the domain. The arrangement of the spheres in the BCC and FCC domains causes more tortuous pathways and, therefore, a lower permeability. In Figure 4.12 (b), the computation time is plotted with respect to the absolute number of used particle, showing a linear behaviour.

In general, a number of simulation time steps is required to reach steady state. A meaningful breakup criterion is for example the mean fluid-particle velocity, the total kinetic energy or the intrinsic permeability. In the present case of a purely gravitation-driven process, it is sufficient to use the related directional velocity, cf. Figure 4.13. In Figure 4.13, the temporal evolution of possible breakup-inducing parameters are given, where the operator  $\text{AM}(\beta) = \bar{\beta}_{\text{arithm}}$  denotes the arithmetic mean of velocity. Furthermore, the ratio of the intrinsic and the Kozeny-Carman permeability are given, showing a constant value in dependence of the packing type. For BCC domains the Kozeny-Carman approach is revealed. For the other packing types, it is also possibility to adopt the material-dependent factor  $\alpha^{KC}$  included in (4.49).

The IBVP build in PANDAS is designed to be an equivalent to the previously performed SPH simulations. Therefore, input and output parameters from HOOSPH are used here to link both models. The simulation domain is again a cubic box with edge length  $l^{\text{edge}} = 1 \text{ mm}$  and volume  $V = 1 \text{ mm}^3$ . The body force used in the SPH simulations is

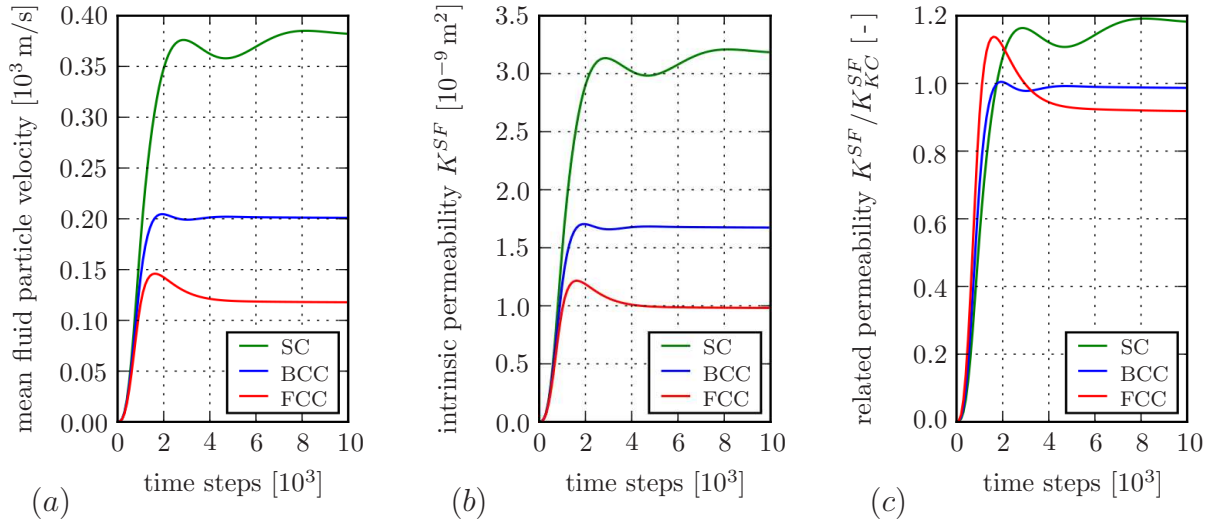


**Figure 4.13:** Time step dependent evolution of parameters; Mean fluid-particle velocity in vertical direction in (a) and intrinsic permeability  $K^{SF}$  in (b) which is in (c) related to the reference permeability given by the Kozeny-Carman approach to obtain a simulation breakup criterion for the simulation input parameters  $n^F = 0.5$  and  $L = 100$ .

compensated by a respective driving pressure difference via

$$\underbrace{\Delta p^{FR}}_{\text{PANDAS parameter}} = \underbrace{\rho^F \mathbf{g} \Delta h}_{\text{HOOSPH parameters}} = 10 \frac{\text{kg}}{\text{m}^3} \cdot 10 \frac{\text{m}}{\text{s}^2} \cdot 0.001 \text{ m} = 0.1 \text{ Pa}. \quad (4.52)$$

This pressure difference is used to prescribe the Dirichlet boundary conditions at the upper and lower boundary surface. In particular, a higher pressure is applied on the upper boundary and, thus, the resulting pressure gradient points downwards. Regarding the boundary conditions at the sides, the solid displacements are fixed and no flow conditions are given.

The governing balance relations in their weak forms are given by the volume balance of the fluid

$$\begin{aligned} \mathcal{G}_{p^F}(p^{FR}, \mathbf{u}_S, \delta p^{FR}) &= \int_{\Omega} \delta p^{FR} \operatorname{div}(\mathbf{u}_S)'_S \, dv + \int_{\Omega} \operatorname{grad} \delta p^{FR} \frac{K^{SF}}{\gamma^{FR}} \operatorname{grad} p^{FR} \, dv \\ &+ \int_{\partial\Omega_{\bar{v}^F}^N} \delta p^F \underbrace{(n^F \mathbf{w}_F \cdot \mathbf{n})}_{\bar{v}^F} \, da, \quad \forall \delta p^{FR} \in \mathcal{T}^{p^{FR}}, \end{aligned} \quad (4.53)$$

and the momentum balance of the overall aggregate

$$\begin{aligned} \mathcal{G}_{\mathbf{u}_S}(p^{FR}, \mathbf{u}_S, \delta \mathbf{u}_S) &= \int_{\Omega} \operatorname{grad} \delta \mathbf{u}_S \cdot (\mathbf{T}_E^S - p^{FR} \mathbf{I}) \, dv \\ &- \int_{\partial\Omega_{\bar{\mathbf{t}}}^N} \delta \mathbf{u}_S \underbrace{(\mathbf{T}_E^S - p^F \mathbf{I}) \mathbf{n}}_{\bar{\mathbf{t}}} \, da, \quad \forall \delta \mathbf{u}_S \in \mathcal{T}^{\mathbf{u}_S}, \end{aligned} \quad (4.54)$$

with the overall external stress vector  $\bar{\mathbf{t}}$  on the *Neumann* boundary and the volumetric efflux  $\bar{v}^F$  for the fluid phase. For a review on the numerical procedure compare Chapter 3.

In the following, the set up of two equivalent models is discussed, cf. Figure 4.14. For the microscopic model, the REV-size, the resolution  $L$ , the packing type BCC, the EOS, the material parameter  $\mu^{FR}$  and  $\rho^{FR}$ , the porosity  $n^F$  and the gravitation  $\mathbf{g}$  are chosen freely but in compliance with previously introduced restrictions. A high porosity  $n^F = 0.5$  is chosen to prevent the problem of too thin pore throats. Within the macroscopic model, the solid skeleton's material properties  $\mu^S$  and  $\lambda^S$  of the so-called Fontainebleau sandstone, cf., e. g., Sulem & Ouffroukh [257] are used to obtain a rigid skeleton under the applied moderate pressures. This guarantees negligible displacement of the skeleton in the TPM at low Re-number flow, which is convenient since the solid particles in the SPH simulations are assumed to be rigid. An SPH simulation results the mean fluid particle velocity and, as a result, the intrinsic permeability, respectively, viz.:

$$\operatorname{AM}((\dot{\mathbf{x}}_F)_{x,i}) = 3.341 \cdot 10^{-4} \frac{\text{m}}{\text{s}} \quad \text{and} \quad K^{SF} = 1.6707 \cdot 10^{-9} \text{ m}^2. \quad (4.55)$$

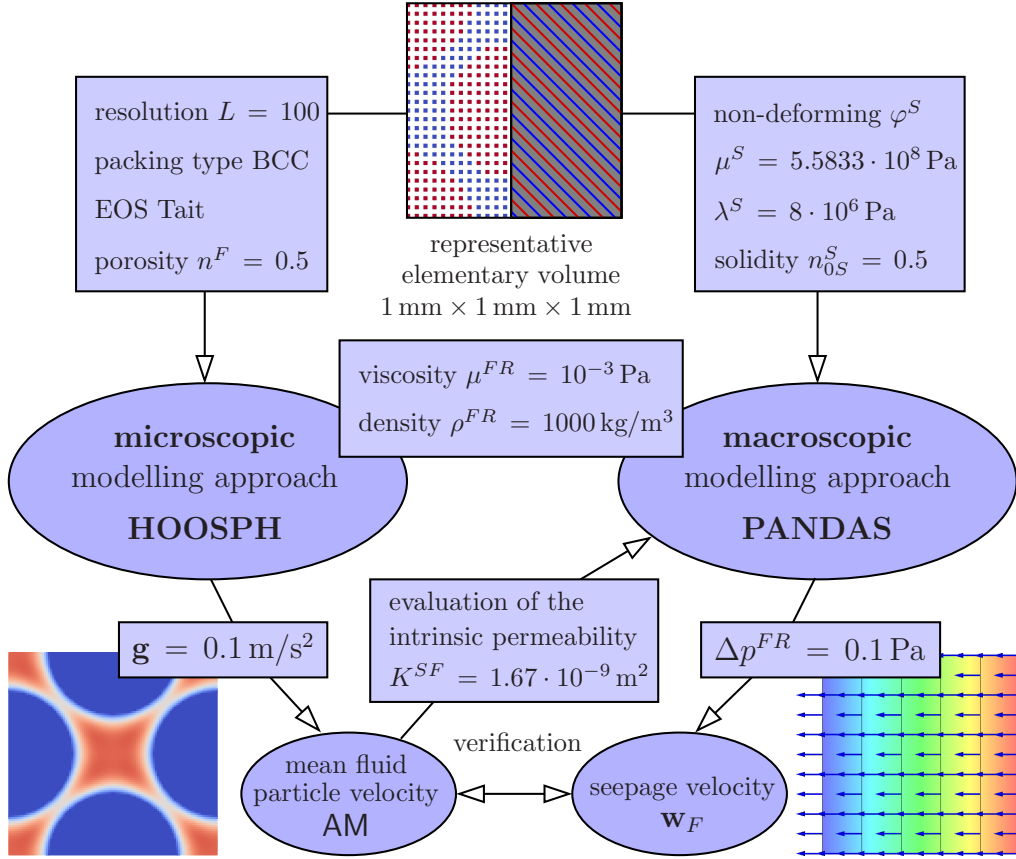


**Figure 4.14:** Basic input, output and comparable parameters to setup flow simulations on different scales using the software environments HOOSPH and PANDAS.

Obviously, the present conditions allow for a calculation of the seepage velocity by using the Darcy equation, yielding

$$n^F \|\mathbf{w}_F\| \approx 1.6707 \frac{\text{m}}{\text{s}} \quad \text{with} \quad \|\mathbf{w}_F\| \approx 3.341 \frac{\text{m}}{\text{s}}. \quad (4.56)$$

Therein, the magnitude  $\|\mathbf{w}_F\|$  corresponds to seepage velocity  $w_{F1}$  in the horizontal direction, while the perpendicular directions  $w_{F2}$  and  $w_{F3}$  are approximately zero. These results exactly meet the PANDAS simulations, compare the seepage velocity and the pore-pressure distribution in Figure 4.15. Note in passing that the assumption of a rigid solid skeleton for the SPH model is justified, since the resulting solid displacements of the TPM are in the range of  $\mathcal{O}(\mathbf{u}_S) = 10^{-18} - 10^{-31}$ .

**Discussion of model performances:** Basically, SPH methods require a time-consuming looping over all particles while the TPM based methods require the solution of a set of PDEs. This indicates that the SPH simulations are numerically more expensive for comparable simulation domains. Using computationally intensive SPH simulation methods, it is most important to exploit sophisticated algorithms and minimise processed data. The used software environment HOOSPH is written in Python (<http://www.python.org>), build on the C++ based HOOMD. It is furthermore possible to optimise its performance by compiling down the Python code using the Cython compiler (<http://cython.org>) which

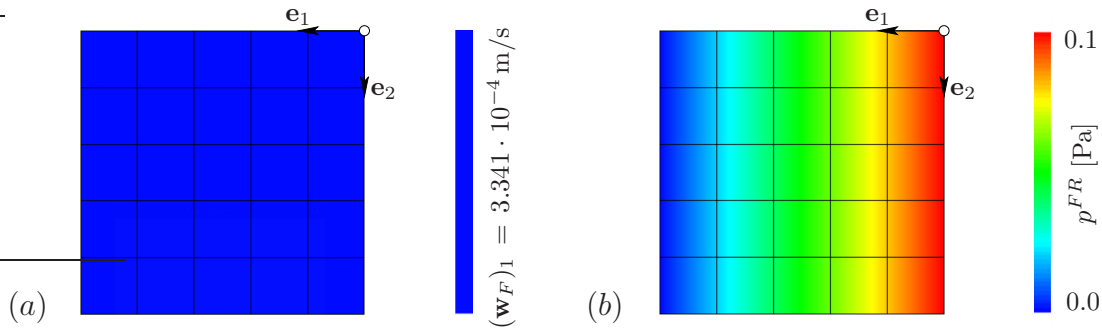


**Figure 4.15:** Seepage velocity in  $\mathbf{e}_1$  (horizontal)-direction in (a) and (b) pore-pressure distribution in the  $\mathbf{e}_1$ - $\mathbf{e}_2$ -plane.

is exploiting gcc (<http://gcc.gnu.org>). This procedure is particularly suitable since the SPH calculations involve a huge amount of loops, thus, allowing for an considerable time saving [126]. In contrast, PANDAS modules are scripted in C/C++.

To compare both simulations, and for the sake of replicability in general, it is necessary to perform simulations on the same computer architecture. Here, an Intel i5-4590 with 32 GB of memory running at clock speed of 3.30 GHz was used. Since PANDAS is designed for a single core, the HOOSPH simulations are computed on a single kernel too. For the previously discussed example, the TPM-based simulations are absurdly fast in comparison to the SPH-based simulations. In particular, for the cube with 8 finite elements the steady state is reached quickly and the simulation of 1 000 timesteps needs only 52 s in comparison to 16 465 s of the SPH simulation. Nevertheless, the code of HOOSPH is parallelised. In this regard, a comparison of the computation time depending on the used amount of kernels is given in Figure 4.16 (a). Each curve exhibits an almost linear behaviour and, obviously, the absolute simulation time decreases with an increasing number of used cores.

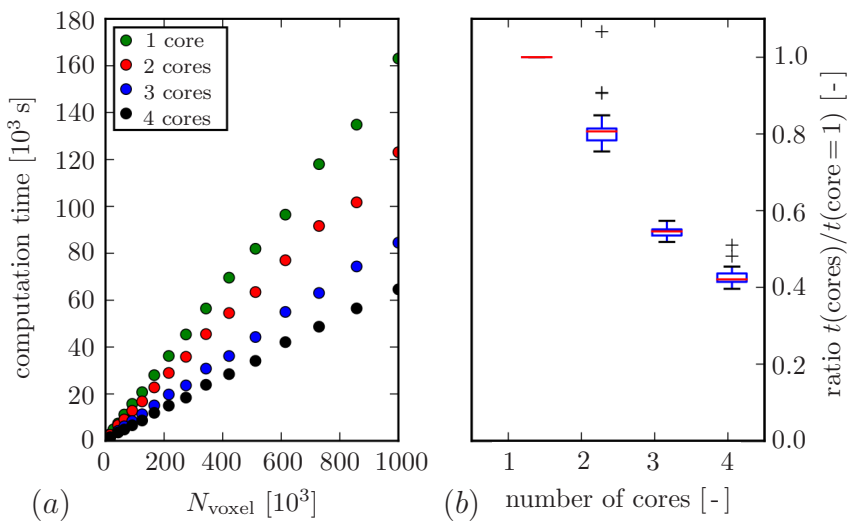


**Figure 4.16:** Computation time (a) of SPH simulations depending on amount of voxels and used cores as well as the ratio with respect to one kernel (b).

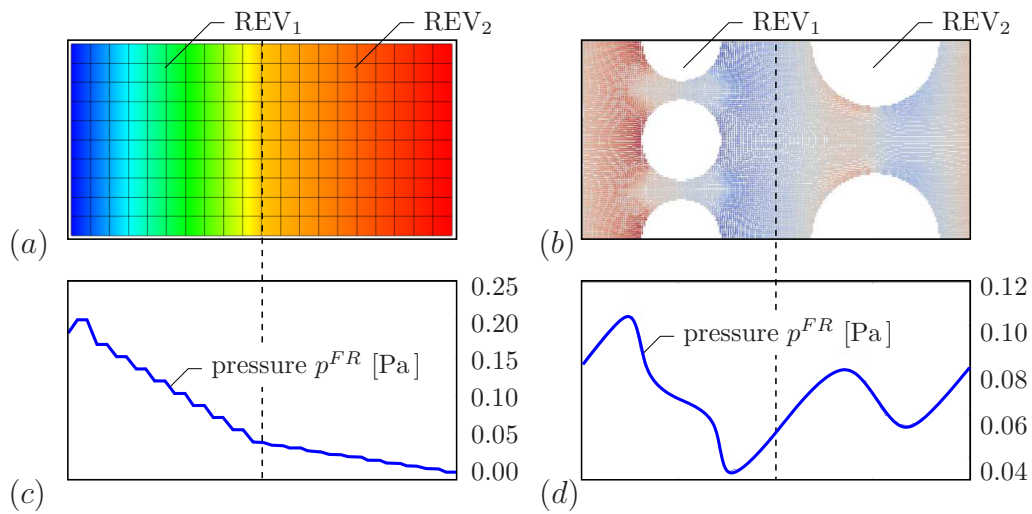


**Figure 4.17:** Simulation of heterogeneous porous domains with the TPM model (a) and the SPH model (b). Pore pressure distribution (in each case below) in a continuous form in (c) obtained from the TPM model and pore-scale resolved in (d) obtained from the SPH model.

Nevertheless, the application of four cores instead of a single one does not quarter the simulation time, cf. Figure 4.16 (b). Therein, the ratios are averaged (red lines) and the precision, or rather the deviation, is indicated by an error bar. The mathematical correlation of the mean values is not linear as a consequence of the exchange of messages between the involved cores.

**Scope of model applications:** Obviously, the SPH model can provide local information on the pore scale while the TPM model provides an averaged outcome on the REV scale. However, a heterogeneous model can be investigated using the TPM in terms of a domain decomposition, cf. Figure 4.17 (a). This poses the well-known question of suited REV sizes. As an example, a heterogeneous domain is constructed using two equally sized REVs ( $REV_1$  and  $REV_2$ ) with different sphere packings and grain diameters resulting a different porosity on the pore scale of the SPM model. In particular,  $REV_1$  has a permeability of 0.4 while the  $REV_2$  has a permeability of 0.6. Both REVs are investigated separately using the previously described approach to determine their intrinsic permeability. The  $REV_1$  has a lower permeability than  $REV_2$ . In Figure 4.17(c), the continuous (approximately bi-linear) spatial pressure distribution is obtained with a faster decrease in the first  $REV_1$  of the domain. In contrast, the (smoothed) pressure distribution of the SPH model in Figure 4.17(d) exhibits a wave-like behaviour with a strong dependency to the topology of the respective sphere packings. The periodic BCs lead to same pressure values on both sides of the domain.

## 4.2 Experimental-data-based approaches

Instead of using underlying pore-scale models, data can be used to estimate (macroscopic) REV quantities. Obviously, the permeability is strongly characterised by the underlying microscopical architecture. For porous material with a heterogeneous and anisotropic pore-structure aggregation, the usage of second-order permeability tensors is required. For the purpose of this section, the estimation of these permeabilities is exemplarily shown at the examples of x-ray microtomography ( $\mu$ CT or micro-CT) and diffusion-tensor imaging (DTI) data for hard porous materials and soft (water-saturated) porous materials, respectively. Obviously, a sufficient quality of underlying data is required for a meaningful evaluation of data-based quantities.

### 4.2.1 Inclusion of $\mu$ CT data

BIBLIOGRAPHIC NOTE: The content of this section is based on the following original article: Bleiler, C., Wagner, A., Stadelmann, V., Windolf, M., Köstler, H., Boger, A., Georghiev-Rüegg, B., Ehlers, W. & Röhrle, O.: Multiphasic modelling of bone-cement injection into vertebral cancellous bone. *International Journal for Numerical Methods in Biomedical Engineering* **31** (2015), 37–57 [27].

» A promising approach for a data-based permeability estimation is to directly proceed from x-ray microtomography ( $\mu$ CT or micro-CT) image data. X-ray microtomography uses x-rays to create non-destructive cross-sections (2-dim. slices) of a physical object. These images can then be used for several issues, such as the recreation of a (3-dim.) virtual model or, as discussed here, the computation of anisotropic permeability parameters of a porous structure. The prefix micro (or  $\mu$ ) indicates the pixel sizes (resolution) of the data. Therefore, in terms of a high-resolution x-ray tomography the pixel (or voxel) dimensions are in the range of micrometres. The first efforts to build a  $\mu$ CT system for the creation of  $\mu$ CT images of a small tropical snail (pixel size about 50 micrometers) go back to Elliott & Dover [100] in the early 1980s.

Today,  $\mu$ CT has a wide range of applications, for example in the fields of medical imaging or industrial uses. In general, two types of scanner set-ups can be distinguished. On the one hand, a stationary configuration where the x-ray source and the detector are fixed during the scan while the sample rotates. On the other hand, a set-up where the sample is fixed in space while the x-ray tube and the detector rotate around.

**Fundamentals of image processing:** In particular, diffusion-based image processing methods are adapted in order to estimate anisotropic permeability tensors of the porous structure from image data. In the field of image processing, diffusion-based methods are well-founded and got enhanced over the years, cf., e. g., Wang *et al.* [282], Wei [283], Weickert [284] and Yeo *et al.* [295]. However, the basis of diffusion-based image processing methods trace back to Ficks first law [108]

$$\mathbf{j} = -\mathbf{D} \text{grad } c. \quad (4.57)$$

Therein,  $\mathbf{j}$  is the flux vector that appears with changes of the concentration field. In this

particular case, the concentration corresponds to a scalar image intensity field  $c(\mathbf{x}, t)$  at a certain pixel or voxel with the corresponding location  $\mathbf{x}$  and time  $t$ , whereas  $\mathbf{D}$  is a positive definite diffusion tensor. An additional superscript to indicate the dependency of a quantity on a particular spatial location is omitted to improve readability.

The tensorial representation of  $\mathbf{D}$  enables anisotropic considerations. Extending Fick's first law (4.57) by a general continuity equation for concentration  $c$  yields the second law of Fick

$$\frac{\partial c}{\partial t} = \operatorname{div}(\mathbf{D} \operatorname{grad} c), \quad (4.58)$$

the so-called diffusion equation. The spatial gradient  $\operatorname{grad} c$  results a mass-conserving diffusive process on a spatial distribution of the scalar intensity value  $c$ . With the help of the image intensity gradient  $\operatorname{grad} c$ , which can be seen as an edge estimator, the orientation of changes in greyscale values for each pixel or voxel is captured with the symmetric, positive semi-definite structure tensor

$$\mathcal{J} = \operatorname{grad} c \otimes \operatorname{grad} c. \quad (4.59)$$

Note in passing that the previously introduced structural tensor  $\mathcal{M}^S$  is not identical to the structure tensor  $\mathcal{J}$ . A component-by-component averaging of the tensor  $\mathcal{J}$ , for example via Gaussian smoothing with standard deviation  $\sigma$  in order to improve robustness with respect to noise in the image data yields a modified structure tensor

$$\mathcal{J}_\sigma = \begin{bmatrix} J_{11} & J_{12} & J_{13} \\ J_{21} & J_{22} & J_{23} \\ J_{31} & J_{32} & J_{33} \end{bmatrix} \mathbf{e}_i \otimes \mathbf{e}_j = \begin{bmatrix} \xi_1 & 0 & 0 \\ 0 & \xi_2 & 0 \\ 0 & 0 & \xi_3 \end{bmatrix} \mathbf{v}_i \otimes \mathbf{v}_i \quad (4.60)$$

with the corresponding eigenvalues  $\xi_1, \xi_2, \xi_3$  and eigenvectors  $\mathbf{v}_1, \mathbf{v}_2$ , and  $\mathbf{v}_3$ . The eigenvector associated with the largest eigenvalue of  $\mathcal{J}_\sigma$  indicates the greatest structural change, i. e., denotes the direction perpendicular to edges (in 2-dim. data) or surfaces (in 3-dim. data). The diffusion tensor  $\mathbf{D}$  can be obtained through anisotropic diffusion approaches, e. g. coherence-enhancing-diffusion or edge-enhancing-diffusion (cf. Weickert [284]) influencing the homogenisation process. Both methods transform the eigenvalues  $\xi_i$  of  $\mathcal{J}_\sigma$  to the eigenvalues  $\omega_i$  of  $\mathbf{D}$  without effecting the orthonormal basis of the eigenvectors  $\mathbf{v}_i$ .

**Bridge to permeability tensors:** Comparing Fick's first law (4.57) and Darcy's law for the perfusion of a porous media, an analogy between the diffusion tensor  $\mathbf{D}$  and the permeability tensor  $\mathbf{K}^{SF}$  can be observed. Both of them describe a flow (on the left-hand side of the respective equation) which is caused by a gradient (on the right-hand side). This similarity provides the basis for transferring methods from image processing to derive the anisotropic permeability tensors describing the occurring flow within an imaged porous structure. This is assured by the fact that the diffusion tensor  $\mathbf{D}$  depends within nonlinear and anisotropic image processing methods entirely on the underlying structure of the image just like the intrinsic permeability tensor  $\mathbf{K}^{SF}$  depends on the intrinsic porous structure. However, obtaining the permeability tensors from image data requires a few substantial modifications of standard image processing algorithms.

The fundamental step in the analysis of the structural data of an image is the gradient-based computation of the structure tensor  $\mathcal{J}_\sigma$  using the relation (4.59). As was mentioned

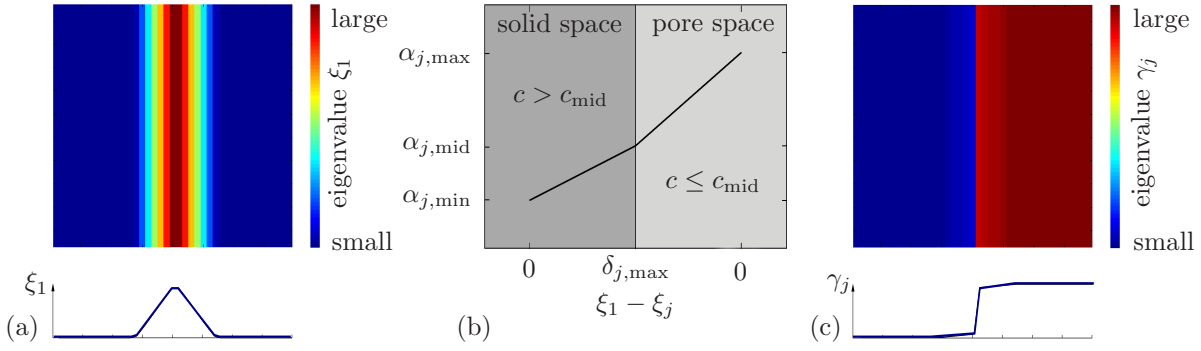


**Figure 4.18:** Profile of the largest eigenvalue  $\xi_1$  of the structure tensor  $\mathcal{J}_\sigma$  across an image edge (a). Profile of the intermediate quantities  $\alpha_j$  for  $j = \{2, 3\}$  for image intensities larger than  $c_{mid}$  (left) and smaller or equal to  $c_{mid}$  (right) in (b) and (c) profile of the largest eigenvalue  $\gamma_j$  of the permeability tensor  $\mathbf{K}^{SF}$  across an image edge. The corresponding eigenvector is oriented perpendicular to the edge.

before, the largest eigenvalue  $\xi_1$  of  $\mathcal{J}_\sigma$  is oriented along the dominant change in image intensity, i. e., perpendicular to isolines (2-dim.) and isosurfaces (3-dim.) of equal image intensities  $c$ . Since the diffusive process on the image within coherence-enhancing-diffusion or edge-enhancing-diffusion should preferentially act along the local structure, the eigenvalues  $\xi_i$  get modified towards the eigenvalues  $\omega_i$  of the diffusion tensor  $\mathbf{D}$ . Analogically, this proceeding is also required for the computation of permeability tensors  $\mathbf{K}^{SF}$ , because the fluid flow across the local structure should be diminished in a similar manner.

However, the eigenvalue modifications of anisotropic diffusion can not be used for this task directly due to the fact that image processing aims to affect only image areas with significant changes in the image intensity  $c$ . This deficiency is illustrated in the following example. Assume a rectangular area with one vertical edge between two identical areas that represent on the left the solid skeleton ( $c = 1$ ) and on the right the pore space ( $c = 0$ ). Figure 4.18 (a) displays the corresponding profile of the largest eigenvalue  $\xi_1$  of the structure tensor  $\mathcal{J}_\sigma$ , whose affiliated eigenvector  $\mathbf{v}_1$  is perpendicular to the edge resulting in a maximum value of  $\xi_1$ , which is located at the edge. Obviously, regions for the pore space and the solid possess the same eigenvalues despite the different image concentration values  $c$ . The same applies to the diffusion tensor  $\mathbf{D}$  if coherence-enhancing-diffusion or edge-enhancing-diffusion are used. While this feature is appropriate for image processing and smoothing purposes, it is not sufficient for computing the permeabilities describing the fluid flow arising inside the imaged porous structure. For the permeabilities, a profile is needed that increases from the solid to the pore space. Hence, the eigenvalues of  $\mathbf{K}^{SF}$ , which are denoted by  $\gamma_i$ , do not only depend on the eigenvalues  $\xi_i$  of the structure tensor  $\mathcal{J}_\sigma$ , and therefore implicitly on the image intensity  $c$ , but also explicitly on the values of  $c$ . For the general case of non-binary image data, the distinction between the two cases is done by comparing specific pixel/voxel image concentration values  $c$  with  $c_{mid} = (c_{max} + c_{min})/2$ , where  $c_{max}$  and  $c_{min}$  denote the maximal and minimal overall image concentration, respectively. Based on the previous findings, an approach of computing the eigenvalues  $\gamma_i$  is introduced to determine the permeability tensors  $\mathbf{K}^{SF}$ . The approach applied herein is roughly oriented on the above mentioned methods of coherence-enhancing-diffusion

and edge-enhancing-diffusion but considers the explicit dependence on  $c$  by computing intermediate quantities  $\alpha_i$ , which are defined by

$$\begin{aligned}\alpha_1 &= \bar{\alpha}_1, \\ \alpha_2 &= \begin{cases} \frac{\bar{\alpha}_{2,\text{mid}} - \bar{\alpha}_{2,\text{min}}}{\delta_{2,\text{max}}} (\xi_1 - \xi_2) + \bar{\alpha}_{2,\text{min}} & \text{if } c > c_{\text{mid}}, \\ \frac{\bar{\alpha}_{2,\text{mid}} - \bar{\alpha}_{2,\text{max}}}{\delta_{2,\text{max}}} (\xi_1 - \xi_2) + \bar{\alpha}_{2,\text{max}} & \text{else,} \end{cases} \\ \alpha_3 &= \begin{cases} \frac{\bar{\alpha}_{3,\text{mid}} - \bar{\alpha}_{3,\text{min}}}{\delta_{3,\text{max}}} (\xi_1 - \xi_3) + \bar{\alpha}_{3,\text{min}} & \text{if } c > c_{\text{mid}}, \\ \frac{\bar{\alpha}_{3,\text{mid}} - \bar{\alpha}_{3,\text{max}}}{\delta_{3,\text{max}}} (\xi_1 - \xi_3) + \bar{\alpha}_{3,\text{max}} & \text{else,} \end{cases}\end{aligned}\quad (4.61)$$

where  $\bar{\alpha}_1$ ,  $\bar{\alpha}_{2,\text{min}}$ ,  $\bar{\alpha}_{3,\text{min}}$ ,  $\bar{\alpha}_{2,\text{mid}}$ ,  $\bar{\alpha}_{3,\text{mid}}$ ,  $\bar{\alpha}_{2,\text{max}}$ , and  $\bar{\alpha}_{3,\text{max}}$  are constant parameters, while  $\delta_{2,\text{max}}$  and  $\delta_{3,\text{max}}$  denote the maximum values of the differences  $(\xi_1 - \xi_2)$  and  $(\xi_1 - \xi_3)$  of the entire considered image data, respectively. These relations are illustrated in Figure 4.18 (b) and clearly demonstrate the difference to the profile in Figure 4.18 (a) which is not increasing from the middle to the right hand side but tends to zero in homogeneous areas.

In a second step, the intermediate quantities  $\alpha_i$  are transformed to the eigenvalues  $\gamma_i$  using a linear map to cover a realistic range of permeabilities. In particular, the linear map is given by

$$\gamma_i = \frac{\gamma_{\text{max}} - \gamma_{\text{min}}}{\alpha_{\text{max}} - \alpha_{\text{min}}} (\alpha_i - \alpha_{\text{min}}) + \gamma_{\text{min}}, \quad (4.62)$$

where  $\gamma_{\text{max}}$  and  $\gamma_{\text{min}}$  define the range of the final eigenvalues  $\gamma_i$ . The choice of these constants can be established via realistic values extracted from the literature for the considered porous material. Furthermore,  $\alpha_{\text{max}}$  and  $\alpha_{\text{min}}$  indicate the extreme values of the already introduced constants  $\bar{\alpha}_1$ ,  $\bar{\alpha}_{2,\text{min}}$ ,  $\bar{\alpha}_{3,\text{min}}$ ,  $\bar{\alpha}_{2,\text{mid}}$ ,  $\bar{\alpha}_{3,\text{mid}}$ ,  $\bar{\alpha}_{2,\text{max}}$ , and  $\bar{\alpha}_{3,\text{max}}$ . Meaningful results for  $\gamma_i$  can be obtained using the following conditions:

$$\begin{aligned}\bar{\alpha}_1 &\leq \bar{\alpha}_{2,\text{min}} & \text{and} \\ \bar{\alpha}_{2,k} &\leq \bar{\alpha}_{3,k} & \text{for } k = \{\text{min, mid, max}\}.\end{aligned}\quad (4.63)$$

Especially the requirement of a small value for  $\bar{\alpha}_1$ , and consequently for  $\gamma_1$ , is logical since the flow along the direction of the first eigenvalue of  $\mathcal{J}_\sigma$  should be inhibited. This procedure is similar to the approach of coherence-enhancing-diffusion, where  $\omega_1$  takes a small constant value, too. To set an example, the constant parameters are set to

$$\begin{aligned}\bar{\alpha}_1 &= \bar{\alpha}_{2,\text{min}} = \bar{\alpha}_{3,\text{min}} = 0, \\ \bar{\alpha}_{2,\text{mid}} &= \bar{\alpha}_{3,\text{mid}} = 0.5, \\ \bar{\alpha}_{2,\text{max}} &= \bar{\alpha}_{3,\text{max}} = 1.0.\end{aligned}\quad (4.64)$$

Choosing this algorithm, one obtains for the test example in Figure 4.18 (b) with an image intensity jump from 1 to 0 at the vertical mid-line the desired eigenvalue profile, which is depicted in Figure 4.18 (c). Obviously, the profile increases from the left hand side to the right hand side, hence, it delivers small values of  $\gamma_3$  within homogeneous image regions

of high intensity values of  $c$  and large values within homogeneous image regions of low intensity values.

The eigenvalues  $\gamma_i$  within each voxel specify the permeability tensors  $\mathbf{K}^{SF}$  by

$$\mathbf{K}^{SF} = \begin{bmatrix} \gamma_1 & 0 & 0 \\ 0 & \gamma_2 & 0 \\ 0 & 0 & \gamma_3 \end{bmatrix} \mathbf{v}_i \otimes \mathbf{v}_i = \begin{bmatrix} K_{11}^{SF} & K_{12}^{SF} & K_{13}^{SF} \\ K_{21}^{SF} & K_{22}^{SF} & K_{23}^{SF} \\ K_{31}^{SF} & K_{32}^{SF} & K_{33}^{SF} \end{bmatrix} \mathbf{e}_i \otimes \mathbf{e}_j. \quad (4.65)$$

Note that the intrinsic permeability tensors are required to be positive definite in order to fulfil thermodynamical consistency. The positiveness of the eigenvalues  $\gamma_i$  is ensured by the choice of positive values for the constant parameters  $\gamma_{\min}$  and  $\gamma_{\max}$ . Furthermore, the connection between the direction of the highest permeability and the preferred direction of the solid skeletons underlying structure is obvious. Hence, a normalisation of the eigenvector  $\mathbf{v}_3$ , belonging to the largest eigenvalue  $\gamma_3$ , yields the unit vector  $\mathbf{a}_0^S = \mathbf{v}_3 / \|\mathbf{v}_3\|$ , which can be used for several constitutive purposes, such as, for example, an anisotropic stress formulation.

**Homogenisation of the image data:** The macroscopical treatment within the proposed continuum-mechanical modelling framework does not require the knowledge and storage of permeability tensors at each voxel of the micro-structural image data. Hence, homogenisation and upscaling methods, as for example introduced by Durfolsky [74], Dykaar & Kitanidis [76] or Renard & De Marsily [226] can be applied on the obtained permeability data. Alternatively, homogenisation can also be applied in a preceding step directly to the underlying (raw) image data. For this purpose, the three-dimensional image volume can be smoothed, e. g., with an algorithm presented by Kluge [167]. «(p.74)

## 4.2.2 Inclusion of DTI data

In 1994, Basser *et al.* [19] proposed an approach to estimate the restricted perfusion of liquids within a porous structure based on nuclear-magnetic resonance (NMR) spin-echo experiments, commonly known as DTI. In this procedure, specific magnetic-resonance imaging (MRI) sequences of diffusing water molecules are processed to obtain the so-called apparent water-diffusion tensor

$$\mathbf{D}_{\text{awd}}^n = D_{ik}^n \text{awd} (\mathbf{e}_i \otimes \mathbf{e}_k) = \begin{bmatrix} D_{11}^n \text{awd} & D_{12}^n \text{awd} & D_{13}^n \text{awd} \\ D_{21}^n \text{awd} & D_{22}^n \text{awd} & D_{23}^n \text{awd} \\ D_{31}^n \text{awd} & D_{32}^n \text{awd} & D_{33}^n \text{awd} \end{bmatrix} (\mathbf{e}_i \otimes \mathbf{e}_k) \quad (4.66)$$

as a symmetric and positive-definite quantity at each evaluated voxel  $n$ . This method is preferably used for soft biological tissues and can be applied non-invasively in vivo. For more details concerning the foundations, the interested reader is referred to, e. g., Le Bihan *et al.* [180] or Hlawatsch *et al.* [149].

For the local permeability estimation, an eigenvalue decomposition of (4.66) yields

$$\mathbf{D}_{\text{awd}}^n = \begin{bmatrix} \gamma_{1\text{awd}}^n & 0 & 0 \\ 0 & \gamma_{2\text{awd}}^n & 0 \\ 0 & 0 & \gamma_{3\text{awd}}^n \end{bmatrix} (\mathbf{v}_i^n \otimes \mathbf{v}_i^n). \quad (4.67)$$

Therein,  $\gamma_{i\text{awd}}^n$  are the positive eigenvalues and  $\mathbf{v}_i^n$  the corresponding eigenvectors of  $\mathbf{D}_{\text{awd}}$ . The permeability is then derived based on the assumption of Tuch *et al.* [271], stating that the recorded diffusion of deflected water molecules already reflects the geometrical architecture of the porous material and, thus, the permeability. Finally, a calibration is required such that the eigenvalues obtain the requested order of magnitude, viz.:

$$\gamma_{i\mathbf{K}^{SF,n}}^n = \bar{K}^{SF} \frac{\gamma_{i\text{awd}}^n}{\bar{\gamma}_{\text{awd}}^n} \quad \longrightarrow \quad \mathbf{K}_{\text{diag.}}^{SF,n} = \sum_{i=1}^3 \gamma_{i\mathbf{K}^{SF,n}}^n (\mathbf{v}_i^n \otimes \mathbf{v}_i^n). \quad (4.68)$$

Therein, the calibration is implemented with respect to the eigenvalues' mean  $\bar{\gamma}_{\text{awd}}^n = \frac{1}{3}(\gamma_{1\text{awd}}^n + \gamma_{2\text{awd}}^n + \gamma_{3\text{awd}}^n)$ , averaging the calibration for the anisotropic permeabilities. At that point, however, it has to be mentioned that a large uncertainty arises in this calibration procedure due to the somehow arbitrary choice of  $\bar{K}^{SF}$  making a reliable quantitative statement nearly impossible.

According to Wagner [277], the spectral representations given in (4.68)<sub>2</sub> can be transferred back to the Cartesian coordinate system  $\mathbf{e}_i$  via the transformation rules

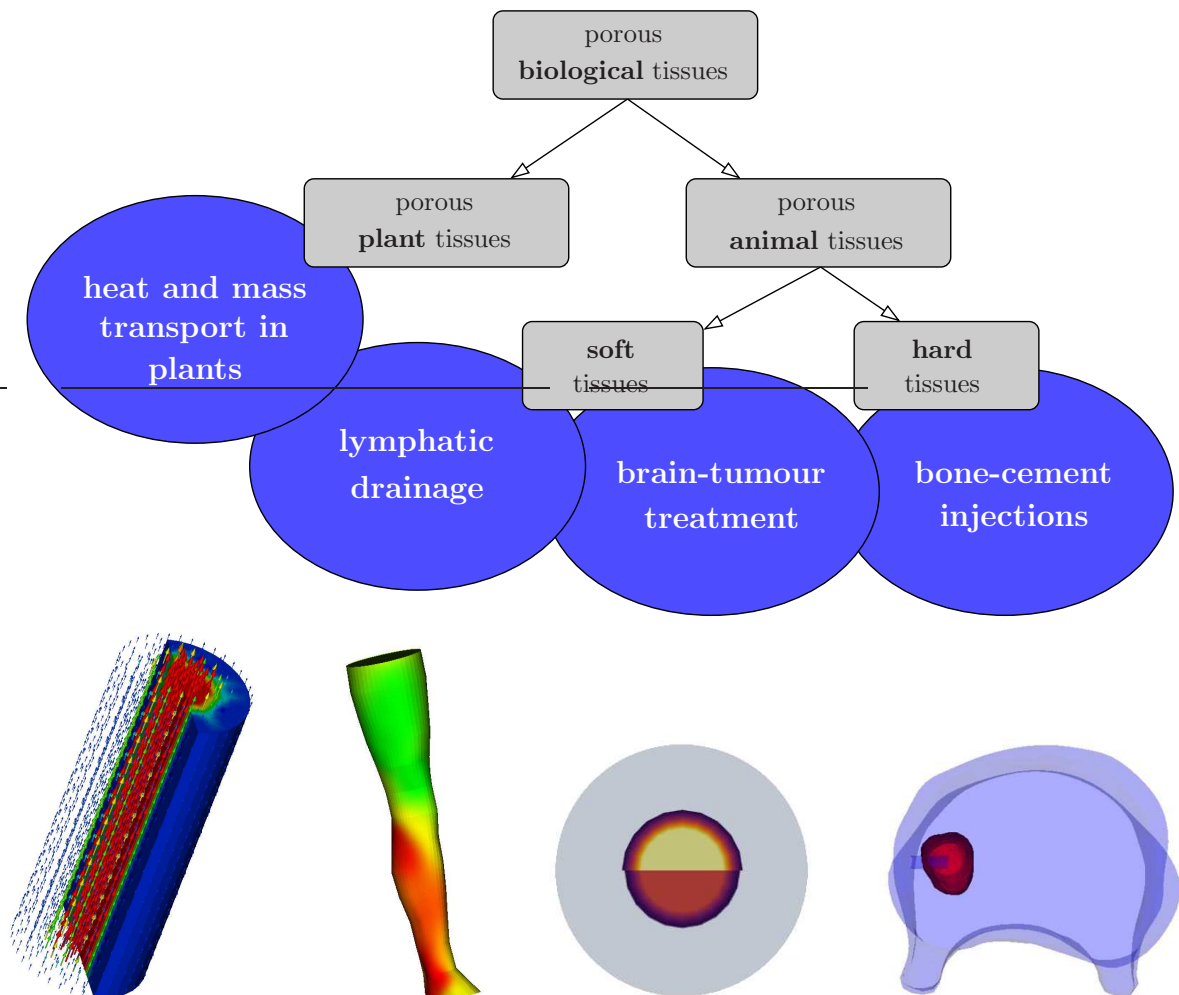
$$\mathbf{K}^{SF,n} = \mathbf{Q}^n \mathbf{K}_{\text{diag.}}^{SF,n} (\mathbf{Q}^n)^{-1}. \quad (4.69)$$

Therein, the rotation tensor  $\mathbf{Q}^n = Q_{ji}^n (\mathbf{e}_j \otimes \mathbf{e}_i)$  contains the coefficients  $v_{ij}^n$  of the three eigenvectors  $\mathbf{v}_i^n = v_{ij}^n \mathbf{e}_j$  as column vectors within the coefficient matrix  $Q_{ji}^n = v_{ij}^n = [v_{1j}^n, v_{2j}^n, v_{3j}^n]$ , cf. Ehlers [79].



## Part II

# Selected Applications for Biological Materials





# Chapter 5:

## Introductory notes to Part II

### 5.1 A brief introduction to continuum biomechanics

BIBLIOGRAPHIC NOTE: The content of this section is based on the following original article: Ehlers, W. & Wagner, A.: Coupled problems in biological systems. In H. Altenbach and A. Öchsner (eds.) *Encyclopedia of Continuum Mechanics*. Springer, Berlin, Heidelberg 2020, pp. 453–465 [97].

» The classical notion *biomechanics* is traditionally linked to (sports and movement) science, where kinematics and kinetics of rigid (multi-body) systems are studied. The discipline *continuum biomechanics* emerged from the classical field of continuum mechanics and is widely used to describe coupled problems in humans, particularly on the organ and/or the tissue scale, although lower and higher scales can be included.

Highly recognised basic work for continuum biomechanics is introduced by Fung [113, 114]. Since then, fundamental contributions are made by, e. g., Humphrey [157, 158], Holzapfel & Ogden [152, 153], Holzapfel & Kuhl [150], Ricken & Bluhm [227] or Ehlers *et al.* [91], to name just a few well-known researchers in this field. Humphrey pointed out in [153] that there is the need to account for different constituents as a collective for the whole. This is a basic requisite for the applications discussed in this part of the monograph. As it is introduced in Ehlers & Wagner [97], a coupled problem is given if more than one component is involved in a biomechanical system and the components are linked to each other, such that they dynamically interact among themselves. Biological systems are composed of biologically relevant components and can span over spatial and temporal scales of more than ten orders of magnitude. As biological materials are always porous materials, they are typically composed of multiple (interacting or interdependent) components (in the sense of matter or substance) that constitute the integrated whole (overall) aggregate. For the continuum-mechanical and numerical treatment of coupled problems in biological materials, the Theory of Porous Media, as a methodology to describe volumetrically coupled and interacting constituents in a macroscopic continuum-mechanical framework, cf. Chapter 2, has proven as a very convenient and powerful tool. In this regard, examples are, e. g., the description of human liver (Ricken *et al.* [229]) or the intervertebral disc (Ehlers *et al.* [88], Karajan [164]) just to name a few.

Coupled problems occur in nearly all biological systems, such that it is necessary to restrict this part to a closer realm. In the framework of continuum biomechanics, biological tissue can be subdivided into plant and animal tissue, where the following mainly addresses human tissue, although the basic equations can also be used for any other kind of biological tissue. In biology, the study of tissue is commonly known as histology. In animal tissues, four basic tissue types can be distinguished, i. e. connective, epithelial, muscle and nervous tissue, cf. Figure 5.1 for a qualitative sketch and, e. g., Junqueira

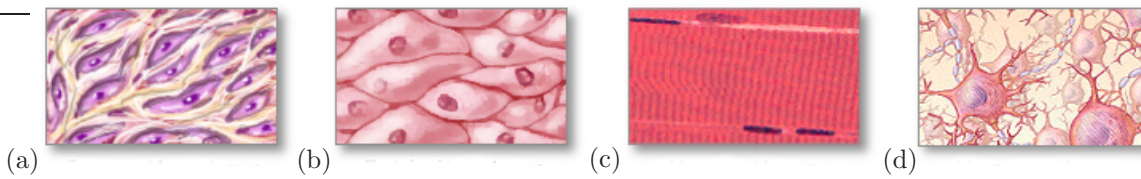


**Figure 5.1:** Exemplary sketch of different animal-tissue types. In particular, (a) shows connective, (b) shows epithelial, (c) shows muscle and (d) shows nervous tissue, according to [[https://commons.wikimedia.org/wiki/File:Four\\_types\\_of\\_tissue.jpg](https://commons.wikimedia.org/wiki/File:Four_types_of_tissue.jpg)].

*et al.* [162] for a comprehensive overview. Connective tissues exhibit a fibrous nature. Examples for connective tissues are, e. g., bone, tendon or ligament. Epithelial tissues are formed by cells covering the organ surfaces such as the surface of the skin. Muscle cells form the active contractile tissue of the body known as muscle tissue or muscular tissue. Cells comprising the central nervous system (CNS) are denoted as nervous (or neural) tissue. In the CNS, the brain and the spinal cord consist of neural tissue. Plant tissues are categorised mainly into three tissue systems, i. e. the epidermis, the ground tissue and the vascular tissue.

For any model including multiple constituents, it is furthermore crucial to consider relevant coupling mechanisms governing the integral behaviour of the system. Coping with spatial scales, a typical classification of human biomechanical systems into categories is given by the definition of body, organ, tissue, cell and molecular scales. In this regard, sports and movement science traditionally use discrete biomechanics to cover biomechanical issues kinematically in terms of multibody systems and/or robotics on the body scales, cf., e. g., Schmitt *et al.* [237]. However, the desire to predict the interaction of an individual human body with its environment in a very detailed and sophisticated way leads to recent efforts in the development of an overall human model. One spatial level below, continuum biomechanics considers the description of biomaterials mainly on the tissue scale, taking effects of the cell and organ scales into account. On the tissue level, several mutually coupled components can be identified, such as solid structures, blood, interstitial fluid, and attached or dissolved components. In terms of a model, this requires the consideration of the classical fields of solid and fluid mechanics as well as combined approaches. This allows to develop models describing parts (organs) of humans including the individual properties of the respective biological tissue. If effects stemming from the cellular or the molecular scale influence the tissue behaviour, approaches from systems biology or molecular biology need to be included, such as chemical reaction kinetics, signal transduction pathways, or molecular dynamics. «(p. 83)

## 5.2 Classification of the selected continuum-biomechanical applications

In this second part, four examples of continuum-biomechanical problems with multiple interacting components are considered, cf. Figure 5.2. The first example in Chapter 6 describes a binary tissue aggregate including mass-exchange processes between a solid

skeleton (tissue cells) and a pore fluid (interstitial fluid) and is exemplarily related to coupled processes in the human leg applied to lymphatic drainage. The second example in Chapter 7 concerns heat and mass transport in plant tissues with regard to ice-formation processes in frost-resistant plants. The third example in Chapter 8 is related to hard animal tissues (vertebral bodies) subjected to injection processes to increase the strength of the porous solid skeleton (affected by osteoporosis) and the fourth and final example in Chapter 9 concerns soft animal tissues and includes blood as an additional pore fluid and furthermore considers dissolved miscible components, such as drugs. This model can be used, for example, in the field of tumour treatment in (nervous) brain tissue. For all intents and purposes, the coupled FE solver PANDAS builds the basis for the investigated numerical simulations.

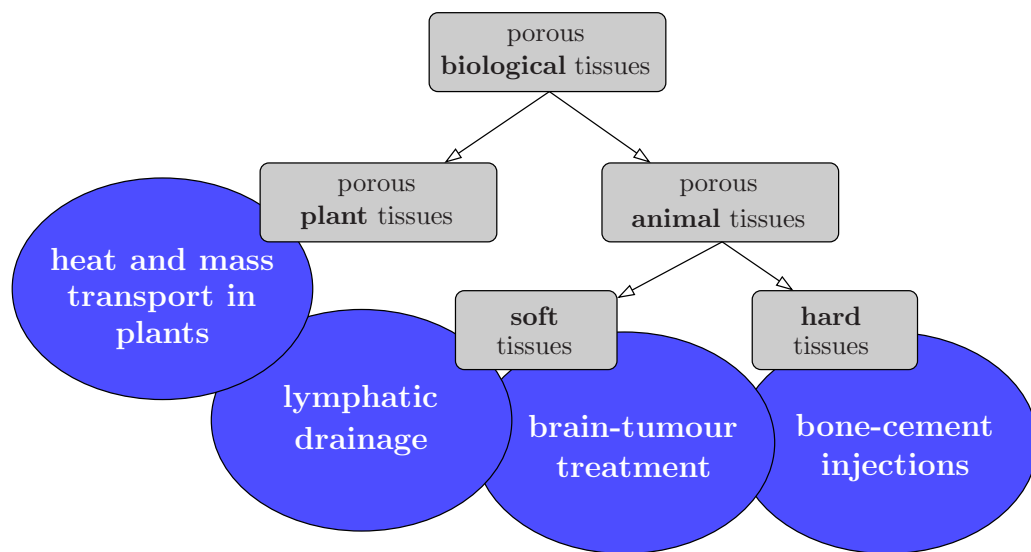


**Figure 5.2:** Classification of porous biological tissues and choice of selected applications.



# Chapter 6:

## Lymphatic drainage

### 6.1 Motivation and introduction

The lymphatic system is a network of vessels and organs designed to help the body to get rid of unwanted substances. Therefore, the major role of the lymphatic system is the drainage of accumulated interstitial fluid in human tissues and to return it into the blood system. If such a drainage fails, interstitial fluid builds up and is trapped in the interstitial space. The resulting accumulation of interstitial fluid is commonly known as lymph oedema and may result in swelling processes accompanied by pain as well as an increased risk of infection.

The discovery of the lymphatic system was comparatively late in the history of medicine, probably due to the transparency of lymph. In a histological examination, it is hard to differentiate lymphatic vessels from small blood capillaries. In 1622, Aselli<sup>1</sup> detected lymphatic vessels and differentiated between lymphatics and veins. He described them as “lacteae venae” or milky veins, cf. Aselli [10]. The first one who recognised the lymphatic network as a system of closed vessels similar to the arteries and veins was Rudbeck<sup>2</sup>. He clarified the existence of lymphatics throughout the body, cf. Chikly [63].

Despite the importance of the lymphatic system in health and disease, it remains overlooked in terms of research, especially compared to the highly recognised circulatory system. However, a profound understanding of the lymphatic system may lead to appropriate treatments of lymph diseases. Current treatment options have only limited success since only symptoms are treated, for example via special massages, which stimulate lymphatic flow. A suited theoretical and numerical modelling may improve the understanding of the bio-physical fundamentals of the lymphatic system and offer the possibility to analyse novel therapeutic options and their impacts in advance. Based on a reliable model of the human leg tissue and the lymphatic drainage mechanisms, numerical simulations help to determine and maybe even predict biomechanical effects as a consequence of treatment methods as for example a specific lymphatic-drainage apparatus.

**Manual lymphatic drainage:** The most common treatment of lymphedema is the manual lymphatic drainage (MLD). In particular, this represents a special type of massage which reduces swelling from lymphedema, firstly applied by Winiwarter<sup>3</sup>, cf. Bringezu

---

<sup>1</sup>Gaspare Aselli (1581–1625) was an Italian physician and surgeon noted for the discovery of the lacteal vessels of the lymphatic system [WIKIPEDIA].

<sup>2</sup>Olaus Rudbeck (also known as Olof Rudbeck the Elder, to distinguish him from his son, and occasionally with the surname latinised as Olaus Rudbeckius) (1630–1702) was a Swedish scientist and writer. Rudbeck is primarily known for his contributions in two fields: human anatomy and linguistics, but he was also accomplished in many other fields including music and botany [WIKIPEDIA].

<sup>3</sup>Alexander von Winiwarter (1848–1917) was an Austrian-Belgian surgeon. In the latter part of the 19th century, Winiwarter introduced specialised massage and compression procedures to treat lymphedema [WIKIPEDIA].

*et al.* [46]. During MLD, a very light pressure is applied to stimulate lymph flow in the lymph vessels located directly underneath the skin. In contrast, too much pressure would cause the vessels to collapse and lymph would not be allowed to move through the vessels. The aim of the massage is to move fluid from swollen areas into an area where the lymphatic system is working normally, cf. Martín *et al.* [199].

**Instrumental lymphatic drainage:** A lymphatic-drainage apparatus stimulates the flow of lymphatic fluid due to instrumental pressure-controlled compression. Next to manual lymphatic drainage, instrumental compression has been standard for years in the physical treatment of lymphedema. As an example, “Lympha-mat Gradient”<sup>4</sup> provides a lymphatic-drainage apparatus. The working principle is an overlapping air chamber system which is successively filled with air in the compression cycle until the last chamber reaches the desired pressure. Then, the air escapes simultaneously. Afterwards, there is a break period, followed by a new inflation cycle. The resulting pressure gradient causes a physiological efficient pressure drop. Liquids are mobilised to flow from higher pressure conditions (100%) to lower pressure conditions (80% and 60%). Thereby, the accumulated interstitial fluid is forced out of the limb and the swelling is alleviated. The applied pressure is typically chosen between 20 and 120 mmHg<sup>5</sup> and a typical treatment duration amounts between 30 and 60 minutes.

## 6.2 Anatomy of the lymphatic system

In the cardiovascular system, blood is pumped through vascular vessels by a central pump, the heart. Thereby, fluid leaks from the vascular capillaries and accumulates in the interstitial tissue. Most of this fluid is directly reabsorbed by the blood vessels. However, the remaining amount is transported via other ways. This task is provided by the lymphatic system which plays an important role in treating pathogens, as it transports the cells of the immune system. Moreover, the lymphatic system transports dietary lipids and fat-soluble vitamins, cf. Herpertz [147]. If the drainage function of the lymphatic system fails, interstitial fluid accumulates in the tissue space. This inappropriate accumulation is called lymphedema and may lead to serious medical consequences.

**Lymphatic vessel system:** Lymphatic vessels begin as open-ended capillaries, as shown in Figure 6.1 (a), which absorb excess interstitial fluid. Once it has entered the lymphatic system, interstitial fluid is termed lymph. Capillaries, also called initial lymphatics, gradually combine to form larger vessels, namely the pre-collectors, collectors, ducts and trunks. Lymph travels through these vessels before it returns to the blood. Along the way, lymph passes lymph nodes where it is filtered before it re-enters the bloodstream, cf. Margaris & Black [193]. In contrast to the cardiovascular system, the lymphatic system does not have a central pump. Therefore, lymph is not actively pumped, but forced through the vessels by movements of the body, contractions of skeletal muscles during body movements and by contractions of the lymphatic vessels which contain smooth muscles in their walls.

<sup>4</sup>“Lympha-mat Gradient” is produced by BÖSL Medizintechnik GmbH, cf. [39].

<sup>5</sup>In comparison, the pressure of a blood pressure monitor is typically twice as high as it has to exceed the systolic blood pressure which is between 100 and 130 mmHg for a healthy human.

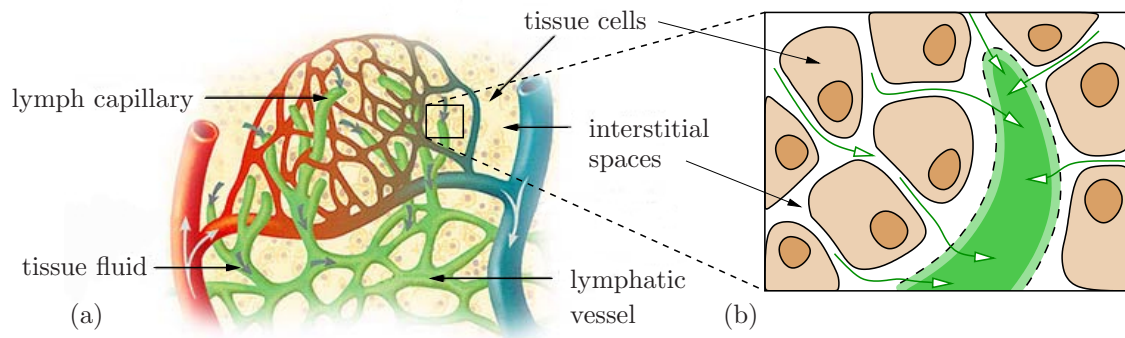


**Figure 6.1:** Lymphatic vessels begin as a fine mesh of open-ended capillaries (a), gradually combine to form larger vessels and finally lead back to the venous system. Lymph enters the lymphatic system (b) through initial lymphatics.

One-way valves keep lymph moving forward and prevent backflow, cf. Herpertz [147].

**Initial lymphatics:** Initial lymphatics, also called lymph capillaries, start in the periphery of the interstitial connective tissue space. The fine-mesh, polygonal capillary network with finger-shaped bossing represents the open end of the system. This is where the interstitial fluid enters the lymphatic system and becomes lymph. The initial lymphatics comprise a one-cell-thick layer of endothelial cells which lie side by side or are simply or multiply interlocked. They are supported by anchoring filaments that keep them from collapsing when interstitial pressure increases. The overlapping edges of the endothelial cells act as inlet valves (primary lymphatic valves). When interstitial pressure is low, the endothelial flaps are closed. As interstitial pressure increases, the spaces between cells open up, allowing fluid to enter. The anchoring filaments pull on the endothelial flaps, opening them even further to support inlet flow. Then, the flaps close again to prevent backwards flow as the internal pressure increases, cf. Figure 6.1 (b). Flow inside the initial lymphatics is facilitated by fluctuations in the interstitial fluid pressure and by the suction of the collecting lymphatics downstream, cf. Foeldi *et al.* [110].

**Pre-collectors and collectors:** Initial vessels enter into larger lymphatic vessels, the pre-collectors. Pre-collectors gather lymph of the capillary network and channel it to the collectors. Although it is one vessel, pre-collectors contain different wall segments. There are wall segments with membrana accessoria, which contain one-way valves, like collectors, and segments with capillary character which have an absorbing function. Thus, the pre-collectors have a dual role, namely the absorption and the propulsion of lymph. In contrast, the wall structure of collectors is similar to veins. Three layers can be identified, namely the intima, media and adventitia layer. Each layer consists of endothelial cells, smooth muscle and collagen fibres. Moreover, they contain one-way valves that cause bulges and give them a beaded appearance, which can be seen in Figure 6.1. The part of the vessel between two valves is known as a lymphangion. Lymph propulsion is performed by the rhythmic contraction of the smooth muscles of lymphangions and is facilitated by one-way valves that prevent retrograde flow, cf. Martín *et al.* [199]. The collection area of a collecting lymphatic is called drainage area.

**Lymphoid organs:** Lymphocytes mature, proliferate and are selected in the lymphoid organs, which enables them to attack pathogens without harming cells of the body. Lymphoid organs are either classified as primary lymphoid organs or as secondary organs. The bone marrow and the thymus gland are primary lymphoid organs. This is where lymphocytes develop and mature. Secondary organs, namely the lymph nodes, the spleen and lymphoid nodules (e.g. tonsils), are responsible for further maturation of lymphocytes and initiate immune responses. The lymph node, which is a small, bean-shaped organ located throughout the lymphatic system, is the only lymphoid organ which plays a role in the active transport of lymph. Its exterior walls are covered with smooth muscle, enabling contractile behaviour like the lymphatic vessels (collectors). Lymph nodes remove debris and pathogens from lymph and are thus sometimes referred to as “filter of the lymph”, cf. Martín *et al.* [199].

**Lymphatic system of the lower extremities:** The lymphatic networks of the lower extremities can be divided into the subcutaneous and the deep system. The subcutaneous or superficial system drains the skin (and the subcutis) and can be stimulated by special massages, as utilised in manual lymph drainage. The deep system drains muscles, joints and nerves, cf. Foeldi *et al.* [110]. The removal of vessels during surgery or occlusion by parasites can cause lymphedema, which results in pain, disfigurement, incapacity and reduced immunity, cf. Macdonald *et al.* [192]. In particular, it is a common complication following reconstructive surgery, for example lower limb atherosclerosis. In consequence, interstitial fluid accumulates within the subcutaneous tissue and the leg volume increases to about 20% compared to the contralateral leg. Such lymphedema concerns the patient and delays rehabilitation following an otherwise successful operation. The microcirculatory changes, responsible for this abnormal accumulation of fluid, are still matter of further research. However, impaired lymph drainage and increased transcapillary filtration have been suggested to be accountable, cf. Haaverstad *et al.* [134].

### 6.3 Modelling approach and constitutive settings

The modelling of lymphatic tissue is still in its infancy. A great obstacle is the lack of anatomical and physiological data. The lymphatic system represents a highly complex system which still requires more intensive research. Nevertheless, there are several attempts to model the biomechanical behaviour of the lymphatic system.

A simplified one-dimensional model of the entire lymphatic network based on the Navier-Stokes equations of fluid mechanics is given by Reddy [223]. It seems that this is the only model of the entire lymphatic circulation so far. In the work of Swartz *et al.* [259], the hypothesis is tested that bulk tissue fluid movement can be evaluated in situ and described by a linear biphasic theory. To accomplish this, a novel experimental and theoretical model using the skin of the mouse tail is developed. Additional experiments are performed on oedematous tails. This model is useful for examining potential treatments for oedema and lymphatic disorders as well as substances which may alter tissue fluid balance and/or lymphatic drainage. Moreover, a comprehensive introduction into the hydraulic conductivity of the tissue and the lymphatic wall is given in Liu & Schlesinger

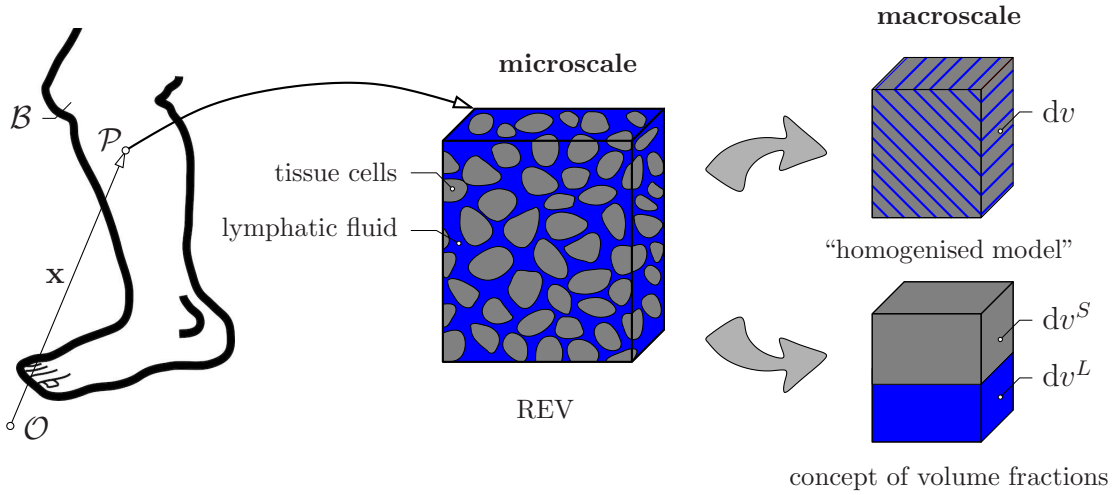


**Figure 6.2:** Representative elementary volume with exemplary displayed micro-structure of human leg tissue and macroscopic biphasic modelling approach.

[187]. Therein, the variation of the tumour interstitial fluid pressure (TIFP) and the hydraulic conductivity is described. A correct description of the hydraulic conductivity is crucial for the determination of the actual TIFP distribution.

The considerations above clearly imply the meaningful application of a multicomponent modelling approach. Therefore, a TPM model is developed to model lymphatic drainage, cf. Figure 6.2. The initially binary model is composed by its particular constituents, via

$$\varphi = \bigcup_{\alpha} \varphi^{\alpha} = \varphi^S \cup \varphi^L, \quad \text{where } \alpha = \{S, L\}. \quad (6.1)$$

Therein, the placeholder  $\alpha$  indicates the solid constituent  $S$  and the liquid constituent  $L$ . In terms of the TPM, these constituents are understood as immiscible and chemically inert constituents. The solid skeleton  $\varphi^S$  is composed of the tissue cells  $\varphi^{SC}$  and trapped water  $\varphi^{SW}$ . In conclusion, this leads to the model

$$\varphi = \underbrace{\varphi^{SC} \cup \varphi^{SW}}_{\varphi^S} \cup \varphi^L. \quad (6.2)$$

In terms of a meaningful consideration of the considered lymphatic draining, density (volume) production between the constituents  $\varphi^{SW}$  and  $\varphi^L$  is included.

**Preliminary assumptions:** The basic formulation of balance equations is subjected to the following preliminary assumptions, yielding possible simplifications for the particularly focused issues within this application. First, the solid constituent  $\varphi^S$  is assumed to be materially incompressible, implying a constant effective density  $\rho^{SR}$  of the solid skeleton. This commonly used assumption holds, since the volumetric bulk deformation of the porous solid material itself is, in general, much smaller than the pore-space dilatation or compression. Furthermore, the individual effective density  $\rho^{LR}$  of the liquid constituent is also assumed to be constant under moderate pressures. This yields

$$\{\rho^{SR}, \rho^{LR}\} = \text{const.} \quad (6.3)$$

By default, the overall aggregate is always fully saturated (closed-system approach) via

$$n^S + n^L = 1. \quad (6.4)$$

As mentioned before, mass exchanges are included satisfying the restriction

$$\hat{\rho}^S + \hat{\rho}^L = 0 \quad \rightarrow \quad \hat{\rho}^S = -\hat{\rho}^L \quad \rightarrow \quad \hat{n}^S = -\frac{\rho^{LR}}{\rho^{SR}} \hat{n}^L. \quad (6.5)$$

Using the definition  $\hat{\rho}^\alpha := \hat{n}^\alpha \rho^{\alpha R}$  shows that the volume production terms  $\hat{n}^\alpha$  are not equivalent (i. e.  $\hat{n}^S \neq \hat{n}^L$ ) for different effective densities  $\rho^{\alpha R}$ . This issue is pursued in Section 6.4.1. Furthermore, quasi-static conditions are assumed, i. e. the constituent's acceleration terms are neglected via  $\overset{\prime\prime}{\mathbf{x}}_\alpha \equiv \mathbf{0}$ . In general, this restricts the validity of the model to slow processes. Beside that, gravitational (body) forces  $\mathbf{b}^\alpha = \mathbf{g} = \mathbf{0}$  are neglected for all constituents. Moreover, non-polar constituents with vanishing angular-momentum productions, i. e.  $\hat{\mathbf{m}}^\alpha \equiv \mathbf{0}$ , are postulated. Therefore, the statement of the balance of angular momentum results in the symmetry of the stress tensors. Finally, a common constant temperature (approximately 37°C) is assumed for all constituents of the living tissue, yielding

$$\theta^\alpha \equiv \theta = \text{const.} \quad (6.6)$$

In conclusion, this leads to an isothermal model without an explicit need to consider the energy balance within the governing set of equations.

**Composition of balance equations:** The model is governed by the mass and momentum balances of the constituents, viz.:

$$\begin{aligned} (\rho^\alpha)'_\alpha + \rho^\alpha \text{div } \overset{\prime}{\mathbf{x}}_\alpha &= \hat{\rho}^\alpha, \\ \mathbf{0} &= \text{div } \mathbf{T}^\alpha + \hat{\mathbf{p}}^\alpha. \end{aligned} \quad (6.7)$$

It can easily be seen that the system of equations given in (6.7) exhibits more unknowns than equations. In particular, two scalar-valued mass balance equations (6.7)<sub>1</sub> as well as two vector-valued (or six scalar-valued) momentum balance equations (6.7)<sub>2</sub> are available for the considered biphasic model. In terms of a standalone viewing, these are 8 scalar-valued equations. However, the set of equations basically implies 28 scalar-valued unknowns, i. e., for the quantities  $\rho^\alpha$  (1 · 2),  $\overset{\prime}{\mathbf{x}}_\alpha$  (3 · 2),  $\mathbf{T}^\alpha$  (6 · 2),  $\hat{\rho}^\alpha$  (1 · 2) and  $\hat{\mathbf{p}}^\alpha$  (3 · 2). Hence, the existing gap needs to be closed (i. e. the closure problem) in terms of constitutive settings of the developed model.

Initially, a distinct choice of balance equations from (6.7) states the governing equations, which are linked to the so-called primary variables of the model. In this regard, the governing balance relations as well as the restrictive frame of the entropy inequality are further adapted. Afterwards, the constitutive modelling process provides the completion of the model. Therefore, all further unknowns (secondary variables) have to be found by combining the remaining balance equations with appropriate constitutive assumptions.

With regard to the adaption of the chosen governing balance equations, the general transformation

$$(\cdot)'_\beta = (\cdot)'_S + \text{grad}(\cdot) \cdot \mathbf{w}_\beta \quad (6.8)$$

of the material time derivative with respect to a particular motion of a constituent is of immense benefit. Therein, material time derivatives with respect to the solid motion can be related to time derivatives with respect to other constituents and vice versa. The placeholder  $(\cdot)$  in (6.8) is used for arbitrary scalar quantities.

**Volume balance of the liquid:** For the development of the volume balance of the liquid phase, the effective density  $\rho^{LR}$  is assumed to be constant (6.3). This yields

$$(n^L)'_L + n^L \operatorname{div} \dot{\mathbf{x}}_L = \hat{n}^L \rightarrow (n^L)'_S + \operatorname{div}(n^L \mathbf{w}_L) + n^L \operatorname{div}(\mathbf{u}_S)'_S = \hat{n}^L. \quad (6.9)$$

Therein, the material time derivative with respect to the interstitial fluid is formulated regarding the solid motion, using (6.8). In (6.9), the constitutive setting of the production term

$$\hat{n}^L = \begin{cases} n^S l_{\text{lymph}} (p^{LR} - p_{\text{crit}}) & \text{if } p^{LR} > p_{\text{crit}} \text{ and } n^S > \hat{n}_{\text{max}}^S \\ 0 & \text{else} \end{cases} \quad (6.10)$$

is postulated in terms of a Starling<sup>6</sup>-type approach. In particular, this formulation enables a volume production  $\hat{n}^L$  if the lymph pressure  $p^{LR}$  exceeds a certain critical pressure  $p_{\text{crit}}$  and the maximal amount of producible volume  $\hat{n}_{\text{max}}^S$  (trapped lymph within the solid phase) is not yet completely consumed. Moreover,  $l_{\text{lymph}}$  denotes a material parameter governing the mobilisation ability of the trapped lymph.

**Volume balance of the solid skeleton:** Based on a materially incompressible solid skeleton, also the solid mass balance can be transferred to its volume balance, viz.:

$$(n^S)'_S + n^S \operatorname{div} \dot{\mathbf{x}}_S = \hat{n}^S. \quad (6.11)$$

In general, the volume balance (6.11) is dedicated to compute the evolution of the volume fraction  $n^S$ . Therefore, the following form can be found

$$n^S = n_{t_S}^S (\det \mathbf{F}_S)^{-1} \quad \text{where} \quad n_{t_S}^S = n_{0_S}^S \exp\left[\int_{t_0}^t \frac{\hat{n}^S}{n^S} d\tilde{t}\right]. \quad (6.12)$$

Therein,  $n_{0_S}^S$  is the solid's volume fraction in the solid's reference configuration. Therefore, the lymph's volume fraction  $n^L = 1 - n^S$  results directly from the saturation condition. In (6.12), the solid's volume production is obtained by the relation (6.5) from the constitutive setting (6.10) of the liquid's volume production. Thus, the solid's volume fraction during lymphatic drainage is obtained as

$$n^S = n_{0_S}^S (\det \mathbf{F}_S)^{-1} \exp\left[-\int_{t_0}^t \frac{\rho^{LR}}{\rho^{SR}} l_{\text{lymph}} (p^{LR} - p_{\text{crit}}) d\tilde{t}\right]. \quad (6.13)$$

For the numerical implementation of (6.13), the required integral (continuous) quantity is computed in terms of a history variable, accumulating discrete incremental updates.

---

<sup>6</sup>Ernest Henry Starling (1866–1927) was a British physiologist who contributed many fundamental ideas to this subject [WIKIPEDIA].

**Volume balance of the overall aggregate:** The summation of the constituent's volume balances (6.9) and (6.11) using the relation (6.5) yields

$$\begin{aligned} \underbrace{(n^S + n^L)'_S}_0 + \underbrace{(n^S + n^L)}_1 \operatorname{div}(\mathbf{u}_S)'_S + \operatorname{div}(n^L \mathbf{w}_L) &= \hat{n}^S + \hat{n}^L \\ \rightarrow \operatorname{div}[(\mathbf{u}_S)'_S + n^L \mathbf{w}_L] &= \frac{\rho^{SR} - \rho^{LR}}{\rho^{SR}} \hat{n}^L. \end{aligned} \quad (6.14)$$

**Momentum balance of the liquid:** For the description of the specific flow characteristics of the liquid, the constitutive ansatz for the extra momentum production term

$$\hat{\mathbf{p}}_E^L = -\mathbf{S}^{LS} \mathbf{w}_L \quad \text{with} \quad \mathbf{S}^{LS} = (n^L)^2 \mu^{LR} (\mathbf{K}^{SL})^{-1} \quad (6.15)$$

and  $\hat{\mathbf{p}}^L = p^{LR} \operatorname{grad} n^L + \hat{\mathbf{p}}_E^L$  and the partial stress tensor  $\mathbf{T}^L = -n^L p^{LR} \mathbf{I}$  of the liquid are inserted into the (quasi-static) momentum balance of the liquid, viz.:

$$\mathbf{0} = \operatorname{div} \mathbf{T}^L + \hat{\mathbf{p}}^L \quad \rightarrow \quad n^L \mathbf{w}_L = -\frac{\mathbf{K}^{SL}}{\mu^{LR}} \operatorname{grad} p^{LR}. \quad (6.16)$$

As a result, a standard Darcy filter law is obtained. This equation is inserted into the overall volume balance (6.14) and yields a formulation in terms of the liquid pressure.

**Momentum balance of the solid skeleton:** The reduced balance of momentum of the solid skeleton reads

$$\mathbf{0} = \operatorname{div} \mathbf{T}^S + \hat{\mathbf{p}}^S. \quad (6.17)$$

Since it is practically not feasible to identify the splitting of an external surface loading to the constituents at the surface of a porous material, the balances of momentum are summed up and used as an overall momentum balance.

**Momentum balance of the overall aggregate:** The quasi-static formulation of the momentum balance of the overall aggregate is derived by the summation of all particular momentum balances (6.7)<sub>2</sub> of the constituents  $\varphi^\alpha$  yielding the overall momentum balance<sup>7</sup> of  $\varphi$ , viz.:

$$\begin{aligned} \mathbf{0} &= \operatorname{div}(\mathbf{T}^S + \mathbf{T}^L) - \hat{\rho}^L \mathbf{w}_L \\ &= \operatorname{div}(\mathbf{T}_E^S - p^{LR} \mathbf{I}) - \hat{\rho}^L \mathbf{w}_L. \end{aligned} \quad (6.18)$$

Therein, the summation over all direct momentum production terms using the relation (6.5) yields

$$\begin{aligned} \sum_\alpha \hat{\mathbf{s}}^\alpha &= \sum_\alpha (\hat{\mathbf{p}}^\alpha + \hat{\rho}^\alpha \dot{\mathbf{x}}_\alpha) = \mathbf{0} \\ \rightarrow \hat{\mathbf{p}}^S + \hat{\mathbf{p}}^L + \hat{\rho}^S \dot{\mathbf{x}}_S + \hat{\rho}^L \dot{\mathbf{x}}_L &= \mathbf{0} \\ \rightarrow \hat{\mathbf{p}}^S + \hat{\mathbf{p}}^L &= -\hat{\rho}^L \mathbf{w}_L. \end{aligned} \quad (6.19)$$

<sup>7</sup>This expression might appear at the first sight in contradiction to Truesdell's third principle. However, it results straightforward by a rigorous summation procedure according to Truesdell's first principle and consequently leads to a correct description of the overall aggregate.

In (6.18), the summation of the partial stresses leads

$$\mathbf{T}^S + \mathbf{T}^L = \mathbf{T}_E^S - p^{LR} \mathbf{I}. \quad (6.20)$$

Therein, the principle of effective stresses is applied as well as the liquid extra stresses are neglected. Finally, the solid's extra stresses

$$\mathbf{T}_E^S = 2\mu^S \boldsymbol{\varepsilon}_S + \lambda^S (\boldsymbol{\varepsilon}_S \cdot \mathbf{I}) \mathbf{I} \quad (6.21)$$

is derived based on a linear elastic (Hookean) approach using the Lamé constants  $\mu^S$  and  $\lambda^S$ . In conclusion, Equation (6.18) can be expressed by the solid displacement field  $\mathbf{u}_S$  (primary variable) via  $\boldsymbol{\varepsilon}_S = \frac{1}{2}(\text{grad } \mathbf{u}_S + \text{grad}^T \mathbf{u}_S)$ .

**Weak formulations of the governing equations:** In terms of the numerical implementation, the governing equations are transferred to weak formulations. In particular, these are the weak forms of the volume balance (6.14) and the momentum balance (6.18) of the overall aggregate, namely

$$\begin{aligned} \mathcal{G}_{p^{LR}} &\equiv \int_{\Omega} [\delta p^{LR} \text{div}(\mathbf{u}_S)'_S - \delta p^{LR} \frac{\rho^{SR} - \rho^{LR}}{\rho^{SR}} \hat{n}^L - n^L \mathbf{w}_L \cdot \text{grad } \delta p^{LR}] dv + \\ &\quad + \int_{\Gamma_N^{\bar{v}^L}} \delta p^{LR} \bar{v}^L da = 0, \quad \text{where } \bar{v}^L = n^L \mathbf{w}_L \cdot \mathbf{n} \quad \text{and} \\ \mathcal{G}_{\mathbf{u}_S} &\equiv \int_{\Omega} [(\mathbf{T}_E^S - p^{LR} \mathbf{I}) \cdot \text{grad } \delta \mathbf{u}_S - \hat{n}^L \rho^{LR} \mathbf{w}_L \cdot \delta \mathbf{u}_S] dv - \\ &\quad - \int_{\Gamma_N^{\bar{\mathbf{t}}}} \bar{\mathbf{t}} \cdot \delta \mathbf{u}_S da = 0, \quad \text{where } \bar{\mathbf{t}} = (\mathbf{T}_E^S - p^{LR} \mathbf{I}) \mathbf{n}. \end{aligned} \quad (6.22)$$

The weak formulations are linked to the primary variables of the problem. In particular, the weak formulation (6.22)<sub>1</sub> of the volume balance is related to the effective pore pressure  $p^{LR}$  of the lymph, whereas the weak formulation (6.22)<sub>2</sub> of the momentum balance is related to the solid displacement field  $\mathbf{u}_S$  via the solid extra stress  $\mathbf{T}_E^S$ , cf. (6.21).

## 6.4 Numerical examples

In this section, two selected numerical examples are shown. These are first a purely academic example to show the occurring processes during a mass exchange process and, second, the application of the model to a realistic scenario of a lymphatic drainage on a human leg.

### 6.4.1 General study of the mass-exchange process

INTRODUCTORY NOTE: The content of this section is based on the work of Tobias Kattmann: *Biphasic model with and without lymph production*. Report of the research module of the study programme Simulation Technology, University of Stuttgart 2017.

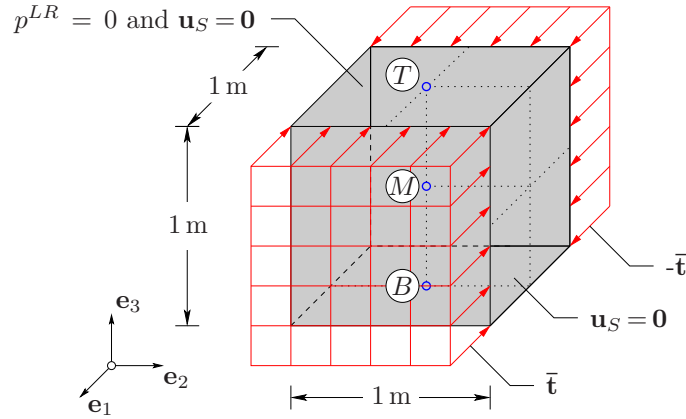


**Figure 6.3:** Geometry and boundary conditions of a cube, discretised with  $7 \times 7 \times 7$  elements.

A simple cube with given dimensions and boundary conditions is studied, cf. Figure 6.3. In particular, a Neumann boundary condition  $\bar{\mathbf{t}}$  is prescribed as a linear increase towards a constant value, viz.:

$$\bar{\mathbf{t}}(t) = \begin{cases} -10t \mathbf{e}_1 \text{ [N/m}^2\text{]} & \text{if } t < 1000 \text{ s,} \\ -10\,000 \mathbf{e}_1 \text{ [N/m}^2\text{]} & \text{else.} \end{cases} \quad (6.23)$$

The material parameters for the performed simulations are given in Table 6.1. Note that a mobilisation of the trapped lymphatic fluid, which is initially accounted to the solid phase, does not result in a change of density or volume. In contrast, if the solid's density is chosen larger than the fluid's density, a volume production occurs due to the system's overall mass conservation, cf. (6.5). However, a volume conservation is guaranteed for

$$\rho^{SR} = \rho^{LR} \quad \longrightarrow \quad \hat{n}^S = -\hat{n}^L, \quad (6.24)$$

Collection of material parameter			
	value	unit	description
$\mu^S$	$3.1 \times 10^5$	[N/m <sup>2</sup> ]	first Lamé constant of $\varphi^S$
$\lambda^S$	$3.45 \times 10^4$	[N/m <sup>2</sup> ]	second Lamé constant of $\varphi^S$
$n_{0S}^S$	0.8	[-]	initial solidity of $\varphi^S$
$k^L$	$6.27 \times 10^{-7}$	[m/s]	Darcy permeability
$\rho^{LR}$	$1.0 \times 10^3$	[kg/m <sup>3</sup> ]	realistic density of the fluid
$\rho^{SR}$	$1.0 \times 10^3$	[kg/m <sup>3</sup> ]	realistic density of the solid
$l_{\text{lymph}}$	$1.0 \times 10^{-8}$	[m <sup>2</sup> /N]	mobilisation ability of the trapped lymph
$\hat{n}_{\text{max}}^S$	0.2	[-]	solidity threshold caused by lymph production
$p_{\text{crit}}$	0.0	[N/m <sup>2</sup> ]	critical pressure for lymph-drainage initiation

**Table 6.1:** Collection of material parameters. Basic parameters for the biphasic model in the upper field and additional lymphatic-drainage parameters for the mass-production model in the lower field.

cf. (6.5), which is assumed here. Physically, this represents a reasonable choice since trapped water is mobilised. Thus, an exchange occurs via the water component, which has the same density no matter whether it is situated in the cells (trapped) or in the interstitial fluid space (mobile).

In the following, the influence of the production term related parameters  $\hat{n}_{\max}^S$ ,  $p_{\text{crit}}$  and, especially,  $l_{\text{lymph}}$  on the model's response is studied. In particular, the parameter  $l_{\text{lymph}}$  is considered with three different values. In particular, these are (i) a low mobility  $l_{\text{lymph}} = 1 \times 10^{-10}$ , (ii) a moderate mobility  $l_{\text{lymph}} = 1 \times 10^{-8}$  and (iii) a high mobility  $l_{\text{lymph}} = 1 \times 10^{-7}$ . For the evaluation, three measurement points are considered, i. e. at the bottom ( $B$ ), middle ( $M$ ) and top ( $T$ ), cf. the blue circles in Figure 6.3. Selected plots of the Darcy velocity  $n^L \mathbf{w}_L$  in vertical direction, the solid volume fraction  $n^S$  and the production term  $\hat{n}^L$  of the lymph are shown. In particular, Figure 6.4 (a) displays the filter velocity  $n^L \mathbf{w}_L$  over time at Point  $T$ , since the highest velocities are obtained here. Independent from the choice of  $l_{\text{lymph}}$ , all computations show the same (out)flow behaviour. The evolution of the filter velocity reveals the loading process, including the arising consolidation process after 1000 s due to the (remaining) constant load. Figure 6.4 (b) shows the solid's volume fraction  $n^S$  at Point  $M$  for different lymph-mobility values. For the lowest mobility, the solid volume fraction remains constant at the initial value of 0.8. In contrast, the other two curves show a decrease in the solid's volume fraction, which indicates an arising lymph production, cf. Figure 6.5. Note that the curve for case (iii) with a high mobility is restricted by the constitutively chosen threshold value of  $\hat{n}_{\max}^S = 0.2$ . At this point the if-statement for  $\hat{n}_{\max}^S$  of the production term, cf. (6.10), is no longer fulfilled such that the volume production suddenly stops. This results in a non-smooth transition. Note in passing that the production term scales with the solid's volume fraction  $n^S$ , such that a lower value of  $\hat{n}_{\max}^S$  leads to a smoother transition. The decrease in the solid volume fraction indicates a lymph production (mobilisation). Figure 6.5 shows the volume production  $\hat{n}^L$  of the lymph at the Point  $B$ , cf. Figure 6.3. Again, the sudden decrease to zero for case (iii) is due to the not fulfilled if-condition in (6.10). This kind of unsteady drop might cause numerical problems. However, in the performed simulations

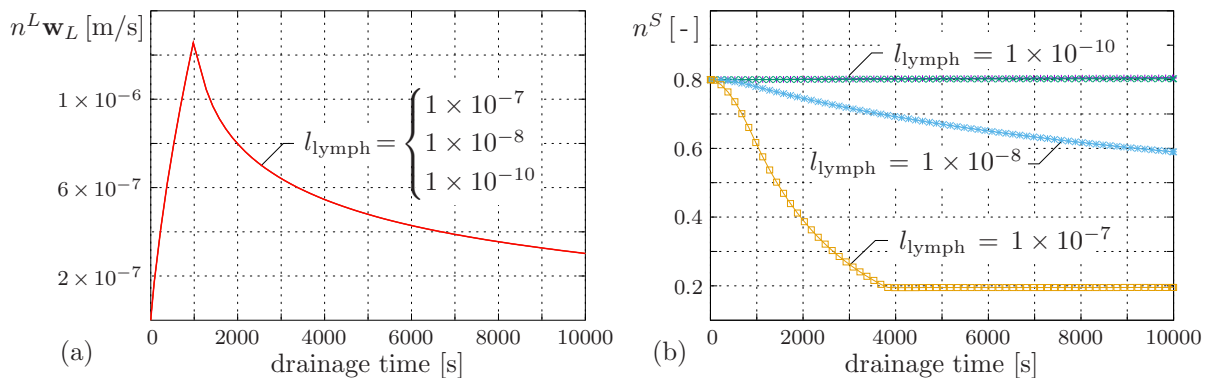


**Figure 6.4:** Filter velocity  $n^L \mathbf{w}_L$  in  $\mathbf{e}_3$  (vertical) direction at the top surface (Point  $T$ ) in (a) and solid's volume fraction  $n^S$  in (b). For  $l_{\text{lymph}} = 1 \times 10^{-7}$ , the restriction of  $\hat{n}_{\max}^S$  is fulfilled at approximately 4000 s, such that the production is deactivated (non-smooth (kink) and non steadily differentiable function).

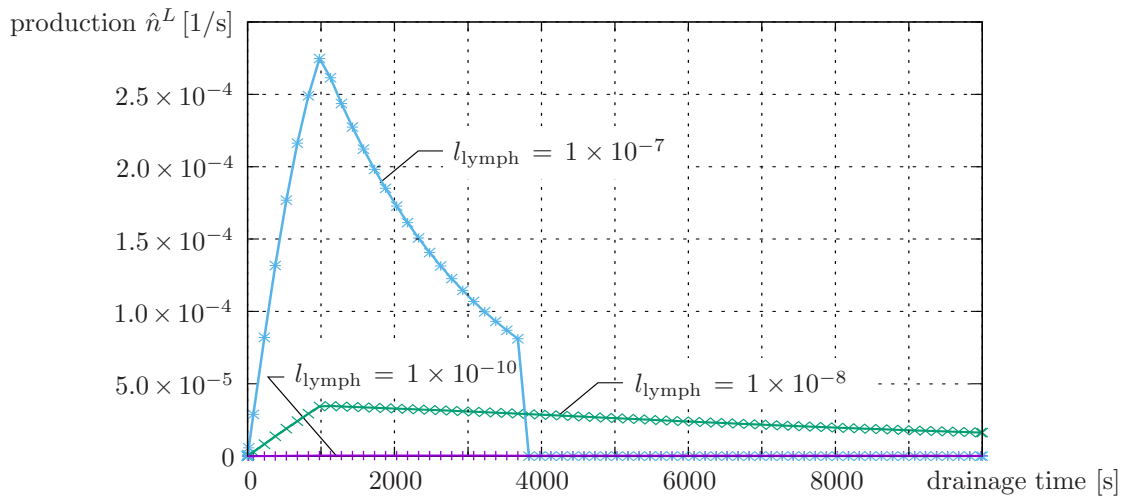


**Figure 6.5:** Lymph's production rate for different values of  $l_{\text{lymph}}$  in Point B. Note that the abrupt decrease for case (iii) is a result of the production-term restriction  $\hat{n}_{\text{max}}^S$ , cf. (6.10).

no evidences for numerical instabilities, e. g. oscillations, are recognised.

## 6.4.2 Application to a human leg

INTRODUCTORY NOTE: The content of this section is based on the bachelor thesis: *Multi-component modelling of the lymphatic vessel system applied to lymphatic drainage*, conducted by Louise Sauter [236].

After the discussion of the general mass-exchange process in the previous section, the model's application to a more realistic scenario of a lymphatic drainage is shown in this section. To start with, a meaningful geometry of a female leg is manually created as it is sketched in Figure 6.6. In particular, the 3-dim. leg model is obtained proceeding from

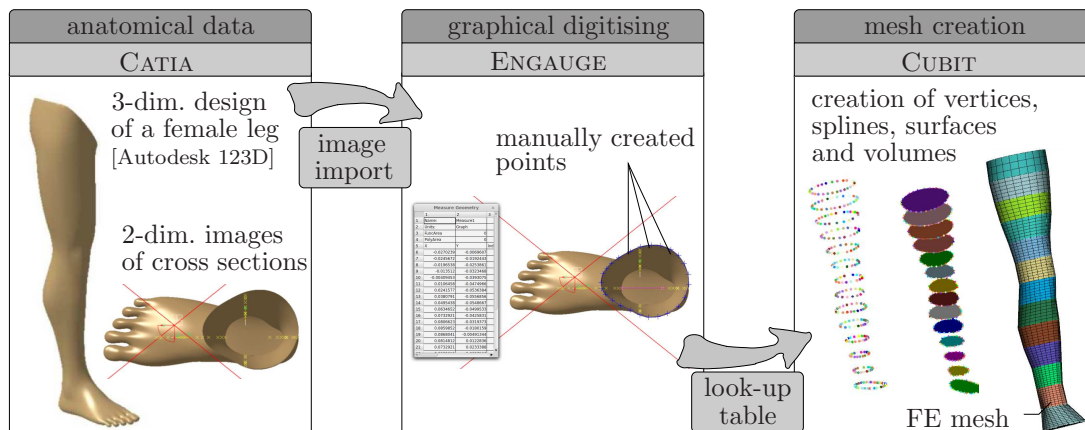


**Figure 6.6:** Development of a discretised female leg geometry: (i) 3-dim. data-scan obtained from Autodesk 123D, (ii) graphical digitising using ENGAUGE and (iii) final mesh generation using CUBIT.

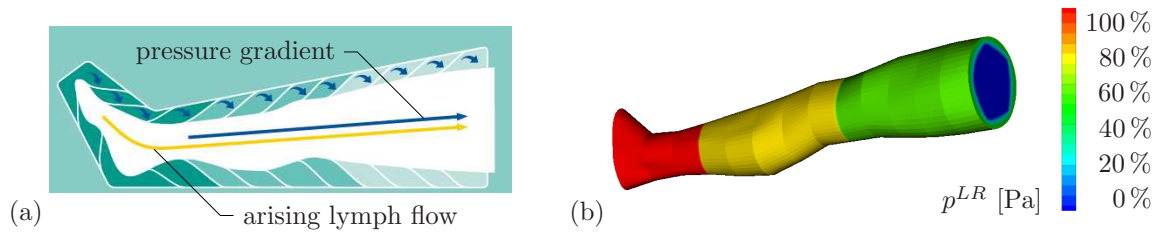


**Figure 6.7:** *Lymphamat-D* by BÖSL Medizintechnik GmbH [39] with overlapping 12-chamber system in (a) and (b) replicated exceed fluid pressure  $p^{LR}$  for the simulation of instrumental lymphatic drainage.

Autodesk 123D<sup>8</sup>. According to the usual practice, an automatic meshing is not possible, e.g. due to redundant parts or surfaces in the provided data set. Therefore, the initial geometry needs to be processed and simplified. The applied step-by-step procedure, given in Figure 6.6, is to “cut” the leg into discs to obtain 2-dim. slices using CATIA<sup>9</sup>, read out the bounding coordinates with ENGAUGE<sup>10</sup> and, hence, build a simplified model by assembling the single discs to segments using CUBIT<sup>11</sup>. Finally, a finite-element mesh is generated in CUBIT which is transferred via an in-house developed python-interface (mesh2pandas) to the FE solver PANDAS. In conclusion, the simplified leg model consists of 5202 mixed Taylor-Hood elements with 24554 nodes. Moreover, 15 sidesets are specified, allowing for the application of boundary conditions. At the example of instrumental lymphatic drainage, the boundary conditions are replicated based on a typical lymphatic-drainage apparatus, cf. the introductory remarks in Section 6.1. An instrumental lymphatic-drainage device controls the air pressure and the compression cycles. The pressure is typically chosen between 20 and 120 mmHg, which corresponds to about 2666 and 15999 Pa. Compression cycles are conducted to facilitate refill of the lymphatic vessels with interstitial fluid after they emptied due to the applied pressure.

Initially, fluid pressure is applied at the surface of each leg segment. It is assumed that the pressure in the lymphatic-drainage apparatus is directly transferred to the lymph in the leg and, therefore, the same fluid pressure prevails at the leg surface. A slowly rising pressure of 10 Pa (respectively 8 Pa and 6 Pa for 80% and 60%) is applied at the outer surface of the leg segments and at the lower surface for every time step until a pressure of 10 kPa (8 kPa / 6 kPa) is reached after 1000 s. Afterwards, the pressure is kept constant. There is no pressure applied to the top surface of the leg to facilitate outflow and reflect physical conditions. The resulting fluid pressure is depicted in Figure 6.7 (b). A 3-dim. visualisation of the seepage velocity of lymph through leg tissue is shown in Figure 6.8. The slowest velocity of  $9.0 \times 10^{-7}$  m/s appears at the lower surface of the leg

<sup>8</sup>Autodesk 123D was a suite of hobbyist CAD and 3-dim. modelling tools created by Autodesk. However, Autodesk 123D was discontinued in March 2017 [WIKIPEDIA].

<sup>9</sup>CATIA (computer aided three-dimensional interactive application), cf. <http://www.3ds.com/products-services/catia>.

<sup>10</sup>ENGAUGE is a digitising software tool that converts an image file showing a graph or map, into numbers, cf. <http://markummittchell.github.io/engage-digitizer>.

<sup>11</sup>CUBIT is a geometry and mesh generation toolkit, cf. <https://cubit.sandia.gov>.

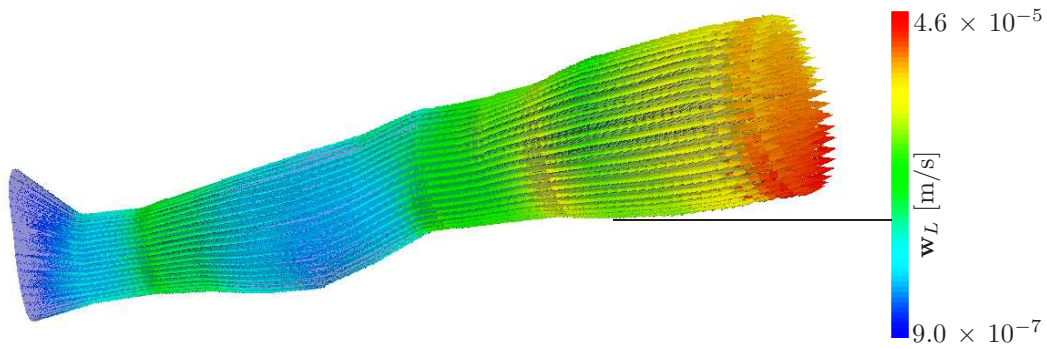


**Figure 6.8:** Seepage velocity  $w_L$  for the model with lymph production.

and the highest velocity of  $4.6 \times 10^{-5}$  m/s, which corresponds to about 2.8 mm/min, at the upper surface. However, at the calf, a lower velocity arises than in the ankle area. To examine this closer, the 3-dim. model is broken down to a 1-dim. model along the vertical axis of the leg in Figure 6.9. In Figure 6.9, the red line marks the seepage velocity in leg (vertical) direction at specific points along the vertical axis of the leg ( $x_1 = 0$  and  $x_2 = 0$ ). As indicated in Figure 6.8, the seepage velocity drops significantly at the tibia area ( $0.1 \leq x_3 \leq 0.25$ ). This is caused by the widening of the leg in this area. Additionally, there is no significant pressure drop in this area which would activate lymph flow. Above, the seepage velocity steadily increases towards the upper surface where it also reaches its peak. Overall, higher velocities are induced in the presented model accounting for lymph production, visualised by the green dashed line in Figure 6.9, than the ones in the reference model without lymph production, which is coloured in red. Note in passing that new produced lymph apparently ensures a further increase of the seepage velocity.

For improvement, the compression sleeve could be modelled as extra body to include additional stiffness as well as a rigid contact area of the leg where it typically rests on

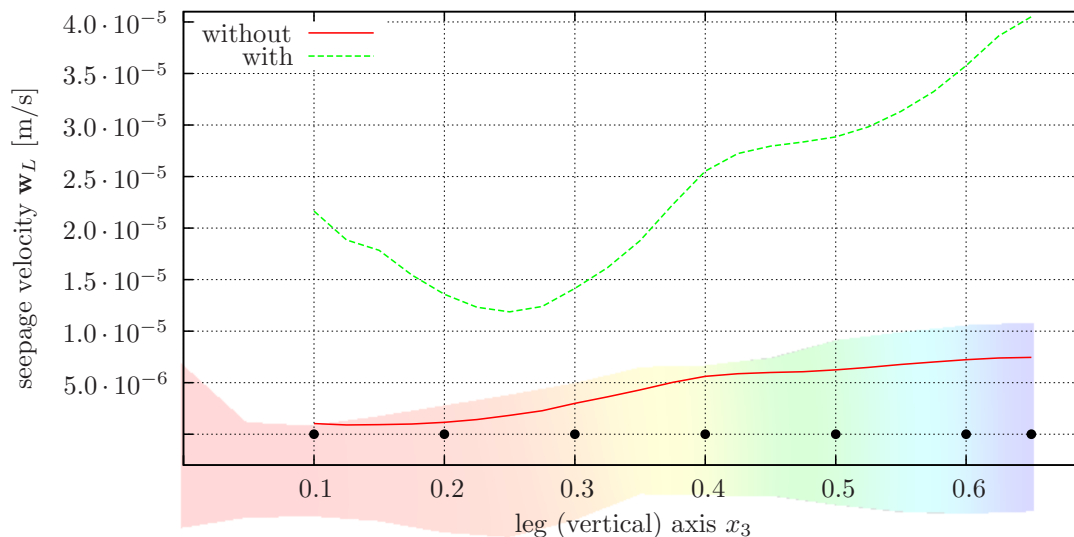


**Figure 6.9:** Seepage velocity  $w_L$  of lymph along leg (vertical) axis  $x_3$  ( $x_1 = 0$ ,  $x_2 = 0$ ) at time  $t = 1500$  s. The red line represents a reference model without lymph production and the green line the presented model with lymph production. The black dots mark the locations where the seepage velocity is evaluated.

the treatment table. Moreover the theoretical modelling approach could be enhanced. Here, only a biphasic modelling approach was utilised. In a more sophisticated TPM model, the blood and bones could additionally be taken into account. Improvement concerning the geometrical model may include to use an oedematous leg or even model a patient-specific leg geometry, e. g. obtained via data from an individual 3-dim. CT scan. Perspectively, the patient treatment and recovery process could be accompanied by simulation to verify the results and determine drawbacks of the computational model. In the long term, an advanced model could even offer novel and enhanced treatment options. In terms of product design, the model of lymphatic drainage might contribute to further improvements of lymphatic drainage devices by detecting weak points and testing new concepts. Consequently, many improvements of the computational model and the evaluation of the numerical results could be executed which, however, remain subject of further studies.



# Chapter 7:

## Heat and mass transport in plants

### 7.1 Motivation and introduction

BIBLIOGRAPHIC NOTE: The content of the sections 7.1 and 7.2 is based on the original article: Eurich, L., Schott, R., Wagner, A., Roth-Nebelsick, A. & Ehlers, W.: *Fundamentals of Heat and Mass Transport in Frost-Resistant Plant Tissues*. In: Knippers J., Nickel K., Speck T. (eds): *Biomimetic Research for Architecture and Building Construction* 8 (2016), Springer, Cham, pp. 97–108 [104].

» Biological structures are mostly porous, since all living materials are produced by cells, and, therefore, consist of cells and/or substances that are exuded by cells. The cellular origin of biological materials allows the construction of complex structures that can be intricately patterned down to the nanometer scale. The porous structure is particularly prevalent in many plant tissues. Plant stems, cut open, often reveal pores that can be identified by the naked eye, cf. Figure 7.1 (a). These belong to the xylem, the water-conducting tissue, consisting of dead cells or cell chains arranged parallel to each other, together with a certain part of living xylem parenchyma. The diameter of wood cells usually ranges from 20  $\mu\text{m}$  to about 200  $\mu\text{m}$ . Wood consists almost entirely of xylem and owes its excellent mechanical properties to the lignified cell walls of the conduits. Less conspicuous are the other tissues that make up the plant stem (or any other plant organ) and whose cells are normally smaller than xylem conduits. Even at first glance, the stem cross section shown in Figure 7.1 reveals the arrangement of diverse tissues. A cross section, however, does not reveal the 3-dim. structure of the various tissues. Xylem conduits are exceedingly long, reaching a length of several meters for ring-porous trees, while showing a width of about 200  $\mu\text{m}$ . The walls of the wood cells are porous themselves, but with much narrower pores, in the nanometer range. In this way, highly

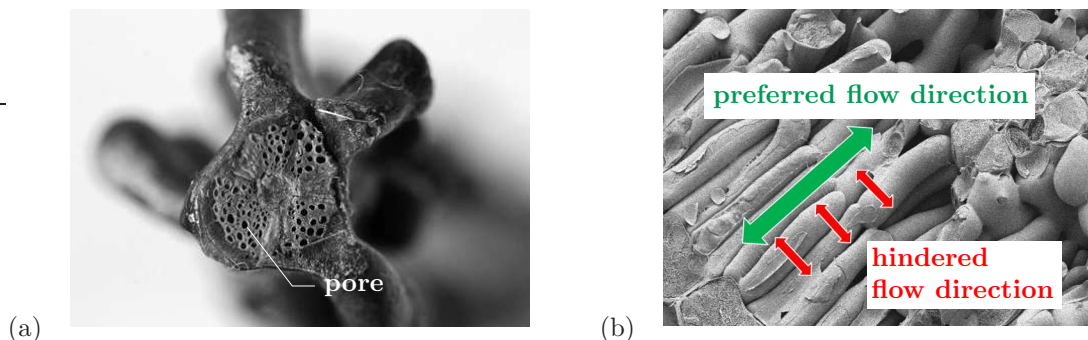


**Figure 7.1:** Stem of the tropical liana *Adenia lobata*, in cross section (diameter about 1.5 cm) in (a) and influence of the anisotropic microscopical architecture on the perfusion properties of plants in (b).

anisotropic porous materials are built. Thus, plant tissues represent porous materials with a graded structure. This strongly anisotropic water-conducting material shows high water conductance in the longitudinal direction and low conductance in the horizontal direction, cf. Figure 7.1 (b).

It is expected that these structural traits affect and control not only water flow, but also heat transport and ice formation. In the course of their evolutionary history, plants have developed an amazing resistance to various weather conditions. This is particularly evident with regard to frost-resistant plants, which are able to withstand many freezing and thawing cycles without any damage. In addition to physiological processes, another crucial factor of frost hardiness is the graded structure of plant materials. Indeed, ice nucleation starts within wood cells and subsequent ice formation proceeds along the longitudinal axis of conduits, cf. Hacker & Neuner [135].

In contrast, a change in the physical state of the aggregation of contained pore water within standard construction materials leads frequently to damage. In particular, this is typically caused by repeated thawing and freezing processes associated with volume changes of the pore water. Since plants have developed individual strategies in order to adapt to such circumstances, a vision is to transfer, at least in part, these properties to construction materials. The transfer of essential properties of plants to industrially feasible, porous construction materials should allow an optimal building physics involving frost resistance, thermal isolation and moisture transport to be obtained in heterogeneous porous structures.

In order to achieve this goal, several steps and basic considerations are necessary. In this section, basic strategies and structural properties of frost-resistant plants are presented. Furthermore, a modelling approach for freezing plant tissues based on the TPM is introduced, yielding the numerical simulations of three selected examples.

## 7.2 Freezing plant tissues

Controlled “ice management” during freezing has repeatedly been reported for plant tissues, with special porous structures being involved, often associated with xylem, cf., e.g., McCully *et al.* [200], Roden *et al.* [231] or Lenné *et al.* [181]. During freezing, the water potential of the water body decreases, leading to a net flux of as yet unfrozen water towards the freezing site, followed by the continuous formation of ice crystals. Plant tissue is composed of “apoplastic” and “symplastic” regions. The apoplast encompasses all spaces belonging to non-living parts of the plant, i.e. cell walls and intercellular spaces. The symplast includes all living parts, i.e. the living content of cells. Ice crystal formation within the symplast is a critical process, threatening the integrity of the living structures, and has to be avoided.

The phenomenon of decreasing water potential during freezing can be utilised by plants to redirect water towards special apoplastic “freezing sites”, while simultaneously dehydrating the symplast. This process has been repeatedly demonstrated. The first impressive demonstration dates back to the 19<sup>th</sup> century. Prillieux [220] (1869, cited by McCully *et al.* [200]) showed, in frost-tolerant herbaceous plants, that ice accumulates in the inter-

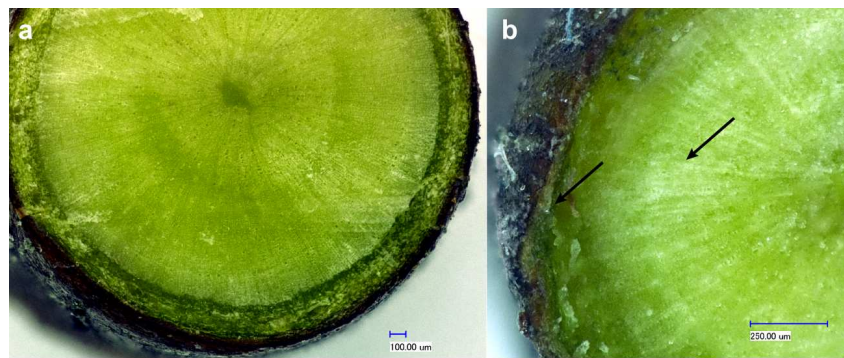


**Figure 7.2:** Cross section of a fresh and unfrozen stem of *Betula nana* in (a) and (b) twig of *Betula nana* in the frozen state. Ice is visible within the xylem and in “pockets” close to the bark (black arrows).

cellular spaces of petioles, whereas the living parenchyma dehydrates and is compacted to a much smaller volume. Upon thawing, the process is completely reversible. Another example is provided by the needles of frost-resistant pines. Here, water freezes within special sites that are prone to deformation, cf. Roden *et al.* [231].

Since the transport of heat and water are coupled in this process, the structure of the considered tissues should be essential, since it dictates the spatial conductances for both quantities. Therefore, these physical aspects of plant-tissue freezing are studied. However, physiological processes are often essential, particularly the adaption of cell membranes. In this regard, the interference with any metabolic processes is neglected here.

### 7.2.1 Stems and wood

Wood or xylem shows a strong degree of porous anisotropy, with the additional property of the absence of a living content in conduits. This also means the absence of osmotic processes that require cell membranes. Consequently, freezing in xylem conduits is comparable with freezing within capillaries: the ice front progresses along the longitudinal axis of the conduits with high velocity (Hacker & Neuner [135]). Additionally, ice nucleation starts normally in xylem conduits, because the ionic content is here much lower than the one in living cells. In this way, the xylem body freezes first, in a directed manner, along the longitudinal axis of the plant, while simultaneously dehydrating the surrounding living cells. Ice-filled conduits have been reported on various occasions, for example, by taking samples from winter wood and observing cross sections by cryo-scanning electron microscopy (cryo-SEM), cf. Utsumi *et al.* [272].

The dwarf birch *Betula nana* is a richly branched copse with a height around 60 cm. Its origin in arctic alpine regions makes it a good example of the freezing tolerance of woody stems. As an example of frozen regions, a cross section of a fresh *Betula nana* stem and a frozen one are prepared<sup>1</sup>, cf. Figure 7.2. The frozen parts, mostly in the bark and the xylem, can be determined visually. The mechanical importance of the intercellular spaces

<sup>1</sup>In the course of a collaboration with the State Museum of Natural History, Stuttgart, Germany. The experiments were examined under the supervision of PD Dr. rer. nat. A. Roth-Nebelsick.

as possible spaces for growing ice crystals becomes evident, since they allow ice formation without damaging living cells. These mechanisms need to be reversible every year.

Particularly frost-resistant is coniferous wood. Its structure differs from that of angiosperm wood by showing only tracheids. These are single cells that lack living content, are strongly elongated and have lignified cell walls. In conifers, the water-transporting capillaries are thus represented by single cells with a maximum length of several millimetres and a diameter of about 20  $\mu\text{m}$ . Another special property of coniferous tracheids is the structure of their pits, which are pores within the tracheid walls. They show a central thickened lens attached to an elastic spoke-like structure acting as valve when the pressure between two adjacent tracheids changes, for example, because of embolism. This special structure together with the narrow tracheids is viewed as a major element of the frost-resistance of coniferous wood. Upon thawing, air bubbles will be present in the water, as products of the freezing process. The small dimensions of the tracheids keep the bubble radii low, facilitating the dissolution of the air in the thawing water.

## 7.2.2 Leaves

Evergreen leaves and needles have to be frost resistant, for example, the leaves of *Buxus sempervirens* *Arborescens*. In contrast to the stem, leaves contain much less woody material and the assimilating cells have to be protected during the freezing process. Therefore, they undergo a special physical adaptation to frost during their normal aging process: the leaves begin to split internally, along their longitudinal axis, which is an irreversible process that provides space for ice crystals to grow. This physical adaptation was investigated by Hacker & Neuner [135] and Hatakeyama & Kato [139]. Observed from the outside, these leaves appear thicker and more inelastic during this ageing process. During ice formation, the expanding ice widens the split, a process that is reversible in the spring, upon thawing. Figure 7.3 shows a Cryo-SEM image of this crack in an older leaf of *Buxus sempervirens* *Arborescens*.  $\ll$ (p. 103)

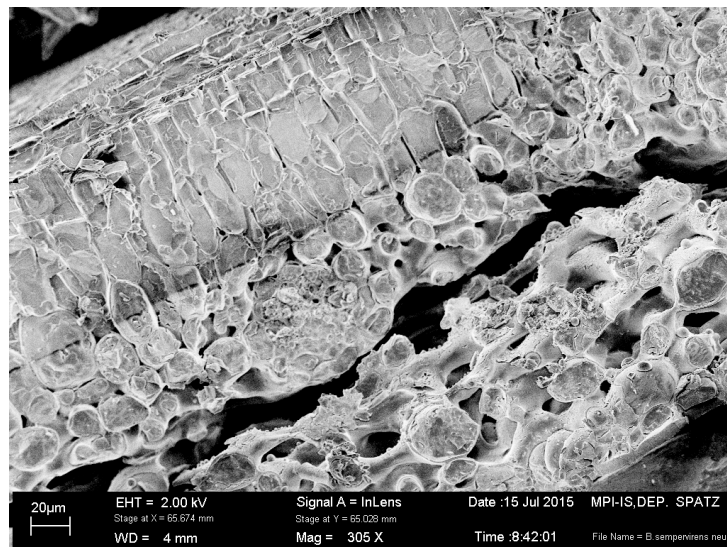


**Figure 7.3:** Cryo-SEM image of a leaf of the evergreen *Buxus sempervirens* *Arborescens*.

## 7.3 Modelling approach and constitutive settings

BIBLIOGRAPHIC NOTE: The content of this section is based on the following original article: Eurich, L., Wagner, A. & Ehlers, W.: Coupled mass interactions in plant tissues under frost conditions. *Proceedings in Applied Mathematics and Mechanics* **18** (2018), e201800143 [107].

### 7.3.1 Basic model setup

» Basically, the plant-tissue model is tailored to reveal relevant strategies when freezing occurs. One of the main characteristics of frost-resistant plant tissues is the dehydration of the tissue cells after an initial ice formation in the intercellular space. This has two consequences: Firstly, it leads to a lower ice nucleation temperature within the cells, which prevents them from freezing and, secondly, water is released to the intercellular space, which is, then, redirected towards locations of initial ice formation in the intercellular space. This is fairly uncritical in terms of survivability of the plant, cf. Schott *et al.* [240]. In conclusion, this section focuses on water transport, ice formation and cell dehydration and their coupling processes in plant tissues.

Based on previous works, cf. Eurich *et al.* [103, 104] and Eurich *et al.* [106], a triphasic, quaternary TPM model is introduced for the description of plant tissues, cf. Figure 7.4. On the microscopic (pore) scale, the model considers tissue cells  $\varphi^S$ , which are modelled

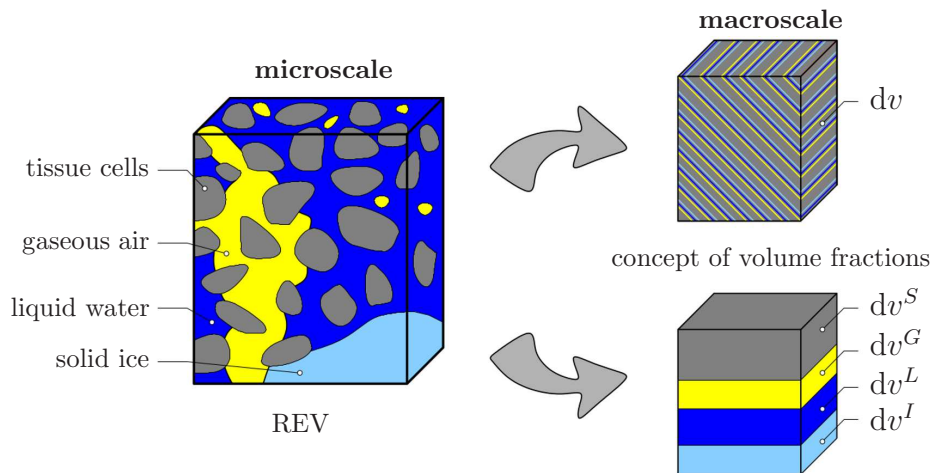


**Figure 7.4:** Representative elementary volume with exemplary displayed pore structure of plant tissue and quaternary TPM modelling approach.

as a thermoelastic solid, gaseous air  $\varphi^G$  and liquid water  $\varphi^L$  in the pore space, which may turn into ice  $\varphi^I$ , which is also modelled as a thermoelastic solid. These constituents are volumetrically averaged over an REV, such that the model consists on the macroscale of four superimposed and mutually interacting constituents  $\varphi^\alpha$ . The primary variables of the plant-tissue model are the solid displacement  $\mathbf{u}_S$ , the turgor pressure  $p^{FR}$ , the liquid saturation  $s^L$ , the solid volume fractions  $n^S$  and  $n^I$  as well as the temperature  $\theta$  of the overall aggregate, which are solved by the governing equations. These are, in the given

order, the momentum balance of the overall aggregate

$$\mathbf{0} = \operatorname{div} (\mathbf{T}^S + \mathbf{T}^G + \mathbf{T}^L + \mathbf{T}^I) + \rho \mathbf{g} - \hat{\rho}^L \mathbf{w}_L, \quad (7.1)$$

the mass balances of the overall aggregate, the liquid water, the solid skeleton and the ice

$$\begin{aligned} (\rho^S + \rho^G + \rho^L + \rho^I)'_S + \rho \operatorname{div} (\mathbf{u}_S)'_S + \operatorname{div} (\rho^L \mathbf{w}_L) + \operatorname{div} (\rho^G \mathbf{w}_G) &= 0, \\ (n^L)'_S \rho^{LR} + n^L (\rho^{LR})'_S + \operatorname{div} (\rho^L \mathbf{w}_L) + \rho^L \operatorname{div} (\mathbf{u}_S)'_S &= \hat{\rho}^L, \\ (n^S)'_S \rho^{SR} + n^S (\rho^{SR})'_S + \rho^S \operatorname{div} (\mathbf{u}_S)'_S &= \hat{\rho}^S, \\ (n^I)'_S \rho^{IR} + n^I (\rho^{IR})'_S + \rho^I \operatorname{div} (\mathbf{u}_S)'_S &= \hat{\rho}^I, \end{aligned} \quad (7.2)$$

as well as the energy balance of the overall aggregate

$$\sum_{\alpha} [\rho^{\alpha} (\varepsilon^{\alpha})'_\alpha - \mathbf{T}^{\alpha} \cdot \mathbf{L}_{\alpha} + \operatorname{div} \mathbf{q}^{\alpha} + \hat{\mathbf{p}}^{\alpha} \cdot \dot{\mathbf{x}}_{\alpha} + \hat{\rho}^{\alpha} \varepsilon^{\alpha}] = 0. \quad (7.3)$$

The above equations account for the case of sufficiently slow processes,  $\theta^{\alpha} = \theta$ ,  $\ddot{\mathbf{x}}_{\alpha} = \mathbf{0}$ ,  $\dot{\mathbf{x}}_{\alpha} \cdot \dot{\mathbf{x}}_{\alpha} \ll \varepsilon^{\alpha}$ , no mass mass interaction with the gaseous phase,  $\hat{\rho}^G = 0$ , gravitation  $\mathbf{b}^{\alpha} = \mathbf{g}$  and no radiation  $r^{\alpha} = 0$ . Furthermore, the solid skeleton, the ice and the liquid water are assumed to be materially incompressible, whereas the gas is considered as materially compressible.

### 7.3.2 Ice formation via interfacial mass interactions

Within the framework of the TPM, the phase transition of water is described as mass transfer across a singular surface  $\Gamma$ , which separates the pore space into a part, where liquid water is present, and a part, where water is present as (solid) ice. According to Ehlers & Häberle [87], this introduces jump conditions into the balance equations, viz.:

$$\begin{aligned} [[\rho^{\alpha} \mathbf{w}_{\alpha\Gamma}]] \cdot \mathbf{n}_{\Gamma} &= 0, \\ [[\rho^{\alpha} \dot{\mathbf{x}}_{\alpha} \otimes \mathbf{w}_{\alpha\Gamma} - \mathbf{T}^{\alpha}]] \mathbf{n}_{\Gamma} &= \mathbf{0}, \\ [[\rho^{\alpha} (\varepsilon^{\alpha} + \frac{1}{2} \dot{\mathbf{x}}_{\alpha} \cdot \dot{\mathbf{x}}_{\alpha}) \mathbf{w}_{\alpha\Gamma} - (\mathbf{T}^{\alpha})^T \dot{\mathbf{x}}_{\alpha} + \mathbf{q}^{\alpha}]] \cdot \mathbf{n}_{\Gamma} &= 0. \end{aligned} \quad (7.4)$$

Note that these relations with regard to mass, momentum and energy, respectively, hold only for the singular surface  $\mathbf{x} = \mathbf{x}_{\Gamma}$ . These jump conditions apply, in particular, to the water component, whereas the solid skeleton as well as the gaseous constituent are not affected by the phase transition at the singular surface. The application of (7.4) requires

$$\hat{\rho}_{\Gamma}^L + \hat{\rho}_{\Gamma}^I = 0 \quad \longrightarrow \quad \hat{\rho}^I = \hat{\rho}_{\Gamma}^L \frac{da_{\Gamma}}{dv} = \hat{\rho}_{\Gamma}^L a_{\Gamma}, \quad (7.5)$$

where the interfacial mass interactions

$$\hat{\rho}_{\Gamma}^L = \rho^L \mathbf{w}_{L\Gamma} \cdot \mathbf{n}_{\Gamma} \quad \text{and} \quad \hat{\rho}_{\Gamma}^I = -\rho^I \mathbf{w}_{I\Gamma} \cdot \mathbf{n}_{\Gamma} \quad (7.6)$$

are identified. Furthermore, the ratio  $a_\Gamma = da_\Gamma/dv$  in (7.5) describes the density of the internal phase-change surfaces with respect to the overall volume and can be, therefore, interpreted as a homogenisation. Note in passing that the volume-specific mass production of liquid water has two parts, the one originating from the phase transition at the singular surface and the other due to cell dehydration. The interfacial mass production  $\hat{\rho}_\Gamma^I$  (and using (7.5)<sub>1</sub> also  $\hat{\rho}_\Gamma^L$ ) are derived by making use of the energy jump of the water component, which leads to

$$\hat{\rho}_\Gamma^I = \frac{(\mathbf{q}^L - \mathbf{q}^I) \cdot \mathbf{n}_\Gamma - (\mathbf{T}^L \dot{\mathbf{x}}_L - \mathbf{T}^I \dot{\mathbf{x}}_S) \cdot \mathbf{n}_\Gamma}{(\zeta^L - \frac{p^{LR}}{\rho^{LR}} + \frac{1}{2} \dot{\mathbf{x}}_L \cdot \dot{\mathbf{x}}_L - \zeta^I + \frac{p^{IR}}{\rho^{IR}} - \frac{1}{2} \dot{\mathbf{x}}_S \cdot \dot{\mathbf{x}}_S)} \approx \frac{(\mathbf{q}^L - \mathbf{q}^I) \cdot \mathbf{n}_\Gamma}{\zeta^L - \zeta^I}. \quad (7.7)$$

Therein, the assumption has been made that thermal quantities dominate the phase transition process. The direction of the singular surface  $\mathbf{n}_\Gamma$  is given by the density gradient, which is in the present case also the temperature gradient, since the densities of the water component are a function of temperature only.

### 7.3.3 Cell dehydration

The cell dehydration represents a multiscale porosity feature of the plant tissue and is treated within the TPM as density production  $\hat{\rho}^S$  in the mass balance of the solid skeleton. The constraint

$$(\dots) - \hat{\rho}^S \left( \psi^S - \psi^L + \frac{p^{FR}}{\rho^{SR}} - \frac{p^{LR}}{\rho^{LR}} \right) \geq 0, \quad (7.8)$$

as a part of the entropy inequality, motivates a Darcy-like equation for the mass-production term for the thermodynamically irreversible process of the cell-wall perfusion, viz.:

$$\hat{\rho}^S = -n^S \frac{k^{\text{mem}}}{\mu^{LR}} \frac{\omega}{t} (\rho^{SR})^2 \left( \psi^S - \psi^L + \frac{p^{FR}}{\rho^{SR}} - \frac{p^{LR}}{\rho^{LR}} \right), \quad (7.9)$$

where  $k^{\text{mem}}$  is the permeability of the cell wall,  $\omega$  the specific surface through which the cell dehydrates with respect to the volume and  $t$  the thickness of the cell wall. Note, furthermore, that due to the fine porosity of the cell wall (in the nanometre range) the cell walls are suitable to stop a moving ice front and is preventing, thereby, the interior of the cells from freezing, cf. Schott *et al.* [240]. «(p.107)

## 7.4 Selected numerical examples

As the water-flow management was identified as one crucial factor for the frost resistance of plants, the first numerical example shows the basic water transport in a stem of a tree, and the second example discusses the water supply of a leaf. These two examples are simulated by a simplified continuum-mechanical model consisting of a single pore fluid without phase transitions within an anisotropic solid skeleton. In contrast, the third example, discussing a so-called winter horsetail, is simulated using the previously described model and shows the evolution of ice formation.

### 7.4.1 Basic water transport in a stem

BIBLIOGRAPHIC NOTE: The content of this section is based on the following original article: Eurich, L., Schott, R., Wagner, A., Roth-Nebelsick, A. & Ehlers, W.: *Fundamentals of Heat and Mass Transport in Frost-Resistant Plant Tissues*. In: Knippers J., Nickel K., Speck T. (eds): *Biomimetic Research for Architecture and Building Construction* 8 (2016), Springer, Cham, pp. 97–108 [104].

» The first example aims to describe the basic properties of water transport in a stem. The structure of such a stem is highly anisotropic. In particular, the permeability in the axial direction is significantly higher than in the transversal direction, as was described in the introduction of this chapter. In Figure 7.5, the simulation set-up including the boundary conditions and the resulting perfusion within the solid skeleton is sketched. The perfusion can be characterised by the seepage velocity of the liquid as the flow of the

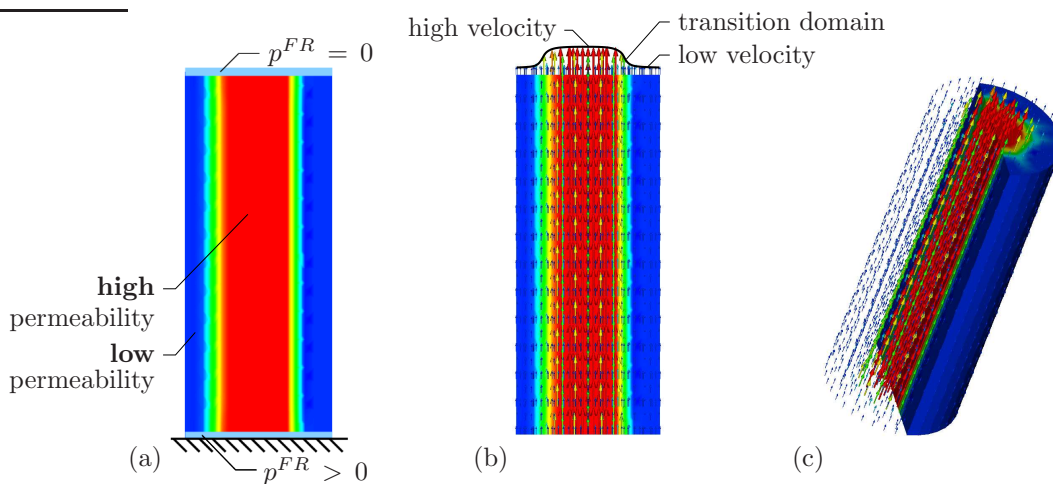


**Figure 7.5:** Problem description with axial permeability conditions in (a), (b) seepage velocity (vertical cut), large arrows indicate a high velocity, small arrows indicate a low velocity and (c) seepage velocity (3-dim. perspective).

liquid through the porous material. For the present model, a general Darcy-type equation using a second-order permeability tensor describes anisotropic perfusion conditions. The axial permeability indicates preferred directions via higher values in the centre of the stem and lower values in the bark, as is shown in Figure 7.5 (a). «(p. 110)

### 7.4.2 Water supply in a leaf

BIBLIOGRAPHIC NOTE: The content of this section is based on the following original article: Eurich, L., Schott, R., Wagner, A., Roth-Nebelsick, A. & Ehlers, W.: *Fundamentals of Heat and Mass Transport in Frost-Resistant Plant Tissues*. In: Knippers J., Nickel K., Speck T. (eds): *Biomimetic Research for Architecture and Building Construction* 8 (2016), Springer, Cham, pp. 97–108 [104].

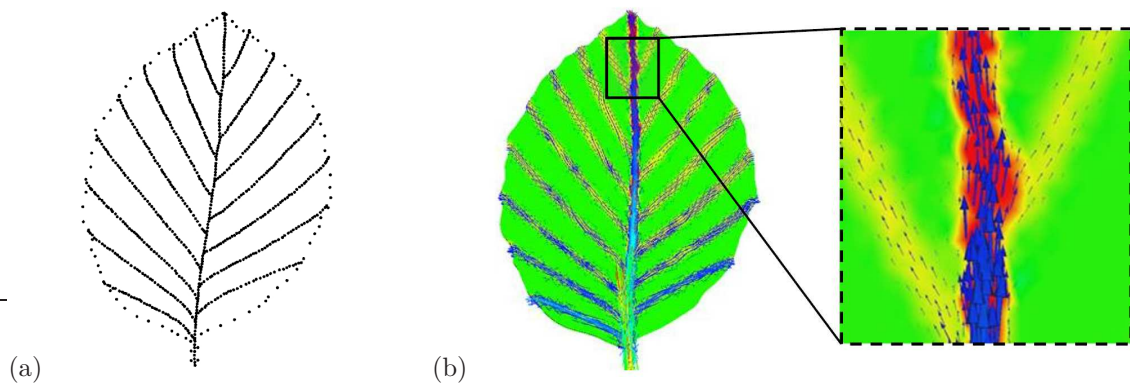


**Figure 7.6:** Shape of a leaf and regions of high permeability (black lines) in (a) and (b) simulation results of the seepage velocity (blue arrows).

» Using a spatially varying permeability, the water transport in a leaf can be simulated, which is schematically shown in this example. The permeability within the veins of a leaf is distinctly higher than that in the rest of the leaf. The actual allocation of the regions of high permeability is sketched in Figure 7.6 (a), where the surrounding curve represents the shape of a leaf, and the inner black lines the veins with a high permeability. At each Gauss point, the permeability is individually assigned, resulting in a locally varying permeability. Applying the boundary condition to the leaf, i. e. a pressure gradient from the stem to the distal end of the veins, the resulting flow in terms of seepage velocity is obtained, cf. Figure 7.6 (b). The arising seepage velocity field shows high perfusion within the main vein in the centre of the leaf, a moderate perfusion in the remaining veins and low perfusion everywhere else in the leaf. This is also reflected by the experimental findings for the corresponding flow within a leaf in which the pressure gradient is mainly caused by the evaporation of the liquid on its surface. «(p.111)

### 7.4.3 Ice nucleation in a winter horsetail

BIBLIOGRAPHIC NOTE: The content of this section is based on the following original article: Eurich, L., Wagner, A. & Ehlers, W.: *Modelling functional properties of frost-resistant plant tissues for transfer to construction materials*. In: von Scheven, M., Keip, M.-A. & Karajan, N. (eds): Proceedings of the 7<sup>th</sup> GACM Colloquium on Computational Mechanics 2017, Stuttgart, Germany, pp. 238–241 [105].

» At the example of the so-called winter horsetail, the coupled processes during ice formation are studied. The cross section has a characteristic shape, with a large gas-filled compartment in its centre and smaller gas bubbles distributed in the cross section. For an idealised cross section, the temperature distribution can be calculated, as shown in Figure 7.7, when a temperature drop on the outer surface is prescribed as during a frost experiment. As the temperature is in the gas-filled compartments for some time higher than in the surrounding tissue, water accumulates at the edges due to condensation of humidity in the air. As condensation is not included in the theoretical model, the simulation accounts for a simplified model, where a film of pure water is assumed to be initially

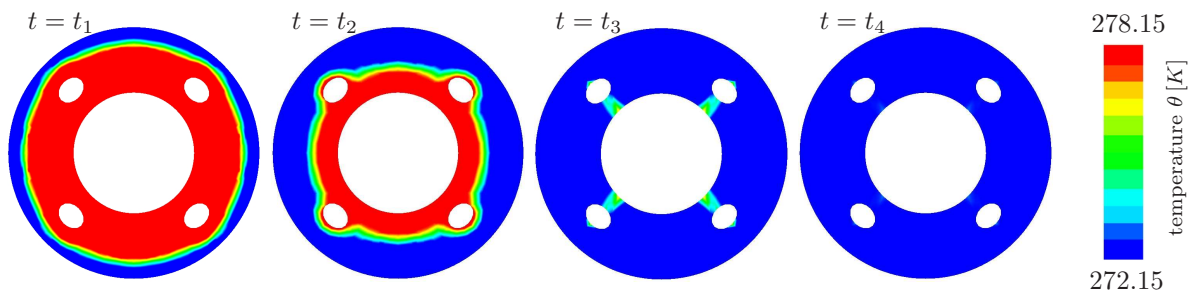


**Figure 7.7:** Temperature distribution in a winter horsetail cross section during a freezing experiment for selected time steps.

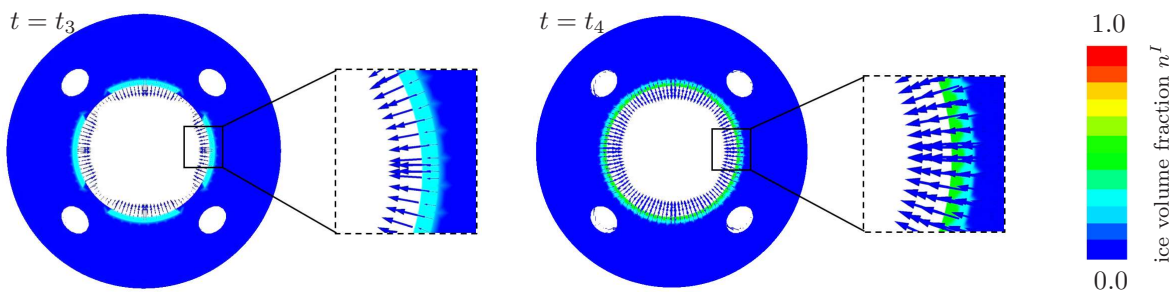


**Figure 7.8:** Evolution of the ice volume fraction  $n^I$  in a winter horsetail cross-section with resulting water efflux. Note that there is no ice formation during time steps  $t = t_1$  and  $t = t_2$ .

present at the inner edge, the gas constituent is assumed to be solely air. Therefore, when the temperature at the inner edge falls below the freezing point at  $273.15\text{ K}$ , the water starts to freeze, as shown in Figure 7.8. Note that the reduced ice nucleation temperature of the trapped water within the tissue is taken into account in the simulation. The ice formation at the inner edge leads, in turn, to a dehydration of the tissue cells, effectively caused by a decrease of the pressure head, as motivated in the preceding section. This example discusses the crucial factors with regard to frost hardiness of plant tissues with a focus on physical processes. The introduced TPM-based modelling approach enables a biologically motivated description of the coupled thermo-hygro-mechanical processes. The numerical example shows the dehydration of the cells due to ice formation on inner surfaces of the cross section and its effect on the water-flow management. The understanding in particular of the underlying physical processes of plant tissues with regard to frost hardiness is the first milestone for the development of smart construction materials in the future. <<(p.111)

# Chapter 8:

## Bone-cement injections into vertebra

BIBLIOGRAPHIC NOTE: The content of this section is based on the following original article: Bleiler, C., Wagner, A., Stadelmann, V., Windolf, M., Köstler, H., Boger, A., Gueorguiev-Rüegg, B., Ehlers, W. & Röhrle, O.: Multiphasic modelling of bone-cement injection into vertebral cancellous bone. *International Journal for Numerical Methods in Biomedical Engineering* **31** (2015), 37–57 [27].

### 8.1 Motivation and introduction

» In the last 25 years, percutaneous vertebroplasty has become one of the most important techniques for the stabilisation of osteoporotic vertebral compression fractures as well as other weakening lesions such as angioma or metastatic tumours. Within percutaneous vertebroplasty, the vertebral body is augmented with bone cement, i.e., by injecting polymethylmethacrylate (PMMA) through a percutaneous cannula, cf. Galibert *et al.* [116]. The injection of PMMA into vertebral bodies leads to an immediate pain relief in 80-90% of the patients, cf. Heini *et al.* [144]. However, this procedure also presents a significant risk through cement leakage, which is a common occurrence, cf. Laredo & Hamze [178]. Cement leakage from the vertebral body occurs in 20-65% of the cases (Heini *et al.* [144]). While most leakage is asymptomatic, serious complications can arise, if the cement causes pulmonary embolism or compressions of the nerve root or spinal cord (Laredo & Hamze [178]). Many biomechanical factors, e.g., the cement viscosity, injection pressure, injection rate, injected volume, consistency of the bone marrow and local tissue morphology, influence the process and, hence, administer cement leakage. In particular, the local tissue morphology representing the underlying bone architecture, the fracture pattern, and the bone marrow condition exhibit a high and often hard-to-predict variability of cement infiltration behaviour due to extreme anisotropic permeabilities.

Since Bohner *et al.* [37] and Baroud *et al.* [11] demonstrated the strong relationship between the uniformity of the filling pattern and the cement viscosity, the cement manufacturers expanded their efforts to develop high-viscosity cement and appropriate delivery systems aiming to stabilise cement flow. However, a clinical study using a commercially available high-viscous cement on sixty-six vertebrae indicated mild leakages in 39% of the cases (Georgy [120]), which is still higher than any other procedural complication rate, e.g., adjacent level fractures. The high leakage incidents stem from the fact that surgeons often administer high-viscosity cements by applying high injection forces, which exceed human physical limits and damage trabecular structures of the vertebral body. This may also lead to pulmonary embolism, if the broken trabeculae are extruded to the vascular system. Furthermore, mechanical stability restoring normal stiffness and strength of the vertebral body is only guaranteed through injecting a certain amount of cement. To restore pre-fractured strength and to avoid re-fracturing of the augmented vertebral body,

amounts greater than 25% of the cancellous bone region are required, cf. Sun & Liebschner [258]. For mechanical stability, one should further ensure that the cement filling reaches both endplates, cf. Chevalier *et al.* [62] or Hulme *et al.* [156].

Since there exists no procedure to pre-operatively predict cement distributions (Boger & Wheeler [36], Rafal *et al.* [221]), continuum-mechanically based software tools allowing surgeons to (i) pre-operatively investigate the cement distribution based on injection pressure and location and to (ii) analyse its resulting strength could significantly reduce the complication rate of cement leakage and the risk of refracturing and, hence, could dramatically improve the long term success of the procedure. Existing simulations of injecting PMMA into a vertebra consider the trabecular structure as porous but rigid. Deformations of the porous structure as well as the displacement of bone marrow are typically not considered. For example, Beaudoin *et al.* [22] modelled the cancellous bone as a bed of parallel capillaries, Lian *et al.* [182] used a branching-pipe geometrical model to simulate the injection based on the Hagen<sup>1</sup>-Poiseuille law, whereas Teo [264] applied the Darcy filter law. Micromechanically based simulations as performed, for example, by Zeiser *et al.* [298] or Kolmeder *et al.* [169] result in complex and computational intensive models limiting the simulations to small samples. Based on the Darcy filter law, Widmer and Ferguson [287] proposed a comprehensive model that considered the displacement of the bone marrow. None of the existing frameworks is currently capable of modelling the fluid flow and the mechanical loading of the solid structures simultaneously. This, however, appears necessary, if one wants to investigate the influence of injection pressure or rheological properties of bone cements on potential leakage risks and, at the same time, predict the mechanical behaviour of cancellous bone under load.

The major advantage of the TPM over existing approaches is the fact that one can not only predict the flow of the cement within an entire vertebra but also determine the stresses and strains resulting from the injection process. The stress and strain data can subsequently be used to predict breakage of trabecular structures, leakage, and its behaviour under load.

Within this work, the TPM allows to describe the entire process of bone-cement injection as a fully coupled mechanical problem of three interacting constituents: (i) the solid bone skeleton, (ii) the liquid bone cement, and (iii) the liquid bone marrow. The mechanical/rheological properties of cement and soft tissue were taken from the literature. The spatially varying, physiological, anisotropic permeability tensors were directly extracted from high-resolution  $\mu$ CT through image processing techniques. This is in contrast to previous studies, which obtained permeability values, for example, by using the Darcy filter law and inverse calculations of an experimentally measured pressure drop within trabecular bone specimen (e.g., Baroud *et al.* [12, 13], Beaudoin *et al.* [22], Cardoso *et al.* [53], Grimm & Williams [129], Kohles *et al.* [168], Nauman *et al.* [214], Ochia & Ching [218]), from numerical computations (e.g., Syahrom *et al.* [260], Zeiser *et al.* [298]), or from regression models (e.g., Teo *et al.* [265], Teo & Teoh [266], Widmer & Ferguson [288]). Based on the extracted permeability tensors, the governing equations of the multiphase model are solved to consistently model a two-pore liquid flow (bone cement and

---

<sup>1</sup>Gotthilf Heinrich Ludwig Hagen (1797–1884) was a German civil engineer who made important contributions to fluid dynamics, hydraulic engineering and probability theory [WIKIPEDIA].

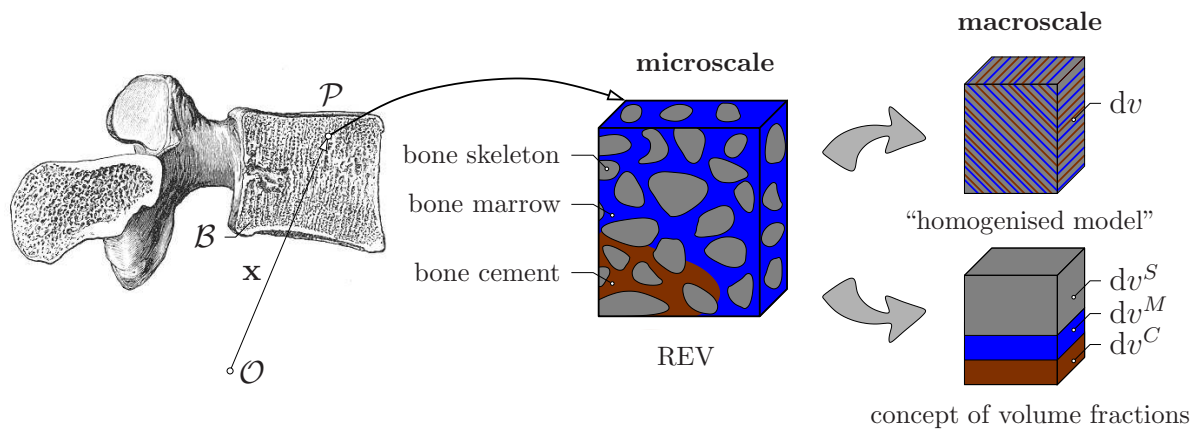


**Figure 8.1:** Representative elementary volume with exemplary displayed micro-structure of vertebra and macroscopic biphasic modelling approach.

marrow) through porous structures. The results are validated against experimental data of bone-cement spread after injection into a vertebra.

## 8.2 Modelling approach and constitutive settings

Although there is an enormous amount of highly resolved image data available, it is obvious that simulating the flow of cement within an entire vertebra using a fully resolved (segmented) model is computationally not feasible. In this regard, it is meaningful to utilise the TPM. Applying the modelling fundamentals of the TPM to the description of bone-cement injection processes into cancellous bone, the microscopic structure is homogenised and averaged over an REV, cf. Figure 8.1, where the superscripts  $S$ ,  $C$ , and  $M$  denote quantities linked to the solid skeleton, the bone cement, and the bone marrow, respectively. This yields a biphasic three-constituent model of superimposed and interacting continua, viz.:

$$\varphi = \bigcup_{\alpha} \varphi^{\alpha} = \varphi^S \cup \varphi^F = \varphi^S \cup \varphi^C \cup \varphi^M$$

$$\text{where } \begin{cases} \alpha = \{S, C, M\}, \\ \varphi^F = \bigcup_{\beta} \varphi^{\beta}, \beta = \{C, M\}. \end{cases} \quad (8.1)$$

In particular, it consists of a deformable solid bone skeleton  $\varphi^S$  and the overall fluid phase  $\varphi^F$ , constituting the pore-volume space. Initially, the pore volume is filled by the liquid bone marrow  $\varphi^M$  which may be replaced by the injected liquid bone cement  $\varphi^C$ . In this context the so-called effective saturation functions

$$s_{\text{eff}}^{\beta} = \frac{s^{\beta} - s_{\text{res}}^{\beta}}{1 - s_{\text{res}}^F} \quad \text{with} \quad s_{\text{res}}^F = \sum_{\beta} s_{\text{res}}^{\beta} \quad (8.2)$$

are introduced for the liquid constituents  $\varphi^{\beta}$ , cf. van Genuchten [119]. In (8.2),  $s_{\text{res}}^{\beta}$  are the residual saturations of the single constituents  $\varphi^{\beta}$  and  $s_{\text{res}}^F$  denotes the residual saturation of the overall fluid phase  $\varphi^F$ .

The set of governing equations for the continuum-mechanical model of bone-cement injection is obtained by combining the partial mass and momentum balances with the consideration of appropriate constitutive assumptions. In particular, these are quasi-static conditions ( $\ddot{\mathbf{x}}_\alpha = \mathbf{0}$ ), uniform body forces  $\mathbf{b}$ , isothermal conditions and vanishing mass exchange between the constituents. Moreover, with the assumption of material incompressibility of all constituents ( $\rho^{\alpha R} = \text{const.}$ ), the mass balances reduce to volume balances and the set of governing equations is given by the volume balances of the liquid constituents

$$0 = (n^\beta)'_S + \text{div}(n^\beta \mathbf{w}_\beta) + n^\beta \text{div}(\mathbf{u}_S)'_S \quad (8.3)$$

and the overall momentum balance

$$\mathbf{0} = \text{div} \mathbf{T} + \rho \mathbf{b}. \quad (8.4)$$

Therein, the overall Cauchy stress in (8.4) is given via

$$\mathbf{T} = \mathbf{T}_E^S - p \mathbf{I}, \quad (8.5)$$

where the solid extra stress  $\mathbf{T}_E^S$  is constituted by an isotropic finite Neo-Hookean elasticity law with a volumetric extension term contributing for the compaction point (cf. Ehlers & Eipper [85]), and an anisotropic (transversely isotropic) contribution (cf. Markert *et al.* [197]), viz.:

$$\begin{aligned} \mathbf{T}_E^S &= \mathbf{T}_{E, \text{iso}}^S + \mathbf{T}_{E, \text{aniso}}^S \quad \text{with} \\ \mathbf{T}_{E, \text{iso}}^S &= \frac{\mu^S}{J_S} (\mathbf{F}_S \mathbf{F}_S^T - \mathbf{I}) + \lambda^S (1 - n_{0S}^S)^2 \left( \frac{1}{1 - n_{0S}^S} - \frac{1}{J_S - n_{0S}^S} \right) \mathbf{I} \quad \text{and} \\ \mathbf{T}_{E, \text{aniso}}^S &= \frac{\tilde{\mu}^S}{J_S} I_4^{-1} (I_4^{\tilde{\gamma}^S/2} - 1) (\mathbf{a}^S \otimes \mathbf{a}^S). \end{aligned} \quad (8.6)$$

Therein,  $\mu^S$  and  $\lambda^S$  denote the Lamé constants,  $\mathbf{F}_S$  is the deformation gradient of the solid skeleton,  $J_S = \det \mathbf{F}_S$  is the Jacobian and  $n_{0S}^S$  is the initial solidity. The anisotropic part contains the mixed invariant  $I_4 = \text{tr}(\mathcal{M}^S \mathbf{C}_S) = \mathbf{a}^S \cdot \mathbf{a}^S$ , representing the squared stretch of the solid skeleton in the preferred direction  $\mathbf{a}^S = \mathbf{F}_S \mathbf{a}_0^S$  in the actual configuration, with the structural tensor  $\mathcal{M}^S = \mathbf{a}_0^S \otimes \mathbf{a}_0^S$  and the right Cauchy-Green deformation tensor  $\mathbf{C}_S$ . The unit vector  $\mathbf{a}_0^S$  denotes the preferred direction of the solid skeleton in the reference configuration. Furthermore,  $\tilde{\mu}^S$  and  $\tilde{\gamma}^S$  are material parameters governing the anisotropic behaviour. The hydrostatic overall pore pressure

$$p = p^{FR} = s^C p^{CR} + s^M p^{MR} \quad (8.7)$$

in (8.5) contains the effective pore pressures  $p^{\beta R}$  and reveals Dalton's law (Dalton [68]) but is investigated here through thermodynamical considerations via an evaluation of the entropy inequality. Moreover, the resulting stress of the solid skeleton  $\varphi^S$  is obtained by

$$\mathbf{T}^S = \mathbf{T}_E^S - n^S p \mathbf{I} \quad (8.8)$$

and the fluid stresses are given by

$$\mathbf{T}^\beta = -n^\beta p^{\beta R} \mathbf{I}. \quad (8.9)$$

In (8.9), the liquid viscous extra stress contributions are neglected in comparison to the local interaction forces between the constituents by arguments of dimensional analysis, cf. Ehlers *et al.* [86]. Further constitutive relations and thermodynamical considerations from the entropy principle combined with the momentum balances of  $\varphi^\beta$  yield the Darcy-like filter velocities  $n^\beta \mathbf{w}_\beta$  for the two pore liquids:

$$\begin{aligned} n^C \mathbf{w}_C &= -\frac{\kappa_r^C \mathbf{K}^S}{\mu^{CR}} (\text{grad } p^{CR} - \rho^{CR} \mathbf{b}), \\ n^M \mathbf{w}_M &= -\frac{\kappa_r^M \mathbf{K}^S}{\mu^{MR}} (\text{grad } p^{MR} - \rho^{MR} \mathbf{b} - \frac{p_{\text{dif.}}}{s^M} \text{grad } s^M). \end{aligned} \quad (8.10)$$

Therein,  $\mu^{\beta R}$  are the dynamic liquid viscosities,  $\kappa_r^\beta$  the relative permeability factors,  $p_{\text{dif.}} = p^{CR} - p^{MR}$  denotes the differential pressure and  $\mathbf{K}^S$  the intrinsic permeability of the solid bone skeleton. Finally, the solidity  $n^S = n_{0S}^S (\det \mathbf{F}_S)^{-1}$  is obtained by a formal integration of the solid's volume balance, while the overall volume fraction  $n^F = 1 - n_{0S}^S (\det \mathbf{F}_S)^{-1}$  of the liquid phase (denoting the porosity) results directly from the saturation condition. In this regard, the actual volume fractions  $n^\beta$  of the pore liquids are specified by a van Genuchten approach (cf. van Genuchten [119]), relating the differential pressure  $p_{\text{dif.}}$  to the effective saturation  $s_{\text{eff}}^M$  of the bone marrow via  $s_{\text{eff}}^M = [1 + (\alpha_{\text{gen}} p_{\text{dif.}})^{j_{\text{gen}}}]^{1/j_{\text{gen}}-1}$  with the parameters  $\alpha_{\text{gen}}$ ,  $j_{\text{gen}}$  (cf., e. g., Ehlers [80]). To summarise, the insertion of the relations (8.5), (8.6) and (8.7) in the overall momentum balance (8.4) as well as (8.10)<sub>1,2</sub> in the liquid volume balances (8.3) result in the governing set of equations related to the three primary unknowns solid displacement field  $\mathbf{u}_S$  and the effective pore-liquid pressures  $p^{\beta R}$ .

### 8.3 Material parameters

Using the data-based permeability estimation from  $\mu\text{CT}$ , cf. Section 4.2.1, the transformation from  $\alpha_i$  to  $\gamma_i$  is required to provide absolute values for the permeability. Here, the range of the permeability values is determined by the two parameters  $\gamma_{\text{max}}$  and  $\gamma_{\text{min}}$ . Table 8.1: Collection of intrinsic permeability values  $k^S$  of cancellous bone obtained from literature (mean  $\pm$  standard deviation).

related study	$k^S$ [ $\times 10^{-10} \text{ m}^2$ ]	orientation	specimen
Grimm & Williams [129]	$35.4 \pm 25.7$	medial-lateral	human calcaneus
Nauman <i>et al.</i> [214]	$80.5 \pm 47.5$	superior-inferior	human vertebra
	$35.9 \pm 19.0$	transverse	
Kohles <i>et al.</i> [168]	$4.65 \pm 3.5$	superior-inferior	bovine tibia
	$4.52 \pm 2.74$	anterior-posterior	
	$2.33 \pm 1.55$	medial-lateral	
Ochia & Ching [218]	$4.90 \pm 4.45$		human vertebra
Zeiser <i>et al.</i> [298]	505	superior-inferior	simulation (LBM)

Table 8.2: Material parameters for the numerical simulation of bone-cement injection.

symbol	value	unit	description/reference
$\rho^{SR}$	$1.8 \times 10^3$	[kg/m <sup>3</sup> ]	effective density of the bone skeleton [115]
$\rho^{CR}$	$1.2 \times 10^3$	[kg/m <sup>3</sup> ]	effective density of the bone cement [298]
$\rho^{MR}$	$1.06 \times 10^3$	[kg/m <sup>3</sup> ]	effective density of the bone marrow [286]
$\mu^{CR}$	200	[Ns/m <sup>2</sup> ]	dynamic viscosity of the considered bone cement [70]
$\mu^{MR}$	0.4	[Ns/m <sup>2</sup> ]	dynamic viscosity of (red) bone marrow [48]
$\mu_0^S$	$77 \times 10^6$	[N/m <sup>2</sup> ]	elastic Lamé constants [125]
$\lambda_0^S$	$110 \times 10^6$	[N/m <sup>2</sup> ]	(according to $E = 2.0 \times 10^{+8}$ N/m <sup>2</sup> ; $\nu = 0.3$ )
$\tilde{\mu}^S$	10	[Ns/m <sup>2</sup> ]	constants for the anisotropic material law
$\tilde{\gamma}^S$	2	[-]	(chosen in assumption of negligible solid strains)
$\alpha_{\text{gen}}$	$0.1 \times 10^{-3}$	[-]	parameters of the van Genuchten model (assumptions)
$j_{\text{gen}}$	3.2	[-]	
$n_{0S}^S$	0.15	[-]	initial solidity (evaluation of the $\mu$ CT dataset)
$n_{0S}^C$	0.05	[-]	initial volume fraction of the bone cement
$n_{0S}^M$	0.80	[-]	initial volume fraction of the bone marrow

The literature reports a wide range of measured data for the permeabilities of cancellous bone, cf. Table 8.1. The first four references in Table 8.1 refer to experimental investigations, while the last one is the outcome of a microscopic-based computer simulation, i. e., using the Lattice-Boltzmann method (LBM). Based on these values,  $\gamma_{\text{max}}$  is chosen as  $5 \times 10^{-9}$  m<sup>2</sup>. The lower bound,  $\gamma_{\text{min}}$ , is set to  $1 \times 10^{-13}$  m<sup>2</sup>. For the proof of robustness, a sensitivity analysis for these two parameters is carried out, cf. Section 8.5.5.

All the remaining material parameters for the TPM-model of bone-cement injection used within this work are given in Table 8.2.

## 8.4 Numerical treatment

### 8.4.1 Weak formulation of the governing equations

The numerical problem of the strongly coupled ternary model is treated by the consideration of weak formulations of the governing equations with the primary unknowns  $\mathbf{u}_S$  and  $p^{\beta R}$ , proceeded by discretisation approaches in the spatial and temporal space, cf., e. g., Ellsiepen [101]. Thus, the volume balances (8.3) are transformed to

$$0 = \int_{\Omega} [(n^{\beta})'_S + n^{\beta} \operatorname{div}(\mathbf{u}_S)'_S] \delta p^{\beta R} dv - \int_{\Omega} n^{\beta} \mathbf{w}_{\beta} \cdot \operatorname{grad} \delta p^{\beta R} dv + \int_{\Gamma_{v\beta}} \bar{v}^{\beta} \delta p^{\beta R} da \quad (8.11)$$

with the corresponding test functions  $\delta p^{\beta R}$  and the effluxes  $\bar{v}^{\beta} = n^{\beta} \mathbf{w}_{\beta} \cdot \mathbf{n}$  of the liquid volumes over the Neumann boundaries  $\Gamma_{v\beta}$ , where  $\mathbf{n}$  is the outward-oriented unit surface normal. Further, the spatial domain  $\Omega$  contains the overall aggregate  $\mathcal{B}$ . The weak

formulation of the overall momentum balance (8.4) reads

$$0 = \int_{\Omega} \mathbf{T} \cdot \text{grad } \delta \mathbf{u}_S \, dv - \int_{\Omega} \rho \mathbf{b} \cdot \delta \mathbf{u}_S \, dv - \int_{\Gamma_t} \bar{\mathbf{t}} \cdot \delta \mathbf{u}_S \, da \quad (8.12)$$

with the corresponding test function  $\delta \mathbf{u}_S$  and the external stress vector  $\bar{\mathbf{t}} = \mathbf{T} \mathbf{n}$  acting on the Neumann boundary  $\Gamma_t$ .

### 8.4.2 Geometrical modelling and numerical implementation

For stable numerical solutions of the coupled problem within a  $\mathbf{u}_S$ - $p^{CR}$ - $p^{MR}$ -formulation, the overall domain  $\Omega$  is spatially discretised using mixed finite elements (FE) with quadratic shape functions for the solid displacement  $\mathbf{u}_S$  and linear shape functions for the effective liquid pressures  $p^{\beta R}$ . Based on a manual segmentation process of the outer shape of the imaged vertebra, a three-dimensional FE mesh containing 5564 tetrahedral Taylor-Hood elements and 8553 nodes has been constructed with a refined mesh size around the injection site (highlighted in Figure 8.2 using a red colour). The numerical problem is implemented in the coupled FE solver PANDAS and a standard Galerkin method is applied with a simultaneous approximation of all primary variables. Further, the given differential-algebraic system of equations is solved in a monolithic manner with an implicit Euler scheme for the discretisation in the time domain.

The evaluation of the weak formulation requires the permeability tensors at the Gauss points. The respective permeability is obtained by taking the tensor data of the nearest voxel. The diffusive homogenisation process explained in Section 4.2.1 is employed to minimise the influence of specific voxel data on the choice of discretisation. This is the key advantage of the diffusive homogenisation process.

### 8.4.3 Boundary conditions

The boundary conditions for the numerical simulation are chosen in accordance to the experimental settings. The injection is modelled with a Dirichlet boundary condition by setting an excess pressure of  $p^C = 50 \text{ kN/m}^2$  for the bone cement at the injection site. The simulation time was set to 600 s, corresponding to the typical duration of vertebroplasty. The pressure of the bone marrow at the boundary of the vertebra was assigned to zero. Furthermore, to avoid the leakage of the two fluids through the modelled cannulae, the according cylindrical surface is imposed with a Neumann non-flow condition for both of the fluids. Considering a fully coupled, multiphasic model, boundary conditions have also to be set for the solid skeleton in the form of specified displacement or external forces. During the experimental vertebroplasty, there are no forces acting on the vertebral surface and the displacement of the bone skeleton is expected to be negligible at the outer surface of the vertebra. Therefore, a Dirichlet displacement boundary condition is assigned to the outer surface as described in Figure 8.2, where the applied boundary conditions for the FE simulation are illustrated.

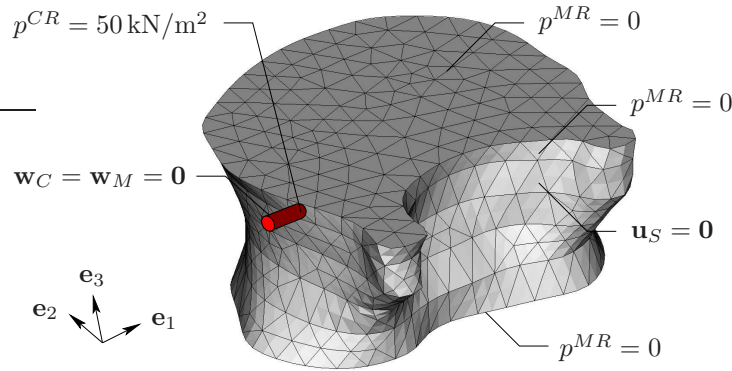


**Figure 8.2:** Geometrical model and boundary conditions for the FE simulation. The injection site is highlighted in red.

## 8.5 Results

The presented modelling framework of predicting cement flow within a porous structure includes the extraction of the anisotropic permeability tensor from image data and the solution of the governing equations of finite elasticity to consistently model a two pore-liquid flow through porous structures, and the validation of the simulations to experimentally acquired data. The results of extracting the permeability tensors are presented in Sections 8.5.1 and 8.5.2, the results of the FE model in Section 8.5.3 and quantitative validation results in Section 8.5.4.

### 8.5.1 Image homogenisation by diffusion

To minimise the influence of specific voxel data on the choice of the discretisation, a diffusion-based image-processing algorithm is applied. Figure 8.3 demonstrates the results of applying the diffusion-based smoothing algorithm to three selected image slices, which are chosen to coincide with the three main anatomical planes. In Figure 8.3, the original image data is placed on the left-hand side and the obtained smoothed data on the right-hand side demonstrating the suitability of the 3-dim. image-processing approach by Kluge [167] for homogenising the microscopic image data. The diffusion-based image processing transforms the original image data with binary image concentration values to an image with a larger range of image intensities and smoother transitions between image areas of formerly high or low intensity, i. e., bone matrix or pore space. Hence, the strict boundaries between the two possible intensities of the original image vanish and the differences of their gradients between adjacent voxels is reduced. These characteristics are essential for a continuum-mechanical modelling, where material parameters with macroscopic attributes are required due to a mismatch between the number of voxels and the necessary Gauss points for evaluating the weak formulation.

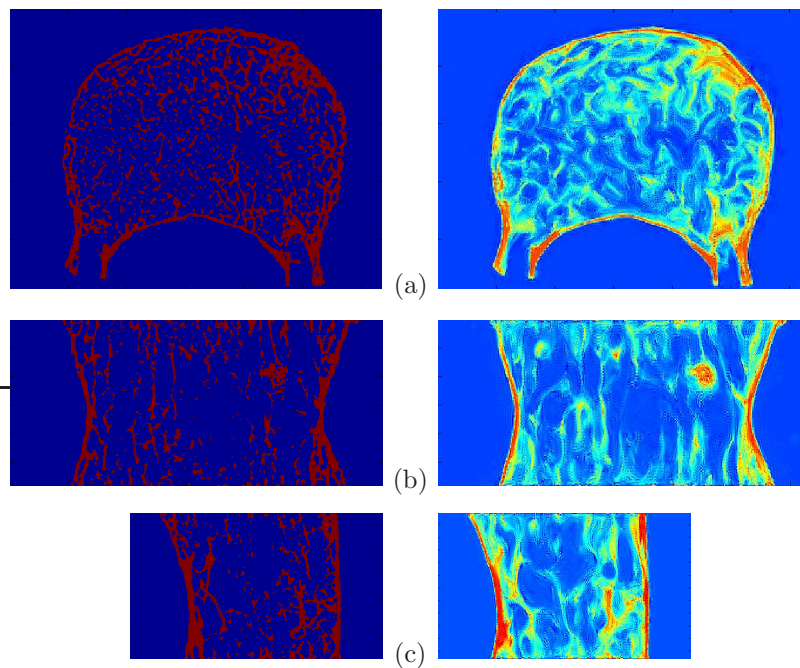


**Figure 8.3:** Comparison between the image intensities  $c$  of the original (left) and the smoothed (right) image data for a transverse (a), a coronal (b), and a sagittal (c) image slice.

### 8.5.2 Permeability field

Based on the homogenised image data, the respective permeabilities at the Gauss points are computed. The distribution of the anisotropic permeability data over the body  $\mathcal{B}$  provides a crucial influence on the fluid flow within the present simulations.

The Figures 8.4 and 8.5 present the six independent coefficients of the symmetric permeability tensor with respect to the global coordinate system for a transverse slice (Figure 8.4) and a coronal slice (Figure 8.5). Therein, the preferred direction of the trabecular structure in the superior-inferior direction, which is indicated by the subscript 33, can be clearly identified in the Figures 8.4 and 8.5 by investigating the magnitude of the permeability tensor coefficient  $K_{33}^S$ . In contrast, small permeability tensor coefficients present areas of high flow resistance, e. g., of the surrounding cortical shell of the bone (cf.  $K_{11}^S$  in Figure 8.4).

### 8.5.3 Finite-element simulation

**Bone-cement spreading:** The main goal of the executed numerical simulation is the prediction of the bone-cement spreading caused by the applied injection pressure. In the present continuum-mechanical modelling, this is identified by changes of the cement volume fraction  $n^C$ . Since the volume fraction of the solid constituent is found to be approximately constant ( $n^S \approx n_{0S}^S$ ), the cement spreading is expressed by the actual effective bone-marrow saturation  $s_{\text{eff}}^M$ , indicating its portion within the pore volume.

Figure 8.6 shows the temporal change of the effective saturation  $s_{\text{eff}}^M$  for a coronal slice at the injection site. In the 3-dim. plots of Figure 8.7, the change of the effective bone-

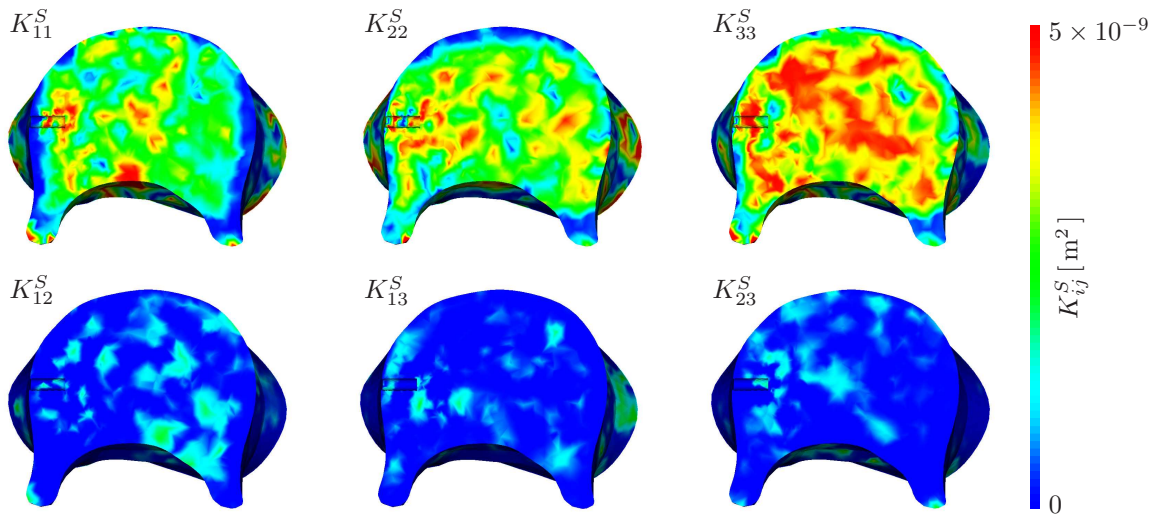


**Figure 8.4:** Illustration of the coefficients of the intrinsic permeability tensor  $\mathbf{K}^S$  in a transversal slice at the injection site.

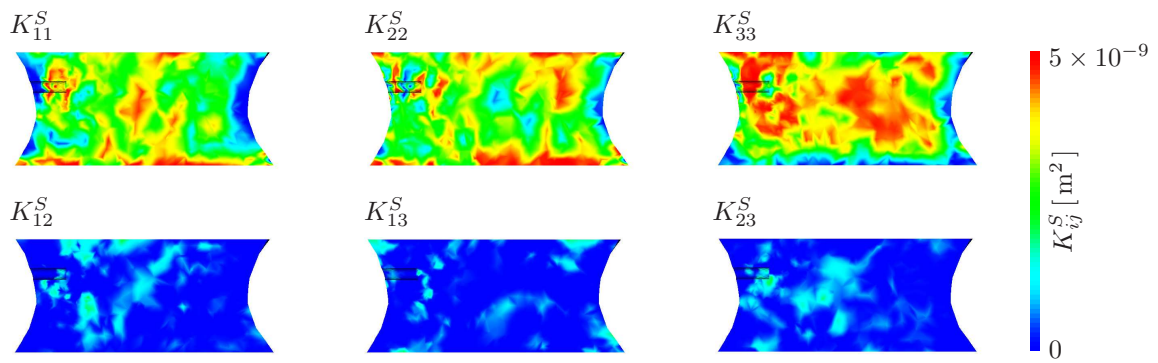


**Figure 8.5:** Illustration of the coefficients of the intrinsic permeability tensor  $\mathbf{K}^S$  in a coronal slice at the injection site.

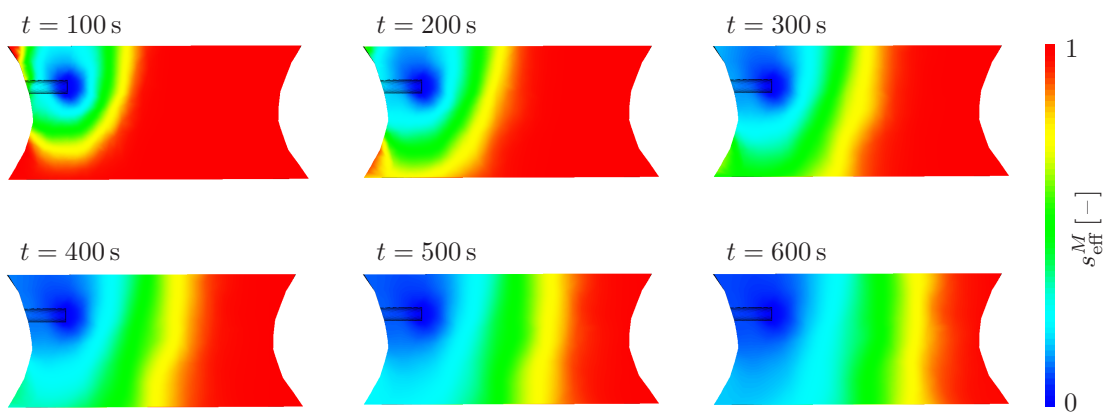


**Figure 8.6:** Illustration of the effective bone-marrow saturation  $s_{\text{eff}}^M$  for different time steps in a coronal slice at the injection site.

marrow saturation  $s_{\text{eff}}^M$  is illustrated by isosurfaces. The isosurfaces are chosen in such a way that they indicate the propagation front of the bone cement.

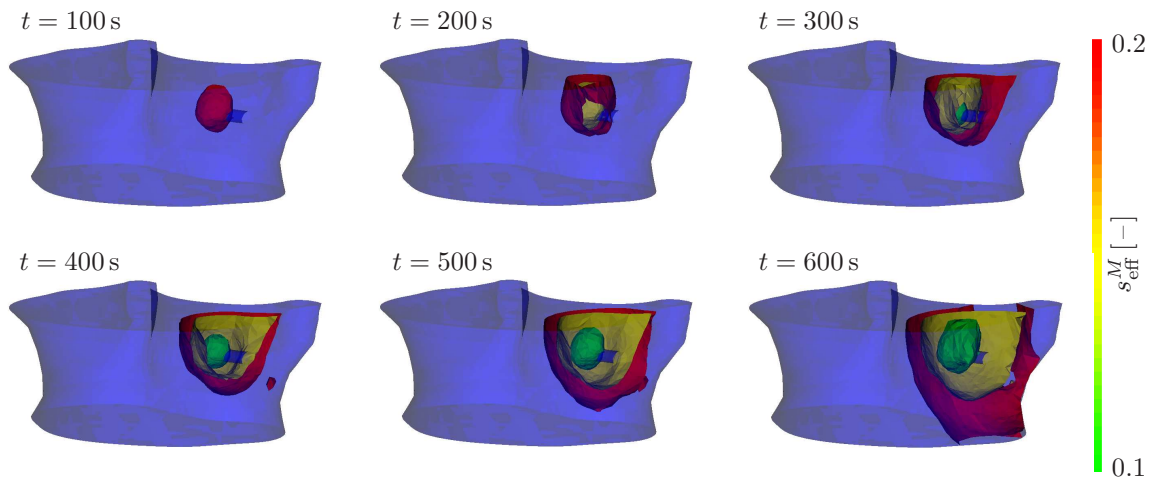


**Figure 8.7:** Illustration of the effective bone-marrow saturation  $s_{\text{eff}}^M$  for different time steps, indicating the bone cement spreading and displacement of the bone marrow.

**Stress and displacement distribution of the bone skeleton:** The multiphasic FE simulation does not only account for the flow of the two pore fluids but also considers the resulting stresses, strains, and deformations of the solid trabecular structure. Under the applied boundary conditions in this study, the stresses were found to be very low. The overall maximum von Mises equivalent stress  $\sigma_v^S$  based on the Cauchy stress  $\mathbf{T}^S$  is found to approximately  $3.6 \times 10^4 \text{ N/m}^2$ . Figure 8.8 illustrates the stress field for characteristic time steps. As a result of the relatively low stress values, the strains and displacement

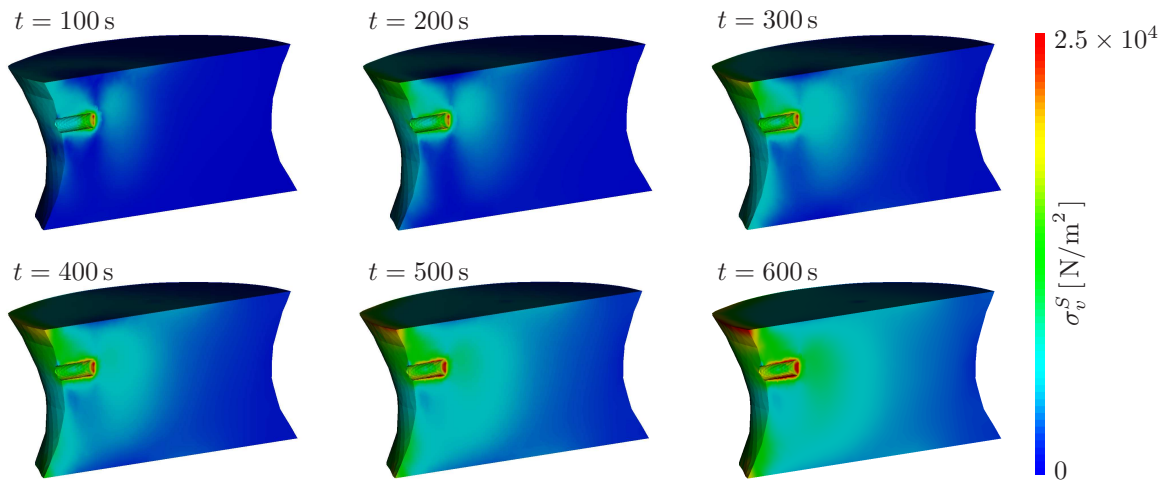


**Figure 8.8:** Illustration of the von Mises equivalent stress  $\sigma_v^S$  based on the solid Cauchy stress  $\mathbf{T}^S$  for different time steps in a coronal slice at the injection site.

of the solid skeleton are of negligible magnitude. The overall maximum absolute value of the displacement vector field  $\mathbf{u}_S$  is in the range of  $10^{-8} \text{ m}$ . Hence, the volume fraction of the solid skeleton is found to be nearly constant, resulting in  $n^S \approx n_{0S}^S$  for the actual volume fraction of the solid phase  $\varphi^S$ .

### 8.5.4 Validation

For a validation of the numerical prediction of bone cement spreading, the obtained results are compared to experimental data. The qualitative comparison between the simulated results and the experiments can be seen for a transversal, coronal, and sagittal slice through the injection site in Figure 8.9. Therein, the distribution of the bone cement after the injection of 6 ml is denoted by the white bulks on the left-hand side images of the experimental results. The Figures 8.9(b), (d), (f) show the isosurfaces of the effective bone-marrow saturation  $s_{\text{eff}}^M$  in corresponding views to compare the experimental and numerical results.

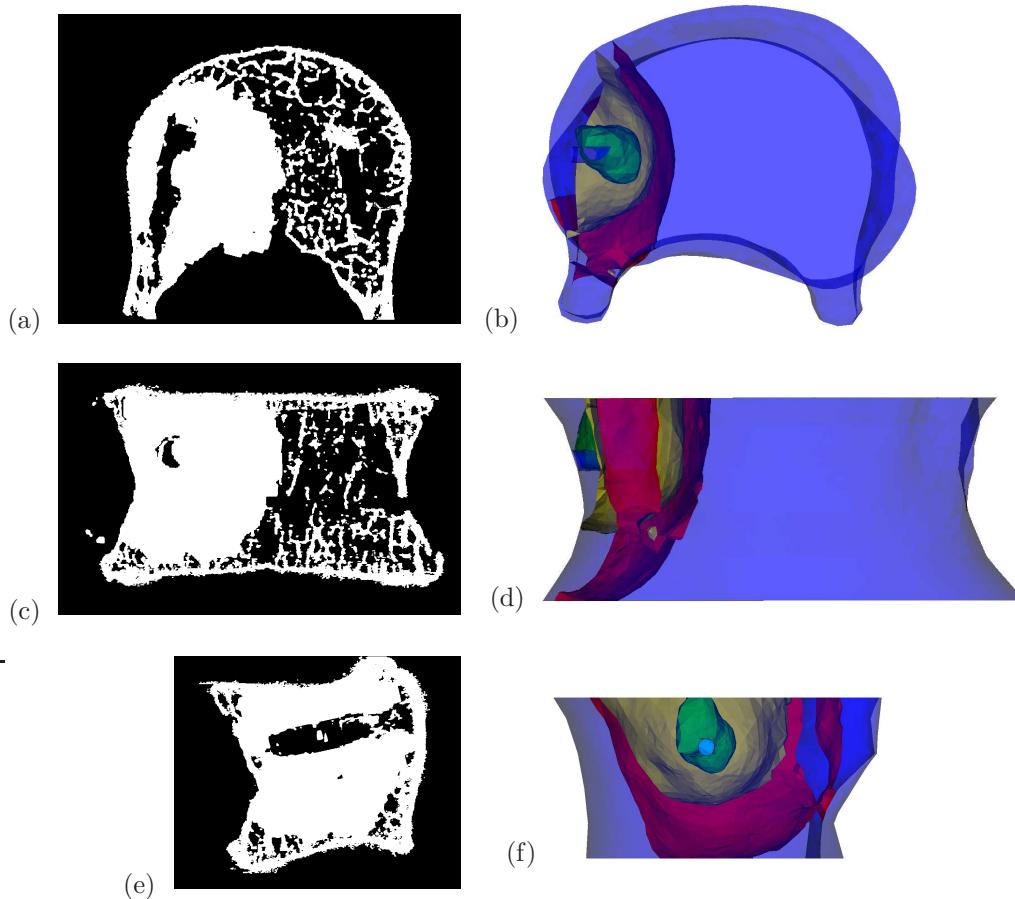


**Figure 8.9:** Comparison between (a) a transversal, (c) a coronal, and (e) a sagittal image slice of the CT data set containing the results of the experimental bone cement spreading by the AO Research Institute and (b), (d), (f) plots of the corresponding directions with the isosurfaces of the effective bone-marrow saturation  $s_{\text{eff}}^M$  (cf. Figure 8.7) of the numerical simulation. On the experimental images on the left hand side, the white bulk indicates the bone cement after the injection of an overall amount of 6 ml. The slices are placed at the injection site.

### 8.5.5 Sensitivity analysis

The permeability is the crucial input to our method predicting the spreading of bone cement using the TPM. Therefore, a sensitivity analysis with respect to the two parameters  $\gamma_{\min}$  and  $\gamma_{\max}$  is carried out. Simulations appealing to various different combinations of these two parameters shall provide some further insights in how these parameters influence the results of the FE analysis and how robust the proposed method is.

The choice of parameter  $\gamma_{\min}$  exhibits very little influence on the overall results, e. g., variations of  $\gamma_{\min}$  in the ranges of  $\pm 100\%$  do not alter the simulation results. This is in contrast to parameter  $\gamma_{\max}$ . Figure 8.10 presents the influence of  $\gamma_{\max}$  on the effective bone-cement saturation  $s_{\text{eff}}^C$  at a representative point  $A$  within the vertebra. The point  $A$  is located 0.005 m in  $\mathbf{e}_1$ -direction from the injection site. Varying  $\gamma_{\max}$  by  $\pm 10\%$  entails a total change of about  $\pm 10\%$  in the propagation speed of the bone-cement spreading. The propagation speed is here defined as the required time of reaching the value  $s_{\text{eff}}^C = 0.5$  at the point  $A$ . Furthermore, it is noteworthy to mention that the simulations produce stable results for the entire range of tested parameter combinations, i. e. the method seems to be quite robust for a large variation of parameters describing the permeability.

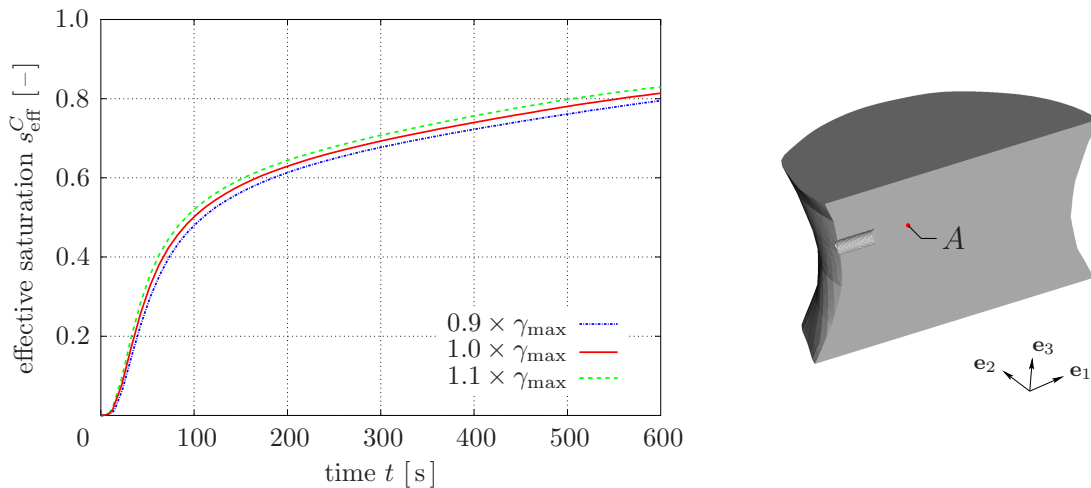


**Figure 8.10:** Sensitivity study for the effective bone-cement saturation  $s_{\text{eff}}^C$  at point  $A$  for different values of  $\gamma_{\max}$ . The point  $A$  is located 0.005 m in  $\mathbf{e}_1$ -direction from the injection site.

## 8.6 Discussion

Although exemplified on a clinically non-relevant case, e. g., on a healthy L1-vertebra that has been imaged within a  $\mu\text{CT}$  scanner, the presented framework has great potential to be further developed into a clinical or general tool to train young or less experienced surgeons, to investigate and design novel cement mixtures with specific properties, to investigate and test surgical equipment, to predict biomechanical implications of cement injection on adjacent tissue, e. g., adjacent vertebrae or intervertebral discs, or to provide guidelines for optimal injection pressures for patients classified according to general osteoporotic

markers/indicators. Moreover, if better imaging modalities or if more reliable relationships between regular CT image data quality and  $\mu$ CT image data become available, the presented tool can be further extended to a surgical planning tool. However, before testing the clinical applicability of such a tool, several further development stages are necessary. After acquiring the required image data, the entire workflow, i. e., the generation of the geometrical model including the FE meshing, the extraction of permeability tensors from image data, the set-up of the mechanical problem and its solution process, needs to be fully automated. Only very few material parameters and boundary conditions, e. g., the injection location or injection pressure, should be allowed as input parameters. Further, rheological properties and validated constitutive laws of the respective bone cement need to be stored within a database such that the medical personnel can either easily select the bone cement of his/her choice or that he/she might obtain statistics on the effectiveness of a particular bone cement choice based on a particular subject's mechanical bone structure.

The choice and the extraction of the permeability tensors from image data also needs further consideration. The extraction of anisotropic permeability tensors from high-resolution CT images is, as demonstrated, feasible. A sensitivity analysis demonstrated that the parameter  $\gamma_{\max}$  is the most important parameter for the permeability tensor estimation. Nevertheless,  $\gamma_{\max}$  influences the simulations in a consistent manner (cf. Figure 8.10). As the permeability tensors have been pre-computed based on the images and externally stored within a file, any other methodology to determine the anisotropic permeability tensors, e. g., computationally or experimentally, can be utilised as well for the flow simulations within this framework. The permeability tensor data is read from the file when needed during the set-up phase of the mechanical model. Especially when aiming to obtain patient-specific permeability data, reliable procedures based on clinical imaging tools (cf., e. g., Widmer & Ferguson [288], Zhang *et al.* [299]) are required since the resolution of  $\mu$ CT is not (yet) available for in vivo measurements.

The overall simulation results and the experimental study of bone cement flow show good agreement in the sense that in both settings the cement preferably flows in the superior-inferior direction and covers large portions of the superior end plate of the vertebra. Existing differences can potentially be attributed to the choice of material parameters, i. e., the material parameters and material laws for the bone, cement and bone marrow, and the choice of the absolute permeability values. Additional experiments under idealised and isolated conditions are necessary to determine and validate the respective material parameters and absolute permeability values since their choice can significantly influence the numerical results. The permeability values reported in the literature substantially vary for a vertebra or cancellous bone in general. They differ up to two orders in magnitude, cf. Nauman *et al.* [214] or Kohles *et al.* [168] for overviews. Despite the large variations in the reported permeability values, the comparison of the experiment and the simulations demonstrate that reasonable values and assumptions have been made. Similar arguments hold for the bone marrow. Material characterisation of bone marrow is extremely challenging and highly subject dependent and established literature values do not exist. However, the proposed choice for the bone marrow parameters does not negatively influence our simulations.

Although the spreading within the results of the multiphasic FE simulation demonstrates good overall comparability with the presented experimental data, further validation experiments have to be carried out in order to make necessary improvements of the modelling assumptions and include them in the presented approach. For example, the viscosity of the bone cement has been assumed to be constant. This assumption seems reasonable as bone cement manufacturers aim to develop cements that maintain their viscosity throughout the injection period. Further experimental studies have to demonstrate if this assumption is a valid approximation, or if non-Newtonian fluid behaviour has to be considered in the respecting material law of the TPM model.

The fact that the presented fully-coupled multiphasic model is capable to show the stress and displacement distribution within the solid bone skeleton during the injection process is a major advantage and the key difference to former studies on this topic. Although the simulations in this work yielded negligible magnitudes for the results of the solid phase, the arising solid stresses during vertebroplasty are of great interest within the testing of new bone cements. Especially high-viscosity cements require high injection pressures which might result in failure of the trabecular structure. This becomes particularly relevant since this high pressures may require injection forces that exceed the physical limits of humans. In such cases, cement deliverable devices capable of generating high pressures are used to generate the necessary forces. The major drawback of this method is that the person administering the cement loses the tactile feedback of simple syringe systems. The lack of feedback can cause unreasonable high stresses within the vertebra and, hence, increase the risk that trabecular structures crack. For such cases in which significant solid stresses and strains occur, the presented model could be optimised through a further investigation of suitable material parameters of bone tissue in the context of anisotropy. Until now, a transverse-isotropic material law for fibre-reinforced materials is used. Hence, additional reflections in this field should consider appropriate formulations of anisotropic elasticity (e. g., Itskov & Aksel [160], Zysset [303]) and material parameters (e. g., Rincón-Kohli & Zysset [230]) for the material modelling of bone. Furthermore, the preferred direction of the trabecular bone structure is derived as a consequence of the anisotropic permeability computation, but can be computed and included in the model through any other approach (e. g., Kersh *et al.* [165], Reisinger *et al.* [224]).

The advantage of the framework, in particular, the fact that multiple constituents can be simultaneously considered and simulated comes with computational cost. The total execution time for simulating the injection of bone cement, i. e., determining the permeabilities and solving the mechanical model, amounts to about 12 hours on a standard desktop PC. Using a parallel implementation and an optimised routine for reading in the computed permeability tensors could significantly reduce its overall cost. However, even if a large amount of processors is available, real-time solutions are not yet achievable without sacrificing any model complexity such as simulating the vertebra as a multiphasic material. If one is willing to invest even more computational resources, the proposed framework can also be further extended. There exist no modelling inherent restrictions. If needed, the TPM can be extended to include other effects such as thermal effects, processes leading to the curing of the cement, or the prediction of fractures. Within the application of vertebroplasty, fractures are of particular interest. If the strength of the

augmented vertebra is not brought to the pre-fractured level, than (re-)fractures are quite common. However, by using methods developed in fracture mechanics (e.g., Ehlers & Luo [89, 90], Gross & Seelig [131], Linder & Raina [184], Linder & Zhang [185], Rempfer [225]) and appropriate yield criteria for bone tissue (e.g., Doblaré *et al.* [73], Wolfram *et al.* [292]), one can simulate the potential fracture risk of an augmented vertebra as well as the occurrence of cracks during the bone-cement injection itself. Damages in the trabecular bone structure even occur in the first stage of the injection process, namely during the insertion of the injection needle, cf. Teoh & Chui [267]. Thoughts have to be made if this should be included in the simulation process, since it may influence the permeability around the area, causing, e.g., backflow at the needle. Further, one could easily extend the model of a single vertebra to a section of the spinal column including the intervertebral disc and other surrounding soft tissues like ligaments or skeletal muscle tissue. In particular, considering actively contracting skeletal muscle models, either as continuum-mechanical skeletal muscle models (e.g., Blemker *et al.* [28], Röhrle & Pullan [233]), chemo-electromechanical skeletal muscle models (e.g., Heidlauf & Röhrle [143], Röhrle *et al.* [232]), or Hill-type skeletal muscle models within multi-body dynamical simulations (e.g., Günther & Schmitt [132], Pandy [219]), provide valuable insights into the dynamic loading conditions during specific movement tasks. By doing so, dynamic loading conditions allow investigations, e.g., through a stress or strain analysis on how an augmentation effects neighbouring tissues. Considering dynamic loading conditions within the proposed framework would provide extremely valuable and desirable indications on long-term implications and are only available through simulations.

In summary, the development stages of this modelling approach can be in general attributed to aspects that directly relate to clinical aspects, to the challenge of determining (subject-specific) material properties, and to various aspects of validation. Nevertheless, this work proposes key advantages by applying a multiphasic modelling approach in the well-founded framework of the TPM, i.e., computing within a strongly coupled continuum-mechanical model the deformations and stresses of an entire vertebra while considering the flow of the injected bone cement and the resulting displacement of bone marrow. <<(p. 113)

# Chapter 9:

## Tumour treatment within brain tissue

### 9.1 Motivation and introduction

Without doubt, a healthy brain with proper functionality of its assigned tasks is crucial for an undisturbed life of human beings. In injured situations, a clinical procedure is often unavoidable. The applied clinical investigations are mainly based on experience (obtained from clinical routines/studies). However, the underlying processes during a medical treatment are often not fully understood. In this regard, modelling and simulation techniques for brain tissue intend to foster the understanding and to enhance the treatment success. In recent years, significant contributions are made in brain mechanics applied to neurosurgery, cf., e. g., Goriely *et al.* [127], Kyriacou *et al.* [177], Miller [202]. In addition, experiments on brain-tissue samples to characterise the material behaviour are realised, cf., e. g., Budday *et al.* [49, 50], Franceschini *et al.* [111], Miller [201]. However, brain-tissue modelling remains challenging due to the complex structure of the entire brain as well as the complex microscopic composition of the nervous tissue. Moreover, for many clinical applications it is necessary to account for the coupled behaviour of multiple included constituents (e. g. cells, interstitial fluid or blood) using multi-X (multiscale, multiphysics, multidata, etc.) approaches.

Based on elementary works (Ehlers & Wagner [93], Wagner [277]), selected aspects of multiphase brain-tissue modelling are discussed in this chapter. In particular, this includes the influence and optimisation of (multiple) catheter placement for a direct therapeutic infusion within tumour treatment, multiscale aspects to consider lower-scale effects on the tissue scale, the application of model-reduction techniques to reduce the computation time and the simulation of tumour-growth processes within brain tissue.

### 9.2 Anatomy of the human brain

**BIBLIOGRAPHIC NOTE:** The content of the sections 9.2 and 9.3 is based on the original article: Ehlers, W. & Wagner, A.: Multiscale aspects in the multiphase modelling of human brain tissue. In Wriggers P., Lenarz T. (eds): *Biomedical Technology. Lecture Notes in Applied and Computational Mechanics* **84**, Springer, Cham 2018, pp. 3–13 [95].

» Amongst other things, brain tissue includes the components interstitial fluid and blood, which are mobile in two basically separated pore compartments. In this regard, the interstitial fluid is situated within the interstitial fluid space, whereas the intravascular space contains the blood. Moreover, further tissue spaces are commonly distinguished, such as the intra- and extracellular space or the extravascular space, cf. Wagner [277]. In general, the highly selective capillary membrane (wall) governs the passing of molecules

from the intravascular to the extravascular space, known as the so-called blood-brain barrier. The interstitial fluid typically occupies a volume fraction of 20% of the brain's bulk volume, cf. Syková & Nicholson [261]. However, a variation between 15% and 30% is normal and even may fall to 5% during global ischaemia. Typical values of the blood volume fraction are in the range of approximately 3% for healthy tissues, cf. Syková & Nicholson [261] based on, e.g., Jain [161]. In contrast, in tumour-affected domains, the blood amount may vary between 1% and 20%.

### 9.3 Modelling approach for brain tissues

Tracing in the direction of real applications, it is reasonable to describe the tissue on a macroscopic scale in a comprehensive manner using continuum-mechanical models. In this regard, multi-component and multi-physical approaches are united in the framework of the well-known TPM. The basis of the macroscopic thermodynamically consistent drug-infusion model is briefly described in this section. For a detailed discussion of the brain-tissue model with a wide range of applications, the interested reader is referred to basic work by Ehlers & Wagner [92, 93], Wagner & Ehlers [279], Wagner [277] and citations therein. Basically, the quaternary TPM model basically includes four constituents. In particular, three immiscible constituents are given by the solid skeleton  $\varphi^S$ , the blood  $\varphi^B$  and the overall interstitial fluid  $\varphi^I$ , where  $\varphi^I$  contains a dissolved miscible therapeutic solute  $\varphi^D$ . The local composition of the aggregate is described by the volume fractions  $n^\alpha$ . Assuming fully saturated conditions (no vacant space within the domain), the well-known saturation condition  $\sum_\alpha n^\alpha = n^S + n^B + n^I = 1$  is obtained. As was already mentioned, the pore liquids are mobile in their individual pore compartments. Therefore, the volumetric amount (saturation) of the blood  $s^B = 1 - s^I = n^B/(1 - n^S)$  is specified in relation to the overall pore space (porosity). The set of model equations proceeds from the specific balance relations for multiphasic materials, cf., e.g., Ehlers [80, 81], where preliminary assumptions are initially included, i.e. isothermal conditions, materially incompressible constituents, common gravitational forces and acceleration terms. Therefore, the governing balance relations are given by the momentum balance (9.1)<sub>1</sub> of the overall aggregate  $\varphi$ , the volume balance (9.1)<sub>2</sub> of  $\varphi^B$ , the volume balance (9.1)<sub>3</sub> of  $\varphi^I$  and the concentration balance (9.1)<sub>4</sub> of  $\varphi^D$ , viz.:

$$\begin{aligned}
 \operatorname{div} \mathbf{T} + \rho \mathbf{b} &= \mathbf{0}, \\
 (n^B)'_S + \operatorname{div}(n^B \mathbf{w}_B) + n^B \operatorname{div}(\mathbf{u}_S)'_S &= 0, \\
 (n^I)'_S + \operatorname{div}(n^I \mathbf{w}_I) + n^I \operatorname{div}(\mathbf{u}_S)'_S &= 0, \\
 n^I (c_m^D)'_S + c_m^D \operatorname{div}(\mathbf{u}_S)'_S + \operatorname{div}(n^I c_m^D \mathbf{w}_D) + c_m^D \operatorname{div}(n^B \mathbf{w}_B) &= 0.
 \end{aligned} \tag{9.1}$$

Therein, the overall Cauchy stress

$$\mathbf{T} = \mathbf{T}_E^S - (s^B p^{BR} + s^I p^{IR}) \mathbf{I}, \quad \text{where} \quad \mathbf{T}_E^S = \mathbf{T}_{E, \text{iso}}^S + \mathbf{T}_{E, \text{aniso}}^S$$

$$\text{with} \quad \begin{cases} \mathbf{T}_{E, \text{iso}}^S &= 2 \frac{\mu_0^S}{J_S} \mathbf{K}_S + \lambda_0^S (1 - n_{0S}^S)^2 \left( \frac{1}{1 - n_{0S}^S} - \frac{1}{J_S - n_{0S}^S} \right) \mathbf{I}, \\ \mathbf{T}_{E, \text{aniso}}^S &= \frac{\tilde{\mu}_1^S}{J_S (\mathbf{a}_S \cdot \mathbf{a}_S)} \left( (\mathbf{a}_S \cdot \mathbf{a}_S)^{\tilde{\gamma}_1^S/2} - 1 \right) (\mathbf{a}_S \otimes \mathbf{a}_S), \end{cases} \quad (9.2)$$

consists of an isotropic and an anisotropic (transversely isotropic) part, where  $\mu_0^S, \lambda_0^S, \tilde{\mu}_1^S$  and  $\tilde{\gamma}_1^S$  denote material parameters. Basically, the constitutive description (9.2) enables for the consideration of finite and anisotropic deformation processes, as was described in Ehlers & Wagner [93]. In this regard, the structural composition of brain tissue, in particular the embedded myelinated nervous fibres, has a significant influence on the local anisotropic perfusion behaviour within white-matter domains. However, the question about their anisotropic mechanical contribution is not finally answered yet. Therefore, we basically provide the possibility to include an anisotropic material behaviour but choose low values for the parameters  $\tilde{\mu}_1^S$  and  $\tilde{\gamma}_1^S$  (governing the fibre stiffness) in the numerical examples. The notion  $(\cdot)'_S$  indicates the material time derivative with respect to the solid motion. In terms of the volume fractions and their temporal changes

$$\begin{aligned} n^S &= n_{0S}^S (\det \mathbf{F}_S)^{-1} & \text{and} & \quad (n^S)'_S = -n^S \operatorname{div}(\mathbf{u}_S)'_S, \\ n^B &= s^B (1 - n^S) & \text{and} & \quad (n^B)'_S = (s^B)'_S (1 - n^S) - s^B (n^S)'_S, \\ n^I &= 1 - n^S - n^B & \text{and} & \quad (n^I)'_S = -(n^S)'_S - (n^B)'_S, \end{aligned} \quad (9.3)$$

it turns out that a constitutive relation for the blood's saturation  $s^B$  is required, since the saturation condition is not sufficient to determine all volume fractions. Note in passing that the temporal change  $(s^B)'_S$  is based on the chosen constitutive ansatz for  $s^B$ , cf. Section 9.5.4. In Equation (9.3), the quantity  $n_{0S}^S$  denotes the initial solid volume fraction and  $\det \mathbf{F}_S$  is the determinant of the solid's deformation gradient  $\mathbf{F}_S = \mathbf{I} + \operatorname{Grad}_S \mathbf{u}_S$ . Therein, the operator  $\operatorname{Grad}_S$  denotes the material gradient of  $\varphi^S$  with respect to its reference position. Finally, the set of equations in (9.1) contains the seepage velocities  $\mathbf{w}_B, \mathbf{w}_I$  and  $\mathbf{w}_D$  which are described via

$$\begin{aligned} n^B \mathbf{w}_B &= -\frac{\mathbf{K}^{SB}}{\mu^{BR}} (\operatorname{grad} p^{BR} + \frac{p^{\text{dif}}}{s^B} \operatorname{grad} s^B - \rho^{BR} \mathbf{b}), \\ n^I \mathbf{w}_I &= -\frac{\mathbf{K}^{SI}}{\mu^{IR}} (\operatorname{grad} p^{IR} - \rho^{IR} \mathbf{b}), \\ n^I c_m^D \mathbf{w}_D &= -\mathbf{D}^D \operatorname{grad} c_m^D + n^I c_m^D \mathbf{w}_I. \end{aligned} \quad (9.4)$$

The perfusion of the solid skeleton by the mobile but separated pore liquids is considered by the permeability tensors  $\mathbf{K}^{SB}$  and  $\mathbf{K}^{SI}$ , whereas  $\mathbf{D}^D$  is the diffusivity of the therapeutic agent. The anisotropic permeability properties of the brain tissue are considered by a spatial diversification of the permeability tensor coefficients obtained from diffusion-weighted

Magnetic Resonance Imaging (DTI), cf. Ehlers & Wagner [93], Wagner [277]. Moreover,  $\mu^{BR}$  and  $\mu^{IR}$  are the effective shear viscosities of the liquids. The pressure difference  $p_{\text{dif.}} = p^{BR} - p^{IR}$  indicates the difference between the individual pore-liquid pressures. Finally, the TPM model is solved for the primary variables solid displacement  $\mathbf{u}_S$ , effective pore-liquid pressures  $p^{BR}$ ,  $p^{IR}$  and therapeutic concentration  $c_m^D$  after inserting the constitutive relations into the set of equations given in (9.1). With regard to the corresponding numerical solution of the coupled system of partial differential equations, the Bubnov-Galerkin mixed FEM is applied using the research code PANDAS. Therefore, the strong formulations in (9.1) are transferred to weak formulations, using the corresponding test functions  $\delta \mathbf{u}_S$ ,  $\delta p^{BR}$ ,  $\delta p^{IR}$  and  $\delta c_m^D$ , yielding

$$\begin{aligned}
\mathcal{G}_{\mathbf{u}_S} &\equiv \int_{\Omega} \mathbf{T} \cdot \text{grad } \delta \mathbf{u}_S \, dv - \int_{\Omega} \rho \mathbf{b} \cdot \delta \mathbf{u}_S \, dv - \int_{\Gamma_N^{\bar{\mathbf{t}}}} \bar{\mathbf{t}} \cdot \delta \mathbf{u}_S \, da = 0, \\
\mathcal{G}_{p^{BR}} &\equiv \int_{\Omega} [(n^B)'_S + n^B \text{div}(\mathbf{u}_S)'_S] \delta p^{BR} \, dv - \\
&\quad - \int_{\Omega} n^B \mathbf{w}_B \cdot \text{grad } \delta p^{BR} \, dv + \int_{\Gamma_N^{\bar{v}^B}} \bar{v}^B \delta p^{BR} \, da = 0, \\
\mathcal{G}_{p^{IR}} &\equiv \int_{\Omega} [(n^I)'_S + n^I \text{div}(\mathbf{u}_S)'_S] \delta p^{IR} \, dv - \\
&\quad - \int_{\Omega} n^I \mathbf{w}_I \cdot \text{grad } \delta p^{IR} \, dv + \int_{\Gamma_N^{\bar{v}^I}} \bar{v}^I \delta p^{IR} \, da = 0, \\
\mathcal{G}_{c_m^D} &\equiv \int_{\Omega} [n^I (c_m^D)'_S + c_m^D \text{div}(\mathbf{u}_S)'_S + c_m^D \text{div}(n^B \mathbf{w}_B)] \delta c_m^D \, dv - \\
&\quad - \int_{\Omega} n^I c_m^D \mathbf{w}_D \cdot \text{grad } \delta c_m^D \, dv + \int_{\Gamma_N^{\bar{j}^D}} \bar{j}^D \delta c_m^D \, da = 0.
\end{aligned} \tag{9.5}$$

Therein, the stress vector  $\bar{\mathbf{t}} = \mathbf{T} \mathbf{n}$  is acting on the boundary of the overall aggregate, where  $\mathbf{n}$  is the outward-oriented unit surface normal vector. The liquid fluxes  $\bar{v}^B = n^B \mathbf{w}_B \cdot \mathbf{n}$  and  $\bar{v}^I = n^I \mathbf{w}_I \cdot \mathbf{n}$  denote the volumetrical efflux out of the domain and  $\bar{j}^D = n^I c_m^D \mathbf{w}_D \cdot \mathbf{n}$  is the molar efflux of the therapeutic agent. «(p. 129)

## 9.4 Numerical case studies for therapeutic infusions

A possible clinical option in brain-cancer therapies proceeds from a direct therapeutical infusion in the affected brain-tissue region via catheters. This procedure is called convection-enhanced drug delivery (CED), cf., e. g., Bobo *et al.* [30], Laske *et al.* [179], Morrison *et al.*

[210] and Voges *et al.* [276] for its application and Ding *et al.* [72], Raghavan *et al.* [222] and Vogelbaum [275] for a detailed review. During such a surgical intervention, small holes are drilled into the skull to provide a targeted placement of infusion catheters into the extravascular space of the brain tissue. The pressure gradient applied by external medical pumps induces an interstitial-fluid movement and, therewith, the distribution of administered therapeutic agents. In cases where the application site is deep in the skull (e.g. deeply situated glioblastoma multiforme), a long-lasting infusion is able to supply even widespread areas. However, this theoretically promising approach has not been established in today's brain-tumour therapy. This may be partly caused by the circumstance that the success of an intervention is still almost entirely dependent on the experience of the practising surgeon, since a reliable process prediction is challenging due to the highly complex multi-component composition of the brain tissue. However, a reliable simulation tool possesses the potential to contribute to the successful planning of a surgical intervention by providing useful supplementary process informations and may also help to avoid severe complications. A detailed discussion of a customised drug-infusion model and its subsequent numerical implementation can be found in Wagner [277]. In the following, a further discussion of the spatial and temporal distribution of infused therapeutics is given in terms of an optimal catheter placement and the usage of multiple catheters.

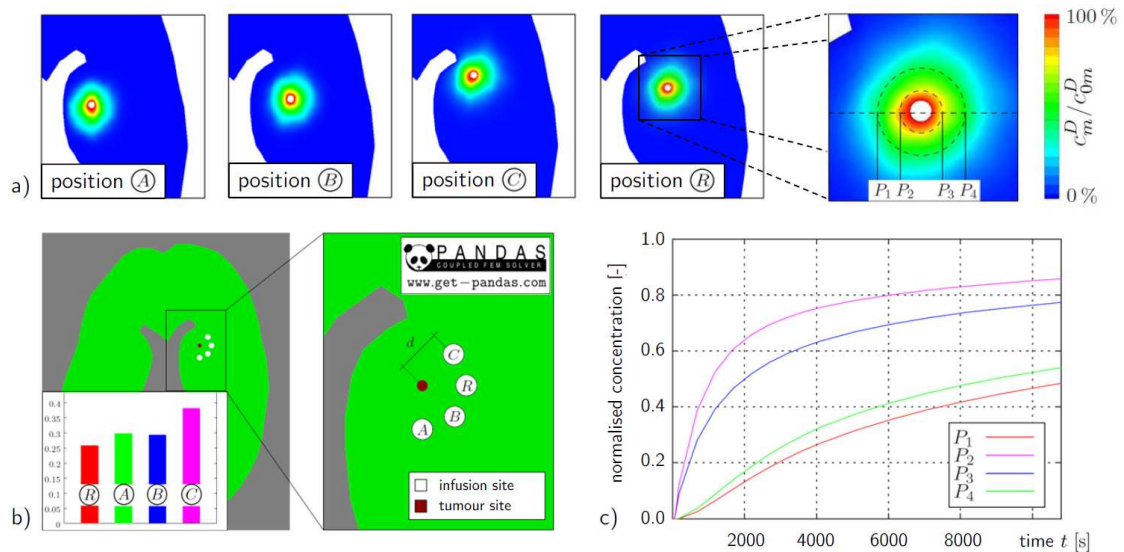


**Figure 9.1:** Resulting distribution profiles of therapeutics for different application sites (a) and (c) anisotropic spreading for case R at evaluated points  $P_1 - P_4$ . Case study (b) for the optimisation of the catheter placement to obtain the most efficient therapeutic impact at a tumour site.

BIBLIOGRAPHIC NOTE: The content of the sections 9.4.1 and 9.4.2 is based on the original article: Wagner, A. & Ehlers, W.: Theoretical and numerical aspects in the multiphasic modelling of human brain tissue. *Proceedings in Applied Mathematics and Mechanics* **15** (2015), 117–118 [280].

### 9.4.1 Influence and optimisation of the catheter placement

» It is obvious that a spatial variation (cf. positions  $A$ ,  $B$ ,  $C$  and  $R$  in Figure 9.1 a) of the application site leads, due to the underlying anisotropic permeabilities, to a change in the resulting distribution profile. In this regard, the evaluation of the therapeutic concentration at four distinct points  $P_1 - P_4$  for the catheter position  $R$  at mutually equidistant points ( $P_1$  and  $P_4$  as well as  $P_2$  and  $P_3$ ) clearly identifies the anisotropic spreading over time, cf. Figure 9.1 (c). In a numerical study, four equidistant catheter placements (with respect to a chosen tumour position) are compared with each other, cf. Figure 9.1 (b). In this example, the catheter position  $C$  proves to be best for an optimal supply. In general, such studies can provide a statement of most suited application sites ahead of the clinical intervention using numerical simulations to study the occurring processes. Note in passing that besides the desired spreading of therapeutic agents, several other coupled effects occur (e.g. deformation of the solid skeleton and interstitial fluid excess pressure), which need to be considered carefully.

### 9.4.2 Application of multiple infusion catheters

In order to obtain a more effective supply of therapeutics within the tumour-affected tissue, the usage of multiple catheters provides a further option. Starting from two infusion catheters, it is recognised that after an initial independent evolution of the concentration field an overlapping of the therapeutically supplied domains occurs. Additionally,

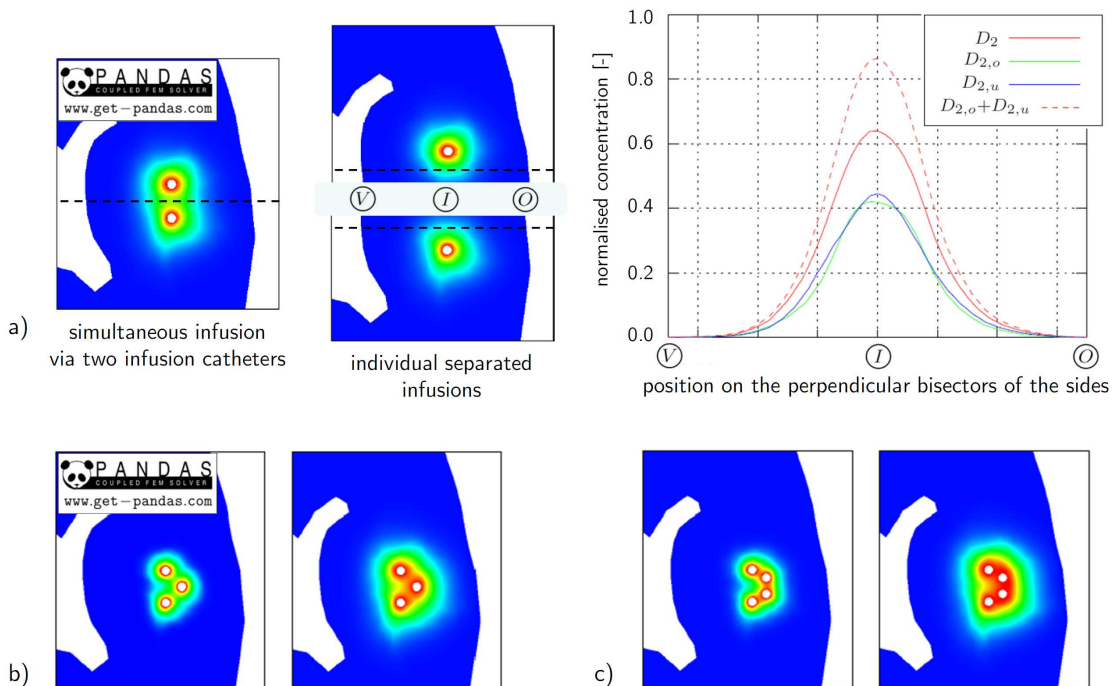


**Figure 9.2:** Study of the mutual interaction (a) during a simultaneous infusion via two catheters through a comparison with two individual infusions. Therapeutic distribution during the application using three (b) and four (c) catheters at different application time steps.

a comparison with two individually separated infusions is carried out. As expected, the infusion using a single catheter ( $D_{2,o}$  or  $D_{2,u}$ ) yields to a lower impact at the target  $I$  in between the two catheters (the small differences between the upper and the lower infusion are caused by the underlying anisotropy), cf. Figure 9.2 (a). The desired effect of a higher concentration in the middle of the two infusion sites is reached if a combined infusion via two infusion catheters ( $D_2$ ) is applied. However, this value is not that high as a simple adding ( $D_{2,o} + D_{2,u}$ ) of the values of two individual infusions and identifies a mutual interaction during the application via multiple catheters. Of course, even more than two catheters can be placed in order to increase the concentration level at the tumour site, cf. Figure 9.2 (b) and (c). Such considerations may be reasonable if the tumour-affected domain cannot be reached nearby or if the expected impact seems to be too low. <<(p.134)

## 9.5 Multiscale aspects for constitutive equations

BIBLIOGRAPHIC NOTE: The content of this section is based on the following original article: Ehlers, W. & Wagner, A.: Multiscale aspects in the multiphase modelling of human brain tissue. In Wriggers P., Lenarz T. (eds): *Biomedical Technology. Lecture Notes in Applied and Computational Mechanics* **84**, Springer, Cham 2018, pp. 3–13 [95].

### 9.5.1 Motivation

» The aim to simulate real applications on the length scale of centimetres to metres requests a macroscopic modelling. However, processes occurring on the complex microscale have a certain impact on the overall behaviour and need to be included. As was already mentioned, the basic TPM model for brain tissue includes two pore liquids. Therefore, a constitutive equation to describe the division for the volume fractions is required. Since there is still no general agreement concerning the stiffness of the blood-vessel system in comparison to the surrounding tissue aggregate (under physiological pressure conditions), the purpose of this section is the consideration of multiscale aspects. In this regard, a microscopic and locally singlephase computation of a representative elementary volume of the brain tissue aggregate is performed. This is realised using the commercial finite-element software tool **ABAQUS** and consequently allows for the assignment of microscopic material parameters for the individual components. In particular, elastically deformable blood vessels, separating the pore compartments, are assumed. Thus, the liquid with the higher pressure displaces the liquid with the lower pressure. The subsequent geometrical evaluation of certain adjusted pressure situations (applied as boundary conditions) within such a microscopic model allow for a meaningful postulation of a macroscopic constitutive equation. Note in passing that the presented study of scale-bridging aspects differs from a complete two-scale approach using the FE<sup>2</sup>-Method (where both the macroscopic as well as the underlying microscopic structure are analysed with the finite-element method, cf. Bartel *et al.* [16] in terms of the TPM). The scale-bridging approach proposed here rather proceeds from an one-time analysis of a specific process on the microstructure and a subsequent transfer to the macroscopic model obtaining a microscopically underlaid constitutive equation.

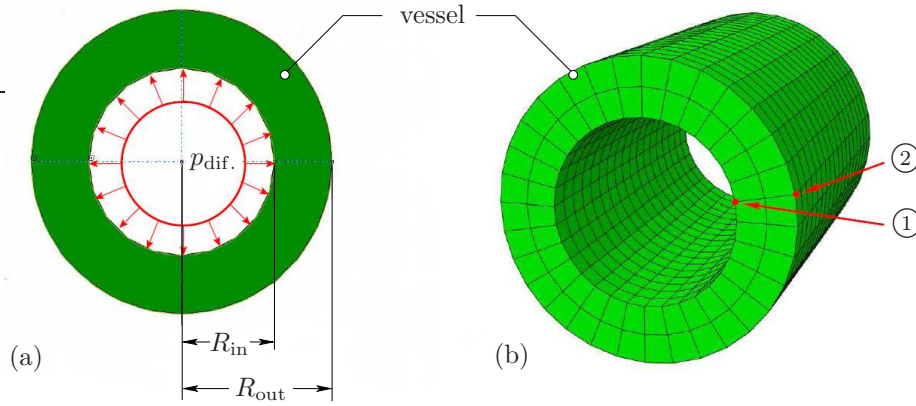


**Figure 9.3:** Boundary conditions for a single blood vessel in (a) and (b) meshed geometry with an exemplar point at the inside (1) and the outside (2) of the vessel, respectively.

### 9.5.2 Microscopic model settings

In terms of a microscopic description, a tube-like geometry is considered for the description of a single vascular vessel, cf. Figure 9.3. In order to apply a pressure difference between the inside and the outside of a blood vessel,  $p_{dif.} = p^{BR} - p^{IR}$  is subjected at the inside of the blood-vessel wall, cf. Figure 9.3 (a). For the sake of simplicity, a linear elastic material behaviour is chosen. The corresponding parameters are collected in Table 9.1.

Due to the elastically deformable blood vessels, the liquid with the higher pressure displaces the liquid with the lower pressure. In particular, three different cases are studied:

- case (i): “soft” vessel walls under unconstrained conditions,
- case (ii): “soft” vessel walls under constrained conditions and
- case (iii): “stiff” vessel walls under unconstrained conditions.

In these microscopic computations, the pressure difference is applied as a boundary condition and the arising volume changes are geometrically evaluated in a subsequent step. To bridge from the microscopic to the macroscopic scale, many single REV are arranged in a regular manner, cf. Figure 9.4. In this regard, the edge length of a single REV is chosen such that the initial saturation under zero pressure difference constitutes to  $s^B = 0.2$ . Physically, a variation of the volume fractions within a single REV requires an inflow (of the blood for a positive pressure difference) and an outflow (of the interstitial fluid for a positive pressure difference) of the liquids. This is provided by free-flow boundary conditions for both liquids in longitudinal direction of the chosen blood-vessel orientation.

### 9.5.3 Geometrical evaluation

Within Abaqus, the displacement of each node of the FE grid is obtained by the solution of the considered initial-boundary-value problems. Note in passing that an analytical solution for the widening of a linear-elastic cylindrical shell under constant internal pressure

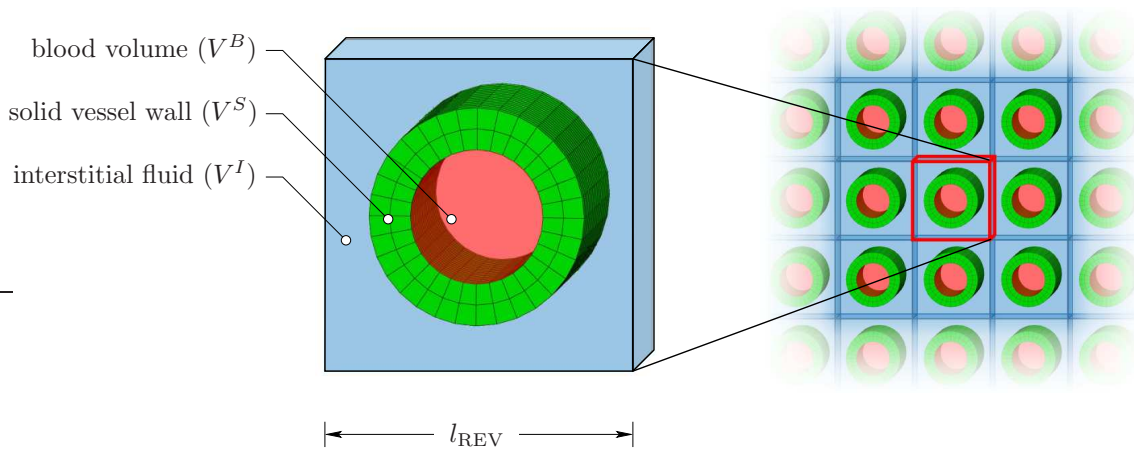


**Figure 9.4:** Exemplary sketch of the macroscopic overall aggregate composed of multiple REVs.

does exist, cf., e. g., Basar & Krätzig [17], and corresponds to an unconstrained microscopic computation. In a geometric evaluation, the deformation of the solid vessel wall can be captured by the displacements of the nodal points under loading conditions. However, the focus of this contribution lies on the evaluation of the liquid's saturations. In this regard, the geometrical evaluation of the arising volume fractions in the unconstrained cases (i) and (iii), cf. Figure 9.5 (a), is trivial, since the displacements of the nodes 1 (located at the inside of the vessel wall) and 2 (corresponding point in radial direction at the outside, cf. Figure 9.3) are known from the computation and allow for the determination using basic geometrical relations. In addition, the widening of a single vessel is at a certain state somehow constrained by the surrounding vessels, which themselves wide in a similar manner, as it is sketched in Figure 9.5 (b). This is approximated by a linear pathway in the contact domain and a circular shape in the edges. For the sake of simplicity, a constant thickness  $t$  of the blood vessel is assumed. Obviously, this represents a simplification, since (at least in the case of mutual contact) a deformation of the vessel wall may occur. However, this assumption allows a relatively simple evaluation of the arising volume fractions. Then, the volume fractions can be computed for the constrained

**Table 9.1:** Collection of parameters for a single blood vessel and an REV.

Quantity	Value	Reference/Remark
blood vessel inner radius $R_{\text{in}}$	$1.6 \times 10^{-4}$ m	Monson <i>et al.</i> [207]
blood vessel outer radius $R_{\text{out}}$	$2.6 \times 10^{-4}$ m	Monson <i>et al.</i> [207]
edge length $l_{\text{REV}}$ of a single REV	$7.3 \times 10^{-4}$ m	assumption to satisfy the initial (physiologic) condition $s^B = 0.2$
Poisson's ratio $\mu$	0.48	for the cases (i) – (iii), according to Carew <i>et al.</i> [54]
Young's modulus $E$	$2792$ N/m <sup>2</sup>	for the cases (i) and (ii), assumption of soft vessel walls
Young's modulus $E$	$1.2 \times 10^5$ N/m <sup>2</sup>	for case (iii), according to Hayashi <i>et al.</i> [141]

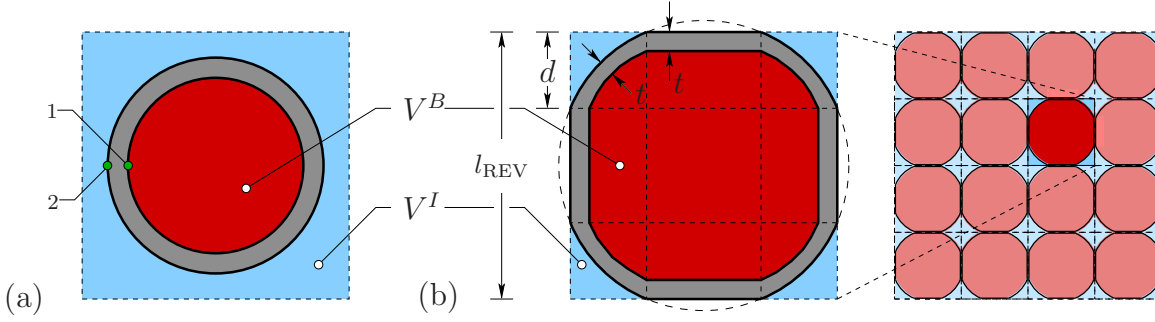


**Figure 9.5:** Unconstrained vessel widening within the REV in (a) and (b) constrained vessel deformation caused by interacting vessels.

case (ii), viz.:

$$\begin{aligned} V^B &= [\pi(d-t)^2 + 4(d-t)(l_{\text{REV}} - 2d) + (l_{\text{REV}} - 2d)^2] h_{\text{REV}}, \\ V^I &= (4d^2 - \pi d^2) h_{\text{REV}}. \end{aligned} \quad (9.6)$$

Therein,  $h_{\text{REV}}$  is the height of the REV required to compute a volume. However,  $h_{\text{REV}}$  vanishes within the determination of the liquid's volume fractions via

$$n^B = \frac{V^B}{V_{\text{REV}}} \quad \text{and} \quad n^I = \frac{V^I}{V_{\text{REV}}} \quad (9.7)$$

and, thus, has no influence. In conclusion, this allows for the evaluation of the liquid's saturations under applied pressure conditions. In particular, this is carried out for typical pressure states.

### 9.5.4 Macroscopic constitutive relation

The aim to simulate bio-technical/engineering applications of human brain tissues requires a thermodynamically consistent setting of the blood-saturation function in the context of the TPM model. This is somehow comparable to the procedure within unsaturated soil mechanics. Therein, the capillary pressure, defined as the difference between the pressures of the non-wetting and the wetting fluids in a common pore space is used to evaluate the saturations via capillary-pressure-saturation conditions, cf., e.g., Ricken & de Boer [228]. However, in the specific case of human brain tissue, the blood and the interstitial fluid are not situated in the same pore compartment such that these relations cannot be applied. Instead, further considerations are made here in order to specify the blood saturation, while bearing the microscopic considerations in mind. In general, the macroscopic constitutive equation should provide the flexibility to capture several circumstances. For the case of sufficiently soft elastic arterial walls, a mutually volumetrical interaction is induced by an upcoming pressure difference. Therefore, a constitutively chosen ansatz for the Helmholtz free energy  $\psi^B$  of the blood constituent is postulated according to Ehlers & Wagner [93], viz.:

$$\psi^B(s^B) = \frac{\tilde{\alpha}^B}{\rho^{BR}} ((\tilde{\beta}^B + 1) \ln(s^B) + \frac{1}{s^B} - \ln(1 - s^B)) + \tilde{\psi}_0^B. \quad (9.8)$$

Therein,  $\tilde{\alpha}^B$  and  $\tilde{\beta}^B$  denote material parameters, which allow via  $\tilde{\alpha}^B$  for the adaption of the pore-pressure difference to typical pressure values as they exist in the skull and for the initial blood saturation via  $\tilde{\beta}^B$ . Furthermore,  $\tilde{\psi}_0^B$  denotes the constant reference potential (standard state potential). This approach satisfies the thermodynamical restrictions and consequently yields a relation for the pressure difference

$$p_{\text{dif.}}(s^B) = s^B \rho^{BR} \frac{\partial \psi^B}{\partial s^B} = \tilde{\alpha}^B \left( \frac{1 - 2s^B}{s^B(s^B - 1)} + \tilde{\beta}^B \right), \quad (9.9)$$

$$\text{where } \frac{\partial \psi^B}{\partial s^B} = \frac{\tilde{\alpha}^B}{\rho^{BR}} \left( \frac{\tilde{\beta}^B}{s^B} - \frac{1}{s^B(s^B - 1)} - \frac{1}{(s^B)^2} \right).$$

The inversion of (9.9) finally leads to the blood saturation function

$$s^B(p_{\text{dif.}}) = \frac{1}{2 \left( \frac{p_{\text{dif.}}}{\tilde{\alpha}^B} - \tilde{\beta}^B \right)} \left( \left( \frac{p_{\text{dif.}}}{\tilde{\alpha}^B} - \tilde{\beta}^B - 2 \right) + \sqrt{4 + \left( \frac{p_{\text{dif.}}}{\tilde{\alpha}^B} - \tilde{\beta}^B \right)^2} \right). \quad (9.10)$$

It should be noted that Equation (9.10) is found by rational investigations of a meaningful inversion of (9.9), which is a second-order function in  $s^B$ . The derived relation for the blood saturation (9.10) allows for a proper determination of the volume fractions using the relations in (9.3). To give an example, an equation satisfying typical initial volume fractions of the brain tissue as well as typical pressure values as they exist in the skull is adapted by  $\tilde{\beta}^B = 3.75$  and  $\tilde{\alpha}^B = 200.0 \text{ N/m}^2$ , cf. Figure 9.6. Physically, this leads to

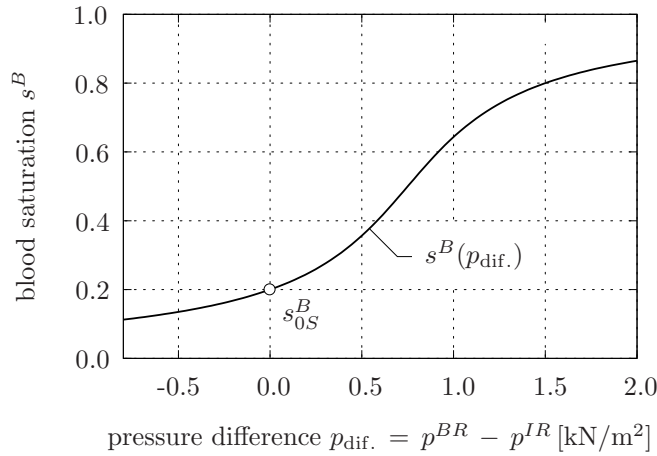


**Figure 9.6:** Thermodynamically consistent constitutive relation for the blood-saturation function  $s^B$ .

a replacement of the interstitial fluid if the pressure difference  $p_{\text{dif.}}$  is positive. Note in passing that a constant value of  $n_{0S}^B = 0.05$  yields an initial value of  $s_{0S}^B = 0.2$  and, as a result,  $p_{\text{dif.}} = 0$ .

### 9.5.5 Results and discussion

In this section, the evaluated results of the microscopic computation are compared with the macroscopic constitutive approach. For the pressure in the vascular system (cere-

bral blood pressure depending on its hierarchical position), the range in the capillary bed varies between 10 millimetres of mercury (mmHg) (corresponds to  $1333 \text{ N/m}^2$ ) at the venous end and 30 mmHg ( $4000 \text{ N/m}^2$ ) at the arterial end. Whereas the interstitial-fluid pressure (tissue pressure) has a typical value of 6 mmHg ( $800 \text{ N/m}^2$ ). To capture such typical conditions, the adjusting blood saturation is evaluated for pressure differences in the range of  $-500 \text{ N/m}^2 \leq p_{\text{dif.}} \leq 2000 \text{ N/m}^2$ . In particular, the pressure difference is applied in steps of  $500 \text{ N/m}^2$  with a subsequent evaluation of the arising volume fractions according to Section 9.5.3. The evaluated pressure states from the microscopic computations are then displayed with diamonds and interpolated with dashed lines, cf. Figure 9.7. The evaluation of case (i) (soft vessel, unconstrained) yields to reasonable

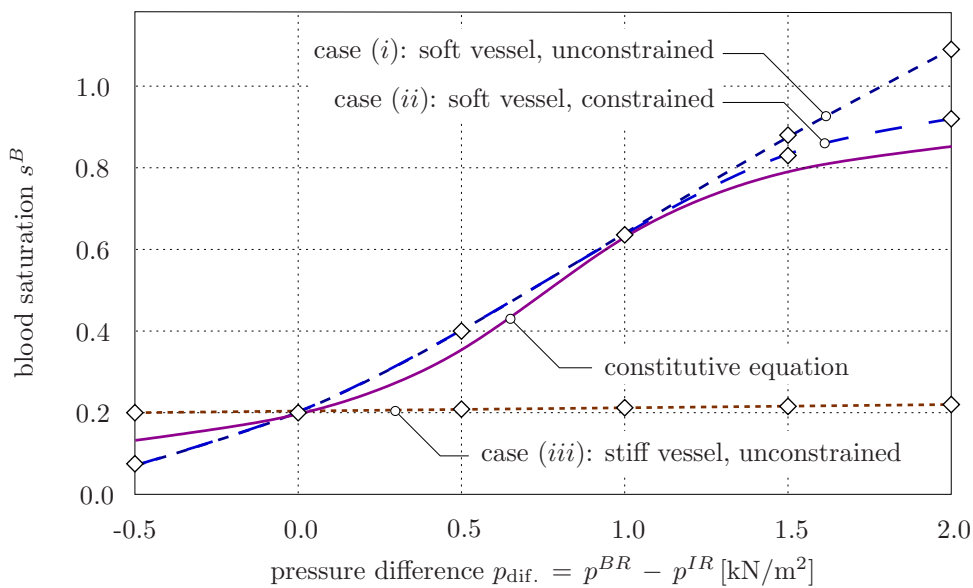


**Figure 9.7:** Comparison of different approaches for the blood-saturation function. Evaluated pressure states from microscopic computations are displayed with diamonds which are connected with dashed lines.

results in the pressure range of  $-500 \text{ N/m}^2 \leq p_{\text{dif.}} \leq 1500 \text{ N/m}^2$ . However, for a further increase of the pressure difference, non-physical results (i. e. a blood saturation greater than one) occur. This is caused by the possibility of an unconstrained widening of the blood vessel. In contrast, in the case (ii) (soft vessel, constrained) it is nicely identified that the microstructural computations yield comparable results in relation to the constitutively chosen pressure-saturation relation (Section 9.5.4) in the domain of nearly fully blood saturated conditions. Again, the constitutive formulation of the blood saturation function is not arbitrary but has to fulfil the thermodynamic restrictions discussed in Section 9.5.4. Therefore, the pathway vary slightly from the graph of case (ii) obtained by microscopic computations. However, this allows for a scale-bridging in terms of microscopic and macroscopic material parameters. In the specific case (ii), the microscopic

material parameters, Young<sup>1</sup>'s modulus  $E = 2792 \text{ N/m}^2$  and Poisson<sup>2</sup>'s ratio  $\mu = 0.48$ , of the blood vessel wall correspond to the macroscopic material parameters  $\tilde{\alpha}^B = 200.0 \text{ N/m}^2$  and  $\tilde{\beta}^B = 3.75$  of the constitutive function. Assuming a higher stiffness of the vessel (corresponding to somehow realistic experimental values of the human intracranial artery) in case (iii) yields within the considered pressure regime a nearly constant blood saturation. This would justify to assume a constant blood-volume fraction within macroscopic simulations.

In conclusion, a constitutive approach for the relation between the pressure difference  $p_{\text{dif}}$  of the liquids and the blood saturation  $s^B$  was presented which satisfies both the thermodynamic consistence as well as physical conditions within human brain tissue. Moreover, this macroscopic saturation condition was motivated and studied by a microscopic computation of a representative microstructure using ABAQUS and a subsequent geometrical evaluation of the arising saturations under applied liquid pressure conditions. With reliable experimental results, this would provide the possibility to identify the macroscopic material parameter of the constitutive function based on the microscopic material parameter in terms of scale-bridging aspects. «(p.135)

## 9.6 Application of model-reduction techniques

BIBLIOGRAPHIC NOTE: The content of this section is based on the following original article: Fink, D., Wagner, A. & Ehlers, W.: Application-driven model reduction for the simulation of therapeutic infusion processes in multi-component brain tissue. *Journal of Computational Science* **24** (2018), 101–115 [109].

### 9.6.1 Introduction

» As described in Section 9.4, a possible clinical option in brain-cancer therapies is a direct therapeutical infusion in the affected brain-tissue region via catheters (CED). Tracing in the direction of real applications, it is reasonable to describe the tissue on a macroscopic scale in a comprehensive manner using continuum-mechanical models. In this regard, multi-component and multi-physical approaches in the framework of the TPM are particularly suited. Besides, several modelling approaches were developed for the prognosis of a CED intervention. Analytical approaches, e. g. Bassar [18], Morrison *et al.* [210], Smith & Humphrey [252] or Wirth & Sobey [290], are only feasible for simplified (cylindrically or spherically) geometries of the brain. In contrast, numerical models with a sound theoretical basis provide a better description of the occurring processes, cf., e. g., Ehlers & Wagner [92, 93], Linninger *et al.* [186], Sarntinoranont *et al.* [235], Støverud *et al.* [254] or Wagner & Ehlers [279]. Such models may allow to study scheduled interventions in

<sup>1</sup>Thomas Young (1773–1829) was a British polymath and physician. Young made notable scientific contributions to the fields of vision, light, solid mechanics, energy, physiology, language, musical harmony and Egyptology [WIKIPEDIA].

<sup>2</sup>Baron Simon Denis Poisson (1781–1840) was a French mathematician, engineer, and physicist who made many scientific advances [WIKIPEDIA].

advance. However, an accompanying use during a clinical routine is typically not feasible due to the high computation time for realistic scenarios.

This drawback motivates to reduce the required computation time, allowing for a potential clinical application. Therefore, model-reduction techniques are applied to the monolithic solution of the strongly coupled TPM model, cf. Section 3.1.4.

## 9.6.2 Underlying brain-tissue models

In this section, the theoretical fundamentals of a general brain-tissue model and a simplification thereof are introduced. In particular, the simplified (linear) brain-tissue model (suited for the description of a therapeutic-agent spreading) is derived using a reasonably condensed formulation of the general (nonlinear) model with all its complexity (e. g. required for the description of solid displacements or stresses). Following this, the computation time of both models is reduced by the application of customised model-reduction techniques. The treatment of the simplified model with the POD method is based on Section 3.2.1, while the application of the POD-DEIM for the general nonlinear model is based on Section 3.2.2.

**General multi-component model for brain tissue:** With regard to the corresponding numerical solution of the coupled system of partial differential equations for the general multi-component model for brain tissue, the Bubnov-Galerkin mixed finite-element method is applied, cf., e. g., Hughes [155] or Wagner [277]. The system of weak formulations can be written in form of an operator equation, yielding

$$\mathcal{G} \equiv \int_{\Omega} (\mathcal{D}(\delta\mathbf{u}, \mathbf{u}, \dot{\mathbf{u}}) + \mathcal{K}(\delta\mathbf{u}, \mathbf{u})) \, dv - \int_{\Gamma} \mathcal{F}(\delta\mathbf{u}) \, da = 0. \quad (9.11)$$

Therein, the vector  $\mathbf{u} := [\mathbf{u}_S \ p^{BR} \ p^{IR} \ c_m^D]^T$  of primary unknowns, the corresponding vector  $\delta\mathbf{u} := [\delta\mathbf{u}_S \ \delta p^{BR} \ \delta p^{IR} \ \delta c_m^D]^T$  of test functions and the operators for the system matrix

$$\begin{aligned} \mathcal{D}(\delta\mathbf{u}, \mathbf{u}, \dot{\mathbf{u}}) &= \underbrace{[(n^B(\mathbf{u}_S, p_{\text{dif}}))'_S + n^B(\mathbf{u}_S, p_{\text{dif}}) \operatorname{div}(\mathbf{u}_S)'_S] \delta p^{BR}}_{\mathcal{D}_{p^{BR}}} + \\ &+ \underbrace{[(n^I(\mathbf{u}_S, p_{\text{dif}}))'_S + n^I(\mathbf{u}_S, p_{\text{dif}}) \operatorname{div}(\mathbf{u}_S)'_S] \delta p^{IR}}_{\mathcal{D}_{p^{IR}}} + \\ &+ \underbrace{[n^I(\mathbf{u}_S, p_{\text{dif}})(c_m^D)'_S + c_m^D \operatorname{div}(\mathbf{u}_S)'_S] \delta c_m^D}_{\mathcal{D}_{c_m^D}}, \end{aligned} \quad (9.12)$$

the stiffness matrix

$$\begin{aligned}
\mathcal{K}(\delta \mathbf{u}, \mathbf{u}) &= \underbrace{\left[ \mathbf{T}_E^S(\mathbf{u}_S) - (s^B(p_{\text{dif}}) p^{BR} + s^I(p_{\text{dif}}) p^{IR}) \mathbf{I} \right] \cdot \text{grad } \delta \mathbf{u}_S}_{\mathcal{K}_{\mathbf{u}_S}} + \\
&+ \underbrace{\frac{\mathbf{K}^{SB}}{\mu^{BR}} \left( \text{grad } p^{BR} + \frac{p_{\text{dif.}}}{s^B(p_{\text{dif}})} \text{grad } s^B(p_{\text{dif}}) \right) \cdot \text{grad } \delta p^{BR}}_{\mathcal{K}_{p^{BR}}} + \\
&+ \underbrace{\frac{\mathbf{K}^{SI}}{\mu^{IR}} \text{grad } p^{IR} \cdot \text{grad } \delta p^{IR}}_{\mathcal{K}_{p^{IR}}} - \\
&- c_m^D \text{div} \left[ \frac{\mathbf{K}^{SB}}{\mu^{BR}} \left( \text{grad } p^{BR} + \frac{p_{\text{dif.}}}{s^B(p_{\text{dif}})} \text{grad } s^B(p_{\text{dif}}) \right) \right] \delta c_m^D + \\
&+ \underbrace{\left[ \mathbf{D}^D \text{grad } c_m^D + c_m^D \frac{\mathbf{K}^{SI}}{\mu^{IR}} \text{grad } p^{IR} \right] \cdot \text{grad } \delta c_m^D}_{\mathcal{K}_{c_m^D}}, \tag{9.13}
\end{aligned}$$

and

$$\mathcal{F}(\delta \mathbf{u}) = \underbrace{\bar{\mathbf{t}} \cdot \delta \mathbf{u}_S}_{\mathcal{F}_{\mathbf{u}_S}} - \underbrace{\bar{v}^B \delta p^{BR}}_{\mathcal{F}_{p^{BR}}} - \underbrace{\bar{v}^I \delta p^{IR}}_{\mathcal{F}_{p^{IR}}} - \underbrace{j^D \delta c_m^D}_{\mathcal{F}_{c_m^D}} \tag{9.14}$$

are included. Therein, the extra stress  $\mathbf{T}_E^S$  and the volume fraction  $n^S$  of the solid are functions of the solid displacement  $\mathbf{u}_S$ , the saturation functions  $s^I$  and  $s^B$  are functions of the differential pressure  $p_{\text{dif.}}$  depending on the pore-liquid pressures  $p^{BR}$  and  $p^{IR}$ , and the volume fractions  $n^I$  and  $n^B$  of the pore-liquids are functions of both the solid displacement  $\mathbf{u}_S$  and the differential pressure  $p_{\text{dif.}}$ . These dependencies on the primary variables are displayed in (9.12) and (9.13) with grey colour (faded) to illustrate the couplings. Note in passing that the terms in the operators (9.12) must be brought to the same dimension (such that the operators  $\mathcal{D}$  and  $\mathcal{K}$  have the dimension  $1/\text{m}^3$  and the operator  $\mathcal{F}$  has the dimension  $1/\text{m}^2$ ) before adding them. Following this, the result of the integration in (9.11) is dimensionless. Finally, the system (9.1) can be formulated in a monolithic way via

$$\mathbf{F}(t, \mathbf{u}(t), \dot{\mathbf{u}}(t)) = \mathcal{D}(\mathbf{u}) \dot{\mathbf{u}} + \mathbf{k}(\mathbf{u}) - \mathbf{f}(t) = \mathbf{0} \tag{9.15}$$

written in an abstract semi-discrete setting. The global system of equations (3.7) with dimension  $N$ , representing the number of degrees of freedom of the full system, includes the system matrix  $\mathcal{D}(\mathbf{u}(t)) \in \mathbb{R}^{N \times N}$ , the system vector  $\mathbf{k}(\mathbf{u}(t)) \in \mathbb{R}^N$  and the vector  $\mathbf{f}(t) \in \mathbb{R}^N$  consisting of the Neumann boundary conditions. Furthermore, all degrees of freedom of the system in (3.7), namely the nodal unknowns of each primary variable, are summarised in the abstract vector  $\mathbf{u} \in \mathbb{R}^N$  of unknowns, and analogously their time

derivatives are summarised in the abstract vector  $\dot{\mathbf{u}} \in \mathbb{R}^N$ , viz.:

$$\begin{aligned}
\mathbf{u} &:= [\mathbf{u}_S \ \mathbf{p}^{BR} \ \mathbf{p}^{IR} \ \mathbf{c}_m^D]^T \\
&= [\mathbf{u}_S^1 \ \dots \ \mathbf{u}_S^n \ p^{BR,1} \ \dots \ p^{BR,n} \ p^{IR,1} \ \dots \ p^{IR,n} \ c_m^{D,1} \ \dots \ c_m^{D,n}]^T, \\
\dot{\mathbf{u}} &:= [\dot{\mathbf{u}}_S \ \dot{\mathbf{p}}^{BR} \ \dot{\mathbf{p}}^{IR} \ \dot{\mathbf{c}}_m^D]^T \\
&= [(\mathbf{u}_S^1)'_S \ \dots \ (\mathbf{u}_S^n)'_S \ (p^{BR,1})'_S \ \dots \ (p^{BR,n})'_S \ (p^{IR,1})'_S \ \dots \\
&\quad \dots \ (p^{IR,n})'_S \ (c_m^{D,1})'_S \ \dots \ (c_m^{D,n})'_S]^T.
\end{aligned} \tag{9.16}$$

Therein,  $n$  indicates the number of nodes (the number of nodal unknowns must not necessarily be equal for all primary variables since different ansatz functions can be used). Following this, the equilibrium equation in global form is given by

$$\begin{aligned}
\underbrace{\begin{bmatrix} \mathbf{0} & \mathbf{0} & \mathbf{0} & \mathbf{0} \\ \mathcal{D}_{21}(\mathbf{u}(t)) & \mathcal{D}_{22}(\mathbf{u}(t)) & \mathcal{D}_{23}(\mathbf{u}(t)) & \mathbf{0} \\ \mathcal{D}_{31}(\mathbf{u}(t)) & \mathcal{D}_{32}(\mathbf{u}(t)) & \mathcal{D}_{33}(\mathbf{u}(t)) & \mathbf{0} \\ \mathcal{D}_{41}(\mathbf{u}(t)) & \mathbf{0} & \mathbf{0} & \mathcal{D}_{44}(\mathbf{u}(t)) \end{bmatrix}}_{\mathcal{D}(\mathbf{u}(t))} \underbrace{\begin{bmatrix} \dot{\mathbf{u}}_S \\ \dot{\mathbf{p}}^{BR} \\ \dot{\mathbf{p}}^{IR} \\ \dot{\mathbf{c}}_m^D \end{bmatrix}}_{\dot{\mathbf{u}}(t)} + \\
+ \underbrace{\begin{bmatrix} \mathbf{k}_1(\mathbf{u}(t)) \\ \mathbf{k}_2(\mathbf{u}(t)) \\ \mathbf{k}_3(\mathbf{u}(t)) \\ \mathbf{k}_4(\mathbf{u}(t)) \end{bmatrix}}_{\mathbf{k}(\mathbf{u}(t))} = \underbrace{\begin{bmatrix} \mathbf{f}_1(t) \\ \mathbf{f}_2(t) \\ \mathbf{f}_3(t) \\ \mathbf{f}_4(t) \end{bmatrix}}_{\mathbf{f}(t)}.
\end{aligned} \tag{9.17}$$

Finally, the occurring time derivatives in the coupled system (9.17) are related to the solid motion and are approximated via a temporal discretisation using an implicit Euler time-integration scheme. The numerical implementation is realised with the finite-element solver PANDAS and, thus, allows for the simulation of initial-boundary-value problems. All computations are performed on a single core of an Intel i5-4590 with 32 GB of memory running at clock speed of 3.30 GHz.

**Simplified drug-infusion model for brain tissue:** During the CED procedure, the temporal and spatial spreading of the applied therapeutic agent is of main interest. In order to represent this procedure in a condensed model (feasible for a treatment using the POD), some simplifications (in terms of further preliminary assumptions) of the previously described general model are complemented. In particular, these are a geometrically linear material behaviour (small deformations) and a constant blood volume fraction  $n^B = n_{0S}^B$ .

This implies for the volume fractions and their temporal changes:

$$\begin{aligned}
n^S &= n_{0S}^S (\det \mathbf{F}_S)^{-1} & \text{and} & \quad (n^S)'_S = -n^S \operatorname{div}(\mathbf{u}_S)'_S, \\
n^B &= n_{0S}^B & \text{and} & \quad (n^B)'_S = 0, \\
n^I &= 1 - n^S - n_{0S}^B & \text{and} & \quad (n^I)'_S = -(n^S)'_S, \\
s^B &= 1 - s^I = \frac{n_{0S}^B}{1 - n^S} & \text{and} & \quad \operatorname{grad} s^B \approx \mathbf{0}.
\end{aligned} \tag{9.18}$$

Therefore, the equilibrium equation in global form is derived in accordance to the procedure followed above via

$$\begin{aligned}
\mathcal{G}_{\mathbf{u}_S} &\equiv \int_{\Omega} (\mathbf{T}_E^S(\mathbf{u}_S) - \frac{1}{1 - n^S(\mathbf{u}_S)} (n_{0S}^B p^{BR} + n^I(\mathbf{u}_S) p^{IR}) \mathbf{I}) \cdot \operatorname{grad} \delta \mathbf{u}_S \, dv - \\
&\quad - \int_{\Gamma_N^{\bar{\mathbf{t}}}} \bar{\mathbf{t}} \cdot \delta \mathbf{u}_S \, da = 0, \\
\mathcal{G}_{p^{BR}} &\equiv \int_{\Omega} n_{0S}^B \operatorname{div}(\mathbf{u}_S)'_S \delta p^{BR} \, dv + \int_{\Omega} \frac{\mathbf{K}^{SB}}{\mu^{BR}} \operatorname{grad} p^{BR} \cdot \operatorname{grad} \delta p^{BR} \, dv + \\
&\quad + \int_{\Gamma_N^{\bar{v}^B}} \bar{v}^B \delta p^{BR} \, da = 0, \\
\mathcal{G}_{p^{IR}} &\equiv \int_{\Omega} (1 - n_{0S}^B) \operatorname{div}(\mathbf{u}_S)'_S \delta p^{IR} \, dv + \int_{\Omega} \frac{\mathbf{K}^{SI}}{\mu^{IR}} \operatorname{grad} p^{IR} \cdot \operatorname{grad} \delta p^{IR} \, dv + \\
&\quad + \int_{\Gamma_N^{\bar{v}^I}} \bar{v}^I \delta p^{IR} \, da = 0, \\
\mathcal{G}_{c_m^D} &\equiv \int_{\Omega} [n^I(\mathbf{u}_S) (c_m^D)'_S + c_m^D \operatorname{div}(\mathbf{u}_S)'_S - c_m^D \operatorname{div}(\frac{\mathbf{K}^{SB}}{\mu^{BR}} \operatorname{grad} p^{BR})] \delta c_m^D \, dv + \\
&\quad + \int_{\Omega} (\mathbf{D}^D \operatorname{grad} c_m^D + c_m^D \frac{\mathbf{K}^{SI}}{\mu^{IR}} \operatorname{grad} p^{IR}) \cdot \operatorname{grad} \delta c_m^D \, dv + \int_{\Gamma_{\bar{J}^D}} \bar{J}^D \delta c_m^D \, da = 0.
\end{aligned} \tag{9.19}$$

Finally, this results in

$$\underbrace{\begin{bmatrix} \mathbf{0} & \mathbf{0} & \mathbf{0} & \mathbf{0} \\ \mathcal{D}_{21} & \mathbf{0} & \mathbf{0} & \mathbf{0} \\ \mathcal{D}_{31} & \mathbf{0} & \mathbf{0} & \mathbf{0} \\ \mathcal{D}_{41} & \mathbf{0} & \mathbf{0} & \mathcal{D}_{44} \end{bmatrix}}_{\mathcal{D}} \underbrace{\begin{bmatrix} \dot{\mathbf{u}}_S \\ \dot{\mathbf{p}}^{BR} \\ \dot{\mathbf{p}}^{IR} \\ \dot{\mathbf{c}}_m^D \end{bmatrix}}_{\dot{\mathbf{u}}(t)} + \underbrace{\begin{bmatrix} \mathbf{k}_1(\mathbf{u}(t)) \\ \mathbf{k}_2(\mathbf{u}(t)) \\ \mathbf{k}_3(\mathbf{u}(t)) \\ \mathbf{k}_4(\mathbf{u}(t)) \end{bmatrix}}_{\mathbf{k}(\mathbf{u}(t))} = \underbrace{\begin{bmatrix} \mathbf{f}_1(t) \\ \mathbf{f}_2(t) \\ \mathbf{f}_3(t) \\ \mathbf{f}_4(t) \end{bmatrix}}_{\mathbf{f}(t)}. \tag{9.20}$$

Resulting from the specified assumptions concerning the simplified model, the system vector  $\mathbf{k}$  approximately results in  $\mathbf{k}(\mathbf{u}(t)) \approx \mathcal{K} \mathbf{u}(t)$  with a constant system matrix  $\mathcal{K} \in \mathbb{R}^{N \times N}$ . Analogously, the system matrix  $\mathcal{D}$  can also be assumed to be approximately constant. Afterwards,  $\mathcal{K}$  exhibits a similar structure as  $\mathcal{D}$ , and (9.20) can be written as

$$\mathcal{D} \dot{\mathbf{u}} + \mathcal{K} \mathbf{u} = \mathbf{f}. \quad (9.21)$$

As before, the occurring time derivatives in (9.20) are related to the solid motion and approximated via a temporal discretisation using an implicit Euler time-integration scheme for a numerical realisation within PANDAS. However, the numerical solution time of realistic scenarios using the full system, either for the complex (full nonlinear) or for the simplified brain-tissue model (with an approximately linear system), is immense. Therefore, possibilities to reduce the system of equations in (9.21) with the POD method for linear systems and (9.17) with the POD-DEIM for general nonlinear systems are applied and customised in the following subsections.

### 9.6.3 Further adaptations

It is, furthermore, necessary to incorporate another important character of the considered simplified brain-tissue model. The vector  $\mathbf{u}$  of unknowns contains as primary variables the solid displacement vector  $\mathbf{u}_S$ , the effective pore-liquid pressures  $p^{IR}$  and  $p^{BR}$  and the molar concentration  $c_m^D$  of the therapeutic agent. Physically, the primary variables exhibit a different behaviour in time. Moreover, the entries of the vector  $\mathbf{u}$  have very huge differences in their absolute values. This may lead to problems when applying the POD method by default. To overcome these problems, the snapshot matrix  $\mathbf{U}$  is separated into smaller snapshot matrices for each primary variable, yielding

$$\mathbf{U}^u = [\mathbf{u}_1^u \ \mathbf{u}_2^u \ \dots \ \mathbf{u}_m^u], \quad \mathbf{U}^p = [\mathbf{u}_1^p \ \mathbf{u}_2^p \ \dots \ \mathbf{u}_m^p] \quad \text{and} \quad \mathbf{U}^c = [\mathbf{u}_1^c \ \mathbf{u}_2^c \ \dots \ \mathbf{u}_m^c]. \quad (9.22)$$

Therein, the vectors  $\mathbf{u}_i^u$  contain all nodal values of the FE-grid for the solid displacement vector  $\mathbf{u}_S$  at time  $t_i$ . In accordance, the vector  $\mathbf{u}_i^p$  includes the values of the effective pore-liquid pressures  $p^{IR}$  and  $p^{BR}$ , while the vector  $\mathbf{u}_i^c$  comprises the values of the molar concentration  $c_m^D$ . Since extended Taylor-Hood elements with different ansatz functions (namely quadratic ones for  $\mathbf{u}_S$  and linear ones for  $p^{IR}$ ,  $p^{BR}$  and  $c_m^D$ ) are used for reasons of numerical stability of the full system, this leads to a total number of  $N = N^u + N^p + N^c$  degrees of freedom. In a next step, the eigenvalue problem (3.16) is solved for each of these snapshot matrices separately. Afterwards, the individually obtained subspace matrices  $\Phi^u$ ,  $\Phi^p$  and  $\Phi^c$  are summarised in the required reduction matrix

$$\Phi = \begin{bmatrix} \Phi^u & \mathbf{0} & \mathbf{0} \\ \mathbf{0} & \Phi^p & \mathbf{0} \\ \mathbf{0} & \mathbf{0} & \Phi^c \end{bmatrix}. \quad (9.23)$$

Therein, the subspace matrices  $\Phi^u$ ,  $\Phi^p$  and  $\Phi^c$  can have different numbers of considered POD modes, leading to totally  $l = l^u + l^p + l^c$  POD modes (which corresponds to the reduced number of unknowns). After generating the resulting reduction matrix  $\Phi$ , the reduction can be performed according to (3.19). Using the general brain-tissue model with all its complexity, it is crucial to account for nonlinearities.

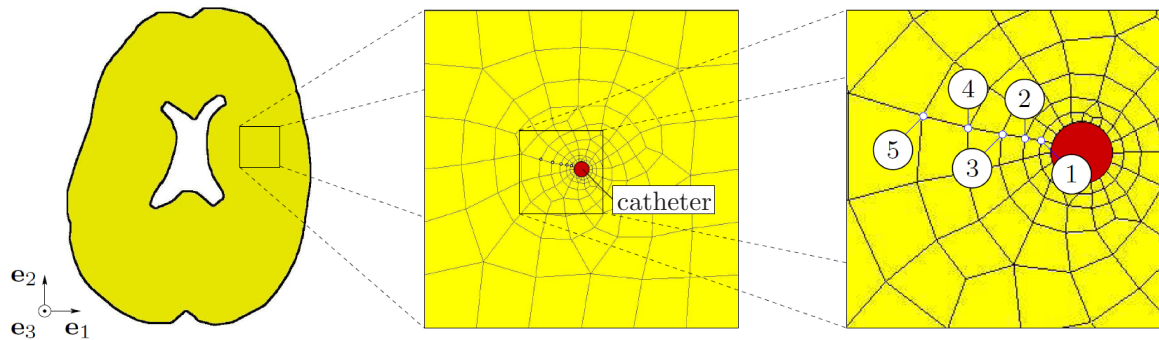


**Figure 9.8:** Geometry of a horizontal cut through a human brain (left), rectangular geometry and mesh of the initial-boundary-value problem (middle) and evaluated points within the domain (right).

### 9.6.4 Numerical example for the POD application

For a comparison of the numerical solutions obtained by the full system and the POD-reduced system, a simple rectangular geometry (a thin slice with the dimensions of  $10 \text{ mm} \times 10 \text{ mm} \times 0.25 \text{ mm}$ , spatially discretised with 160 three-dimensional Taylor-Hood elements) is studied, cf. Figure 9.8. The geometric parts used for the examples correspond to typical anatomically-based geometries of the brain, cf., e. g., Dutta-Roy *et al.* [75] and Taylor & Miller [263]. The chosen simulation and material parameters are collected in Table 9.2, a comprehensive discussion can be found in Wagner [277]. In order to represent the CED procedure within brain tissue, a catheter is placed and a therapeutic solution is applied via an infusion at the surface of the infusion site. In particular, a solution influx (Neumann boundary condition) of  $\bar{v}^I = 4.24 \times 10^{-6} \text{ m}^3/\text{m}^2 \text{ s}$  is combined with a constant therapeutic concentration (Dirichlet boundary condition) of  $c_{0m}^D = 3.7 \times 10^{-3} \text{ mol/l}$ , which is corresponding to a typical application dose of  $Q = 10 \text{ } \mu\text{l}/\text{min}$ . In addition, an efflux of interstitial fluid and therapeutic agents over the surfaces at the outside of the rectangular tissue sample is possible (Neumann boundary condition for the pore pressures and the concentration). In order to mechanically support the domain, the outer surfaces of the geometry are spatially fixed (Dirichlet boundary condition for the solid displacement). Note that in this simple example, isotropic permeability conditions and the further assumptions of the simplified brain-tissue model are assumed for the entire domain. However, a consideration of anisotropic permeability conditions, as well as using the full range of the previously described theoretical brain-tissue model, is in general feasible and will be presented in the next subsection.

**Simulation of a therapeutic infusion process:** In order to perform reduced simulations, snapshots (of state variables) are stored in all time steps and the system matrices in the first time step of the pre-computation. Afterwards, the reduction matrix and the reduced system matrices are generated in the offline phase for different numbers of considered POD modes. Based on these data, the simulation in the online phase is performed with the reduced system using, in a first step, the same problem setting (and such the same material parameters and boundary conditions) as in the pre-computation of the full system to prove the accuracy of the reduced system. The results obtained by the full

system and the reduced system with different numbers of POD modes are shown in Figure 9.9 for the normalised therapeutic concentration  $c_m^D/c_{0m}^D$  at Point 1 (cf. Figure 9.8). Comparing the results, it is concluded that the results are adequately using more than 20-25 POD modes. In addition, the error (normalised root square deviation) averaged over all degrees of freedom and time steps between the full and the reduced simulation is displayed in Figure 9.10 for each primary variable and can be used to estimate the required dimensions of the POD basis. In this case, the minimal error is reached using more than 25 POD modes for the concentration and 35 POD modes for all primary variables. Note in passing that for small dimensions of the reduced basis, individual runaways may occur, e. g., due to rounding errors. This can be seen in Figure 9.10 at the non-smooth convergence of the pore-liquid error, e. g., at 30 POD modes. However, for increasing numbers of POD modes the error converges to its final value. Following this, the POD method is subsequently performed with 25 POD modes for the simulation of the therapeutic-agent evolution at the evaluated points 1 - 5 (cf. Figure 9.8) during the applied infusion, cf. Figure 9.11. Naturally, the resulting therapeutic concentration increases during the infusion, where the points closer to the infusion site reach a higher (therapeutically more effective) level. Again, the accuracy of the normalised therapeutic concentration is ensured for all evaluated points (such that the solid dots in Figure 9.11 almost coincide with the

**Table 9.2:** *Material parameters for the numerical simulations.*

Symbol	Value	Unit	Description/reference
$n_{0S}^B$	0.05	[-]	Initial blood volume fraction [21]
$n_{0S}^I$	0.20	[-]	Initial interstitial fluid volume fraction [261]
$n_{0S}^S$	0.75	[-]	Initial solidity arises as a result of (9.3) <sub>4</sub>
$\rho^{BR}$	$1.035 \times 10^{+3}$	[kg/m <sup>3</sup> ]	Effective density of blood (assumption)
$\rho^{IR}$	$0.993 \times 10^{+3}$	[kg/m <sup>3</sup> ]	Effective density of interstitial fluid (water at 37°C)
$\mu^{BR}$	$3.5 \times 10^{-3}$	[Ns/m <sup>2</sup> ]	Dynamic viscosity of blood (assumption)
$\mu^{IR}$	$0.7 \times 10^{-3}$	[Ns/m <sup>2</sup> ]	Dynamic viscosity of interstitial fluid (water at 37°C)
$\mu_0^S$	$1.0 \times 10^{+3}$	[N/m <sup>2</sup> ]	(First and second) elastic Lamé constants,
$\lambda_0^S$	$5.0 \times 10^{+3}$	[N/m <sup>2</sup> ]	according to [61] and citations therein
$\tilde{\mu}_1^S$	$8.0 \times 10^{+1}$	[N/m <sup>2</sup> ]	Material parameters governing the anisotropic
$\tilde{\gamma}_1^S$	$1.0 \times 10^{+1}$	[-]	material behaviour (assumed low fibre stiffness)
$\tilde{\alpha}^B$	200	[N/m <sup>2</sup> ]	Material parameter in constitutive relation (9.3) <sub>5</sub>
$\tilde{\beta}^B$	3.75	[-]	Material parameter in constitutive relation (9.3) <sub>5</sub>
$D_{ij}^D$	$10^{-9} - 10^{-10}$	[m <sup>2</sup> /s]	Order of magnitude of the spatially varying diffusion coefficient, cf. [21] and citations therein
$K_{ij}^I$	$10^{-7} - 10^{-8}$	[m/s]	order of magnitude of spatial varying Darcy permeability of the interstitial fluid, cf. [163]
$K_{ii}^B$	$3.0 \times 10^{-5}$	[m/s]	isotropic Darcy permeability coefficient, cf. [255]

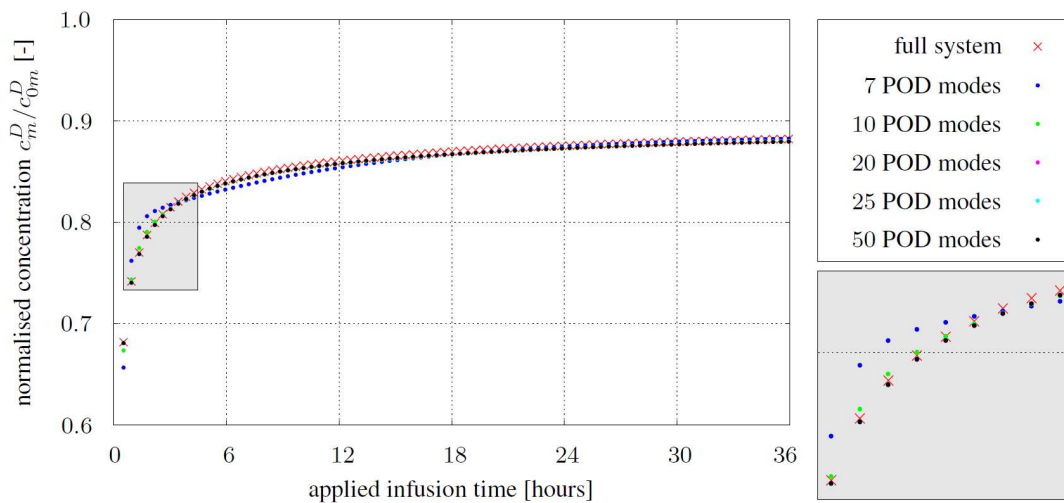


**Figure 9.9:** Normalised concentration of the therapeutic agent at Point 1, obtained by the full system (red crosses) and the reduced system for different numbers of POD modes (coloured circles).

corresponding circles), as well as for the spatial spreading within the domain at the end of the infusion process, cf. Figure 9.12. Due to the separated snapshot and reduction matrices for all primary variables, this is also the case for all other primary variables, as exemplarily shown in Figure 9.13 for the effective pore-liquid pressure  $p^{IR}$ . In terms of the numerical costs of the online phase, the results of the full system are calculated in 494 seconds, whereas the computation time is reduced to 145 seconds using the POD-reduced system, cf. Table 9.3. This results in an enormous time saving and reduces the computational costs of the online phase to less than 30%. In particular, the time to solve the equation system is reduced significantly to less than 1%. In contrast, the time to write out specific data, e.g. the results of the primary variables or the stresses at all nodes of the FE grid, naturally remains the same. In conclusion, the results are very promising concerning the overall time reduction. Note in passing that the time to collect the snapshots in the pre-computation and the time to compute the reduction matrix in the offline

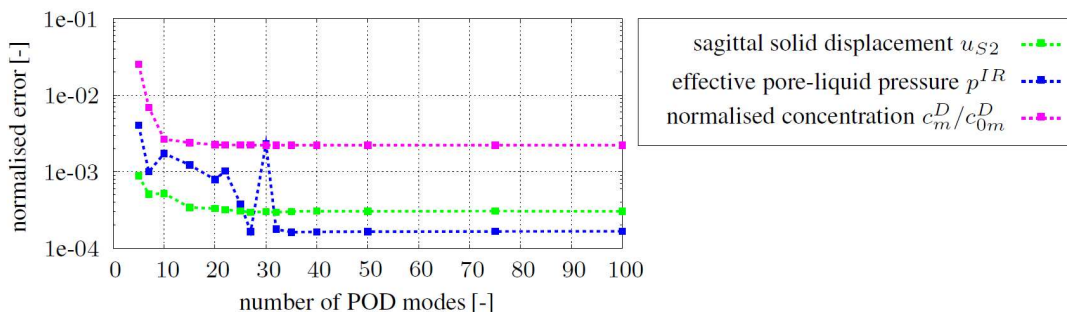


**Figure 9.10:** Error (normalised square root deviation) between the full and the reduced simulation of the sagittal solid displacement (green), the pore-liquid pressure (blue) and the normalised concentration (magenta) averaged over all degrees of freedom and time steps.

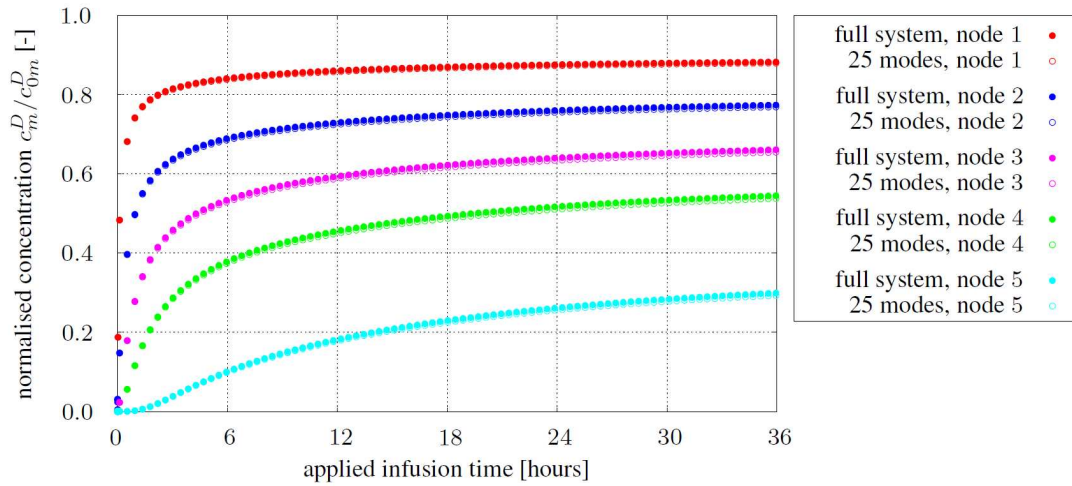


**Figure 9.11:** Normalised concentration of the therapeutic agent at evaluated points, obtained by the full system (solid dots) and the reduced system (circles).

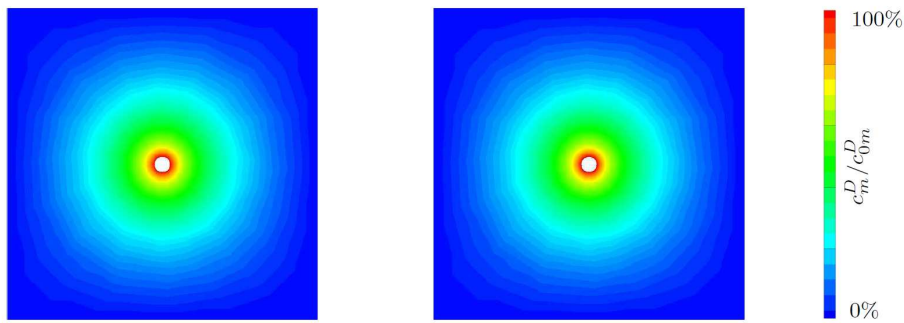


**Figure 9.12:** Therapeutical spreading at the end of an infusion process under isotropic conditions, computed with the full system (left) and the reduced system (right) using 25 POD modes.

phase are not considered here. Following this, a time saving is only obtained if several (at least two or more) simulations are performed within the reduced system. However, this is often required, compare, for example, the study of various infusion scenarios discussed in the following subsection.

**Results for infusion variations:** In the previous section, it was demonstrated that the sophisticated theoretical basis of the simplified brain-tissue model is conserved by the

**Table 9.3:** Computing time on a single core of an Intel i5-4590 with 32 GB of memory running at clock speed of 3.30 GHz (time to solve the equation system and to write out special data summarised for all time steps and total computing time) of the online phase, obtained by the full and the reduced system with 25 POD modes.

	time solving eq. system	time write out data	total CPU time
full system	351 s	143 s	494 s
reduced system	2 s	143 s	145 s

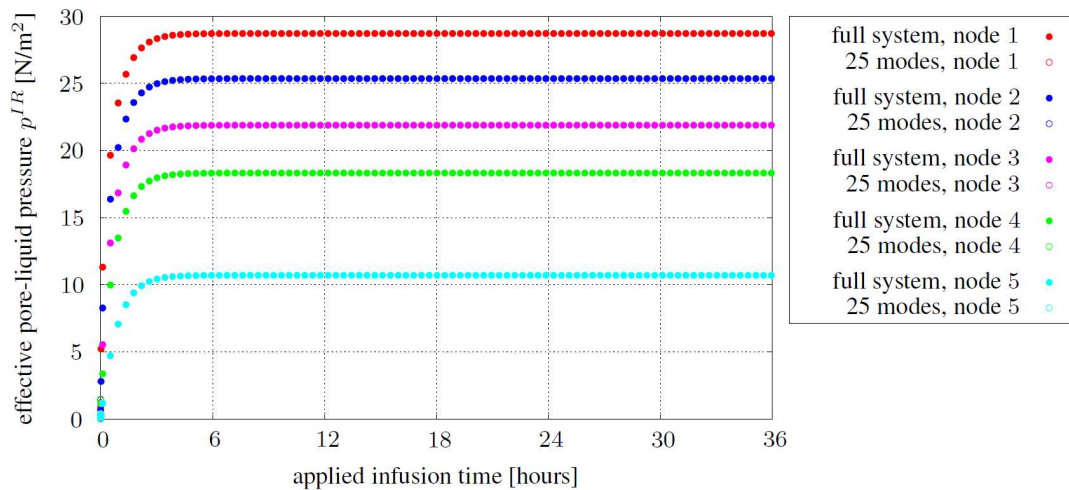


**Figure 9.13:** Pore pressure obtained by the full system (solid dots) and the reduced system (circles).

realised reduced simulation. In this section, the application dose is varied in test cases since the prediction of various infusion scenarios is of particular interest in the planning phase of a scheduled clinical procedure. Therefore, a sufficiently good performance with the reduced system, realised under the re-usage of the previously calculated subspace matrix  $\Phi$ , is required for an effective time benefit. In Figure 9.14, the reduced simulation results for the evolution of the therapeutic concentration at Point 3 are shown for a variation of the applied initial values  $c_{0m}^D$ . Comparing the results with the reference solution of the full system, the accuracy of the therapeutic concentration is ensured. Moreover, a variation of the applied solution influx  $\bar{v}^I$  does not effect the accuracy of the effective pore-liquid pressure  $p^{IR}$ , cf. Figure 9.15. However, the results for the normalised concentration (plotted in Figure 9.16) differ slightly for the moderately chosen application

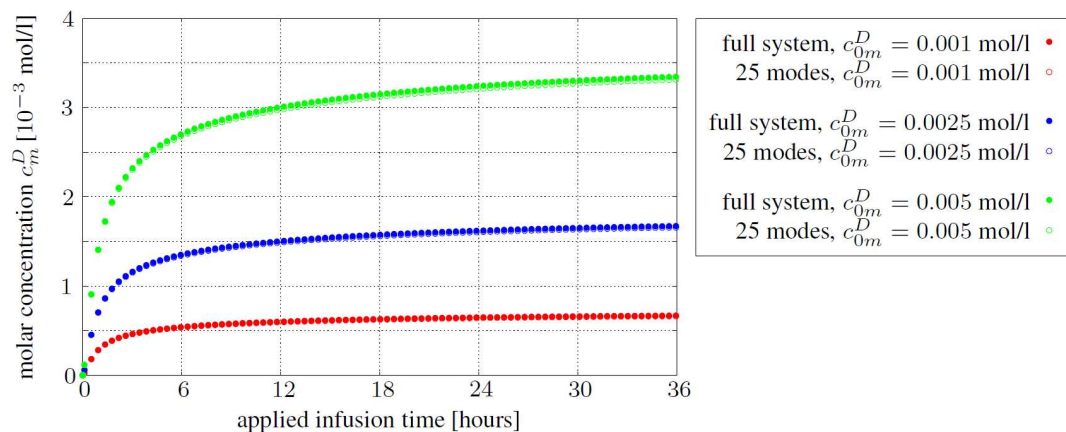


**Figure 9.14:** Therapeutic concentration at Point 3 for a variation in the applied initial values  $c_{0m}^D$ , obtained by the full system (solid dots) and the reduced system (circles).

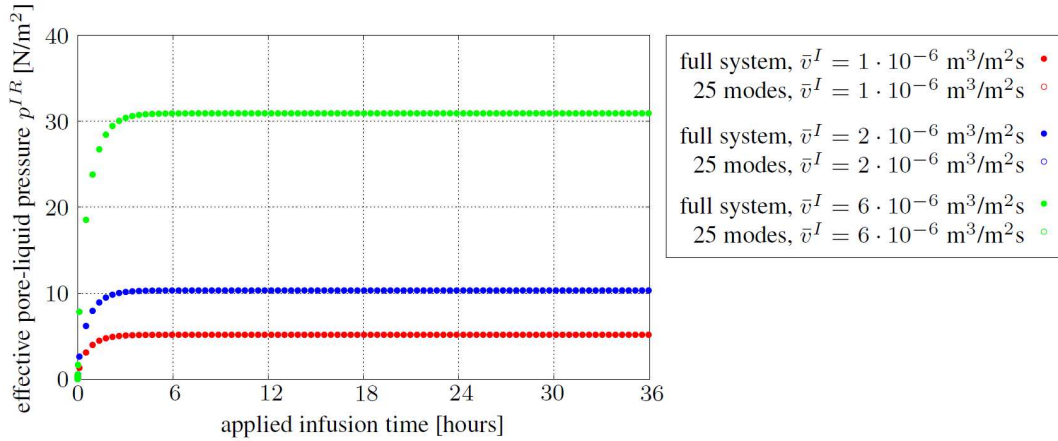


**Figure 9.15:** Effective pore-liquid pressure at Point 3 for different values of the applied solution influx, obtained by the full system (solid dots) and the reduced system (circles).

doses which result a diffusion-dominated spreading. In particular, for an increase of the solution influx, the concentration increases moderately using the full model. In contrast, it remains unchanged using the reduced system. Nevertheless, the difference is negligibly small and the reduced simulation seems to be sufficient.

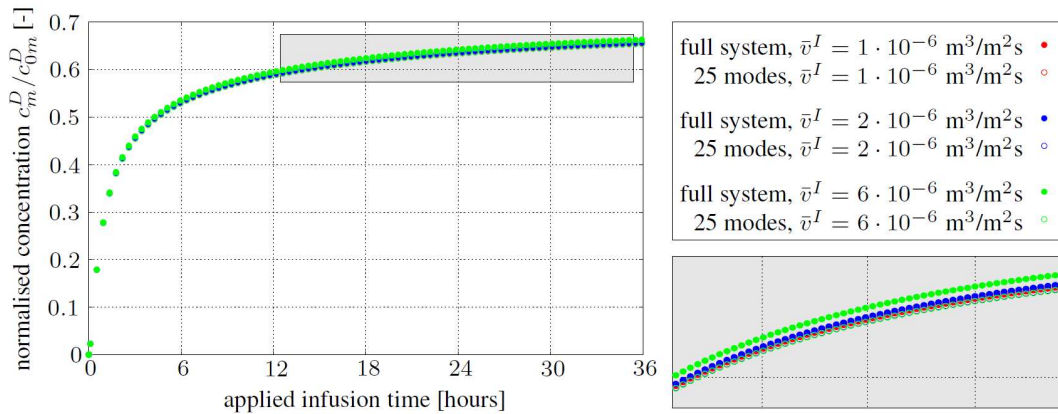


**Figure 9.16:** Normalised concentration of the therapeutic agent at Point 3 for different values of the applied solution influx, obtained by the full system (solid dots) and the reduced system (circles).

### 9.6.5 Numerical example for the POD-DEIM application

In the previous section, a simplified model was used with emphasis on the drug spreading. In a next step, a thin brain slice (horizontal cut, discretised with one three-dimensional element in thickness direction, cf. Figure 9.17) is studied for various aspects based on the general nonlinear model. In particular, a therapeutic solution is applied according

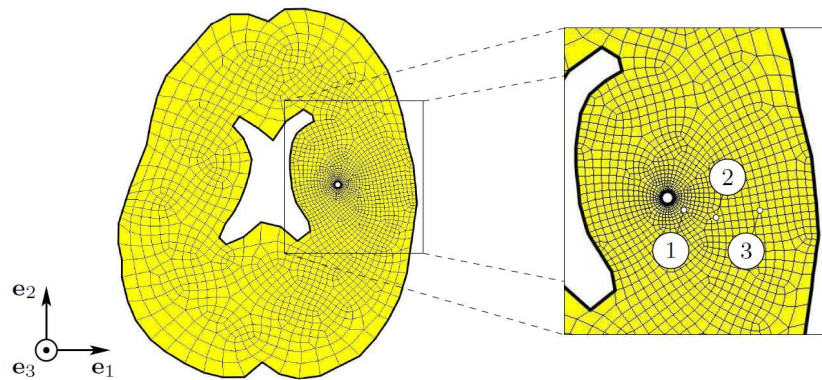


**Figure 9.17:** Rectangular geometry and mesh of the initial-boundary-value problem (left) and evaluated points within the domain (right).

to the previous example. The mechanical support is provided due to the spatially fixed inner surfaces. In contrast to the first simple example, anisotropic permeability conditions are considered for the entire domain of the brain-tissue model. Therefore, the anisotropic permeability tensors  $\mathbf{K}^{SB}$  and  $\mathbf{K}^{SI}$  (and the diffusivity  $\mathbf{D}^D$  of the therapeutic agent analogously) are evaluated from (patient-specific) medical imaging data. The chosen simulation and material parameters are collected in Table 9.2. As there are various appearing nonlinearities resulting especially from nonlinearities in the saturation function (and, thus, in the volume fractions) and from the geometrically nonlinear material behaviour, the application of the POD-DEIM is required to reduce the nonlinear system (9.15) in an appropriate manner. Therefore, the state variables  $\mathbf{u}_i$  are stored in a first step in all time steps of a pre-computation of the initial full system. After computing the reduction matrix  $\Phi$ , a pre-computation is performed with the POD-reduced system (using the same problem setting as in the pre-computation of the full system) and the nonlinear terms  $\mathbf{y}_i$  are stored. This leads to significantly more precise results than storing the nonlinear terms directly in the pre-computation of the full system. Based on this data, the reduction matrices  $\Psi$  and  $\mathbf{P}$  are computed. The simulation is performed for the POD-DEIM-reduced system using, in a first step, the same problem setting as in the pre-computations to prove the accuracy of the reduced system. In Figure 9.18, the evolution of the solid displacement in coronal direction, the pore pressures of the blood and the interstitial fluid and the normalised concentration are shown at the evaluated points 1-3 (cf. Figure 9.17) during the applied infusion. Comparing the results of the primary variables computed within the full and the reduced system, it is obvious that they are sufficiently exact using 18 POD modes and 47 DEIM modes (normalised error of  $10^{-5}$ ). Furthermore, the accuracy of the spatial spreading of the normalised therapeutic concentration and the total stress  $\sigma_{11}$  (and all other stresses analogously) within the domain at the end of the infusion process is ensured, cf. Figures 9.19 and 9.20. Due to the anisotropic properties of the brain-tissue material, the spreading is not uniform. Regarding the evaluated DEIM points (DOF of the FE grid, where the nonlinear terms are computed), it becomes obvious that most of them are near the position of the catheter and, thus, in the area of interest, cf. Figure 9.21. Following this, there are many elements for which the values of the nonlinear term are approximated with the reduction matrix  $\Psi$  instead of computing them individually.

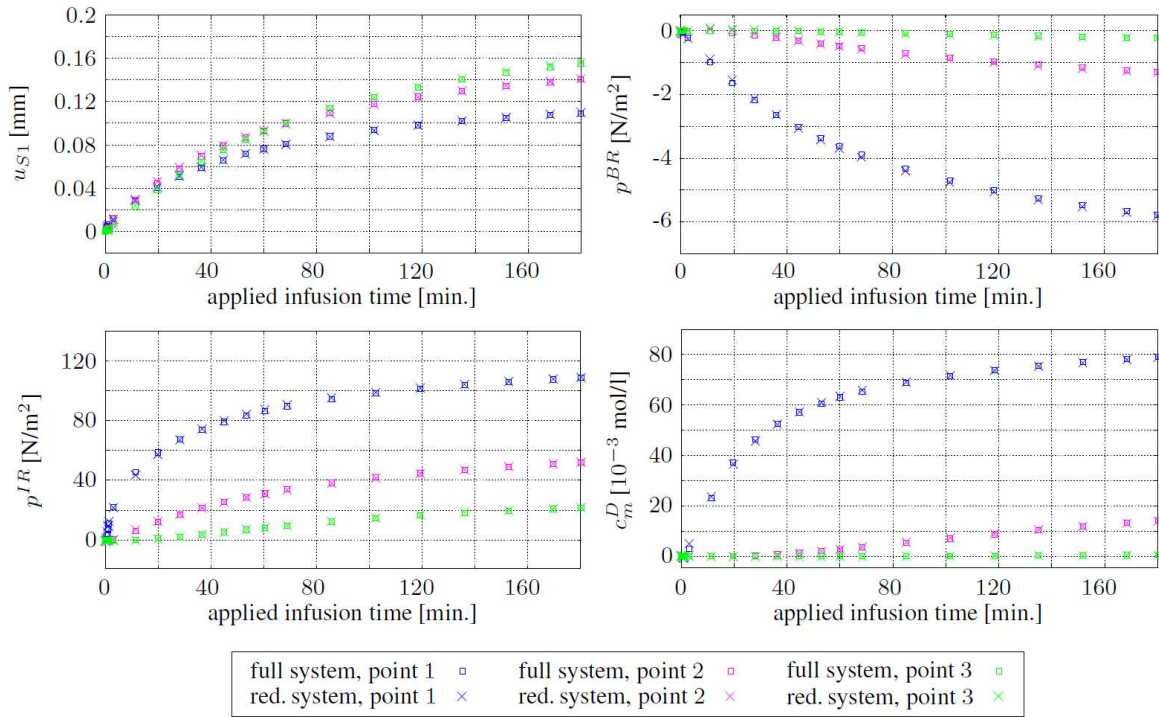


**Figure 9.18:** Values of the solid displacement  $u_{S1}$  in coronal direction, the effective pore-liquid pressures  $p^{BR}$  and  $p^{IR}$  and the molar concentration  $c_m^D$  at selected points 1, 2 and 3 obtained by the full system (squares) and the reduced system (crosses).

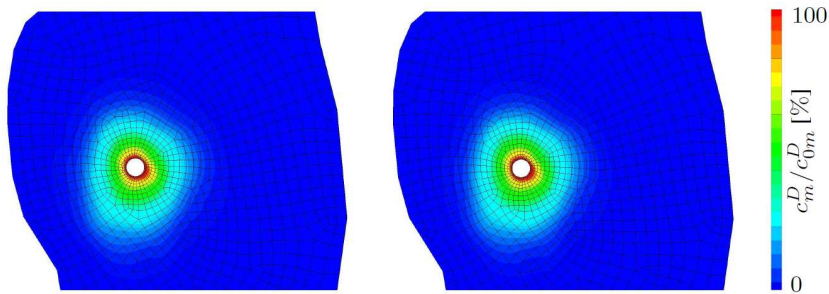


**Figure 9.19:** Therapeutical spreading at the end of an infusion process under anisotropic conditions, computed with the full system (left) and the reduced system (right).

This leads to a significant reduction of the computing time in the online phase, cf. Table 9.4.

**Results for material parameter variations:** In a next step, the reduced model is investigated in terms of the accuracy for changing material parameters to demonstrate the usefulness of the POD-DEIM with relevant test cases. Therefore, the data set of the pre-computations also contains snapshots for different material parameters. Here, the solid skeleton stiffness is exemplarily varied in the elastic material constants  $\mu_0^S$  and  $\lambda_0^S$ . This contribution does not focus on the selection of the snapshots (neither with regard to an optimal snapshot choice in terms of the time steps nor in terms of the

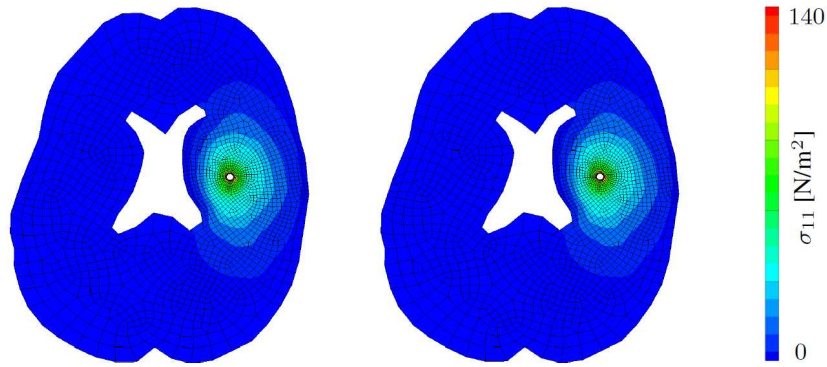


**Figure 9.20:** Stress  $\sigma_{11}$  at the end of an infusion process under anisotropic conditions, computed with the full system (left) and the reduced system (right).

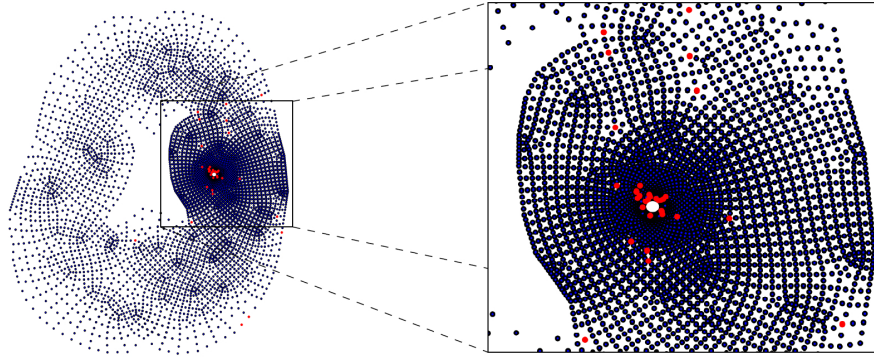


**Figure 9.21:** Evaluated DEIM points within the domain: all 47 corresponding nodes of the selected DOF (left) and zoom into the area of interest (right).

material parameters). Instead, the snapshot selection should be kept as short and simple as possible. For this reason, the material parameters used in the pre-computations are chosen with physical intuition as the minimum ( $\mu_0^S = 1000 \text{ N/m}^2$  and  $\lambda_0^S = 5000 \text{ N/m}^2$ ) and maximum ( $\mu_0^S = 10000 \text{ N/m}^2$  and  $\lambda_0^S = 50000 \text{ N/m}^2$ ) values of the assumed value range and combinations thereof to cover the expected value range of these parameters. In these pre-computations, the snapshots of the primary variables are stored in all time steps and the snapshots of the non-linear terms in all Newton steps. However, a more systematic (and automatic) strategy would be preferable to select the snapshots, especially when varying a large number of material parameters. Afterwards, the simulation is performed for two test cases with different values of the elastic material constants (test case 1:  $\mu_0^S = 5000 \text{ N/m}^2$  and  $\lambda_0^S = 30000 \text{ N/m}^2$ , test case 2:  $\mu_0^S = 8000 \text{ N/m}^2$  and  $\lambda_0^S = 10000 \text{ N/m}^2$ ) to prove the usefulness of the reduced system. In Figure 9.22, the simulation

**Table 9.4:** Computing time on a single core of an Intel i5-4590 with 32 GB of memory running at clock speed of 3.30 GHz (online phase), obtained by the full and the reduced system with 18 POD modes and 47 DEIM modes.

	time solving eq. system	time write out data	total CPU time
full system	156 min	8 min	164 min
reduced system	3 min	8 min	11 min

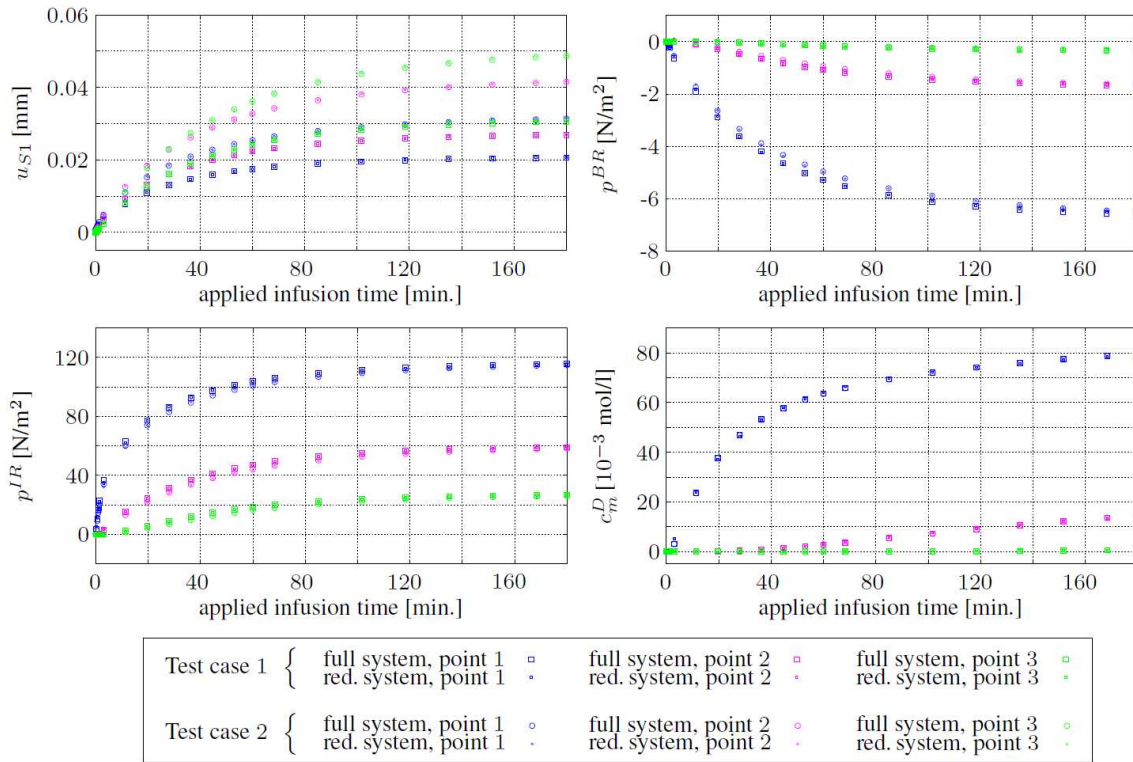


**Figure 9.22:** Values of different primary variables at selected points 1-3 for a variation in the material parameters (test case 1: squares, test case 2: circles), obtained by the full system (large dots) and the reduced system (small dots).

results of the primary variables at selected points 1-3 (cf. Figure 9.17) are shown for both test cases. A variation of the elastic material constants strongly influences the solid displacement. The influence on the pore-liquid pressures is weak and the concentration is almost unaffected. Comparing the results with the reference solutions of the full system, the accuracy of the primary variables is ensured. The same applies for the corresponding stresses. Regarding the computational effort, the time for the generation of the reduced system (offline phase) occurs particularly from pre-computations in the full system (here around 140 minutes per simulation), the pre-computations in the POD-reduced system (here around 75 minutes per simulation), the saving of the snapshots for the POD method and the DEIM (here less than 10 minutes) and the computation of the reduction matrices  $\Phi$ ,  $\Psi$  and  $P$  (here around 47 minutes). The time to solve the equation system for one simulation with a given set of material parameters in the online phase is reduced from around 180 minutes (full system) to around 3 minutes (reduced system). Additionally, both kinds of simulations need around 5 minutes to read in the patient specific data and 8 minutes to write out all necessary data. Following this, performing more than five reduced simulations leads already to a time saving (sum up the times of the offline and the online phase) which grows significantly when performing more reduced simulations, see Table 9.5. As the computational effort is split in a costly offline phase that is performed only once and an inexpensive online phase that is performed in every reduced simulation, fast simulations during a clinical routine becomes possible. There, the computing time of the offline phase plays only a minor role. Furthermore, multiple simulations with varying

Table 9.5: Computing time on a single core of an Intel i5-4590 with 32 GB of memory running at clock speed of 3.30 GHz for different numbers of performed simulations, obtained by the full and the reduced system when taking into account the time for the offline phase.

	offline phase		online phase					
number of simulations	arbitrary	1	2	3	5	10	20	50
full system [min]	0	193	386	579	965	1930	3860	9650
reduced system [min]	917	16	32	48	80	160	320	800

material parameters or infusion boundary conditions become increasingly time efficient.

### 9.6.6 Discussion

The application of the POD method and the POD-DEIM based on a multi-component brain-tissue model showed that the numerical effort to solve the linearised system of equations in each iteration step can be reduced significantly. Thereby, the computational effort was split up to a costly offline phase and an inexpensive online phase. Since the offline phase is computed only once, the time saving especially grows when multiple reduced simulations are performed. Therefore, fast simulations are feasible due to the cheap online phase of reduced models. This allows the justified desire to realise even real-time simulations during clinical routines in the near future. Moreover, the presented work demonstrated that the requirements concerning the accuracy of the results can be also satisfied. In particular, this was achieved by a customised adaptation of the POD method, where a split of the snapshot matrix (yielding separated reduction matrices) was necessary due to the different time-dependent behaviour of the particular primary variables. Moreover, the properties of the firstly discussed simplified model resulted in a system with constant system matrices. In general, this is not necessarily the case and may also lead to a nonlinear system with non-constant system matrices as was shown by a second example using the general model. For such problems, the nonlinear terms still need to be computed with the full amount of degrees of freedom. To overcome this drawback, the POD method was extended for nonlinear systems by a further combination with the DEIM. For both approaches, accurate results have been obtained for the reduced simulations. In addition, a variation of simulation parameters, i. e. material parameters or infusion boundary conditions, was discussed in the presented contribution.

An aspect that has not been discussed here is the selection of considered snapshots (neither with regard to an optimal snapshot choice in terms of the time steps nor in terms of material parameters). However, a suitable selection can significantly improve the reduced simulation results. On the one hand, only states and phenomena which are represented by the snapshot data set can be properly represented by the reduced system (for which the results can only be as good as the used data). On the other hand, too many (especially the consideration of irrelevant) snapshots can diminish the results and the necessary number of POD modes. Regarding the selection of the snapshots with respect to the parameter variation, a uniform distribution can be a good choice if only few parameters need to be varied and/or less information about the variable distribution is available. However,

a systematic and automatic strategy is in general preferable to select the snapshots, especially if many parameters are varied. In this regard, there are certainly various open issues which still need to be considered. However, the presented approach provides the possibility to run a variety of simulations with changing material/simulation parameters in a considerably less time with the perspective to realise even real-time simulations during clinical interventions.  $\ll$ (p. 141)

## 9.7 Simulation of brain tumours

For humans, cancer is one of the most leading causes of death, cf. the World Cancer Report of 2014 [289] and the related webpage<sup>3</sup> of the WHO. Basically, cancer arises from normal cells which are transformed into tumour cells. Although cancer cells are produced in humans every day (in a very small number), these cells are usually eliminated (as desired) by the immune system. Conventionally, we are talking about cancer if a malignant tumour is formed during a multistage process from a pre-cancerous lesion. The individual processes are commonly subdivided into the famous hallmarks of cancer, cf. Hanahan & Weinberg [137]. The genesis is caused by the interaction between a person's genetic factors and external agents, such as physical (e.g. ionising radiation), chemical (e.g. tobacco smoke) or biological (e.g. virus infections) carcinogens.

The problem with cancer is the rapid creation of abnormal cells, resulting in a space-demanding growth process. This leads to an invasion of adjoining parts of the body and, even more serious, to a spreading towards other organs, known as metastasis. In this regard, metastases represent a major cause of death from cancer.

Therefore, a general TPM model for the description of metastatic processes is presented in this section. The application of the model is customised to lung-cancer metastases proliferation within brain tissue, a frequently occurring case.

BIBLIOGRAPHIC NOTE: The content of this section is composed by merging and extending a series of proceedings of Schröder *et al.* [241, 242, 243, 244, 245, 246].

### 9.7.1 Model adaptation

» The basic TPM model for brain tissue, cf. Ehlers & Wagner [93], is further extended to include tumour growth and regression processes. The modelling approach basically proceeds from three constituents  $\varphi^\alpha$ , where the placeholder  $\alpha = \{S, B, I\}$  indicates a solid skeleton  $\varphi^S$  with its two saturating pore-liquids  $\varphi^\beta$  with  $\beta = \{B, I\}$  standing for the blood  $\varphi^B$  and the interstitial fluid  $\varphi^I$ . These basic constituents are adopted to describe tumour-related processes. Thus, the solid skeleton is subdivided into brain cells  $\varphi^{SB}$  and lung-cancer metastases  $\varphi^{SC}$ . The blood constituent  $\varphi^B$  is maintained as a single liquid  $\varphi^{BL}$ , while the interstitial fluid  $\varphi^I$  is treated as a mixture of multiple components  $\varphi^{I\gamma}$  with  $\gamma = \{L, N, C, V, D\}$ . In particular,  $\varphi^I$  consists of a liquid solvent  $\varphi^{IL}$ , nutrients  $\varphi^{IN}$ ,

<sup>3</sup><https://www.who.int/news-room/fact-sheets/detail/cancer>, retrieved 31 January 2020.

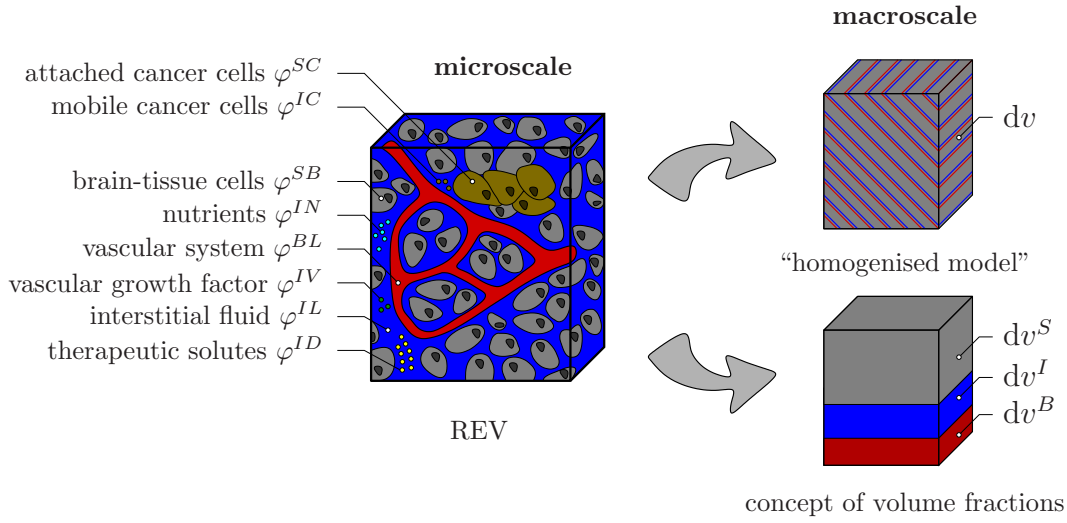


**Figure 9.23:** Representative elementary volume with exemplarily displayed micro-structure of tumour-affected brain tissue and macroscopic multiphasic and multicomponential modelling approach.

cancer cells  $\varphi^{IC}$ , a vascular growth factor (VEGF)  $\varphi^{IV}$  and a drug  $\varphi^{ID}$ , cf. Figure 9.23. Thus, the description of the metastatic processes yield the following modelling ansatz

$$\varphi = \bigcup_{\alpha} \varphi^{\alpha} = \varphi^S \cup \varphi^B \cup \varphi^I, \quad \text{with} \quad \begin{cases} \varphi^S = \varphi^{SB} \cup \varphi^{SC}, \\ \varphi^B = \varphi^{BL}, \\ \varphi^I = \varphi^{IL} \cup \varphi^{IN} \cup \varphi^{IC} \cup \varphi^{IV} \cup \varphi^{ID}. \end{cases} \quad (9.24)$$

The premise of suited preliminary assumptions within a closed-system approach (where no mass interactions with the blood constituent occur) leads to the volume balances of the blood and the overall interstitial fluid mixture via

$$\begin{aligned} (n^B)'_S + \operatorname{div}(n^B \mathbf{w}_B) + n^B \operatorname{div}' \mathbf{x}_S &= 0, \\ (n^I)'_S + \operatorname{div}(n^I \mathbf{w}_I) + n^I \operatorname{div}' \mathbf{x}_S &= \hat{n}^I. \end{aligned} \quad (9.25)$$

In contrast, the solid's volume balance is analytically integrated, cf. (6.12), yielding

$$n^S = n_{0S}^S \exp\left(\int_{t_0}^t \frac{\hat{n}^S}{n^S} dt\right) (\det \mathbf{F}_S)^{-1} =: n_g^S (\det \mathbf{F}_S)^{-1}. \quad (9.26)$$

Therein,  $n_g^S$  accounts for the growth-dependent part of the solid's volume fraction. From (9.26), it is recognised that the volume production  $\hat{n}^S$  plays a crucial role for the description of tumour growth and regression. Initially, the existence of some single cancer cells is described by their concentration. During the cancer-cell proliferation and the further infiltration into the brain tissue, a volumetric growth occurs. Thus, the cancer-cell component is subsequently described by a volume fraction after exceeding a certain critical

cancer-cell concentration, via

$$n^{ST} = \frac{n^I c_m^{IC} M_m^{IC}}{\rho^{STR}} \quad \text{for } c_m^{IC} > \tilde{c}_m^{IC} \quad \text{with } \tilde{c}_m^{IC} = \frac{\bar{N}^c}{dv^I M_m^{IC} M^C}. \quad (9.27)$$

Therein, the effective partial density  $\rho^{STR}$  of the solid tumour is found via

$$\rho^{IC} = \frac{dm^{IC}}{dv} = \underbrace{\frac{dv^{IC}}{dv}}_{n^{ST}} \underbrace{\frac{dm^{IC}}{dv^{IC}}}_{\rho^{STR}}, \quad (9.28)$$

where it is assumed that realistic densities  $\rho^{ICR} = \rho^{STR}$  are identical and the cancer-cell volume  $dv^{IC}$  equals the metastases volume  $dv^{ST}$  during an accumulation/proliferation process. In (9.27), the concentration threshold  $\tilde{c}_m^{IC}$  indicates the micrometastatic switch, related to the critical cancer-cell number  $\bar{N}^c$  [mol]. Moreover,  $M_m^{IC}$  is the molar mass of the cancer cells and  $M^C$  [1/kg] is the number of cells per mass unit. Typically, micrometastases are characterised by a specific diameter size of approximately  $500 \mu\text{m}$ , which can be related to the number  $\bar{N}_c = 28\,900$  of cells, cf. Freyer & Sutherland [112]. This yields to a cancer-cell-concentration threshold  $\tilde{c}_m^{IC} = 3.5709 \times 10^{-18}$  [mol/m<sup>3</sup>]. Besides the volume balances of the solid and the bulk (overall) fluids, the concentration balances

$$n^I (c_m^{I\gamma})'_S + n^I \operatorname{div} (c_m^{I\gamma} \mathbf{w}_{\gamma I}) + c_m^{I\gamma} \operatorname{div} (n^B \mathbf{w}_\beta) + c_m^{I\gamma} \operatorname{div} (\mathbf{u}_S)'_S - \frac{\hat{\rho}^{I\gamma}}{M_m^{I\gamma}} = 0 \quad (9.29)$$

of the interstitial fluid components  $\varphi^{\gamma I}$  and the overall (quasi-static) momentum balance

$$\mathbf{0} = \operatorname{div} \sum_{\alpha} \mathbf{T}^{\alpha} + \rho \mathbf{g} + \sum_{\alpha} \hat{\mathbf{p}}^{\alpha} \quad (9.30)$$

are providing the set of materially independent balance equations, cf. Schröder *et al.* [244]. As common, additional constitutive relations are required to close the system of equations. Basically equivalent approaches as derived for the basic brain tissue model are chosen, cf. Section 9.3. Therefore, a specific focus is led here on the description of the production terms governing tumour growth processes.

Since the modelling approach is closed for mass, a gain (or loss) of the solid is linked with a gain (or loss) of the interstitial fluid, via

$$\hat{\rho}^S + \hat{\rho}^I = 0 \quad \text{with } \hat{\rho}^I = \hat{\rho}^{IL} + \hat{\rho}^{IC} + \hat{\rho}^{IN} + \hat{\rho}^{IV} + \hat{\rho}^{ID}. \quad (9.31)$$

For example, the metastatic proliferation  $\hat{\rho}_{\oplus IN}^{SC}$  corresponds to its nutrient consumption  $\hat{\rho}_{\ominus SC}^{IN}$ . In particular, the nutrients are supplying the cancer cells with energy for basal reactions as well as their proliferation. Thereby, nutrients are only consumed by the cancer cells during the proliferation process, cf. Guppy *et al.* [133]. All further substances needed for the cell proliferation are assumed to be available in a sufficient amount. In malnutrition states, i. e. undersupply of nutrients, the solid skeleton (cancer and regular cells) will undergo a necrotic process via  $\hat{\rho}_{\ominus IN}^{SC}$  and  $\hat{\rho}_{\ominus IN}^{SB}$ . In addition, the apoptosis reaction  $\hat{\rho}_{\ominus ID}^{SC}$  based on the effect of the therapeutic agent is also considered resulting in

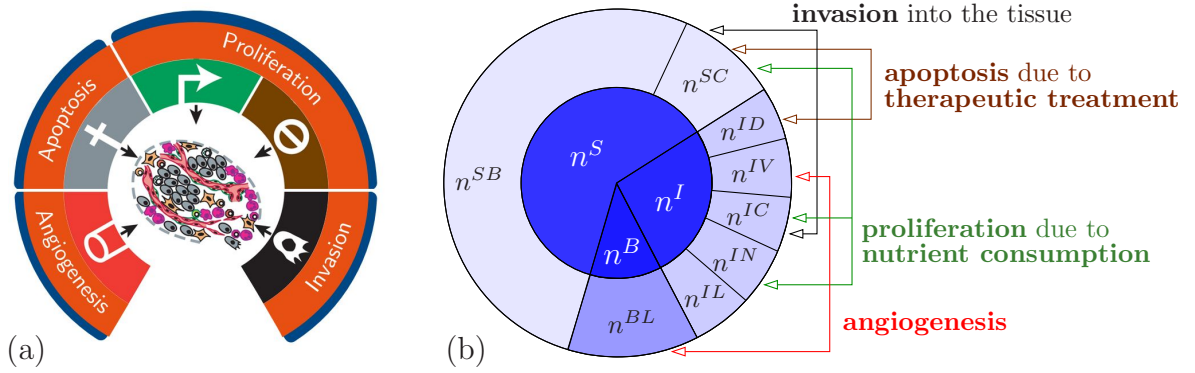


**Figure 9.24:** (a) selected cancer processes adopted from Hanahan & Weinberg [137] and (b) related mass (volume) interactions in the metastases model. Proliferation appears through nutrient consumption, whereas atrophy is either related to insufficient nutrient supply (necrosis) or apoptosis which can be caused by the presence of a drug. These processes interchange volume (mass) between the solid and the interstitial fluid.

the mass loss term. In conclusion, the mass-production term of the solid skeleton is found as

$$\hat{\rho}^S = \hat{\rho}_{\oplus,IN}^{SC} - \hat{\rho}_{\ominus,IN}^{SC} - \hat{\rho}_{\ominus,ID}^{SC} - \hat{\rho}_{\ominus,IN}^{SB}. \quad (9.32)$$

For the description of the individual mass production terms, Monod-like kinetics are used in accordance to Ambrosi & Preziosi [4], Shelton [248] and Gray *et al.* [128]. Basically, the constitutive approaches are subdivided for the constituents and the dissolved components. For example, the growth and atrophy (due to therapeutical treatment) can be modelled via

$$\begin{aligned} \hat{\rho}_{\oplus,IN}^{SC} &= \rho^{SC} \mu_{SC,\max} \frac{c_m^{IN} - \bar{c}_m^{IN}}{K_{gr} + (c_m^{IN} - \bar{c}_m^{IN})}, \\ \hat{\rho}_{\ominus,ID}^{SC} &= \rho^{SC} \mu_{SC,\max} \frac{c_m^{ID} - \bar{c}_m^{ID}}{K_{gr} + (c_m^{ID} - \bar{c}_m^{ID})}. \end{aligned} \quad (9.33)$$

Therein, the rate  $\mu_{SC,\max}$  characterises the maximal reaction rate and the value  $K_{gr}$  indicates the concentration at which the maximal reaction rate reaches half of its value.

### 9.7.2 Numerical example of apoptosis due to therapeutic treatment

As it is required for the finite-element procedure, the governing equations are transformed into weak forms. In particular, the balance of momentum

$$\begin{aligned} \int_{\Omega} \left( \sum_{\alpha} \mathbf{T}^{\alpha} \right) \cdot \text{grad } \delta \mathbf{u}_S \, dv - \int_{\Omega} \rho \mathbf{g} \cdot \delta \mathbf{u}_S \, dv - \\ - \int_{\Gamma} \bar{\mathbf{t}} \cdot \delta \mathbf{u}_S \, da - \int_{\Omega} \sum_{\alpha} (\hat{\rho}^{\alpha} \dot{\mathbf{x}}_{\alpha}) \cdot \delta \mathbf{u}_S \, dv = 0, \end{aligned} \quad (9.34)$$

where  $\bar{\mathbf{t}} = \sum_{\alpha} \mathbf{T}^{\alpha} \cdot \mathbf{n}$  is the total external load vector acting as a Neumann boundary condition. In the same manner, the volume balances of the overall interstitial fluid and

the blood are obtained in their weak forms, viz.:

$$\begin{aligned} & \int_{\Omega} \left\{ (n^{\beta})'_S + n^{\beta} \operatorname{div} (\mathbf{u}_S)'_S - \hat{n}^{\beta} \right\} \delta p^{\beta R} dv - \\ & - \int_{\Omega} n^{\beta} \mathbf{w}_{\beta} \cdot \operatorname{grad} \delta p^{\beta R} dv + \int_{\Gamma} \bar{v}^{\beta} \delta p^{\beta R} da = 0, \end{aligned} \quad (9.35)$$

where  $\bar{v}^{\beta} = n^{\beta} \mathbf{w}_{\beta} \cdot \mathbf{n}$  is the pore liquid's volumetric efflux. The dissolved species of the interstitial-fluid mixture are described by the weak formulations of the concentration balances via

$$\begin{aligned} & \int_{\Omega} \left\{ n^I (c_m^{I\gamma})'_S + c_m^{I\gamma} \operatorname{div} (\mathbf{u}_S)'_S + c_m^{I\gamma} \operatorname{div} (n^B \mathbf{w}_{\beta}) - \frac{\hat{\rho}^{I\gamma}}{\rho_I^{I\gamma}} \right\} \delta c_m^{I\gamma} dv - \\ & - \int_{\Omega} n^I c_m^{I\gamma} \mathbf{w}_{I\gamma} \cdot \operatorname{grad} \delta c_m^{I\gamma} dv + \int_{\Gamma} \bar{j}^{I\gamma} \delta c_m^{I\gamma} da = 0. \end{aligned} \quad (9.36)$$

Therein,  $\bar{j}^{\beta\gamma} = n^{\beta} c_m^{\beta\gamma} \mathbf{w}_{\gamma} \cdot \mathbf{n}$  are the molar fluxes. Basically, the choice of governing equations and the constitutive setting of included secondary variables is in accordance to the basic brain-tissue model which is further developed in terms of the considered production terms.

**Parameter identification and optimisation based on experimental data:** Due to the large number of model parameters, a high uncertainty is found for a quantitative description. Partly, this problem can be solved by accounting for data obtained from measured experiments. Thereby, a first step is to identify which parameters are sensitive for the currently considered process and in a second step to optimise these crucial parameters.

The parameter identification is based on the parameter-sampling method originated from Morris [209] and the introduced sensitivity measure of Campolongo *et al.* [52]. In this context, the deviation between the model and the data is denoted as the model output  $y$ . The dependency of  $y$  on each parameter is evaluated using the elementary effect

$$EE(p_i) = \frac{y_1(p_1, \dots, p_i + \Delta, p_k) - y_2(p_1, \dots, p_i, p_k)}{\Delta}, \quad (9.37)$$

introduced by Morris [209] and further improved in Campolongo *et al.* [52]. Therein, the change of the model output  $y$  is computed by modifying one of the  $k$  parameters  $p_i$  with a specific step size  $\Delta$ . Then, the two model outputs  $y_1$  and  $y_2$  are compared to each other in (9.37). This process is repeated until all parameters have been changed, cf. Morris [209] or King & Perera [166]. The final quantity of interest in determining the importance of a parameter is achieved by the absolute mean

$$\mu_i^* = \sum_i |EE(p_i)| / r, \quad (9.38)$$

of all  $r$  absolute elementary effects of the parameter  $p_i$ . The calculated mean  $\mu_i^*$  related to a parameter allows for the comparison between the other parameters. Consequently, the

parameters with the highest values are considered as most significant, cf. King & Perera [166]. However, the introduced method allows only for a (sensitivity) ordering of the parameters. The actual choice of relevant parameters needs still to be decided manually by the user.

In a second step, the parameter-optimisation strategy is based on the maximum likelihood estimation, cf. Myung [213]. To relate the simulation results  $y_{\text{simu}}$  to the measured data  $y_{\text{data}}$  an logarithmic error  $\log \epsilon = \log(y_{\text{data}}) - \log(y_{\text{simu}})$  is introduced. This error is assumed to be Gaussian distributed resulting in the likelihood function, viz.:

$$\mathcal{L} = \sum_i \log \left( \frac{1}{\sigma_i \sqrt{2\pi}} \right) - \frac{(y_{\text{data},i} - y_{\text{simu},i})^2}{2\sigma^2}. \quad (9.39)$$

Therein,  $\mathcal{L}$  is the summed likelihood function including the data at  $i$  and measurement including the variance of the data  $\sigma_i$ . In order to optimise the crucial model parameters, the likelihood function can be minimised, using e. g. the commercial software `Matlab` with its optimiser `fmincon`.

**Experimental-data based simulation of apoptosis:** As an example, the previously described procedure of parameter identification and optimisation is initially applied to data from apoptosis experiments, shown in Figure 9.25. Here, the evaluation of data for apoptosis caused by medication experiments is investigated based on in-vitro experiments

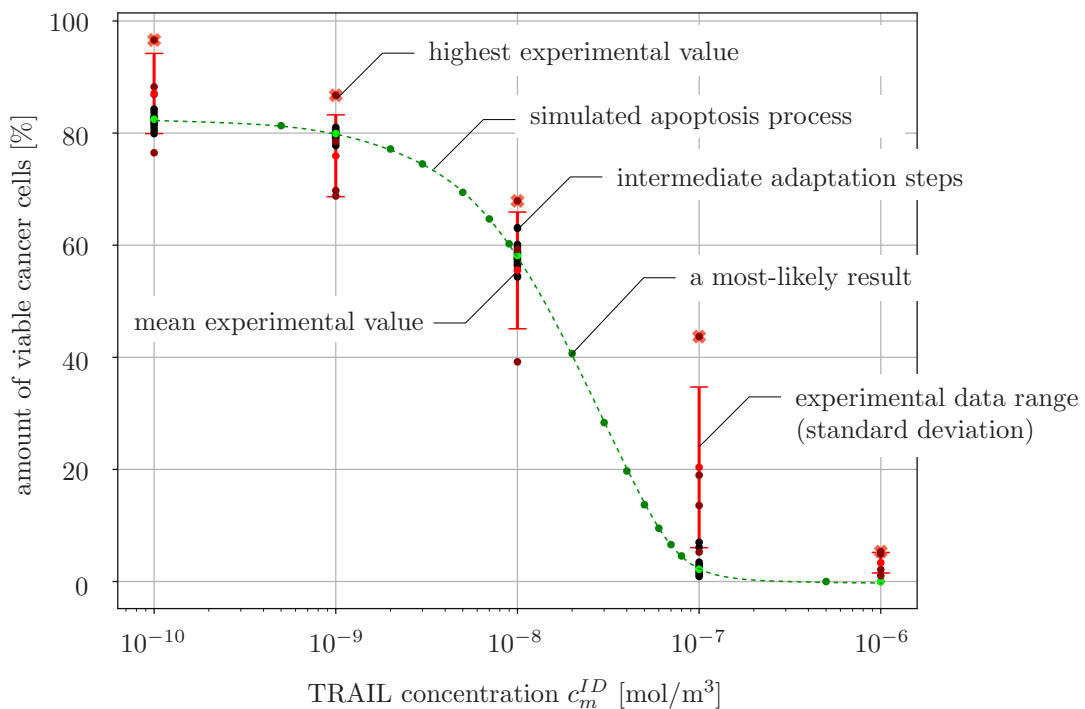


**Figure 9.25:** The mean viable cancer cell data from the experiment are depicted in red and the single viable cell ratios are depicted in dark red, whereas the cross indicates the experiment with the highest values. The simulation results resulting from the optimisation are given in black including the best result in light green. Additional simulation results corresponding to the best parameter set are given in dark green.

on cancer-cell cultures performed by the group of Markus Morrison (current head of the Institute of Cell Biology and Immunology at the University of Stuttgart). In particular, the medication represents an immediate interaction with the cancer cells, respectively the metastases, with the drug TRAIL (tumour necrosis factor-related apoptosis-inducing ligand), or more precise, four experiments investigating the response of the cancer-cell line NCI-H4600 to  $\text{Db}_{\alpha\text{EGFR}}\text{-scTRAIL}$  are considered.

As a consequence, the related apoptosis simulation results in a good quantitative agreement (within the standard deviation) compared to the experimental data. In the initial-boundary-value problem, the drug concentration is varied per simulation from  $10^{-10}$  [mol/m<sup>3</sup>] to  $10^{-6}$  [mol/m<sup>3</sup>] to map the experimental setting, cf. Figure 9.25. Dirichlet boundary condition are assigned in (9.34) to the displacement, in (9.35) to the pressures and in (9.36) to the nutrient concentration, whereas the drug flux is regulated in (9.36) by a Neumann boundary. Initially, the two-dimensional problem contains a metastases volume fraction of  $n^{SC} = 0.1$  in the centre area (diameter of 4 cm) within the circular domain (diameter of 10 cm). The system is solved numerically by the FE tool PANDAS applying Taylor-Hood elements for the spatial discretisation and an implicit Euler time-integration scheme for the temporal discretisation<sup>4</sup>. During the time period of 24 hours the metastases decline is leading to a shrinkage of the solid which extrudes the interstitial fluid and the containing death-receptor agonist into the metastases, cf. Figure 9.26.  $\ll$ (p.158)

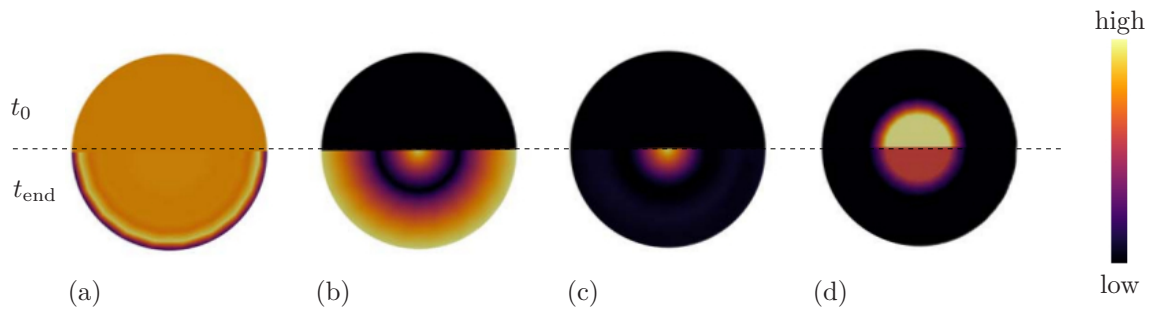


**Figure 9.26:** Simulation of apoptosis. The upper half of the circular simulation domain shows the conditions at the initial time  $t_0$ , while the lower half shows qualitative results at the final state at  $t_{\text{end}} = 24$  hours with (a) drug consumption indicated by the concentration  $c_m^{ID} \in [6.3 \cdot 10^{-8}, 1.1 \cdot 10^{-7}]$  in mol/m<sup>3</sup>, (b) outward-oriented radial solid deformation  $\mathbf{u}_S \in [-3.3 \cdot 10^{-4}, 0]$  in m, (c) outward-oriented radial seepage velocity  $\mathbf{w}_I \in [-4.8 \cdot 10^{-9}, -3.0 \cdot 10^{-12}]$  in m/s, and (d) metastases volume fraction  $n^{ST} \in [0, 0.1]$  in [-].

<sup>4</sup>If required for a more detailed (prospective) inclusion of cellular pathways, cf., e. g., Eissing *et al.* [99] for caspase activation, a ODE can be solved at each Gauss point of the domain via a forward Euler scheme to evaluate the change in the density-production terms.

# Chapter 10:

## Concluding remarks

BIBLIOGRAPHIC NOTE: The content of this section is based on the following original article: Wagner, A., Fink, D., Schröder, P. & Ehlers, W.: Towards a virtual mechanical human brain. *Proceedings in Applied Mathematics and Mechanics* **17** (2017), 225–226 [281].

» As shown in the previously discussed selected applications of continuum biomechanics, a virtual substitute (i. e. having common attributes without sharing its real physical form) allows for a prediction (via simulations) of interactions with its environment under certain conditions. In addition to the expertise of the practising clinician, modelling and simulation can contribute to further improve a personalised healthcare. In particular, if the individual risk of a specific application is high, predictive personalised simulations are urgently requested as an add-on for the clinical decision-making process. Therefore, the challenge of an overall human model (OHM) faced within SimTech (Simulation Technology is a Cluster of Excellence located at the University of Stuttgart, Germany, cf. <http://www.simtech.uni-stuttgart.de>) is very attractive. The idea is that such an OHM includes and unites already available models selected from an OHM-toolbox to bridge several scales of representation in time and space and to combine also different physical effects as well as the respective numerical methods, which are used on each scale.

As a future perspective, a transfer towards the clinic is desired. A possible procedure is shown in Figure 10.1 at the example of brain-tumour treatment. To do this, the cooperation between the research institutions and the clinics must be intensified. The motivation of the basic research is often initiated by open questions in desired clinical applications. In particular, if the risk of a specific application is very high, predictive simulations are

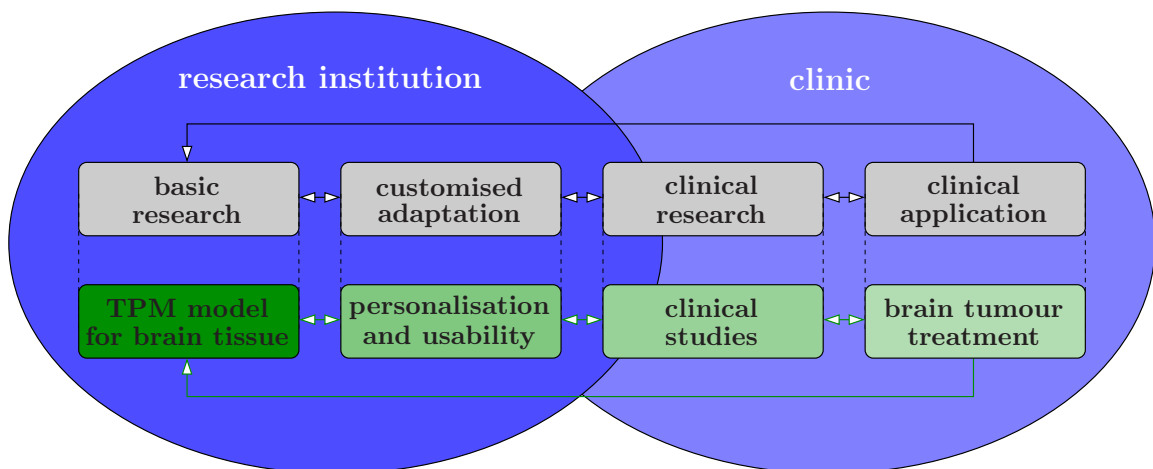


**Figure 10.1:** General schematic pathway for improved patient-specific health care (top) applied to the example of brain tumour treatment (bottom).

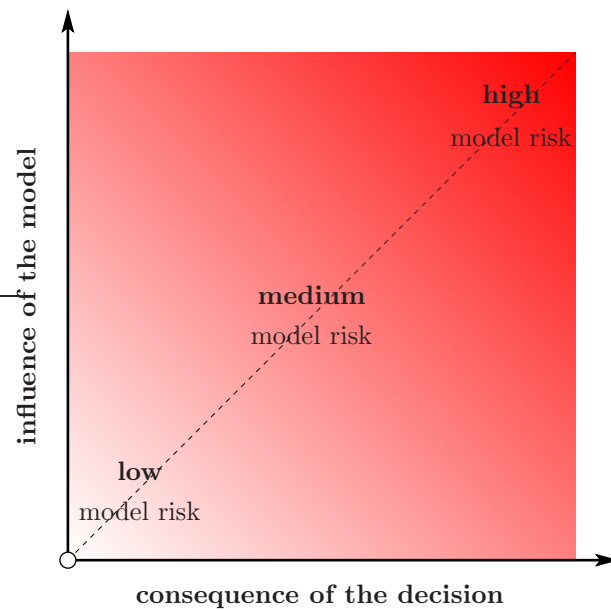


**Figure 10.2:** Illustration of model risk and medical necessity of verification and validation of computational modelling and simulation.

requested. In the specific case of the brain model, the basic research was carried out by the development of a multi-component brain tissue model, cf. Chapter 9. Therein, also the discussion of translating the knowledge toward a clinical usage and provide a bridge between basic science and human medicine is of fundamental importance. This implies, the creation of personalised models, e.g. in terms of patient-specific properties (such as geometry or permeabilities). Moreover, the immense numerical cost of a numerical simulation serves as restrictive element for clinical studies. Therefore, model-reduction techniques were applied to the model in order to allow for a parallel clinical usage. However, for this example clinical studies are still missing and hinder the transfer to a predictive medicine. Nevertheless, first promising examples already exist. Since 2018, Yosibash *et al.* [296] hold a US patent for an *automated patient-specific method for biomechanical analysis of bone*. Therein, an accompanied automated biomechanical FE analysis of a bone-implant system upon patient-specific medical-imaging data provide information for surgical planning. Furthermore, a Swedish-Austrian team around Thomas Christian Gasser has developed an analysis system for patient-specific vascular diagnostics (VAS-COPS, <http://www.vascops.com>) such as for aortic aneurysms, cf., e.g., Gasser [117]. If such a procedure is established, this can substantially contribute to bring personalised health care to a higher level. In this context, another important question concerns the required verification<sup>1</sup> and validation<sup>2</sup> of computational modelling and simulation for biomedical applications. In this regard, uncertainties resulting from the theoretical modelling approach (such as model assumptions) as well as from the numerical application (such as

<sup>1</sup>Verification can be understood as mathematical evidence. In particular, this means that the theoretical (mathematical) model is solved correctly

<sup>2</sup>Validation can be understood as “experimental” evidence by means of representing with the applied model the “reality” in a correct manner

computation errors) are of crucial importance. A possibility to obtain the required effort in verification and validation of the model is displayed in Figure 10.2.

Therein, the two axes of the diagram are occupied by the influence of the model and the consequence of the decision. In particular, the influence of the model is the contribution of the computational modelling and the numerical simulation to the decision in relation to other available evidence (such as experience of the medical doctor). The consequence of the decision is the significance of an adverse outcome (non-patient-related impacts) resulting from an incorrect decision. These two axes frame the area of model risk, where model risk can be understood as a possibility that the computational modelling and numerical simulation leads to an incorrect decision and consequently results in undesirable patient harm. «(p. 165)



# Bibliography

- [1] Acartürk, A.: *Simulation of Charged Hydrated Porous Media*. Dissertation, Report No. II-18 of the Institute of Applied Mechanics (CE), University of Stuttgart 2009.
- [2] Adami, S.; Hu, X. & Adams, N.: A generalized wall boundary condition for Smoothed Particle Hydrodynamics. *Journal of Computational Physics* **231** (2012), 7057–7075.
- [3] Altenbach, H.: *Kontinuumsmechanik: Einführung in die materialunabhängigen und materialabhängigen Gleichungen*. Springer-Verlag, Berlin 2012.
- [4] Ambrosi & Preziosi: On the closure of mass balance models for tumor growth. *Mathematical Models and Methods in Applied Sciences* **12** (2002), 737–754.
- [5] Ammann, M.: *Parallel Finite Element Simulations of Localization Phenomena in Porous Media*. Dissertation, Report No. II-11 of the Institute of Applied Mechanics (CE), University of Stuttgart 2005.
- [6] Anderson, J. A.; Glaser, J. & Glotzer, S. C.: HOOMD-blue: A Python package for high-performance molecular dynamics and hard particle Monte Carlo simulations. *Computational Materials Science* **173** (2020), 109363.
- [7] Anderson, J. A.; Lorenz, C. D. & Travesset, A.: General purpose molecular dynamics simulations fully implemented on graphics processing units. *Journal of Computational Physics* **227** (2008), 5342–5359.
- [8] Antoulas, A. C.: *Approximation of large-scale dynamical systems*, vol. 6. Society for Industrial and Applied Mathematics (SIAM), Philadelphia 2005.
- [9] Antoulas, A. C. & Sorensen, D. C.: Approximation of large-scale dynamical systems: An overview. *Applied Mathematics and Computer Science* **11** (2001), 1093–1122.
- [10] Aselli, G.: *De lactibus, sive lacteis venis, quarto vasorum mesaraicorum genere, novo invento Gasparis Asellii*. J. Maire 1640.
- [11] Baroud, G.; Crookshank, M. & Bohner, M.: High-Viscosity Cement Significantly Enhances Uniformity of Cement Filling in Vertebroplasty: An Experimental Model and Study on Cement Leakage. *Spine* **31** (2006), 2562–2568.
- [12] Baroud, G.; Falk, R.; Crookshank, M.; Sponagel, S. & Steffen, T.: Experimental and theoretical investigation of directional permeability of human vertebral cancellous bone for cement infiltration. *Journal of Biomechanics* **37** (2004), 189–196.
- [13] Baroud, G.; Wu, J. Z.; Bohner, M.; Sponagel, S. & Steffen, T.: How to determine the permeability for cement infiltration of osteoporotic cancellous bone. *Medical Engineering & Physics* **25** (2003), 283–288.

- [14] Barrande, M.; Bouchet, R. & Denoyel, R.: Tortuosity of porous particles. *Analytical Chemistry* **79** (2007), 9115 – 9121.
- [15] Barrault, M.; Maday, Y.; Nguyen, N. C. & Patera, A. T.: An ‘empirical interpolation’ method: application to efficient reduced-basis discretization of partial differential equations. *Comptes Rendus Mathématique* **339** (2004), 667–672.
- [16] Bartel, F.; Ricken, T.; Schröder, J. & Bluhm, J.: A two-scale homogenisation approach for fluid saturated porous media based on TPM and FE<sup>2</sup>-method. *Proceedings in Applied Mathematics and Mechanics* **15** (2015), 447–448.
- [17] Basar, Y. & Krätzig, W. B.: *Mechanik der Flächentragwerke: Theorie, Berechnungsmethoden, Anwendungsbeispiele*. Springer-Verlag 2013.
- [18] Basser, P. J.: Interstitial pressure, volume, and flow during infusion into brain tissue. *Microvascular Research* **44** (1992), 143–165.
- [19] Basser, P. J.; Mattiello, J. & Lebihan, D.: Estimation of effective self-diffusion tensor from the NMR spin-echo. *Journal of Magnetic Resonance* **103** (1994), 247–254.
- [20] Bathe, K. J.: *Finite-Elemente-Methoden*. 2nd edn. Springer-Verlag, Berlin 2002.
- [21] Baxter, L. T. & Jain, R. K.: Transport of fluid and macromolecules in tumors: I. role of interstitial pressure and convection. *Microvascular Research* **37** (1989), 77–104.
- [22] Beaudoin, A.; Mihalko, W. M. & Krause, W. R.: Finite element modelling of polymethylmethacrylate flow through cancellous bone. *Journal of Biomechanics* **24** (1991), 127–136.
- [23] Bennethum, L. S. & Cushman, J. H.: Multiscale, hybrid mixture theory for swelling systems – I: balance laws. *International Journal of Engineering Science* **34** (1996), 125–145.
- [24] Berkooz, G.; Holmes, P. & Lumley, J. L.: The proper orthogonal decomposition in the analysis of turbulent flows. *Annual Review of Fluid Mechanics* **25** (1993), 539–575.
- [25] Biot, M. A.: General theory of three-dimensional consolidation. *Journal of Applied Physics* **12** (1941), 155–164.
- [26] Bleiler, C.: *Application of medical imaging to simulate anisotropic flow in porous media*. Diplomarbeit, Report No. 12-II-9 of the Institute of Applied Mechanics (CE), University of Stuttgart 2012.
- [27] Bleiler, C.; Wagner, A.; Stadelmann, V. A.; Windolf, M.; Köstler, H.; Boger, A.; Gueorguiev-Rüegg, B.; Ehlers, W. & Röhrle, O.: Multiphasic modelling of bone-cement injection into vertebral cancellous bone. *International Journal for Numerical Methods in Biomedical Engineering* **31** (2015), 37–57.

- [28] Blemker, S. S.; Pinsky, P. M. & Delp, S. L.: A 3D model of muscle reveals the causes of nonuniform strains in the biceps brachii. *Journal of Biomechanics* **38** (2005), 657–665.
- [29] Bluhm, J.; Serdas, S. & Schröder, J.: Theoretical framework of modeling of ionic EAPs within the Theory of Porous Media. *Archive of Applied Mechanics* **86** (2016), 3–19.
- [30] Bobo, R. H.; Laske, D. W.; Akbasak, A.; Morrison, P. F.; Dedrick, R. L. & Oldfield, E. H.: Convection-enhanced delivery of macromolecules in the brain. *Proceedings of the National Academy of Sciences* **91** (1994), 2076–2080.
- [31] de Boer, R.: Highlights in the historical development of porous media theory: toward a consistent macroscopic theory. *Applied Mechanics Review* **49** (1996), 201–262.
- [32] de Boer, R.: *Theory of Porous Media*. Springer-Verlag, Berlin 2000.
- [33] de Boer, R.: Reflections on the development of the theory of porous media. *Applied Mechanics Reviews* **56** (2003), R27–R42.
- [34] de Boer, R.: *Trends in continuum mechanics of porous media, Vol. 18*. Theory and applications of transport in porous media, Springer, Dordrecht 2005.
- [35] de Boer, R. & Ehlers, W.: A historical review of the formulation of porous media theories. *Acta Mechanica* **74** (1988), 1–8.
- [36] Boger, A. & Wheeler, K.: A Medium Viscous Acrylic Cement Enhances Uniformity of Cement Filling and Reduces Leakage in Cancellous Bone Augmentation. *ISRN Materials Science* **2011** (2011).
- [37] Bohner, M.; Gasser, B.; Baroud, G. & Heini, P. F.: Theoretical and experimental model to describe the injection of a polymethylmethacrylate cement into a porous structure. *Biomaterials* **24** (2003), 2721–2730.
- [38] Bonet, J. & Lok, T.-S.: Variational and momentum preservation aspects of Smooth Particle Hydrodynamic formulations. *Computer Methods in applied mechanics and engineering* **180** (1999), 97–115.
- [39] BÖSL Medizintechnik GmbH: lymphamat gradient 12 gradient intermittent compression for specific treatment of lymphatic oedema (2014), URL [http://www.boesl-med.de/download/lymphamat\\_E.pdf](http://www.boesl-med.de/download/lymphamat_E.pdf).
- [40] Bowen, R. M.: Toward a thermodynamics and mechanics of mixtures. *Archive for Rational Mechanics and Analysis* **24** (1967), 370–403.
- [41] Bowen, R. M.: Theory of mixtures. In Eringen, A. C. (ed.): *Continuum Physics, Vol. 3*. Academic Press, New York 1976, pp. 1–127.

- [42] Bowen, R. M.: Incompressible porous media models by use of the theory of mixtures. *International Journal of Engineering Science* **18** (1980), 1129–1148.
- [43] Bowen, R. M.: Compressible porous media models by use of the theory of mixtures. *International Journal of Engineering Science* **20** (1982), 697–735.
- [44] Braess, D.: *Finite Elemente*. Springer-Verlag, Berlin 1997.
- [45] Brezzi, F. & Fortin, M.: *Mixed and Hybrid Finite Element Methods*. Springer-Verlag, New York 1991.
- [46] Bringezu, G.; Hinkelthein, E.; Schreiner, O. & Wenz, C.: Die Therapieform Manuelle Lymphdrainage. In *Lehrbuch der Entstauungstherapie*. Springer Berlin Heidelberg 2014, pp. 75–165.
- [47] Brookshaw, L.: A method of calculating radiative heat diffusion in particle simulations. *Publications of the Astronomical Society of Australia* **6** (1985), 207–210.
- [48] Bryant, J. D.; David, T.; Gaskell, R. H.; King, S. & Lond, G.: Rheology of bovine bone marrow. *Proceedings of the Institution of Mechanical Engineers, Part H: Journal of Engineering in Medicine* **203** (1989), 71–75.
- [49] Budday, S.; Nay, R.; de Rooij, R.; Steinmann, P.; Wyrobek, T.; Ovaert, T. C. & Kuhl, E.: Mechanical properties of gray and white matter brain tissue by indentation. *Journal of the mechanical behavior of biomedical materials* **46** (2015), 318–330.
- [50] Budday, S.; Sommer, G.; Birkl, C.; Langkammer, C.; Haybaeck, J.; Kohnert, J.; Bauer, M.; Paulsen, F.; Steinmann, P.; Kuhl, E. *et al.*: Mechanical characterization of human brain tissue. *Acta biomaterialia* **48** (2017), 319–340.
- [51] Bui-Thanh, T.; Damodaran, M. & Willcox, K. E.: Aerodynamic data reconstruction and inverse design using proper orthogonal decomposition. *American Institute of Aeronautics and Astronautics* **42** (2004), 1505–1516.
- [52] Campolongo, F.; Cariboni, J. & Saltelli, A.: An effective screening design for sensitivity analysis of large models. *Environmental modelling & software* **22** (2007), 1509–1518.
- [53] Cardoso, L.; Fritton, P., Susannah; Gailani, G.; Benalla, M. & Cowin, S. C.: Advances in assessment of bone porosity, permeability and interstitial fluid flow. *Journal of Biomechanics* **46** (2013), 253–265.
- [54] Carew, T. E.; Vaishnav, R. N. & Patel, D. J.: Compressibility of the arterial wall. *Circulation Research* **23** (1968), 61–68.
- [55] Carman, P.: Fluid flow through granular beds. *Chemical Engineering Research and Design* **75** (1997), S32–S48.

- [56] Carman, P. C.: The determination of the specific surface of powders. *Journal of the Society of Chemical Industry* **57** (1938), 225.
- [57] Carman, P. C.: *Flow of gases through porous media*. Butterworths Scientific Publications, London 1956.
- [58] Chaturantabut, S. & Sorensen, D. C.: Discrete empirical interpolation for nonlinear model reduction. In *Decision and Control. Proceedings of the 48th Institute of Electrical and Electronics Engineers Conference*, 2009, pp. 4316–4321.
- [59] Chaturantabut, S. & Sorensen, D. C.: Nonlinear model reduction via discrete empirical interpolation. *SIAM Journal on Scientific Computing* **32** (2010), 2737–2764.
- [60] Chaturantabut, S. & Sorensen, D. C.: Application of POD and DEIM on dimension reduction of non-linear miscible viscous fingering in porous media. *Mathematical and Computer Modelling of Dynamical Systems* **17** (2011), 337–353.
- [61] Chen, X. & Sarntinoranont, M.: Biphasic finite element model of solute transport for direct infusion into nervous tissue. *Annals of Biomedical Engineering* **35** (2007), 2145–2158.
- [62] Chevalier, Y.; Pahr, D.; Charlebois, M.; Heini, P.; Schneider, E. & Zysset, P.: Cement Distribution, Volume, and Compliance in Vertebroplasty: Some Answers From an Anatomy-Based Nonlinear Finite Element Study. *Spine* **33** (2008), 1722–1730.
- [63] Chikly, B.: Who discovered the lymphatic system? *Lymphology* **30** (1997), 186–193.
- [64] Class, H.: *Models for non-isothermal compositional gas-liquid flow and transport in porous media*. Habilitation thesis, University of Stuttgart 2007.
- [65] Cossins, P. J.: Smoothed Particle Hydrodynamics. *arXiv preprint arXiv:1007.1245* (2010).
- [66] Courant, R.; Friedrichs, K. & Lewy, H.: Über die partiellen Differenzgleichungen der mathematischen Physik. *Mathematische Annalen* **100** (1928), 32–74.
- [67] Coussy, O.; Dormieux, L. & Detournay, E.: From mixture theory to Biot’s approach for porous media. *International Journal of Solids and Structures* **35** (1998), 4619–4635.
- [68] Dalton, J.: Essay iv. on the expansion of elastic fluids by heat. *Memoirs of the Literary and Philosophical Society of Manchester* **5** (1802), 595–602.
- [69] Darcy, H.: *Les fontaines publiques de la ville de Dijon*. Dalmont 1856.
- [70] Deusser, S.; Sattig, C. & Boger, A.: Rheological and Curing Behaviour of a Newly Developed, Medium Viscous Acrylic Bone Cement. *ISRN Materials Science* **2011** (2011).

- [71] Dias, R.; Teixeira, J. A.; Mota, M. & Yelshin, A.: Tortuosity variation in a low density binary particulate bed. *Separation and Purification Technology* **51** (2006), 180–184.
- [72] Ding, D.; Kanaly, C. W.; Brady, M. L.; Mittermeyer, S.; Raghavan, R. & Sampson, J. H.: Convection-enhanced drug delivery to the brain. In Jain, K. K. (ed.): *Drug Delivery to the Central Nervous System*. Humana Press, New York 2010, pp. 291–318.
- [73] Doblaré, M.; García, J. M. & Gómez, M. J.: Modelling bone tissue fracture and healing: a review. *Engineering Fracture Mechanics* **71** (2004), 1809–1840.
- [74] Durfolsky, L. J.: Numerical calculation of equivalent grid block permeability tensors of heterogeneous porous media. *Water Resources Research* **28** (1991), 299–708.
- [75] Dutta-Roy, T.; Wittek, A. & Miller, K.: Biomechanical modelling of normal pressure hydrocephalus. *Journal of Biomechanics* **41** (2008), 2263–2271.
- [76] Dykaar, B. B. & Kitanidis, P. K.: Determination of the effective hydraulic conductivity for heterogeneous porous media using a numerical spectral approach: 1. method. *Water Resources Research* **28** (1992), 1155–1166.
- [77] Ehlers, W.: *Vector and Tensor Calculus: An Introduction*. Lecture notes, Institute of Applied Mechanics, Chair of Continuum Mechanics, University of Stuttgart 1995–2018, <https://www.mib.uni-stuttgart.de/en/institute/team/Ehlers-00008/>.
- [78] Ehlers, W.: *Einführung in die Kontinuumsmechanik von Mehrphasenmaterialien*. Lecture notes, Institute of Applied Mechanics, Chair of Continuum Mechanics, University of Stuttgart 1997.
- [79] Ehlers, W.: *Numerische Methoden in der Mechanik*. Lecture notes, Institute of Applied Mechanics, Chair of Continuum Mechanics, University of Stuttgart 1998.
- [80] Ehlers, W.: Foundations of multiphase and porous materials. In Ehlers, W. & Bluhm, J. (eds.): *Porous Media: Theory, Experiments and Numerical Applications*. Springer-Verlag, Berlin 2002, pp. 3–86.
- [81] Ehlers, W.: Challenges of porous media models in geo- and biomechanical engineering including electro-chemically active polymers and gels. *International Journal of Advances in Engineering Sciences and Applied Mathematics* **1** (2009), 1–24.
- [82] Ehlers, W.: *Poröse Medien – ein kontinuumsmechanisches Modell auf der Basis der Mischungstheorie*. Nachdruck der Habilitationsschrift aus dem Jahre 1989 (Forschungsbericht aus dem Fachbereich Bauwesen der Universität-GH-Essen, Heft 47, Essen 1989), Bericht Nr. II-21 aus dem Institut für Mechanik (Bauwesen), Universität Stuttgart 2011.

- [83] Ehlers, W.: Porous media in the light of history. In Stein, E. (ed.): *The History of Theoretical, Material and Computational Mechanics - Mathematics Meets Mechanics and Engineering. Lecture Notes in Applied Mathematics and Mechanics* **1**. Springer-Verlag, Berlin 2014, pp. 211–227.
- [84] Ehlers, W.: Effective stresses in multiphasic porous media: A thermodynamic investigation of a fully non-linear model with compressible and incompressible constituents. *Geomechanics for Energy and the Environment* **15** (2018), 35–46.
- [85] Ehlers, W. & Eipper, G.: Finite elastic deformations in liquid-saturated and empty porous solids. *Transport in Porous Media* **34** (1999), 179–191.
- [86] Ehlers, W.; Ellsiepen, P.; Blome, P.; Mahnkopf, D. & Markert, B.: *Theoretische und numerische Studien zur Lösung von Rand- und Anfangswertproblemen in der Theorie Poröser Medien, Abschlußbericht zum DFG-Forschungsvorhaben Eh 107/6-2*. Bericht Nr. 99-II-1 aus dem Institut für Mechanik (Bauwesen), Universität Stuttgart 1999.
- [87] Ehlers, W. & Häberle, K.: Interfacial mass transfer during gas–liquid phase change in deformable porous media with heat transfer. *Transport in Porous Media* **114** (2016), 525–556.
- [88] Ehlers, W.; Karajan, N. & Markert, B.: An extended biphasic model for charged hydrated tissues with application to the intervertebral disc. *Biomechanics and Modeling in Mechanobiology* **8** (2009), 233–251.
- [89] Ehlers, W. & Luo, C.: A phase-field approach embedded in the Theory of Porous Media for the description of dynamic hydraulic fracturing. *Computer Methods in Applied Mechanics and Engineering* **315** (2017), 348–368.
- [90] Ehlers, W. & Luo, C.: A phase-field approach embedded in the Theory of Porous Media for the description of dynamic hydraulic fracturing, Part II: the crack-opening indicator. *Computer Methods in Applied Mechanics and Engineering* **341** (2018), 429–442.
- [91] Ehlers, W.; Markert, B. & Röhrle, O.: Computational continuum biomechanics with application to swelling media and growth phenomena. *GAMM-Mitteilungen* **32** (2009), 135–156.
- [92] Ehlers, W. & Wagner, A.: Constitutive and computational aspects in tumor therapies of multiphasic brain tissue. In Holzapfel, G. A. & Kuhl, E. (eds.): *Computer Models in Biomechanics*. Springer Netherlands, Dordrecht 2013, pp. 263–276.
- [93] Ehlers, W. & Wagner, A.: Multi-component modelling of human brain tissue: a contribution to the constitutive and computational description of deformation, flow and diffusion processes with application to the invasive drug-delivery problem. *Computer Methods in Biomechanics and Biomedical Engineering* **18** (2015), 861–879.

- [94] Ehlers, W. & Wagner, A.: Die Bedeutung der Mechanik für die Gesellschaft: gestern heute und morgen. *Österreichische Ingenieur- und Architekten-Zeitschrift (OIAZ)* **161** (2016), 167–171.
- [95] Ehlers, W. & Wagner, A.: Multiscale aspects in the multiphase modelling of human brain tissue. In Wriggers, P. & Lenarz, T. (eds.): *Biomedical Technology*. Springer, Cham 2018, pp. 3–13.
- [96] Ehlers, W. & Wagner, A.: Modelling and simulation methods applied to coupled problems in porous-media mechanics. *Archive of Applied Mechanics* **89** (2019), 609–628.
- [97] Ehlers, W. & Wagner, A.: Coupled problems in biological systems. In Altenbach, H. & Öchsner, A. (eds.): *Encyclopedia of Continuum Mechanics*. Springer, Berlin, Heidelberg 2020, pp. 453–465.
- [98] Ehlers, W.; Zinatbakhsh, S. & Markert, B.: Stability analysis of finite difference schemes revisited: A study of decoupled solution strategies for coupled multifield problems. *International Journal for Numerical Methods in Engineering* **94** (2013), 758–786.
- [99] Eissing, T.; Conzelmann, H.; Gilles, E. D.; Allgöwer, F.; Bullinger, E. & Scheurich, P.: Bistability analyses of a caspase activation model for receptor-induced apoptosis. *Journal of Biological Chemistry* **279** (2004), 36892–36897.
- [100] Elliott, J. & Dover, S.: X-ray microtomography. *Journal of Microscopy* **126** (1982), 211–213.
- [101] Ellsiepen, P.: *Zeit- und ortsadaptive Verfahren angewandt auf Mehrphasenprobleme poröser Medien*. Dissertation Bericht Nr. II-3 aus dem Institut für Mechanik (Bauwesen), Universität Stuttgart 1999.
- [102] Eurich, L.; Schott, R.; Shahmoradi, S.; Wagner, A.; Borja, R. I.; Roth-Nebelsick, A. & Ehlers, W.: A thermodynamically consistent quasi-double-porosity thermo-hydro-mechanical model for cell dehydration of plant tissues at subzero temperatures. *Archive of Applied Mechanics* (2021).
- [103] Eurich, L.; Schott, R.; Wagner, A.; Roth-Nebelsick, A. & Ehlers, W.: From functional properties of frost-resistant plant tissues towards customised construction materials - a continuum-mechanical approach. *Proceedings in Applied Mathematics and Mechanics* **16** (2016), 81–82.
- [104] Eurich, L.; Schott, R.; Wagner, A.; Roth-Nebelsick, A. & Ehlers, W.: Fundamentals of heat and mass transport in frost-resistant plant tissues. In Knippers, J.; Nickel, K. & Speck, T. (eds.): *Biomimetic Research for Architecture and Building Construction*. Springer, Cham 2016, pp. 97–108.

- [105] Eurich, L.; Wagner, A. & Ehlers, W.: Modelling functional properties of frost-resistant plant tissues for transfer to construction materials. In M. von Scheven; Keip, M.-A. & Karajan, N. (eds.): *Proceedings of the 7th GACM Colloquium on Computational Mechanics*. Stuttgart 2017, pp. 238–241.
- [106] Eurich, L.; Wagner, A. & Ehlers, W.: Numerical realisation of freezing processes in frost-resistant plant tissues. *Proceedings in Applied Mathematics and Mechanics* **17** (2017), 185–186.
- [107] Eurich, L.; Wagner, A. & Ehlers, W.: Coupled mass interactions in plant tissues under frost conditions. *Proceedings in Applied Mathematics and Mechanics* **18** (2018), e201800143.
- [108] Fick, A.: Über Diffusion. *Annalen der Physik und Chemie* **94** (1855), 59–86.
- [109] Fink, D.; Wagner, A. & Ehlers, W.: Application-driven model reduction for the simulation of therapeutic infusion processes in multi-component brain tissue. *Journal of Computational Science* **24** (2018), 101–115.
- [110] Foeldi, M.; Foeldi, E. & Kubik, S.: *Lehrbuch der Lymphologie für Mediziner, Masseur und Physiotherapeuten*. Urban & Fischer Verlag/Elsevier GmbH; Auflage 6, 2005.
- [111] Franceschini, G.; Bigoni, D.; Regitnig, P. & Holzapfel, G. A.: Brain tissue deforms similarly to filled elastomers and follows consolidation theory. *Journal of Mechanics and Physics of Solids* **54** (2006), 2592–2620.
- [112] Freyer, J. P. & Sutherland, R. M.: Regulation of growth saturation and development of necrosis in EMT6/Ro multicellular spheroids by the glucose and oxygen supply. *Cancer Research* **46** (1986), 3504–3512.
- [113] Fung, Y.-C.: *Biomechanics: motion, flow, stress, and growth*. Springer Verlag, New York 1990.
- [114] Fung, Y.-C.: *Biomechanics: mechanical properties of living tissues*. Springer Verlag, New York 1993.
- [115] Galante, J.; Rostoker, W. & Ray, R. D.: Physical Properties of Trabecular Bone. *Calcified Tissue Research* **5** (1970), 236–246.
- [116] Galibert, P.; Deramond, H.; Rosat, P. & Le Gars, D.: Note préliminaire sur le traitement des angiomes vertébraux par vertébroplastie percutanée. *Neurochirurgie* **33** (1987), 166–168.
- [117] Gasser, T. C.: The biomechanical rupture risk assessment of abdominal aortic aneurysms - method and clinical relevance. In Wriggers, P. & Lenarz, T. (eds.): *Biomedical Technology*. Springer, Cham 2018, pp. 233–253.

- [118] Gaul, L.; Kögl, M. & Wagner, M.: *Boundary element methods for engineers and scientists: an introductory course with advanced topics*. Springer Science & Business Media 2013.
- [119] van Genuchten, M. T.: A Closed-form Equation for Predicting the Hydraulic Conductivity of Unsaturated Soils. *Soil Science Society of America Journal* **44** (1980), 892–898.
- [120] Georgy, B. A.: Clinical Experience with High-Viscosity Cements for Percutaneous Vertebral Body Augmentation: Occurrence, Degree, and Location of Cement Leakage Compared with Kyphoplasty. *American Journal of Neuroradiology* **31** (2010), 504–508.
- [121] Gingold, R. & Monaghan, J.: Kernel estimates as a basis for general particle methods in hydrodynamics. *Journal of Computational Physics* **46** (1982), 429–453.
- [122] Gingold, R. A. & Monaghan, J. J.: Smoothed Particle Hydrodynamics: theory and application to non-spherical stars. *Monthly notices of the royal astronomical society* **181** (1977), 375–389.
- [123] Gipsen, K.: Der gefesselte Prometheus: Die Ingenieure in Großbritannien und in der Vereinigten Staaten 1750-1945. In Kaiser, W. & König, W. (eds.): *Geschichte des Ingenieurs: ein Beruf in sechs Jahrtausenden*. Hanser Verlag, München 2006, pp. 127–177.
- [124] Glaser, J.; Nguyen, T. D.; Anderson, J. A.; Lui, P.; Spiga, F.; Millan, J. A.; Morse, D. C. & Glotzer, S. C.: Strong scaling of general-purpose molecular dynamics simulations on GPUs. *Computer Physics Communications* **192** (2015), 97–107.
- [125] Goldstein, S. A.: The mechanical properties of trabecular bone: dependence on anatomic location and function. *Journal of Biomechanics* **20** (1987), 1055–1061.
- [126] Gorelick, M. & Ozsvald, I.: *High Performance Python: Practical Performant Programming for Humans*. O'Reilly Media, Inc. 2014.
- [127] Goriely, A.; Geers, M. G.; Holzapfel, G. A.; Jayamohan, J.; Jérusalem, A.; Sivaloganathan, S.; Squier, W.; van Dommelen, J. A.; Waters, S. & Kuhl, E.: Mechanics of the brain: perspectives, challenges, and opportunities. *Biomechanics and Modeling in Mechanobiology* **14** (2015), 931–965.
- [128] Gray, G. S. W.; Ferrari, M.; Decuzzi, P. & Schrefler, B.: On computational modeling in tumor growth. *Archives of Computational Methods in Engineering* **20** (2013), 327–352.
- [129] Grimm, M. J. & Williams, J. L.: Measurements of permeability in human calcaneal trabecular bone. *Journal of Biomechanics* **30** (1997), 743–745.
- [130] Gross, D.; Hauger, W.; Schröder, J. & Wall, W.: *Technische Mechanik 1: Statik*. Springer-Verlag, Berlin 2016.

- [131] Gross, D. & Seelig, T.: *Bruchmechanik mit einer Einführung in die Mikromechanik*. Springer-Verlag, Berlin Heidelberg 2011.
- [132] Günther, M. & Schmitt, S.: A macroscopic ansatz to deduce the Hill relation. *Journal of Theoretical Biology* **263** (2010), 407–418.
- [133] Guppy, M.; Leedman, P.; Zu, X. & Russell, V.: Contribution by different fuels and metabolic pathways to the total ATP turnover of proliferating MCF-7 breast cancer cells. *Biochemical Journal* **364** (2002), 309–315.
- [134] Haaverstad, R.; Romslo, I. & Myhre, H. O.: The concentration of high molecular weight compounds in interstitial tissue fluid: A study in patients with post-reconstructive leg oedema. *European Journal of Vascular and Endovascular Surgery* **13** (1997), 355–360.
- [135] Hacker, J. & Neuner, G.: Ice propagation in plants visualized at the tissue level by infrared differential thermal analysis (IDTA). *Tree physiology* **27** (2007), 1661–1670.
- [136] Hall, K. C.; Thomas, J. P. & Dowell, E. H.: Proper orthogonal decomposition technique for transonic unsteady aerodynamic flows. *American Institute of Aeronautics and Astronautics* **38** (2000), 1853–1862.
- [137] Hanahan, D. & Weinberg, R. A.: Hallmarks of cancer: the next generation. *Cell* **144** (2011), 646–674.
- [138] Hassanizadeh, M. & Gray, W. G.: General conservation equations for multi-phase systems: 2. mass, momenta, energy, and entropy equations. *Advances in Water Resources* **2** (1979), 191–203.
- [139] Hatakeyama, I. & Kato, J.: Studies on the water relation of buxus leaves. *Planta* **65** (1965), 259–268.
- [140] Haupt, P.: *Continuum Mechanics and Theory of Materials*. Springer 2002.
- [141] Hayashi, K.; Handa, H.; Nagasawa, S.; Okumura, A. & Moritake, K.: Stiffness and elastic behavior of human intracranial and extracranial arteries. *Journal of Biomechanics* **13** (1980), 175–184.
- [142] Hayward, A. T. J.: Compressibility equations for liquids: a comparative study. *British Journal of Applied Physics* **18** (1967), 965.
- [143] Heidlauf, T. & Röhrle, O.: Modeling the Chemoelectromechanical Behavior of Skeletal Muscle Using the Parallel Open-Source Software Library OpenCMISS. *Computational and Mathematical Methods in Medicine* **2013** (2013), 14 pages.
- [144] Heini, P. F.; Wälchli, B. & Berlemann, U.: Percutaneous transpedicular vertebroplasty with PMMA: operative technique and early results. A prospective study for the treatment of osteoporotic compression fractures. *European Spine Journal* **9** (2000), 445–450.

- [145] Helmig, R.: *Multiphase Flow and Transport Processes in the Subsurface*. Springer-Verlag, Berlin 1997.
- [146] Herkt, S.; Dressler, K. & Pinnau, R.: Model reduction of nonlinear problems in structural mechanics. *Report of the Fraunhofer Institute for Industrial Mathematics ITWM* **175** (2009), 1–23.
- [147] Herpertz, U.: *Ödeme und Lymphdrainage: Diagnose und Therapie-Lehrbuch der Ödematologie*. Schattauer Verlag 2013.
- [148] Hill, R. J.; Koch, D. L. & Ladd, A. J.: Moderate-Reynolds-number flows in ordered and random arrays of spheres. *Journal of Fluid Mechanics* **448** (2001), 243–278.
- [149] Hlawatsch, M.; Vollrath, J. E.; Sadlo, F. & Weiskopf, D.: Coherent structures of characteristic curves in symmetric second order tensor fields. *IEEE Transactions on Visualization and Computer Graphics* **17** (2011), 781–794.
- [150] Holzapfel, G. & Kuhl, E. (eds.): *Computer models in biomechanics: from nano to macro*, Springer 2012.
- [151] Holzapfel, G. A.: *Nonlinear Solid Mechanics: A Continuum Approach for Engineering*. Wiley, Chichester 2000.
- [152] Holzapfel, G. A. & Ogden, R. W. (eds.): *Mechanics of biological tissue*, Springer-Verlag Heidelberg, 2006.
- [153] Holzapfel, G. A. & Ogden, R. W. (eds.): *Biomechanical modelling at the molecular, cellular and tissue levels*, Springer Wien New York, 2009.
- [154] Hu, X. Y. & Adams, N. A.: A multi-phase SPH method for macroscopic and mesoscopic flows. *Journal of Computational Physics* **213** (2006), 844–861.
- [155] Hughes, T. J. R.: *The Finite Element Method: Linear Static and Dynamic Finite Element Analysis*. Dover Publications, New York 2012.
- [156] Hulme, P. A.; Boyd, S. K.; Heini, P. F. & Ferguson, S. J.: Differences in endplate deformation of the adjacent and augmented vertebra following cement augmentation. *European Spine Journal* **18** (2009), 614–623.
- [157] Humphrey, J. D.: *Cardiovascular solid mechanics: cells, tissues, and organs*. Springer-Verlag, New York, 2002.
- [158] Humphrey, J. D.: Continuum biomechanics of soft biological tissues. *Proceedings of the Royal Society of London. Series A: Mathematical, Physical and Engineering Sciences* **459** (2003), 3–46.
- [159] Hwang, C.-O.: *A new fluid permeability estimation in periodic grain consolidation models and nonoverlapping and overlapping mono-sized sphere models of porous media*. Ph.D. thesis, University of Southern Mississippi (1999).

- [160] Itskov, M. & Aksel, N.: A class of orthotropic and transversely isotropic hyperelastic constitutive models based on a polyconvex strain energy function. *International Journal of Solids and Structures* **41** (2004), 3833–3848.
- [161] Jain, R. K.: Determinants of tumor blood flow: a review. *Cancer Research* **48** (1988), 2641–2658.
- [162] Junqueira, L. C. U.; Carneiro, J. & Gratzl, M.: *Histologie*. Springer Medizin Verlag Heidelberg 2005.
- [163] Kaczmarek, M.; Subramaniam, R. P. & Neff, S. R.: The hydromechanics of hydrocephalus: steady-state solutions for cylindrical geometry. *Bulletin of Mathematical Biology* **59** (1997), 295–323.
- [164] Karajan, N.: *An Extended Biphasic Description of the Inhomogeneous and Anisotropic Intervertebral Disc*. Dissertation, Report No. II-19 of the Institute of Applied Mechanics (CE), University of Stuttgart 2009.
- [165] Kersh, M. E.; Zysset, P. K.; Pahr, D. H.; Wolfram, U.; Larsson, D. & Pandy, M. G.: Measurement of structural anisotropy in femoral trabecular bone using clinical-resolution CT images. *Journal of Biomechanics* **46** (2013), 2659–2666.
- [166] King, D. M. & Perera, B.: Morris method of sensitivity analysis applied to assess the importance of input variables on urban water supply yield – a case study. *Journal of Hydrology* **477** (2013), 17–32.
- [167] Kluge, T.: *Development and GPU-Based Implementation of an Anisotropic Non-Linear Diffusion Filter for 3D CTA Image Preprocessing*. Master’s thesis, Friedrich-Alexander-Universität Erlangen-Nürnberg. (2012).
- [168] Kohles, S. A.; Roberts, J. B.; Upton, L., Maureen; Wilson, C. G.; Bonassar, L. J. & Schlichting, A. L.: Direct perfusion measurements of cancellous bone anisotropic permeability. *Journal of Biomechanics* **34** (2001), 1197–1202.
- [169] Kolmeder, S.; Lion, A.; Landgraf, R.; Ihlemann, J.; Lebsack, H.; Kober, C. & Blatter, T. R.: Modelling and simulation of injecting acrylic bone cement into osteoporotic vertebral bones within percutaneous vertebroplasty. *Proceedings in Applied Mathematics and Mechanics* **12** (2012), 103–104.
- [170] Koponen, A.; Kataja, M. & Timonen, J.: Tortuous flow in porous media. *Physical Review E* **54** (1996), 406–410.
- [171] Kozeny, J.: Über kapillare Leitung des Wassers im Boden. *Wien, Akademie der Wissenschaften* **136(2a)** (1927), 271.
- [172] Krach, D.: *A quantitative comparison of multiscale models for single-phase flow in porous media*. Master thesis, Report Nr. 18-II-11 of the Institute of Applied Mechanics (CE), University of Stuttgart 2018.

- [173] Krischok, A. & Linder, C.: On the enhancement of low-order mixed finite element methods for the large deformation analysis of diffusion in solids. *International Journal for Numerical Methods in Engineering* **106** (2016), 278–297.
- [174] Kunisch, K. & Volkwein, S.: Control of the burgers equation by a reduced-order approach using proper orthogonal decomposition. *Journal of Optimization Theory and Applications* **102** (1999), 345–371.
- [175] Kunisch, K. & Volkwein, S.: Galerkin proper orthogonal decomposition methods for parabolic problems. *Numerische Mathematik* **90** (2001), 117–148.
- [176] Kunisch, K. & Volkwein, S.: Galerkin proper orthogonal decomposition methods for a general equation in fluid dynamics. *Society for Industrial and Applied Mathematics Journal on Numerical Analysis* **40** (2002), 492–515.
- [177] Kyriacou, S. K.; Mohamed, A.; Miller, K. & Neff, S.: Brain mechanics for neurosurgery: modeling issues. *Biomechanics and Modeling in Mechanobiology* **1** (2002), 151–164.
- [178] Laredo, J. D. & Hamze, B.: Complications of percutaneous vertebroplasty and their prevention. *Skeletal Radiology* **33** (2004), 493–505.
- [179] Laske, D. W.; Youle, R. J. & Oldfield, E. H.: Tumor regression with regional distribution of the targeted toxin TF-CRM107 in patients with malignant brain tumors. *Nature Medicine* **3** (1997), 1362–1368.
- [180] Le Bihan, D.; Mangin, J.-F.; Poupon, C.; Clark, C. A.; Pappata, S.; Molko, N. & Chabriat, H.: Diffusion tensor imaging: Concepts and applications. *Journal of Magnetic Resonance Imaging* **13** (2001), 534–546.
- [181] Lenné, T.; Bryant, G.; Hocart, C. H.; Huang, C. X. & Ball, M. C.: Freeze avoidance: a dehydrating moss gathers no ice. *Plant, cell & environment* **33** (2010), 1731–1741.
- [182] Lian, Z.; Chui, C.-K. & Teoh, S.-H.: A biomechanical model for real-time simulation of PMMA injection with haptics. *Computers in Biology and Medicine* **38** (2008), 304–312.
- [183] Libersky, L. D.; Petschek, A. G.; Carney, T. C.; Hipp, J. R. & Allahdadi, F. A.: High strain Lagrangian hydrodynamics: a three-dimensional SPH code for dynamic material response. *Journal of computational physics* **109** (1993), 67–75.
- [184] Linder, C. & Raina, A.: A strong discontinuity approach on multiple levels to model solids at failure. *Computer Methods in Applied Mechanics and Engineering* **253** (2013), 558–583, ISSN 0045-7825.
- [185] Linder, C. & Zhang, X.: A marching cubes based failure surface propagation concept for three-dimensional finite elements with non-planar embedded strong discontinuities of higher order kinematics. *International Journal for Numerical Methods in Engineering* **96** (2013), 339–372.

- [186] Linninger, A. A.; Somayaji, M. R.; Mekarsk, M. & Zhang, L.: Prediction of convection-enhanced drug delivery to the human brain. *Journal of Theoretical Biology* **250** (2008), 125–138.
- [187] Liu, L. & Schlesinger, M.: Interstitial hydraulic conductivity and interstitial fluid pressure for avascular or poorly vascularized tumors. *Journal of Theoretical Biology* **380** (2015), 1–8.
- [188] Liu, M. & Liu, G.: Smoothed Particle Hydrodynamics (SPH): an overview and recent developments. *Archives of computational methods in engineering* **17** (2010), 25–76.
- [189] Lorenz, H.: Die neuere Entwicklung der Mechanik und ihre Bedeutung für den Schiffbau. In *Jahrbuch der Schiffbautechnischen Gesellschaft*. Springer-Verlag, Berlin 1906, pp. 162–181.
- [190] Lucy, L. B.: A numerical approach to the testing of the fission hypothesis. *The astronomical journal* **82** (1977), 1013–1024.
- [191] Luding, S.: Introduction to discrete element methods: basic of contact force models and how to perform the micro-macro transition to continuum theory. *European Journal of Environmental and Civil Engineering* **12** (2008), 785–826.
- [192] Macdonald, A. J.; Arkill, K. P.; Tabor, G. R.; McHale, N. G. & Winlove, C. P.: Modeling flow in collecting lymphatic vessels: one-dimensional flow through a series of contractile elements. *American Journal of Physiology - Heart and Circulatory Physiology* **295** (2008), 305–313.
- [193] Margaris, K. N. & Black, R. A.: Modelling the lymphatic system: challenges and opportunities. *Journal of the Royal Society Interface* **9** (2011), 601–612.
- [194] Markert, B.: *Porous Media Viscoelasticity with Application to Polymeric Foams*. Dissertation, Report No. II-12 of the Institute of Applied Mechanics (CE), University of Stuttgart 2005.
- [195] Markert, B.: *Weak or strong: on coupled problems in continuum mechanics*. Habilitation, Report No. II-20 of the Institute of Applied Mechanics (CE), University of Stuttgart 2010.
- [196] Markert, B.: Coupled thermo- and electro-dynamics of multiphase continua. In *Advances in Extended and Multifield Theories for Continua*. Springer 2011, pp. 129–152.
- [197] Markert, B.; Ehlers, W. & Karajan, N.: A general polyconvex strain-energy function for fiber-reinforced materials. *Proceedings in Applied Mathematics and Mechanics* **5** (2005), 245–246.
- [198] Markert, B.; Heider, Y. & Ehlers, W.: Comparison of monolithic and splitting solution schemes for dynamic porous media problems. *International Journal for Numerical Methods in Engineering* **82** (2010), 1341–1383.

- [199] Martín, M. L.; Hernández, M. A.; Avendaño, C.; Rodríguez, F. & Martínez, H.: Manual lymphatic drainage therapy in patients with breast cancer related lymphoedema. *BMC cancer* **11** (2011), 1–6.
- [200] McCully, M. E.; Canny, M. & Huang, C.: The management of extracellular ice by petioles of frost-resistant herbaceous plants. *Annals of Botany* **94** (2004), 665–674.
- [201] Miller, K.: Method of testing very soft biological tissues in compression. *Journal of Biomechanics* **38** (2005), 153–158.
- [202] Miller, K.: *Biomechanics of the Brain*. Springer 2011.
- [203] Monaghan, J. & Gingold, R.: Shock simulation by the particle method SPH. *Journal of Computational Physics* **52** (1983), 374–389.
- [204] Monaghan, J. J.: An introduction to SPH. *Computer Physics Communications* **48** (1988), 89–96.
- [205] Monaghan, J. J.: Smoothed particle hydrodynamics. *Annual Review of Astronomy and Astrophysics* **30** (1992), 543–574.
- [206] Monaghan, J. J.: Smoothed Particle Hydrodynamics. *Reports on Progress in Physics* **68** (2005), 1703.
- [207] Monson, K. L.; Goldsmith, W.; Barbaro, N. M. & Manley, G. T.: Axial mechanical properties of fresh human cerebral blood vessels. *Journal of Biomechanical Engineering* **125** (2003), 288–294.
- [208] Morris, J. P.; Fox, P. J. & Zhu, Y.: Modeling low Reynolds number incompressible flows using SPH. *Journal of Computational Physics* **136** (1997), 214–226.
- [209] Morris, M. D.: Factorial sampling plans for preliminary computational experiments. *Technometrics* **33** (1991), 161–174.
- [210] Morrison, P. F.; Laske, D. W.; Bobo, H.; Oldfield, E. H. & Dedrick, R. L.: High-flow microinfusion: tissue penetration and pharmacodynamics. *American Journal of Physiology* **266** (1994), 292–305.
- [211] Mota, M.; Teixeira, J. & Yelshin, A.: Image analysis of packed beds of spherical particles of different sizes. *Separation and Purification Technology* **15** (1999), 59–68.
- [212] Moukalled, F.; Mangani, L.; Darwish, M. *et al.*: *The finite volume method in computational fluid dynamics*, vol. 113. Springer 2016.
- [213] Myung, I. J.: Tutorial on maximum likelihood estimation. *Journal of Mathematical Psychology* **47** (2003), 90–100.
- [214] Nauman, E. A.; Fong, K. E. & Keaveny, T. M.: Dependence of intertrabecular permeability on flow direction and anatomic site. *Annals of Biomedical Engineering* **27** (1999), 517–524.

- [215] Neethirajan, S.; Karunakaran, C.; Jayas, D. & White, N.: X-ray computed tomography image analysis to explain the airflow resistance differences in grain bulks. *Biosystems Engineering* **94** (2006), 545–555.
- [216] Negri, F.; Manzoni, A. & Amsallem, D.: Efficient model reduction of parametrized systems by matrix discrete empirical interpolation. *Journal of Computational Physics* **303** (2015), 431–454.
- [217] Nguyen, T. D.; Phillips, C. L.; Anderson, J. A. & Glotzer, S. C.: Rigid body constraints realized in massively-parallel molecular dynamics on graphics processing units. *Computer Physics Communications* **182** (2011), 2307–2313.
- [218] Ochia, R. S. & Ching, R. P.: Hydraulic Resistance and Permeability in Human Lumbar Vertebral Bodies. *Journal of Biomechanical Engineering* **124** (2002), 533–537.
- [219] Pandy, M. G.: Computer Modeling and Simulation of Human Movement. *Annual Review of Biomedical Engineering* **3** (2001), 245–273.
- [220] Prillieux, E.: Sur la formation de glaçons a l'intérieur des plantes. In *Annales des Sciences Naturelles*, 1869, vol. 12, pp. 125–134.
- [221] Rafal, R.; Wheeler, K.; Boger, A. & Bach, C.: In-vitro models concerning cement leakage and distribution using human cadaveric vertebrae are not representative in clinical relevance. *Proceeding European Spine Congress* (2009).
- [222] Raghavan, R.; Brady, M. L.; Rodriguez-Ponce, M. I.; Hartlep, A.; Pedain, C. & Sampson, J. H.: Convection enhanced delivery of therapeutics for brain disease and its optimization. *Neurosurgical Focus* **20** (2006), E12.
- [223] Reddy, N. P.: *A discrete model of the lymphatic system*. Dissertation, Texas A & M University, 1974.
- [224] Reisinger, A. G.; Pahr, D. H. & Zysset, P. K.: Elastic anisotropy of bone lamellae as a function of fibril orientation pattern. *Biomechanics and Modeling in Mechanobiology* **10** (2011), 67–77.
- [225] Rempfer, H.-U.: *Damage in Multi-Phasic Materials Computed with the Extended Finite-Element Method*. Dissertation, Report No. II-23 of the Institute of Applied Mechanics (CE), Universität Stuttgart 2012.
- [226] Renard, P. & De Marsily, G.: Calculating equivalent permeability: a review. *Advances in Water Resources* **20** (1997), 253–278.
- [227] Ricken, T. & Bluhm, J.: Remodeling and growth of living tissue: a multiphase theory. *Archive of Applied Mechanics* **80** (2010), 453–465.
- [228] Ricken, T. & de Boer, R.: Multiphase flow in a capillary porous medium. *Computational Materials Science* **28** (2003), 704–713.

- [229] Ricken, T.; Dahmen, U. & Dirsch, O.: A biphasic model for sinusoidal liver perfusion remodeling after outflow obstruction. *Biomechanics and Modeling in Mechanobiology* **9** (2010), 435–450.
- [230] Rincón-Kohli, L. & Zysset, P. K.: Multi-axial mechanical properties of human trabecular bone. *Biomechanics and Modeling in Mechanobiology* **8** (2009), 195–208.
- [231] Roden, J. S.; Canny, M. J.; Huang, C. X. & Ball, M. C.: Frost tolerance and ice formation in pinus radiata needles: ice management by the endodermis and transfusion tissues. *Functional Plant Biology* **36** (2009), 180–189.
- [232] Röhrle, O.; Davidson, J. B. & Pullan, A. J.: A physiologically based, multi-scale model of skeletal muscle structure and function. *Frontiers in Striated Muscle Physiology* **3** (2012).
- [233] Röhrle, O. & Pullan, A. J.: Three-dimensional finite element modelling of muscle forces during mastication. *Journal of Biomechanics* **40** (2007), 3363–3372.
- [234] Rowley, C. W.; Colonius, T. & Murray, R. M.: Model reduction for compressible flows using pod and galerkin projection. *Physica D: Nonlinear Phenomena* **189** (2004), 115–129.
- [235] Sarntinoranont, M.; Chen, X.; Zhao, J. & Mareci, T. M.: Computational model of interstitial transport in the spinal cord using diffusion tensor imaging. *Annals of Biomedical Engineering* **34** (2006), 1304–1321.
- [236] Sauter, L.: *Multi-component modelling of the lymphatic vessel system applied to lymphatic drainage*. Bachelor thesis, Report Nr. 16-II-3 of the Institute of Applied Mechanics (CE), University of Stuttgart 2016.
- [237] Schmitt, S.; Günther, M. & Häufle, D. F.: The dynamics of the skeletal muscle: A systems biophysics perspective on muscle modeling with the focus on Hill-type muscle models. *GAMM-Mitteilungen* **42** (2019), e201900013.
- [238] Schneider, H.: Die Techniker der Antike. In Kaiser, W. & König, W. (eds.): *Geschichte des Ingenieurs: ein Beruf in sechs Jahrtausenden*. Hanser Verlag, München 2006, pp. 33–69.
- [239] Schoenberg, I. J.: Contributions to the problem of approximation of equidistant data by analytic functions. In *IJ Schoenberg Selected Papers*. Springer 1988, pp. 3–57.
- [240] Schott, R. T.; Voigt, D. & Roth-Nebelsick, A.: Extracellular ice management in the frost hardy horsetail equisetum hyemale l. *Flora* **234** (2017), 207–214.
- [241] Schröder, P.; Wagner, A. & Ehlers, W.: Towards the continuum-mechanical modelling of metastatic tumour growth in the brain. *Proceedings in Applied Mathematics and Mechanics* **15** (2015), 107–108.

- [242] Schröder, P.; Wagner, A. & Ehlers, W.: Multi-component modelling and simulation of metastases proliferation within brain tissue. *Proceedings in Applied Mathematics and Mechanics* **16** (2016), 101–102.
- [243] Schröder, P.; Wagner, A.; Stöhr, D.; Rehm, M. & Ehlers, W.: Data-driven simulation of metastatic processes within brain tissue. *Proceedings in Applied Mathematics and Mechanics* **17** (2017), 221–222.
- [244] Schröder, P.; Wagner, A.; Stöhr, D.; Rehm, M. & Ehlers, W.: Variation of different growth descriptions in a metastatic proliferation model. In M. von Scheven; Keip, M.-A. & Karajan, N. (eds.): *Proceedings of the 7th GACM Colloquium on Computational Mechanics*. Stuttgart 2017, pp. 259–262.
- [245] Schröder, P.; Wagner, A.; Stöhr, D.; Rehm, M. & Ehlers, W.: Continuum-mechanical modelling of apoptosis. *Proceedings in Applied Mathematics and Mechanics* **19** (2019).
- [246] Schröder, P.; Wagner, A.; Stöhr, D.; Rehm, M.; Jensch, A.; Radde, N. & Ehlers, W.: Modelling of lung-metastases apoptosis within brain tissue. *Proceedings in Applied Mathematics and Mechanics* **18** (2018), e201800323.
- [247] Schwarz, H. R.: *Methode der finiten Elemente*. Teubner, Stuttgart 1991.
- [248] Shelton, S. E.: *Mechanistic Modeling of Cancer Tumor Growth Using a Porous Media Approach*. Master's thesis, University of North Carolina at Chapel Hill (2011).
- [249] Sirovich, L.: Turbulence and the dynamics of coherent structures, Part I: coherent structures. *Quarterly of Applied Mathematics* **45** (1987), 561–571.
- [250] Sivanesapillai, R.: *Pore-scale study of non-Darcian fluid flow in porous media using Smoothed-Particle Hydrodynamics*. Dissertation, University of Bochum 2016.
- [251] Smith, G. D.: *Numerical solution of partial differential equations: finite difference methods*. Oxford university press 1985.
- [252] Smith, J. H. & Humphrey, J. A.: Interstitial transport and transvascular fluid exchange during infusion into brain and tumor tissue. *Microvascular Research* **73** (2007), 58–73.
- [253] Stefan, J.: Über das Gleichgewicht und die Bewegung, insbesondere die Diffusion von Gasgemengen. *Sitzungsberichte der Kaiserlichen Akademie der Wissenschaften (Wien), Abteilung IIa* **63** (1871), 63–124.
- [254] Støverud, K. H.; Darcis, M.; Helmig, R. & Hassanizadeh, S. M.: Modeling concentration distribution and deformation during convection-enhanced drug delivery into brain tissue. *Transport in Porous Media* **92** (2011), 119–143.
- [255] Su, S.-W. & Payne, S. J.: A two phase model of oxygen transport in cerebral tissue. In *Annual International Conference of the Engineering in Medicine and Biology Society*, 2009, pp. 4921–4924.

- [256] Succi, S.; Benzi, R. & Higuera, F.: The lattice Boltzmann equation: a new tool for computational fluid-dynamics. *Physica D: Nonlinear Phenomena* **47** (1991), 219–230.
- [257] Sulem, J. & Ouffroukh, H.: Hydromechanical behaviour of Fontainebleau sandstone. *Rock Mechanics and Rock Engineering* **39** (2006), 185.
- [258] Sun, K. & Liebschner, M. A. K.: Evolution of Vertebroplasty: A Biomechanical Perspective. *Annals of Biomedical Engineering* **32** (2004), 77–91.
- [259] Swartz, M. A.; Kaipainen, A.; Netti, P. A.; Brekken, C.; Boucher, Y.; J. Grodzinsky, A. & Jain, R. K.: Mechanics of interstitial-lymphatic fluid transport: theoretical foundation and experimental validation. *Journal of Biomechanics* **32** (1999), 1297–1307.
- [260] Syahrom, A.; Kadir, M. R. A.; Abdullah, J. & Öchsner, A.: Permeability studies of artificial and natural cancellous bone structures. *Medical Engineering & Physics* **35** (2013), 792–799.
- [261] Syková, E. & Nicholson, C.: Diffusion in brain extracellular space. *Physiological reviews* **88** (2008), 1277–1340.
- [262] Szabó, I.: *Geschichte der mechanischen Prinzipien und ihrer wichtigsten Anwendungen*. Birkhaeuser Verlag, Basel-Boston-Berlin 1977.
- [263] Taylor, Z. & Miller, K.: Reassessment of brain elasticity for analysis of biomechanics of hydrocephalus. *Journal of Biomechanics* **37** (2004), 1263–1269.
- [264] Teo, J. C. M.: *Patient specific finite volume modeling for intraosseous PMMA cement flow simulation in vertebral cancellous bone*. Dissertation, University of Singapore 2007.
- [265] Teo, J. C. M.; Si-Hoe, K. M.; Keh, J. E. L. & Teoh, S. H.: Correlation of cancellous bone microarchitectural parameters from microct to ct number and bone mechanical properties. *Materials Science and Engineering* **27** (2007), 333–339.
- [266] Teo, J. C. M. & Teoh, S. H.: Permeability study of vertebral cancellous bone using micro-computational fluid dynamics. *Computer Methods in Biomechanics and Biomedical Engineering* **15** (2012), 417–423.
- [267] Teoh, S. H. & Chui, C. K.: Bone material properties and fracture analysis: Needle insertion for spinal surgery. *Journal of the Mechanical Behavior of Biomedical Materials* **1** (2008), 115–139.
- [268] Thom, A. & Ricken, T.: Development of a thermodynamically consistent model towards biogeochemical processes within Antarctic sea ice microstructure within the extended Theory of Porous Media (eTPM). In Zigoni, A. (ed.): *Advances in Engineering Materials, Structures and Systems: Innovations, Mechanics and Applications*, CRC Press, Cape Town, 2019, pp. 292–296.

- [269] Trivedi, Z.: *Theoretical and numerical investigations of fluid flow in porous media with regular microstructures*. Master thesis, Report Nr. 18-II-10 of the Institute of Applied Mechanics (CE), University of Stuttgart 2018.
- [270] Truesdell, C.: *Rational Thermodynamics*, 2nd edn. Springer-Verlag, New York 1984.
- [271] Tuch, D. S.; Wedeen, V. J. & Dale, A. M.: Conductive tensor mapping of the human brain using diffusion tensor MRI. *Proceedings of the National Academy of Sciences USA* **98** (2001), 11697–11701.
- [272] Utsumi, Y.; Sano, Y.; Funada, R.; Ohtani, J. & Fujikawa, S.: Seasonal and perennial changes in the distribution of water in the sapwood of conifers in a sub-frigid zone. *Plant Physiology* **131** (2003), 1826–1833.
- [273] Valdes-Parada, F. J.; Ochoa-Tapia, J. A. & Alvarez-Ramirez, J.: Validity of the permeability Carman–Kozeny equation: a volume averaging approach. *Physica A: Statistical Mechanics and its Applications* **388** (2009), 789–798.
- [274] Violeau, D.: *Fluid mechanics and the SPH method: theory and applications*. Oxford University Press 2012.
- [275] Vogelbaum, M. A.: Convection enhanced delivery for treating brain tumors and selected neurological disorders: symposium review. *Journal of Neuro-Oncology* **83** (2007), 97–109.
- [276] Voges, J.; Reszka, R.; Gossmann, A.; Dittmar, C.; Richter, R.; Garlip, G.; Kracht, L.; Coenen, H. H.; Sturm, V.; Wienhard, K.; Heiss, W.-D. & Jacobs, A. H.: Imaging-guided convection-enhanced delivery and gene therapy of glioblastoma. *Annals of Neurology* **54** (2003), 479–487.
- [277] Wagner, A.: *Extended modelling of the multiphasic human brain tissue with application to drug-infusion processes*. Dissertation, Report No. II-27 of the Institute of Applied Mechanics (CE), University of Stuttgart 2014.
- [278] Wagner, A.; Eggenweiler, E.; Weinhardt, F.; Trivedi, Z.; Krach, D.; Lohrmann, C.; Jain, K.; Karadimitriou, N.; Bringedal, C.; Volland, P.; Holm, C.; Class, H.; Steeb, H. & Rybak, I.: Permeability estimation of regular porous structures: a comparison of methods. *Transport in Porous Media* **138** (2021), 1–23.
- [279] Wagner, A. & Ehlers, W.: Continuum-mechanical analysis of human brain tissue. *Proceedings in Applied Mathematics and Mechanics* **10** (2010), 99–100.
- [280] Wagner, A. & Ehlers, W.: Theoretical and numerical aspects in the multiphasic modelling of human brain tissue. *Proceedings in Applied Mathematics and Mechanics* **15** (2015), 117–118.
- [281] Wagner, A.; Fink, D.; Schröder, P. & Ehlers, W.: Towards a virtual mechanical human brain. *Proceedings in Applied Mathematics and Mechanics* **17** (2017), 225–226.

- [282] Wang, Y.; Wei, G.-W. & Yang, S.: Partial differential equation transform-variational formulation and fourier analysis. *International Journal for Numerical Methods in Biomedical Engineering* **27** (2011), 1996–2020.
- [283] Wei, G. W.: Generalized perona-malik equation for image restoration. *IEEE Signal processing letters* **6** (1999), 165–167.
- [284] Weickert, J.: *Anisotropic Diffusion in Image Processing*. B. G. Teubner 1998.
- [285] Wendland, H.: Piecewise polynomial, positive definite and compactly supported radial functions of minimal degree. *Advances in computational Mathematics* **4** (1995), 389–396.
- [286] White, D. R.; Woodard, H. Q. & Hammond, S. M.: Average soft-tissue and bone models for use in radiation dosimetry. *British Journal of Radiology* **60** (1987), 907–913.
- [287] Widmer, R. & Ferguson, S. J.: A Mixed Boundary Representation to Simulate the Displacement of a Biofluid by a Biomaterial in Porous Media. *Journal of Biomechanical Engineering* **133** (2011).
- [288] Widmer, R. & Ferguson, S. J.: On the interrelationship of permeability and structural parameters of vertebral trabecular bone: a parametric computational study. *Computer Methods in Biomechanics and Biomedical Engineering* (2012).
- [289] Wild, C. P. & Stewart, B. W.: *World Cancer Report 2014*. World Health Organization Geneva (Switzerland) 2014.
- [290] Wirth, B. & Sobey, I.: Analytic solution during an infusion test of the linear unsteady poroelastic equations in a spherically symmetric model of the brain. *Mathematical Medicine and Biology* **26** (2009), 25–61.
- [291] Wirtz, D.; Sorensen, D. C. & Haasdonk, B.: A posteriori error estimation for DEIM reduced nonlinear dynamical systems. *SIAM Journal on Scientific Computing* **36** (2014), A311–A338.
- [292] Wolfram, U.; Gross, T.; Pahr, D. H.; Schwiedrzik, J.; Wilke, H.-J. & Zysset, P. K.: Fabric-based Tsai-Wu yield criteria for vertebral trabecular bone in stress and strain space. *Journal of the Mechanical Behavior of Biomedical Materials* **15** (2012), 218–228.
- [293] Woltman, R.: *Beyträge zur Hydraulischen Architektur, Vol. 3*. Dietrich, Göttingen 1794.
- [294] Xu, P. & Yu, B.: Developing a new form of permeability and Kozeny–Carman constant for homogeneous porous media by means of fractal geometry. *Advances in water resources* **31** (2008), 74–81.

- [295] Yeo, S. Y.; Xie, X.; Sazonov, I. & Nithiarasu, P.: Segmentation of biomedical images using active contour model with robust image feature and shape prior. *International Journal for Numerical Methods in Biomedical Engineering* **30** (2014), 232–248.
- [296] Yosibash, Z.; Trabelsi, N.; Myers, K. & Milgrom, C.: Automated patient-specific method for biomechanical analysis of bone (2018), US Patent 9,937,011.
- [297] Yun, M.; Yu, B.; Zhang, B. & Huang, M.: Geometry model for tortuosity of stream-tubes in porous media with spherical particles. *Chinese Physics Letters* **22** (2005), 1464–1467.
- [298] Zeiser, T.; Bashoor-Zadeh, M.; Darabi, A. & Baroud, G.: Pore-scale analysis of Newtonian flow in the explicit geometry of vertebral trabecular bones using lattice Boltzmann simulation. *Proceedings of the Institution of Mechanical Engineers, Part H: Journal of Engineering in Medicine* **222** (2008), 185–194.
- [299] Zhang, J.; Yan, C.-H.; Chui, C.-K. & Ong, S. H.: Accurate Measurement of Bone Mineral Density Using Clinical CT Imaging With Single Energy Beam Spectral Intensity Correction. *IEEE Transactions on Medical Imaging* **29** (2010), 1382–1389.
- [300] Zhu, Y.; Fox, P. J. & Morris, J. P.: A pore-scale numerical model for flow through porous media. *International Journal for Numerical and Analytical Methods in Geomechanics* **23** (1999), 881–904.
- [301] Zienkiewicz, O. C. & Taylor, R. L.: *The Finite Element Method*, 5th edn. Butterworth-Heinemann, Oxford 2000.
- [302] Zinatbakhsh, S.: *Coupled problems in the mechanics of multi-physics and multi-phase materials*. Dissertation, Report No. II-30 of the Institute of Applied Mechanics (CE), University of Stuttgart 2015.
- [303] Zysset, P. K.: A review of morphology-elasticity relationships in human trabecular bone: theories and experiments. *Journal of Biomechanics* **36** (2003), 1469–1485.



## Presently published contributions in this report series

- II-1 Gernot Eipper: *Theorie und Numerik finiter elastischer Deformationen in fluid-gesättigten porösen Festkörpern*, 1998.
- II-2 Wolfram Volk: *Untersuchung des Lokalisierungsverhaltens mikropolarer poröser Medien mit Hilfe der Cosserat-Theorie*, 1999.
- II-3 Peter Ellsiepen: *Zeit- und ortsadaptive Verfahren angewandt auf Mehrphasenprobleme poröser Medien*, 1999.
- II-4 Stefan Diebels: *Mikropolare Zweiphasenmodelle: Formulierung auf der Basis der Theorie Poröser Medien*, 2000.
- II-5 Dirk Mahnkopf: *Lokalisierung fluidgesättigter poröser Festkörper bei finiten elasto-plastischen Deformationen*, 2000.
- II-6 Heiner Müllerschön: *Spannungs-Verformungsverhalten granularer Materialien am Beispiel von Berliner Sand*, 2000.
- II-7 Stefan Diebels (Ed.): *Zur Beschreibung komplexen Materialverhaltens: Beiträge anlässlich des 50. Geburtstages von Herrn Prof. Dr.-Ing. Wolfgang Ehlers*, 2001.
- II-8 Jack Widjajakusuma: *Quantitative Prediction of Effective Material Parameters of Heterogeneous Materials*, 2002.
- II-9 Alexander Droste: *Beschreibung und Anwendung eines elastisch-plastischen Materialmodells mit Schädigung für hochporöse Metallschäume*, 2002.
- II-10 Peter Blome: *Ein Mehrphasen-Stoffmodell für Böden mit Übergang auf Interface-Gesetze*, 2003.
- II-11 Martin Ammann: *Parallel Finite Element Simulations of Localization Phenomena in Porous Media*, 2005.
- II-12 Bernd Markert: *Porous Media Viscoelasticity with Application to Polymeric Foams*, 2005.
- II-13 Saeed Reza Ghadiani: *A Multiphasic Continuum Mechanical Model for Design Investigations of an Effusion-Cooled Rocket Thrust Chamber*, 2005.
- II-14 Wolfgang Ehlers & Bernd Markert (Eds.): *Proceedings of the 1st GAMM Seminar on Continuum Biomechanics*, 2005.
- II-15 Bernd Scholz: *Application of a Micropolar Model to the Localization Phenomena in Granular Materials: General Model, Sensitivity Analysis and Parameter Optimization*, 2007.

- II-16** Wolfgang Ehlers & Nils Karajan (Eds.): *Proceedings of the 2nd GAMM Seminar on Continuum Biomechanics*, 2007.
- II-17** Tobias Graf: *Multiphasic Flow Processes in Deformable Porous Media under Consideration of Fluid Phase Transitions*, 2008.
- II-18** Ayhan Acartürk: *Simulation of Charged Hydrated Porous Materials*, 2009.
- II-19** Nils Karajan: *An Extended Biphasic Description of the Inhomogeneous and Anisotropic Intervertebral Disc*, 2009.
- II-20** Bernd Markert: *Weak or Strong – On Coupled Problems In Continuum Mechanics*, 2010.
- II-21** Wolfgang Ehlers & Bernd Markert (Eds.): *Proceedings of the 3rd GAMM Seminar on Continuum Biomechanics*, 2012.
- II-22** Wolfgang Ehlers: *Poröse Medien – ein kontinuumsmechanisches Modell auf der Basis der Mischungstheorie*, 2012. Nachdruck der Habilitationsschrift aus dem Jahr 1989 (Forschungsberichte aus dem Fachbereich Bauwesen der Universität-GH-Essen 47, Essen 1989).
- II-23** Hans-Uwe Rempler: *Damage in multi-phasic Materials Computed with the Extended Finite-Element Method*, 2012.
- II-24** Irina Komarova: *Carbon-Dioxide Storage in the Subsurface: A Fully Coupled Analysis of Transport Phenomena and Solid Deformation*, 2012.
- II-25** Yousef Heider: *Saturated Porous Media Dynamics with Application to Earthquake Engineering*, 2012.
- II-26** Okan Avci: *Coupled Deformation and Flow Processes of Partial Saturated Soil: Experiments, Model Validation and Numerical Investigations*, 2013.
- II-27** Arndt Wagner: *Extended Modelling of the Multiphasic Human Brain Tissue with Application to Drug-Infusion Processes*, 2014.
- II-28** Joffrey Mabuma: *Multi-Field Modelling and Simulation of the Human Hip Joint*, 2014.
- II-29** Robert Krause: *Growth, Modelling and Remodelling of Biological Tissue*, 2014.
- II-30** Seyedmohammad Zinatbakhsh: *Coupled Problems in the Mechanics of Multi-Physics and Multi-Phase Materials*, 2015.
- II-31** David Koch: *Thermomechanical Modelling of Non-isothermal Porous Materials with Application to Enhanced Geothermal Systems*, 2016.
- II-32** Maik Schenke: *Parallel Simulation of Volume-coupled Multi-field Problems with Special Application to Soil Dynamics*, 2017.

- II-33** Steffen Mauthe: *Variational Multiphysics Modeling of Diffusion in Elastic Solids and Hydraulic Fracturing in Porous Media*, 2017.
- II-34** Kai Häberle: *Fluid-Phase Transitions in a Multiphasic Model of CO<sub>2</sub> Sequestration into Deep Aquifers: A fully coupled analysis of transport phenomena and solid deformation*, 2017.
- II-35** Chenyi Luo: *A Phase-field Model Embedded in the Theory of Porous Media with Application to Hydraulic Fracturing*, 2018.
- II-36** Sami Bidier: *From Particle Mechanics to Micromorphic Continua*, 2019.
- II-37** Davina Fink: *Model Reduction applied to Finite-Element Techniques for the Solution of Porous-Media Problems*, 2019.
- II-38** Jan Lukas Eurich: *A quasi-double-porosity thermo-hydro-mechanical model with application to plant tissues*, 2021.
- II-39** Arndt Wagner: *Continuum Mechanics of Multicomponent Materials – Modelling, Numerics and Applications for Biological Materials in the Framework of the Theory of Porous Media*, 2021.

